Contribution à l'estimation de canal multi-trajets dans un contexte de modulation OFDM

Vincent Savaux

N° d'ordre : 2013-28-TH

SUPELEC

Ecole Doctorale MATISSE
« Mathématiques, Télécommunications, Informatique, Signal, Systèmes Electroniques »

THÈSE DE DOCTORAT

DOMAINE : STIC
Spécialité : Télécommunications

Soutenue le 29 novembre 2013

par :

Vincent SAVAUX

Contribution à l'estimation de canal multi-trajets dans un contexte de modulation OFDM

Directeur de thèse :	Yves LOUËT	Professeur à Supélec, Rennes
Co-directeur de thèse :	Moïse DJOKO-KOUAM	Enseignant-chercheur à L'ECAM Rennes

Composition du jury :

Président du jury :	Didier LE RUYET	Professeur au CNAM, Paris
Rapporteurs :	Philippe CIBLAT	Professeur à Télécom ParisTech, Paris
	Christophe LAOT	Professeur à Télécom Bretagne, Brest
Examinateurs :	Dirk SLOCK	Professeur à EURECOM, Sophia Antipolis
Membres invités :	Alexandre SKRZYPCZAK	Ingénieur de recherche à Zodiac Aerospace, Caen

Remerciements

Je tiens tout d'abord à remercier chaleureusement Yves Louët, Moïse Djoko-Kouam et Alexandre Skrzypczak d'avoir respectivement dirigé, co-dirigé et co-encadré cette thèse. Merci tout d'abord de m'avoir proposé un sujet, ainsi que pour le temps passé à me conseiller, à m'apporter vos expériences, et merci aussi pour la confiance et l'autonomie que vous m'avez accordées.

Je remercie Christophe Laot et Philippe Ciblat d'avoir accepté d'être rapporteur de mon manuscrit de thèse. Vos remarques et critiques sont particulièrement constructives et, je l'espère, vont me permettre d'enrichir encore le travail effectué pendant trois ans. Merci aussi à Dirk Slock et Didier Le Ruyet pour leurs rôles d'examinateur et président de jury lors de ma soutenance.

Merci aux permanents de l'ECAM Rennes qui m'ont accueilli pendant trois ans comme collègue après m'avoir eu pour certains trois ans comme élève. Merci aussi aux professeurs et enseignants-chercheurs de l'équipe SCEE de Supélec pour leur accueil, leurs avis, critiques et conseils toujours constructifs, sur le plan scientifique pur et sur le milieu de la recherche en général. Merci à eux de m'accueillir maintenant en post-doc.

Bien sûr, un grand merci à tous les stagiaires, doctorants et post-doc avec qui j'ai pu travailler ou passé de bons moments conviviaux. Je pense à Geoffroy, Matthieu, Pierre-Luc à l'ECAM, et à Supélec Abel, Caroline, Catherine, Eren, Hadi, Hanan, Jérôme, Lama, Marwa, Oussama, Samba, Sumit, Xiguang et Ziad. J'espère continuer à partager avec vous, que ce soit pour le travail ou dans un cadre moins sérieux, et je vous souhaite à tous bon courage pour l'accomplissement de vos thèses ou/et une belle réussite professionnelle.

Il serait impossible de ne pas mentionner et remercier aussi ceux qui ont eu la patience de m'écouter leur parler passionnément de mon sujet, qui m'ont sorti la thèse de l'esprit parfois, et m'ont remotivé pour m'y remettre d'autres fois, et qui ont eu la gentillesse de me suivre jusqu'au bout. Un grand merci Adil, Alex, Angie, Caro, Fred, Gaël, Gwen, Hannah, James, Jo, Joëlle, Johann, Lolo, Nico, Pierrot, Pilou, Polo, Romain, Sosso, Thété, ainsi qu'à tous les autres tourangeaux, parisiens et rennais que j'aurais pu oublier par mégarde. Par dessus tout, je souhaite exprimer ma gratitude à Laure, qui m'a écouté, soutenu et supporté tout au long de ma thèse. Un immense merci à toi !

Enfin, je remercie ma famille, et tout particulièrement mes parents, ainsi que mes frères Benoît et Romain. Vous m'avez motivé et m'avez fait confiance pour toujours aller plus loin. La réussite de cette thèse est aussi le fruit de votre soutien, aussi je la partage avec vous.

Table des matières

Acronyms

ACA-LMMSE Artificial Channel Aided-Linear Minimum Mean Square Error
AWGN Additive White Gaussian Noise
BER Bit Error Rate
BPSK Binary Phase Shift Keying
BS Base Station
CCIR Consultative Committee for International Radio
CDD Cyclic Delay Diversity
CIR Channel Impulse Response
CP Cyclic Prefix
DAB Digital Audio Broadcasting
DD Delay Diversity
DFT Discrete Fourier Transform
DRM Digital Radio Mondiale
DVB-T Digital Video Broadcasting-Terrestrial
GI Guard Interval
ICI Intercarrier Interference
IDFT Inverse Discrete Fourier Transform
IR Impulse Response
ISI InterSymbol Interference
LMMSE Linear Minimum Mean Square Error
LOS Line Of Sight
LS Least Square
MIMO Multi Input Multi Output
ML Maximum Likelyhood
MMSE Minimum Mean Square Error
MSE Mean Square Error
NLOS Non Line Of Sight
NMSE Normalized Mean Square Error
NN Nearest Neighbor

OFDM Orthogonal Frequency Division Multiplexing

PD Phase Diversity

pdf Probability Density Function

PSD Power Spectral Density

PU Primary User

QAM Quadrature Amplitude Modulation

RISIC Residual InterSymbol Interference Cancellation

ROC Receiver Operating Characteristic

RS Reed Solomon

RSB Rapport signal-Ãă-bruit

SFN Single Frequency Network

SISO Single Input Single Output

SNR Signal to Noise Ratio

SU Secondary User

TEB Taux d'Erreur Binaire

WSSUS Wide Sense Stationary Uncorrelated Scattering

Notations

x	Scalaire / Scalar
x^*	Conjugué de x / Complex conjugate of x
$\hat{x}$	Estimation de la variable x / Estimate of the variable x
$\mathbf{x}$	Vecteur (domaine temporel) / Vector (time domain)
$\mathbf{X}$	Vecteur (domaine fréquentiel) / Vector (frequency domain)
$\underline{\mathbf{X}}$	Matrice / Matrix
$\underline{\mathbf{X}}^T$	Matrice transposée / Transpose matrix
$\underline{\mathbf{X}}^H$	Matrice transposée conjuguée (ou transposée Hermitienne) / Conjugate transpose matrix (or Hermitian transpose)
$\underline{\mathbf{X}}^{-1}$	Matrice inverse / Invere matrix
$\underline{\mathbf{R}}_H$	Matrice d'autocovariance fréquentielle / Frequency autocovariance matrix
$E\{.\}$	Espérance mathématique / Mathematical expectation
$\mathfrak{Re}(.)$	Partie réelle / Real part
$\mathfrak{Im}(.)$	Partie imaginaire / Imaginary part
$tr(.)$	Application trace / Trace application
$\|.\|$	Module / Modulus
$\|\|.\|\|$	Norme Euclidienne / Euclidian Norm
$\|\|.\|\|_F$	Norme de Frobenius / Frobenius norm
$(. \star .)$	Produit de convolution / Convolution
$\underline{\mathbf{I}}$	Matrice identité / Identity matrix
$\mathcal{N}(\mu, \sigma^2)$	Loi normale de moyenne μ et de variance σ^2 / Normal ditribution with mean μ and variance σ^2
$\delta(t)$	Impulsion de Dirac / Dirac delta function
$\mathcal{U}(.)$	Fonction de Heaviside / Heaviside step function
$J_0(.)$	Fonction de Bessel de première espèce et d'ordre zéro / Bessel function of the first kind with order zero
$I_0(.)$	Fonction de Bessel modifiée de première espèce et d'ordre zéro / Modified Bessel function of the first kind with order zero
$\mathrm{erf}(.)$	Fonction d'erreur / Error function
$\Pi(.)$	Fonction porte / Rectangular function
δ	Symbol de Kronecker / Kronecker delta
M	Taille de la FFT ou DFT / FFT or DFT size
T_C	Temps de cohérence / Coherence time
T_{CP}	Durée du préfixe cyclique / Cyclic prefix duration
T_s	Temps symbol / Symbol time duration

τ_s	Temps d'échantillonage / Sampling time
$B(.)$	Biais d'estimation / Bias of estimation
B_C	Bande de cohérence / Coherence bandwidth
$\mathcal{P}$	Puissance des pilotes / Pilots power
$\Gamma(\tau)$	Profil d'intensité du canal / Channel intensity profile
λ_m	Valeur propre de la matrice de covariance du canal / Eigenvalue of the channel covariance matrix
σ^2	Variance du bruit / Noise variance
M_2	Moment de second ordre du signal / Second order-moment of the signal
Tx	Antenne d'émission / Transmit antenna
Rx	Antenne de réception / Receiving antenna
P_d	Probabilité de détection / Detection Probability
P_{fa}	Probabilité de fausse alarme / False alarm probability
δ_f	Ecart fréquentiel entre deux pilote consécutifs / Frequency gap between two consecutive pilot tones

Résumé étendu

Introduction

Dans les systèmes de communications sans fil, l'environnement situé entre une antenne d'émission et une antenne de réception peut perturber le signal. En effet, le signal reçu est une somme de plusieurs versions retardées du signal émis. On dit alors que le signal est émis dans un canal multi-trajets. Ce type de canal engendre des évanouissements en fréquence, c'est à dire des trous dans le spectre, pouvant être destructeurs pour le signal.

Une solution pour lutter contre ces phénomènes est d'utiliser une modulation multiporteuses, telle que l'OFDM (Orthogonal Frequency Division Multiplexing). Le principe est de diviser la bande fréquentielle du signal en sous canaux étroits, chacun portant une partie de l'information. Ainsi, si un évanouissement fréquentiel dû au canal affecte une partie de l'information, le reste est transmis sans perturbation. Associé à un codage canal, le CODFM (pour Coded OFDM) garantit un faible nombre d'erreurs dans le signal reçu, ce qui fait que cette modulation est largement utilisée dans les standards actuels.

Un autre avantage de l'OFDM est que, considérant que chaque sous canal est un canal plat, l'égalisation est facile car il suffit d'effectuer une simple division du signal reçu par le gain du canal pour récupérer le symbole émis. Ainsi, la qualité de l'égalisation est directement liée à la précision de l'estimation de canal. Cette dernière a donc un rôle clef dans la performance du système de communication et c'est pourquoi on trouve un grand nombre de publications sur le sujet.

Dans ce résumé de thèse seront présentées deux méthodes permettant d'approcher l'estimateur optimal, appelé LMMSE (Linear Minimum Mean Square Error) en évitant ses inconvénients. En plus des canaux "classiques", on abordera deux cas particuliers, où les délais des canaux seront supposés très longs, ou à l'inverse, très courts. De plus, une étude statistique des erreurs d'interpolation dans le cadre de l'estimation de canal sera proposée. La plupart des simulations sont effectuées en suivant le standard DRM/DRM+ [1], utilisé pour la transmission radio dans les actuelles bandes AM et FM. Cependant, on remarquera que les méthodes proposées peuvent être appliquées dans un contexte général d'une transmission OFDM.

Le mémoire de thèse est composé des parties suivantes :

- Dans un premier temps, on rappelle les fondamentaux concernant le canal de propagation et la transmission d'un signal OFDM.
- Un état de l'art des principales méthodes d'estimation de canal dans un contexte OFDM est proposé. Deux estimateurs sont principalement détaillés : l'estimateur LS (pour Least Square, ou moindres carrés) et l'estimateur LMMSE.

- Une méthode appelée ACA-LMMSE (pour Artificial Channel Aided-LMMSE), qui permet d'éviter la connaissance *a priori* de la matrice de covariance du canal nécessaire à l'estimation LMMSE, est proposée. Cette méthode permet aussi de réduire le nombre de calculs par rapport à l'estimateur LMMSE classique, dans un contexte de canal variant dans le temps. De plus, il est possible de combiner cette méthode avec un algorithme appelé RISIC (pour Residual ISI Cancellation)
- Pour ACA-LMMSE, le niveau de bruit est supposé connu du récepteur, or en pratique, la variance du bruit nécessite une estimation. Une méthode d'estimation conjointe du canal et du rapport signal à bruit (RSB) est alors présentée dans une nouvelle partie. L'estimateur se base sur le critère de l'erreur quadratique moyenne minimum (ou MMSE en anglais). Comme l'estimation d'un paramètre alimente l'estimation de l'autre, l'estimateur proposé est itératif. De plus, il est montré que l'algorithme peut servir à la détection de bandes libres dans le cadre de la radio intelligente.
- L'estimation de canal nécessite parfois une interpolation pour estimer les coefficients entre deux points connus appelés pilotes. Cependant, les interpolations créent des erreurs résiduelles ayant un impact sur la qualité de l'estimation. Dans cette partie, une analyse statistique des erreurs d'interpolation pour l'estimation d'un canal de Rayleigh est effectuée. Deux mesures de performance, l'erreur quadratique moyenne (ou MSE en anglais) et la borne inférieure du taux d'erreur binaire, sont analytiquement déduits de cette étude.
- Dans une dernière partie, une application de la diversité de délai cyclique (ou CDD en anglais) aux réseaux de type SFN (Single Frequency Network) est présentée. Dans ce type de réseau, quand le récepteur se situe dans les zones de recouvrement entre deux cellules apparait un phénomène d'évanouissement large bande, qui peut perturber la totalité du signal. En effet, la diversité fréquentielle du COFDM est perdue, car toute les porteuses du signal sont touchées. La solution est alors d'augmenter artificiellement la sélectivité fréquentielle du canal grâce à la CDD. Une application à la norme DRM/DRM+ est effectuée, et il est montré que l'augmentation de la sélectivité fréquentielle par la CDD impacte aussi la qualité de l'estimation de canal.

Cette dernière étude a été menée dans le cadre du projet OCEAN (Optimisation d'une Chaîne Emission-Réception pour la Radio Numérique terrestre), projet collaboratif rassemblant deux partenaires industriels (Digidia et Kenta) et deux partenaires académique (ECAM Rennes et Télécom Bretagne), et financé par la région Bretagne et Rennes métropole.

r.1 Contexte et modèle

Dans cette partie, on va rappeler les éléments importants concernant le canal de propagation à trajets multiples. De plus, on formalisera l'écriture de la transmission d'un signal OFDM dans ce type de canal.

r.1.1 Le canal de transmission multi-trajet

r.1.1.1 Le modèle WSSUS

Dans un grand nombre de transmissions, les antennes d'émission et de réception ne sont pas en ligne de mire. Dans ce cas, le signal est réfléchi, diffracté ou diffusé par l'environnement de propagation, composé par des bâtiments, véhicules ou des obstacles naturels. Le signal émis passe alors par plusieurs trajets différents avant d'être reçu. Ce type d'environnement, appelé canal multi-trajet, est caractérisé par le nombre de trajets L, les retards τ_l et les gains h_l, $l = 0, 1, ..., L-1$ des différents trajets qui le composent.

D'une manière générale, la réponse impulsionnelle du canal h s'exprime :

$$h(t, \tau) = \sum_{l=0}^{L-1} h_l(t)\delta(\tau - \tau_l), \tag{r.1}$$

où δ est l'impulsion de Dirac. On considèrera par la suite le très répandu modèle de canal WSSUS (pour Wide Sense Stationary Uncorrelated Scattering) décrit par Bello [2]. Plus précisément, pour tout $l = 0, 1, ..., L-1$ les coefficients h_l sont stationnaires au sens large, *i.e.* la moyenne $E\{h_l(t)\}$ est indépendante du temps et $E\{h_l(t_1)h_l(t_2)^* = 0\}$ si $t_1 \neq t_2$, et décorrélés, *i.e.* $E\{h_{l_1}(t)h_{l_2}(t)^* = 0\}$ si $l_1 \neq l_2$, où $E\{.\}$ est l'espérance mathématique et * la conjugaison complexe.

r.1.1.2 Le canal Rayleigh

On va maintenant caractériser la statistique suivie par $|h(t)|$. En première approximation, on considère dans la suite du résumé que du point de vue du récepteur, le canal $h(t)$ est une somme de K composantes indépendantes de moyennes nulles provenant de toutes les directions et telles que K tend vers l'infini. En appliquant le théorème central limite, on déduit que $h(t)$ suit une loi gaussienne centrée, et donc que $|h(t)|$ suit une distribution de Rayleigh [3], notée $p_{r,Ray}$. Sa variance σ_h^2 est égale à $E\{|h(t)|^2\}$. Alors, pour une variable positive r, $p_{r,Ray}(r)$ s'exprime

$$p_{r,Ray}(r) = \frac{r}{\sigma_h^2} e^{\frac{-r^2}{2\sigma_h^2}}. \tag{r.2}$$

Le canal de Rayleigh est un modèle largement utilisé dans la littérature, car il est simple et approxime bien la réalité. Cependant, des modèles plus spécifiques ou plus proches des mesures pratiques ont été proposés, tels que le modèle de Weibull [4], celui de Nakagami [5], ou celui généralisé donné par la distribution $\kappa - \mu$ [6].

r.1.1.3 Relations temps-fréquence du canal

Dans un grand nombre d'applications, il est plus intéressant (car plus simple) d'étudier le canal dans le domaine fréquentiel. La réponse fréquentielle du canal $H(t, f)$ est obtenue

en appliquant une transformée de Fourier (notée FT, pour Fourier Transform) à la réponse impulsionnelle (r.1). On obtient alors

$$\begin{aligned} H &= FT_{\tau}(h) \\ \Rightarrow H(t,f) &= \int_{-\infty}^{+\infty} h(t,\tau)e^{-2j\pi f\tau}d\tau \\ H(t,f) &= \sum_{l=0}^{L-1} h_l(t)e^{-2j\pi f\tau_l}. \end{aligned} \tag{r.3}$$

On remarque que la réponse fréquentielle s'obtient en appliquant la TF sur la variable de retard τ. La réponse fréquentielle $H(t,f)$ est donc une fonction pouvant varier dans le temps t, comme l'illustre la figure r.1. Quand la variation du canal est très lente, on dit qu'il est quasi-statique, s'il ne varie pas au cours du temps, le canal est dit statique.

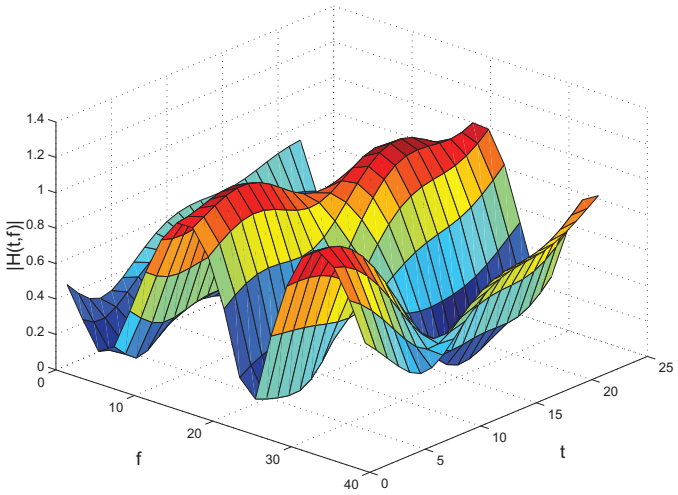

FIGURE r.1 – Réponse fréquentielle du canal $H(t,f)$.

On définit aussi deux fonctions très utilisées dans le traitement du signal, car elles caractérisent statistiquement le canal dans les domaines temporels et fréquentiels :

- le profil d'intensité du canal $\Gamma(\tau)$. Un modèle couramment répandu est le profil exponentiel décroissant [7–9].
- la fonction de corrélation fréquentielle du canal $R_H(\Delta_f)$

Ce deux fonctions sont reliées par une transformée de Fourier :

$$\begin{aligned} \Gamma &= FT^{-1}_{\Delta_f}(R_H) \\ \Leftrightarrow R_H &= FT_{\tau}(\Gamma). \end{aligned} \tag{r.4}$$

Pour plus de précisions sur l'expression de la corrélation fréquentielle, on peut se référer à [7], ou à l'annexe A.1.

r.1.2 Transmission d'un signal OFDM

r.1.2.1 Représentation continue

En bande de base, dans le formalisme continu, le signal OFDM s'exprime :

$$s(t) = \sum_{n\in\mathbb{Z}} s_n(t) = \sqrt{\frac{1}{T_s}} \sum_{n\in\mathbb{Z}} \sum_{m=0}^{M-1} C_{m,n}\Pi(t - nT_s)e^{2j\pi mF_s t}, \tag{r.5}$$

où $s_n(t)$ est le $n^{\text{ème}}$ symbole OFDM, T_s est le temps symbole, $F_s = 1/T_s$ l'écart inter-porteuse et $\Pi(t)$ la fonction porte qui vaut 1 si $-\frac{T_s}{2} \leq t < \frac{T_s}{2}$ et 0 sinon. M est le nombre de porteuses (*i.e.* de sous-canaux) par symbole, donc si on note B la bande passante du signal, on a $F_s = B/M$. L'OFDM a la propriété que les porteuses composant le symbole sont orthogonales entre elles. Ainsi, il n'y a aucune interférence entre porteuses dans le domaine fréquentiel, et on peut traiter chaque porteuse indépendamment les unes des autres. Le signal reçu $u(t)$ est le produit de convolution de $s(t)$ par $h(t)$, auquel est additionné un bruit blanc gaussien noté $w(t)$. Dans le domaine fréquentiel, par propriété de la transformée de Fourier, le produit de convolution devient un produit simple :

$$u(t) = (h \star s)(t) + w(t) \tag{r.6}$$

$$\overset{FT}{\Longrightarrow} U(f) = H(f).C(f) + W(f). \tag{r.7}$$

Pour tout $m = 0, 1, ..., M-1$, $C_{m,n}$ est un symbole d'information d'une constellation donnée (e.g. BPSK, QPSK). Pour lutter contre les interférences entre symboles (qu'on notera ISI) dues aux trajets retardés du canal de transmission, on ajoute au début de chaque symbole OFDM à l'émission un intervalle de garde (GI). Si le GI est plus long que le délai maximum du canal, alors, la suppression du GI en réception permet de supprimer l'ISI. Dans la suite, on considèrera que le GI est un préfixe cyclique (CP), c'est à dire que la fin de chaque symbole OFDM est recopiée au début. Comme il est indiqué plus loin, en plus de supprimer l'ISI, l'ajout d'un CP confère des propriétés cycliques au symbole OFDM. On notera T_{CP} la durée du préfixe cyclique.

La figure r.2 montre les propriétés temporelles et fréquentielles du signal OFDM. La sous-figure r.2 (a) illustre, dans le domaine temporel, la suppression de l'ISI grâce à l'ajout du CP. La sous-figure r.2 (b) montre l'orthogonalité en fréquence des porteuses. De plus, en considérant l'écart en fréquence F_s suffisamment petit, on peut considérer le canal comme constant sur chacune des porteuses. Ainsi, si l'une d'elle est affectée par le canal de transmission, on appliquera une simple division pour retrouver la valeur de départ.

r.1.2.2 Représentation discrète

Cette représentation des porteuses parallèles amène naturellement à une représentation discrète du signal OFDM, d'autant qu'on fait un traitement numérique du signal et que la version discrète de la FT, appelée transformée de Fourier rapide (ou FFT en anglais), permet une génération simple des symboles OFDM. Dans le formalisme discret, l'utilisation du CP transforme la convolution linéaire (r.6) en convolution cyclique [10]. Après la suppression de l'intervalle de garde, le $n^{ème}$ symbole OFDM reçu est donné par :

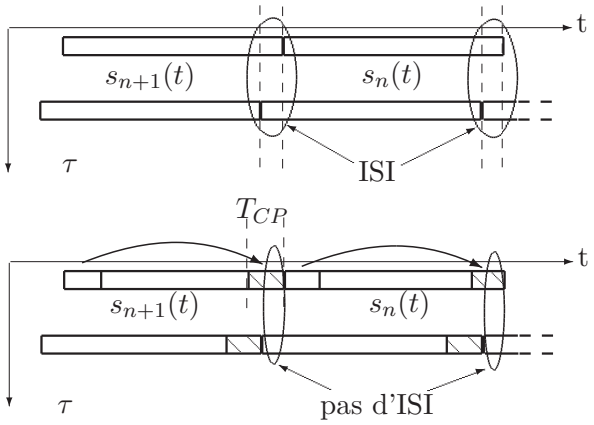

(a) Suppression de l'ISI par ajout d'un CP.

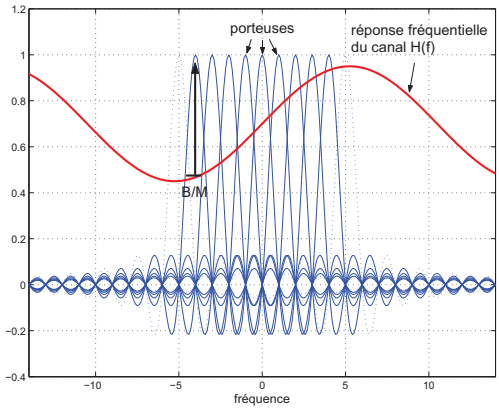

(b) Orthogonalité fréquentielle et effet d'un canal multi-trajet en fréquence.

FIGURE r.2 – Propriétés temporelles et fréquentielles de l'OFDM avec CP.

$$\mathbf{u}_n = \begin{pmatrix} h_{0,n} & 0 & \cdots & \cdots & h_{L-1,n} & \cdots & h_{1,n} \\ h_{1,n} & h_{0,n} & 0 & \ddots & \ddots & \ddots & \vdots \\ \vdots & \ddots & \ddots & & \ddots & \ddots & h_{L-1,n} \\ h_{L-1,n} & \ddots & \ddots & h_{0,n} & 0 & \ddots & 0 \\ 0 & \ddots & \ddots & & \ddots & \ddots & \vdots \\ \vdots & \ddots & \ddots & & \ddots & \ddots & 0 \\ 0 & \cdots & 0 & h_{L-1,n} & \cdots & h_{1,n} & h_{0,n} \end{pmatrix} \begin{pmatrix} s_{0,n} \\ s_{1,n} \\ \vdots \\ \vdots \\ s_{M-1,n} \end{pmatrix} + \mathbf{w}_n$$
$$= \underline{\mathbf{h}}_n \mathbf{s}_n + \mathbf{w}_n, \qquad \text{(r.8)}$$

où $\underline{\mathbf{h}}_n$ est la matrice de canal circulante de taille $M \times M$, $\mathbf{s}_n$ est le vecteur de taille $M \times 1$ contenant les échantillons de $s_n(t)$ et $\mathbf{w}_n$ le vecteur de taille $M \times 1$ contenant les échantillons du bruit. Une propriété des matrices circulantes est qu'elles sont diagonalisables dans la base de Fourier (voir [11, 12] ou Annexe A.2), dont la matrice $\underline{\mathcal{F}}$ est donnée par

$$\underline{\mathcal{F}} = \frac{1}{\sqrt{M}} \begin{pmatrix} 1 & 1 & 1 & \cdots & 1 \\ 1 & \omega & \omega^2 & \cdots & \omega^{(M-1)} \\ 1 & \omega^2 & \omega^4 & \cdots & \omega^{2(M-1)} \\ \vdots & \vdots & \vdots & \ddots & \vdots \\ 1 & \omega^{(M-1)} & \omega^{2(M-1)} & \cdots & \omega^{(M-1)^2} \end{pmatrix}, \qquad \text{(r.9)}$$

avec $\omega = e^{-\frac{2j\pi}{M}}$. On remarque que $\underline{\mathcal{F}}$ est une matrice orthonormale, *i.e.* $\underline{\mathcal{F}}\underline{\mathcal{F}}^H = \underline{\mathbf{I}}$, où $\underline{\mathbf{I}}$ est la matrice identité et ^{H} est la transformée hermitienne ou transconjugaison. C'est la matrice $\underline{\mathcal{F}}$ qui permet la transformée de Fourier rapide. On calcule alors le vecteur des échantillons fréquentiels du signal reçu par $\mathbf{U}_n = \underline{\mathcal{F}}\mathbf{u}_n$. En tenant compte du changement de base, on peut alors simplifier :

$$\begin{aligned}\mathbf{U}_n &= \underline{\mathcal{F}\mathbf{h}}_n\underline{\mathcal{F}}^H\underline{\mathcal{F}}\mathbf{s}_n + \mathbf{W}_n \\ &= \underline{\mathcal{F}\mathbf{h}}_n\underline{\mathcal{F}}^H\mathbf{C}_n + \mathbf{W}_n \\ &= \underline{\mathbf{H}}_n\mathbf{C}_n + \mathbf{W}_n, \end{aligned} \tag{r.10}$$

où $\mathbf{C}_n = \underline{\mathcal{F}}\mathbf{s}_n$ est le vecteur de taille $M \times 1$ contenant les symboles d'informations $C_{m,n}$. Par propriété de la matrice de canal $\underline{\mathbf{h}}_n$, son dual fréquentiel $\underline{\mathbf{H}}_n$ est diagonal et contient les échantillons H_m de la réponse fréquentielle qui s'expriment :

$$\begin{aligned}H_{m,n} &= \sum_{l=0}^{L-1} h_{l,n}e^{-2j\pi f_m\beta_l\tau_s} \\ &= \sum_{l=0}^{L-1} h_{l,n}e^{-2j\pi\frac{m}{M}\beta_l}, \end{aligned} \tag{r.11}$$

où $f_m = \frac{m}{M\tau_s}$ et $\beta_l = \frac{\tau_l}{\tau_s}$ sont les versions échantillonnées de f et τ_l, avec τ_s le temps d'échantillonnage. Comme $\underline{\mathbf{H}}_n$ est diagonale, on rencontre fréquemment l'équivalent de (r.10) :

$$\begin{aligned}&\mathbf{U}_n = \underline{\mathbf{H}}_n\mathbf{C}_n + \mathbf{W}_n \\ \Leftrightarrow\ &\mathbf{U}_n = \underline{\mathbf{C}}_n\mathbf{H}_n + \mathbf{W}_n, \end{aligned} \tag{r.12}$$

où $\underline{\mathbf{C}}_n$ est la matrice diagonale de taille $M \times M$ contenant les symboles d'information $C_{m,n}$. De plus, on peut écrire chacun des échantillons $U_{m,n}$ comme une simple multiplication

$$U_{m,n} = H_{m,n}C_{m,n} + W_{m,n}. \tag{r.13}$$

Etant donnée sa simplicité, cette expression est largement utilisée pour l'estimation de canal, comme il sera montré plus loin.

r.2 Techniques d'estimation : état de l'art

Parmi le grand nombre de méthodes d'estimation de canal, on s'intéresse ici aux techniques dites semi-aveugles, effectuées dans le domaine fréquentiel.

r.2.1 Les pilotes

On appelle les méthodes semi-aveugles, ou assistées par pilotes celles qui utilisent des porteuses dites "pilotes" pour effectuer l'estimation. Les pilotes sont des porteuses dont le gain, la phase et la position dans la trame OFDM sont connus de l'émetteur et du récepteur. Le motif des pilotes dans la trame OFDM dépend de la sélectivité du canal [13]. Ainsi, pour un canal très sélectif en fréquence mais pas en temps, on utilisera un préambule dans le domaine fréquentiel, où chaque sous porteuse d'un symbole OFDM donné est dédiée à l'estimation. C'est le motif utilisé quand on considère un canal quasi-statique. Pour un canal moyennement sélectif en fréquence, mais très sélectif en temps, on utilisera plutôt un préambule dans le domaine temporel, où certaines fréquences sont exclusivement dédiées à l'estimation de canal

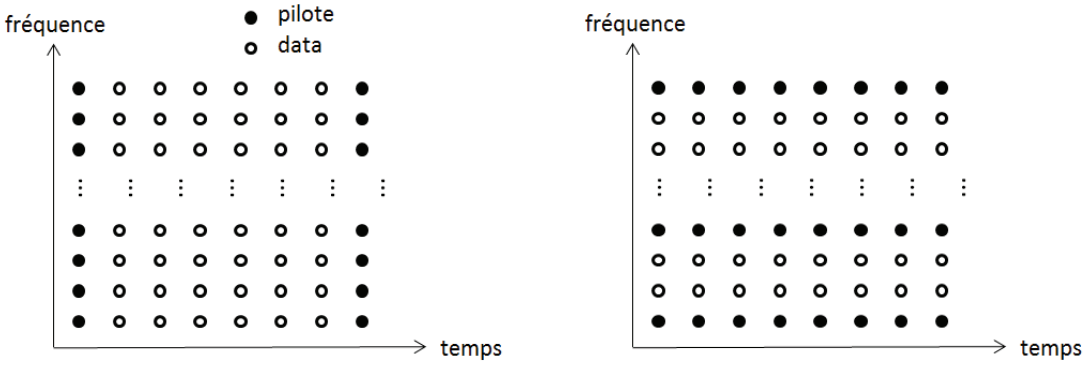

(a) Préambule dans le domaine fréquentiel. (b) Préambule dans le domaine temporel.

FIGURE r.3 – Deux motifs possibles de disposition des pilotes.

pour chaque symbole OFDM. La figure r.3 illustre ces deux dispositions : les porteuses pilotes sont en noir et les porteuses d'information en blanc.

Selon la sélectivité des canaux considérés, d'autres motifs peuvent être utilisés : dans le standard DRM/DRM+ [1], les pilotes sont disposés en quinconce, un motif rectangulaire, hexagonal ou une disposition aléatoire peuvent aussi être considérés [14]. On remarque, comme sur la figure r.3 (b), que si le canal est connu au niveau des pilotes, une interpolation sera nécessaire pour estimer la réponse fréquentielle du canal sur tout le réseau temps-fréquence. Certaines méthodes d'estimation vont être abordées par la suite.

r.2.2 Les critères LS et MMSE

Parmi les méthodes d'estimation, celles basées sur le critère des moindres carrés ou LS (pour Least Square en anglais) et sur le critère de l'erreur quadratique moyenne minimum ou MMSE (pour Minimum Mean Square Error en anglais) sont celles les plus étudiées. Les développements suivants sont effectués avec un préambule dans le domaine fréquentiel, bien qu'on verra que leur validité sera aussi montrée pour d'autres motifs. De plus, pour simplifier l'écriture, on ne notera pas l'indice n dans les prochains développements.

r.2.2.1 Estimation LS

a. Expression de $\hat{\mathbf{H}}^{LS}$

Le critère des moindres carrés vise à minimiser la fonction de coût J_{LS}, définie comme la norme au carrée de la différence entre le vecteur du signal reçu $\mathbf{U}$ et le produit du vecteur de signal émis $\mathbf{C}$ par une matrice diagonale $\underline{\mathbf{D}}$ dont les coefficients sont à optimiser :

$$J_{LS} = |\mathbf{U} - \underline{\mathbf{D}}\mathbf{C}|^2. \tag{r.14}$$

On définit la matrice optimale $\underline{\mathbf{D}}_{opt} = \underline{\hat{\mathbf{H}}}^{LS}$, où $\underline{\hat{\mathbf{H}}}^{LS}$ est l'estimation LS de la réponse fréquentielle du canal de transmission. Après développement, pour tout $m = 0, 1, ..., M-1$, la minimisation de J_{LS} donne

$$\hat{H}_m^{LS} = \frac{U_m}{C_m} = H_m + \frac{W_m}{C_m}. \tag{r.15}$$

Comme on considère un préambule, on peut réécrire (r.15) sous sa forme vectorielle :

$$\hat{\mathbf{H}}^{LS} = \mathbf{U}\underline{\mathbf{C}}^{-1} = \mathbf{H} + \mathbf{W}\underline{\mathbf{C}}^{-1}. \tag{r.16}$$

A partir de (r.16), on remarque que l'estimateur LS est sensible au bruit, ce qui sera vérifié plus loin. Plusieurs variantes de l'estimateur LS (scaled LS ou encore shifted scaled LS) sont proposées dans la littérature [15, 16].

b. Caractéristiques de l'estimation LS

On montre facilement que l'estimateur LS est non biaisé. En effet, si on note le biais $B(.)$, comme $\mathbf{W}$ est une variable gaussienne centrée, on a

$$B(\hat{\mathbf{H}}^{LS}) = E\{\hat{\mathbf{H}}^{LS} - \mathbf{H}\} = E\{\mathbf{W}\underline{\mathbf{C}}^{-1}\} = 0. \tag{r.17}$$

L'expression de l'erreur quadratique moyenne minimum de l'estimateur LS, que l'on note $MMSE_{LS}$ et développée dans [15,17,18], s'obtient après minimisation de la fonction d'erreur $J_{\hat{\mathbf{H}}^{LS}} = \frac{1}{M}E\{||\hat{\mathbf{H}}^{LS} - \mathbf{H}||_F^2\}$, où $||.||_F$ est la norme de Frobenius [1]. On obtient finalement :

$$MMSE_{LS} = \frac{1}{M}E\{tr(\mathbf{W}\underline{\mathbf{C}}^{-1}(\mathbf{W}\underline{\mathbf{C}}^{-1})^H)\} = \frac{\sigma^2}{\mathcal{P}}, \tag{r.18}$$

où $\mathcal{P} = C_m C_m^*$. On remarque que l'erreur quadratique moyenne de LS est équivalente à l'inverse du rapport signal-à-bruit RSB. On montrera dans la partie r.5 qu' il est aussi possible d'obtenir une expression de $MMSE_{LS}$ dans le cas de pilotes séparés dans la trame OFDM.

r.2.2.2 Estimation LMMSE

a. Expression de $\hat{\mathbf{H}}^{LMMSE}$

Le critère du minimum d'erreur quadratique moyenne vise à minimiser la fonction de coût J_{MMSE}, définie comme l'erreur quadratique moyenne du vecteur $\mathbf{H} - \underline{\mathbf{D}}\mathbf{U}$, comme il est montré dans [19] :

$$J_{MMSE} = E\{||\mathbf{H} - \underline{\mathbf{D}}\mathbf{U}||_F^2\}, \tag{r.19}$$

où $\underline{\mathbf{D}}$ est la matrice diagonale dont les coefficients sont à optimiser. Comme on considère que le canal est gaussien sur chaque porteuse, on appelle l'estimateur MMSE linear-MMSE, ou LMMSE [7]. Après un développement effectué dans [15], on trouve finalement l'estimation LMMSE :

$$\begin{aligned}\hat{\mathbf{H}}^{LMMSE} &= \underline{\mathbf{D}}_{opt}\mathbf{U} \\ \hat{\mathbf{H}}^{LMMSE} &= \underline{\mathbf{R}}_H(\underline{\mathbf{R}}_H + (\underline{\mathbf{C}}\underline{\mathbf{C}}^H)^{-1}\sigma^2\underline{\mathbf{I}})^{-1}\hat{\mathbf{H}}^{LS},\end{aligned} \tag{r.20}$$

où $\underline{\mathbf{R}}_H$ est la matrice de covariance du canal de taille $M \times M$ donnée par $\underline{\mathbf{R}}_H = E\{\mathbf{H}_n\mathbf{H}_n^H\}$ et σ^2. On remarque qu'une inversion et une multiplication sont nécessaires dans (r.20), ce

1. La norme matricielle de Frobenius $\underline{\mathbf{A}}$ est donnée par $||\underline{\mathbf{A}}||_F = \sqrt{tr(\underline{\mathbf{A}}\underline{\mathbf{A}}^H)}$.

qui rend LMMSE plus complexe que LS, surtout pour de grandes valeurs de M. Cependant, cet estimateur est optimal au sens de l'erreur quadratique moyenne. De plus, comme il est montré dans [7], cet estimateur peut servir d'interpolateur tout en restant optimal.

Bien que cet estimateur soit optimal, son utilisation est limitée par deux inconvénients majeurs : sa complexité, et la nécessité de connaître la matrice de covariance $\underline{\mathbf{R}}_H$, qui est *a priori* inconnue du récepteur.

b. Caractéristiques de l'estimation LMMSE

A partir de (r.20), on donne simplement le biais de l'estimateur LMMSE. Comme $\underline{\mathbf{R}}_H$ est une constante, et que $\mathbf{H}$ et $\mathbf{W}$ sont deux variables aléatoires gaussiennes centrées décorrélées, on déduit :

$$\begin{aligned} B(\hat{\mathbf{H}}^{LMMSE}) &= E\{\hat{\mathbf{H}}^{LMMSE} - \mathbf{H}\} \\ &= E\{(\underline{\mathbf{R}}_H(\underline{\mathbf{R}}_H + (\underline{\mathbf{C}}\underline{\mathbf{C}}^H)^{-1}\sigma^2\underline{\mathbf{I}})^{-1} - \underline{\mathbf{I}})\mathbf{H} \\ &\quad + \underline{\mathbf{R}}_H(\underline{\mathbf{R}}_H + (\underline{\mathbf{C}}\underline{\mathbf{C}}^H)^{-1}\sigma^2\underline{\mathbf{I}})^{-1}\mathbf{W}\underline{\mathbf{C}}^{-1}\} \\ &= 0. \end{aligned} \tag{r.21}$$

L'erreur quadratique moyenne de l'estimateur LMMSE se calcule en minimisant la fonction d'erreur $J_{\hat{\mathbf{H}}^{LMMSE}} = \frac{1}{M}E\{||\mathbf{H} - \hat{\mathbf{H}}^{LMMSE}||_F^2\}$. A partir de [15, 19], on donne directement le résultat sous sa forme matricielle :

$$MMSE_{LMMSE} = \frac{M\sigma^2}{M\mathcal{P}/\sigma^2 + tr(\underline{\mathbf{R}}_H^{-1})}. \tag{r.22}$$

On remarque dans (r.22) que l'expression de $MMSE_{LMMSE}$ nécessite l'inversion de la matrice de covariance du canal de taille $M \times M$. On a vu dans la partie r.1 que le canal est de longueur L, avec $L \leq M$. Or, L est le rang de la matrice $\underline{\mathbf{R}}_H$, donc celle-ci peut ne pas être inversible. Dans la majorité des cas, on ne peut pas utiliser (r.22) comme expression du MMSE. A partir de cette considération, une nouvelle expression scalaire de l'erreur quadratique minimum a été publiée dans [20]. Cette nouvelle expression peut être utilisée aussi bien dans le cas où $\underline{\mathbf{R}}_H$ est inversible ou non, et est donnée par :

$$MMSE_{LMMSE} = \frac{1}{M}.\frac{L^2\sigma^2}{L\mathcal{P} + \sum_{m=0}^{L-1}\frac{\sigma^2}{\lambda_m}}, \tag{r.23}$$

où λ_m, $m = 0, 1, ..., L-1$ sont les $L-1$ valeurs propres non nulles de la matrice de covariance $\underline{\mathbf{R}}_H$. On remarque que pour $L = M$, on retrouve l'équivalence entre (r.23) et (r.22).

r.2.3 Techniques d'interpolation

L'estimation LS permet d'obtenir la réponse fréquentielle (bruitée) sur les porteuses pilotes. Dans un grand nombre de cas, il est alors nécessaire d'effectuer une interpolation pour estimer le canal sur l'ensemble du réseau temps-fréquence. On a vu que LMMSE pouvait servir de filtre interpolateur. Cependant, sa complexité fait qu'on préfère souvent utiliser des interpolations plus simples, telles que celles présentées dans cette partie. Celles-ci ont la particularité d'être basées uniquement sur des polynômes interpolateurs, et n'ont besoin d'aucune caractéristique du canal ou du signal. On suppose dans la suite que P porteuses pilotes sont

régulièrement distribuées dans chaque symbole OFDM. Ainsi, on va décrire des méthodes d'interpolations sur l'axe fréquentiel.

r.2.3.1 Interpolation nearest-neighbor

L'interpolation nearest-neighbor (NN) ou dite du plus proche voisin en français, est la plus simple car elle se base sur un polynôme interpolateur de degré zéro. Si on note f_p la position fréquentielle d'un pilote et δ_f l'écart fréquentiel entre deux porteuses pilotes consécutives, alors, $\forall\ f \in [f_p - \delta_f/2, f_p + \delta_f/2]$, on obtient :

$$\hat{H}(f) = \hat{H}(f_p), \tag{r.24}$$

où $\hat{H}(f_p)$ est l'estimation de canal LS au niveau du pilote. Fig. r.4 (a) illustre le principe de l'interpolation NN autour d'une position pilote f_p. Malgré sa simplicité, il est évident que cette interpolation n'est adaptée que pour des canaux très peu sélectifs.

r.2.3.2 Interpolation linéaire

L'interpolation linéaire est elle aussi relativement simple, car elle se base sur un polynôme interpolateur de degré un. Pour une valeur $f \in [f_p, f_{p+\delta_f}]$, le canal estimé $\hat{H}(f)$ est la moyenne entre $\hat{H}(f_p)$ et $\hat{H}(f_{p+\delta_f})$, pondérée par la distance $f_{p+\delta_f} - f_p$. Ainsi, on obtient :

$$\hat{H}(f) = \hat{H}(f_p) + (f - f_p)\frac{\hat{H}(f_{p+\delta_f}) - \hat{H}(f_p)}{f_{p+\delta_f} - f_p}. \tag{r.25}$$

Fig. r.4 (b) illustre le principe de l'interpolation linéaire entre deux positions fréquentielles de pilotes f_p et $f_p + \delta_p$. Bien que plus précise que l'interpolation NN, l'interpolation linéaire présente des mauvais résultats quand les canaux sont très sélectifs.

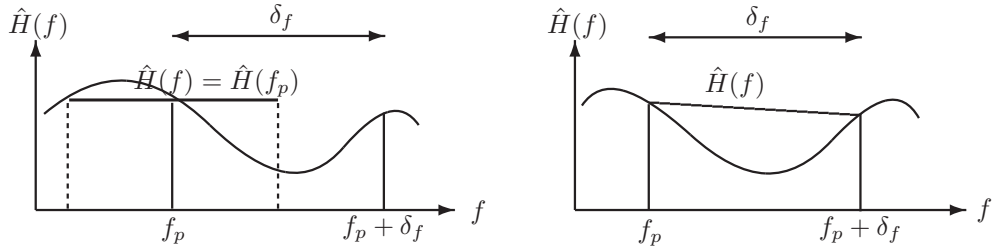

(a) Interpolation NN. (b) Interpolation linéaire.

FIGURE r.4 – Illustration du principe des interpolations NN et linéaire.

r.2.3.3 Interpolation polynomiale

Le principe de l'interpolation polynomiale est d'approximer H_f par un polynôme de degré $P-1$, où P est le nombre de pilotes par symbole OFDM. En utilisant comme base les polynômes de Lagrange $\{\mathcal{L}_0, \mathcal{L}_1, ..., \mathcal{L}_{P-1}\}$, on obtient $\chi(f)$ le polynôme interpolateur :

$$\chi(f) = \sum_{p=0}^{P-1} \mathcal{L}_p(f)\chi(f_p) = \sum_{p=0}^{P-1} \mathcal{L}_p(f)\hat{H}(f_p), \tag{r.26}$$

où $\mathcal{L}_p(f_p) = 1$ et $\chi(f_p) = \hat{H}(f_p)$. Il est prouvé dans [21] que $\chi(f)$ est l'unique polynôme de degré $P-1$ passant par tous les points $(f_p, \hat{H}(f_p))$. Il est aussi montré que quand P augmente, le polynôme $\chi(f)$ a tendance à diverger entre chaque point de contrôle. Dans certains cas, il est même possible que l'erreur entre la fonction originelle et le polynôme interpolateur tende vers l'infini. Ce phénomène, appelé effet Runge, rend l'interpolation par polynômes de Lagrange peu applicable en pratique. Une solution pour limiter l'effet Runge est de découper l'ensemble des points de contrôle par paquets de quatre points consécutifs $\{f_p, ..., f_p + 3\delta_p\}$ et d'appliquer une interpolation par un polynôme de degré trois sur chacun des intervalles. Cette méthode appelée interpolation cubique par morceau est couramment utilisée.

Cependant, cette technique rend la fonction interpolante discontinue sur chaque nœud entre les différents morceaux considérés. Pour obtenir une fonction continue sur tout l'intervalle d'étude (correspondant à la bande B), il est possible d'utiliser l'interpolation cubique spline. Elle utilise comme base les polynômes d'Hermite qui assure la continuité en chaque point de contrôle en ajoutant une condition sur la dérivée première du polynôme en chacun des points de contrôle. Une différence supplémentaire avec l'interpolation cubique par morceau de Lagrange, c'est qu'un polynôme de degré trois est utilisé entre chaque nœud.

r.2.4 Autres méthodes d'estimation de canal

Il est impossible de faire une liste exhaustive de toutes les méthodes d'estimation de canal, mais une vingtaine de techniques usuelles sont décrites dans [22–27]. Parmi elles, on peut citer trois des plus couramment utilisées :

- Le filtre de Wiener 2D, décrit dans [28], est l'estimateur optimal au sens de l'erreur quadratique moyenne. Il peut être vu comme une généralisation de LMMSE dans les deux dimensions temps et fréquence. Cependant, sa complexité en limite son utilisation.
- L'interpolation iFFT (pour interpolated Fast Fourier Transform) est décrite dans [13, 29]. Après avoir fait une estimation LS au niveau des pilotes, on repasse dans le domaine temporel au moyen d'une IFFT de taille P. L'interpolation est alors faite en rajoutant $M - P$ zéros au vecteur obtenu (zero padding), puis en appliquant une FFT de taille M.
- L'estimation du maximum de vraisemblance (ou ML, pour Maximum Likelihood), décrite dans [30, 31], vise à maximiser la fonction de coût J_{ML} :

$$J_{ML} = \ln(p(\mathbf{U}_n|\mathbf{H}_n, \underline{\mathbf{C}}_n, \sigma^2)), \tag{r.27}$$

  où $p(\mathbf{U}_n|\mathbf{H}_n, \underline{\mathbf{C}}_n, \sigma^2))$ est la densité de probabilité (ddp) conditionnelle du signal reçu. Classiquement, on considère un bruit blanc gaussien, alors la ddp conditionnelle est une loi normale à M variables, ce qui explique la présence du logarithme népérien dans (r.27).

Dans la suite, on va s'intéresser à l'estimateur LMMSE, ainsi qu'aux interpolations décrites dans la partie r.2.3.

r.3 Estimation ACA-LMMSE

Dans cette partie, on propose une méthode d'estimation de canal basée sur l'estimation LMMSE, mais qui est réalisée sans la connaissance *a priori* de la matrice de covariance du

canal. De plus, dans le contexte d'un canal variant rapidement dans le temps, la méthode proposée permet de réduire la complexité de l'estimation LMMSE.

r.3.1 Principe du ACA-LMMSE

Dans la littérature, la matrice de covariance $\underline{\mathbf{R}}_H$ utilisée pour l'estimation LMMSE (r.20) est souvent supposée connue, comme dans [32], ou doit être régulièrement estimée [33] pour suivre les variations du canal. Pour éviter ces contraintes, on propose une méthode appelée ACA-LMMSE, pour Artificial Channel Aided-LMMSE, ou "LMMSE assistée d'un canal artificiel" en français. Le principe est de masquer le canal de transmission par un filtre $\mathcal{G}$ ayant les caractéristiques d'un canal de transmission pour effectuer une estimation LMMSE du canal physique et du filtre en utilisant seulement les propriétés statistiques du filtre $\mathcal{G}$. Cette technique a été publiée dans [34, 35]. Les étapes de la méthode, résumées par la figure r.5, sont les suivantes :

1. A la réception, un signal artificiel composé uniquement de pilotes et filtré par $\mathcal{G}$ est additionné au signal physique $\mathbf{U}_n$. Les pilotes du signal artificiel ont les mêmes gains, phases, et positions que ceux du signal physique. Le filtre $\mathcal{G}$ est parfaitement connu et maîtrisé par le récepteur. De plus, comme il agit comme un canal, on emploiera la terminologie du canal de transmission pour le caractériser, et on nommera $\mathcal{G}$ ce canal artificiel. Ainsi, du point de vue du récepteur, les porteuses pilotes reçues sont affectées par la somme des canaux réels et artificiels :

$$\tilde{U}_{m,n} = (H_{m,n} + G_{m,n})C_{m,n} + W_{m,n}. \tag{r.28}$$

   On note $K_{m,n} = H_{m,n} + G_{m,n}$ les échantillons du canal hybride formé du canal physique et du filtre.

2. Une estimation LS du canal hybride $\mathbf{H}_n$ est effectuée au niveau des pilotes $K_{m,n} = \tilde{U}_{m,n}C_{m,n}^{-1}$, puis une estimation LMMSE en est déduite :

$$\begin{aligned}\hat{\mathbf{K}}_n^{LMMSE} &= \underline{\mathbf{R}}_K(\underline{\mathbf{R}}_K + \sigma^2(\underline{\mathbf{C}}_n\underline{\mathbf{C}}_n^H)^{-1})^{-1}\hat{\mathbf{K}}_n^{LS} \\ &= \underline{\mathbf{R}}_K(\underline{\mathbf{R}}_K + \frac{\sigma^2}{\mathcal{P}}\underline{\mathbf{I}})^{-1}\hat{\mathbf{K}}_n^{LS},\end{aligned} \tag{r.29}$$

   Pour éclaircir l'écriture, on notera $\underline{\mathbf{B}} = \underline{\mathbf{R}}_K(\underline{\mathbf{R}}_K + \frac{\sigma^2}{\mathcal{P}}\underline{\mathbf{I}})^{-1}$ dans la suite.

3. Comme les coefficients du filtre sont connus, on peut les soustraire de (r.29) pour obtenir l'estimation ACA-LMMSE du canal physique :

$$\hat{\mathbf{H}}_n^{ACA} = \hat{\mathbf{K}}_n^{LMMSE} - \mathbf{G}_n. \tag{r.30}$$

On note D et L_K, $\tau_{max}^{(G)}$ et $\tau_{max}^{(K)}$ les nombres de trajets et les délais maximums de $\mathcal{G}$ et $\mathcal{K}$, respectivement.

Comme le canal physique est supposé inconnu, on ne pourra pas en pratique utiliser $\underline{\mathbf{R}}_K$ dans (r.29). Le but de ACA-LMMSE est donc de masquer les statistiques de $\mathcal{H}$ par celles de $\mathcal{G}$ et n'utiliser que la matrice $\underline{\mathbf{R}}_G$ pour estimer $\hat{\mathbf{K}}_n^{LMMSE}$. Il sera montré plus loin comment obtenir la propriété de masquage du canal $\mathcal{H}$ par le filtre $\mathcal{G}$, qui se traduit par l'approximation $\underline{\mathbf{R}}_G \approx \underline{\mathbf{R}}_K$.

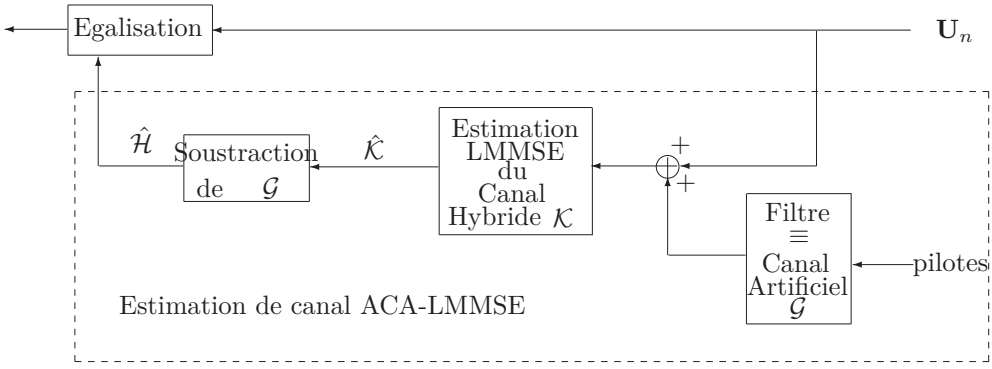

FIGURE r.5 – Schéma-bloc de l'estimation ACA-LMMSE dans une chaîne de réception simplifiée.

r.3.2 Complexité de ACA-LMMSE

r.3.2.1 Calcul de la matrice de corrélation

Pour réaliser l'estimation LMMSE (r.20), il faut connaître la matrice de covariance $\underline{\mathbf{R}}_H = E\{\mathbf{H}_n\mathbf{H}_n^H\}$ ce qui n'est jamais le cas en pratique. Elle est donc approchée avec l'estimation LS de la réponse fréquentielle, *i.e.* $\underline{\tilde{\mathbf{R}}}_H = \hat{\mathbf{H}}_n^{LS}(\hat{\mathbf{H}}_n^{LS})^H$. Comme $\underline{\tilde{\mathbf{R}}}_H$ est une matrice hermitienne de taille $M \times M$, son calcul nécessite $\frac{M(M+1)}{2}$ opérations simples [2]. De plus, cette matrice doit être régulièrement mise à jour, en fonction des variations du canal de transmission.

Pour effectuer l'estimation ACA-LMMSE, on construit la matrice $\underline{\mathbf{R}}_K$ (ou de manière équivalente $\underline{\mathbf{R}}_G$ si on suppose $\underline{\mathbf{R}}_G \approx \underline{\mathbf{R}}_K$) en suivant les recommandations de [7], ou l'annexe A.1. Ainsi, pour $u, v = 0, 1, ..., M-1$, on note $(\underline{\mathbf{R}}_K)_{u,v}$ les éléments de $\underline{\mathbf{R}}_K$, à la $u^{ème}$ ligne et $v^{ème}$ colonne :

$$(\underline{\mathbf{R}}_K)_{u,v} = \sum_{l_K=0}^{L_K-1} \int_0^{\beta_{max}} \Gamma_{l_K}(\beta) e^{-2j\pi \frac{(u-v)}{M}\beta} d\beta. \tag{r.31}$$

Comme $\underline{\mathbf{R}}_G$ est une matrice de Toeplitz hermitienne de taille $M \times M$, son calcul nécessite seulement M opérations. De plus, cette matrice étant indépendante des variations du canal, elle ne nécessite d'être calculée qu'une seul fois au cours de toute la durée de la transmission, ce qui réduit beaucoup la complexité, comparativement à LMMSE.

r.3.2.2 Calcul de la matrice $\underline{\mathbf{B}}$

Le calcul de $\underline{\mathbf{B}} = \underline{\mathbf{R}}_H(\underline{\mathbf{R}}_H + (\underline{\mathbf{C}}\underline{\mathbf{C}}^H)^{-1}\sigma^2\underline{\mathbf{I}})^{-1}$ nécessite $2M^3$ opérations (M^3 pour l'inversion et M^3 pour la multiplication matricielle), pour LMMSE et ACA-LMMSE (où $\underline{\mathbf{R}}_H$ est remplacé par $\underline{\mathbf{R}}_G$). Cependant, comme $\underline{\mathbf{R}}_H$ doit être mise à jour régulièrement, $\underline{\mathbf{B}}$ doit l'être aussi dans le cas LMMSE. Pour l'estimation ACA-LMMSE, $\underline{\mathbf{B}}$ ne doit être calculée qu'une seule fois en début de transmission.

Ainsi, si on note N le nombre de mises à jour nécessaires pendant la transmission, on résume dans le Tableau r.1 les complexités totales de LMMSE et de ACA-LMMSE. On remarque

2. Par opération simple, on entend le nombre de multiplications ou de divisions.

bien que ACA-LMMSE est moins complexe que LMMSE, ce qui est d'autant plus sensible si N devient grand, *i.e.* si le canal varie rapidement et si la transmission dure longtemps.

TABLE r.1 – Comparaison de la complexité entre LMMSE et ACA-LMMSE.

Opérations	$\underline{\mathbf{B}}$	$\underline{\tilde{\mathbf{R}}}_H$ ou $\underline{\mathbf{R}}_G$	mise à jour	Total
LMMSE	$2M^3$	$\frac{M(M+1)}{2}$	N	$N(2M^3 + \frac{M(M+1)}{2})$
ACA-LMMSE	$2M^3$	M	-	$2M^3 + M$

r.3.3 Choix des paramètres de $\mathcal{G}$

Conformément à (r.31), les échantillons $(\underline{\mathbf{R}}_G)_{u,v}$ de la matrice $\underline{\mathbf{R}}_G$ sont exprimés par :

$$(\underline{\mathbf{R}}_G)_{u,v} = \sum_{d=0}^{D-1} \int_0^{\beta_{max}^{(G)}} \Gamma_d(\beta) e^{-2j\pi \frac{(u-v)}{M}\beta} d\beta, \tag{r.32}$$

L'effet de masquage de $\mathcal{H}$ par $\mathcal{G}$ est obtenu si $\underline{\mathbf{R}}_G \approx \underline{\mathbf{R}}_K$. En observant (r.32) et (r.31), on remarque que les matrices de covariance dépendent de trois paramètres : les nombres de trajets D ou L_K, les délais maximum $\beta_{max}^{(G)}$ ou β_{max} et les profils d'intensité $\Gamma_d(\beta)$ et $\Gamma_{l_K}(\beta)$.

Pour assurer le masquage, il faut que (r.32) soit le plus proche possible de (r.31), et donc faire concorder les paramètres de $\underline{\mathbf{R}}_G$ et $\underline{\mathbf{R}}_K$. Pour cela, les choix sont guidés par les paramètres de transmission d'un signal OFDM, comme il est montré dans [34, 35] :

- Comme le système est supposé être bien conçu, la longueur du CP est plus grande que le délai maximum du canal, *i.e.* $\beta_{max}^{(H)}\tau_s \leq T_{CP}$. Ainsi, en choisissant $\beta_{max}^{(G)}\tau_s = T_{CP}$, on assure $\beta_{max} = \beta_{max}^{(G)}$ dans (3.6).
- Pour assurer l'effet de masquage, il faut que $D > L$. Or, comme L est inconnu, il faut donc fixer une valeur D arbitrairement grande. Comme on est dans un formalisme discret, la longueur de la réponse impulsionnelle du canal artificiel est limitée par $\beta_{max}^{(G)}$. On sait alors qu'on peut fixer une limite supérieure $D \leq \tau_{max}^{(G)}/\tau_s$.
- Le profil d'intensité $\Gamma_d(\beta)$ peut être n'importe quelle fonction intégrable sur $[0, \beta_{max}^{(G)}]$. Cependant, on sait qu'un grand nombre de canaux a un profil exponentiel décroissant [7–9]. On choisira donc ce profil pour $\Gamma_d(\beta)$.

Dans [35], il est montré que le paramètre le plus limitant est le choix du délai maximum $\beta_{max}^{(G)}$, qui doit logiquement être supérieur à $\beta_{max}^{(H)}$.

r.3.4 Résultats de simulations

r.3.4.1 Paramètres de simulations

Les paramètres de simulations sont ceux du standard DRM/DRM+ [1]. Le canal considéré, *US Consortium* est un canal à quatre trajets tels que les retards (échantillonnés) et les gains correspondant sont donnés par $\beta_l \in \{0\ 7\ 15\ 22\}$ et $\sigma_l \in \{1\ 0,7\ 0,5\ 0,25\}$. Les paramètres du signal sont donnés dans le tableau r.2. De plus, les pilotes sont en quinconce dans la trame, avec une régularité d'une sur quatre porteuses sur l'axe fréquentiel et un sur deux symboles sur l'axe temporel.

TABLE r.2 – Paramètres de la robustesse C de la norme DRM/DRM+.

Robustesse C	
Durée d'un symbole	14.66 ms
Durée du CP	5.33 ms
Durée d'une trame	400 ms
Nombre de porteuses	148
Largeur de bande	10 kHz
Constellation	64-QAM

Le filtre $\mathcal{G}$ possède alors les paramètres suivants : $D = 15$, $\tau_{max}^{(G)} = T_{CP} = 5.33$ et le profil d'intensité Γ_d est une exponentielle décroissante, ce qui est conforme aux recommandations précédentes.

r.3.4.2 Erreur quadratique moyenne de l'estimateur ACA-LMMSE

La figure r.6 compare les performances de ACA-LMMSE avec celles du LS et du LMMSE en terme d'erreur quadratique moyenne minimum (ou MMSE), en fonction du rapport $\mathcal{P}/\sigma^2$ sur une fenêtre de 1 à 12 dB. Deux motifs pour l'agencement des pilotes sont considérés : sur la figure r.6 (a), un préambule (noté préamb. en légende) concordant avec les résultats théoriques (r.18) et (r.23) ; et sur la figure r.6 (b), un motif en quinconce (noté quinc. en légende), en accord avec les recommandations de la norme DRM/DRM+. L'estimation LMMSE est effectuée en considérant la matrice de covariance connue du récepteur, ce qui est le cas idéal. Une interpolation spline a été faite pour le scénario LS avec les pilotes en quinconce.

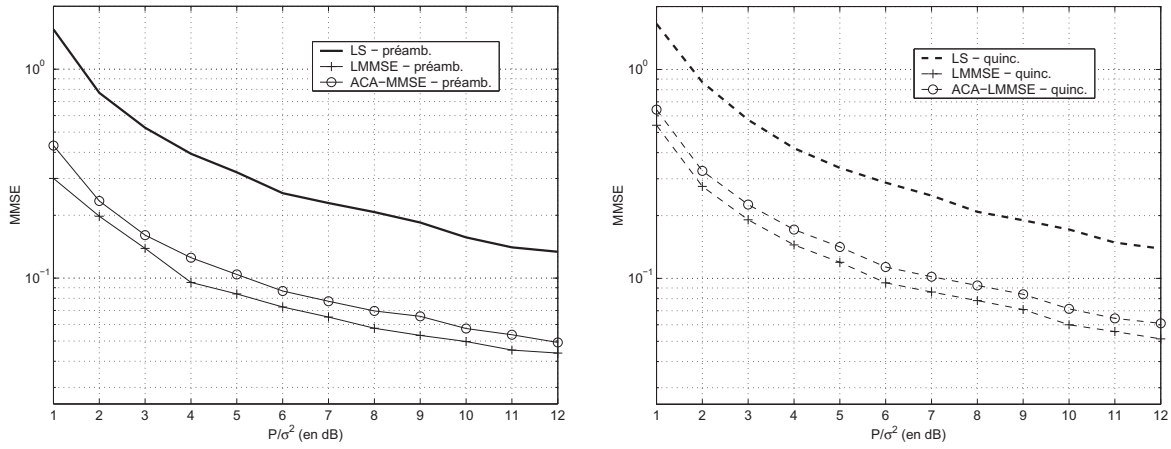

(a) Préambule en fréquence.

(b) Pilotes en quinconce.

FIGURE r.6 – Erreur quadratique moyenne de ACA-LMMSE comparée à LS et LMMSE.

Quel que soit le motif de la distribution des porteuses pilotes, on remarque qu'ACA-LMMSE a de meilleures performances que LS et n'est qu'à 2 dB de LMMSE (en terme de MMSE), dans le cas idéal. Cette légère dégradation est évidemment due à l'approximation $\underline{\mathbf{R}}_G \approx \underline{\mathbf{R}}_K$.

r.3.4.3 Taux d'erreur binaire de l'estimateur ACA-LMMSE

La figure r.7 montre les performances du ACA-LMMSE en terme de TEB (Taux d'Erreur Binaire) en fonction de E_b/N_0 et compare ACA-LMMSE avec LMMSE et LS. Pour LMMSE, deux cas sont considérés : l'un où la matrice de covariance du canal est parfaitement connue, et l'autre où elle est estimée par $\underline{\tilde{\mathbf{R}}}_H = \hat{\mathbf{H}}_n^{LS}(\hat{\mathbf{H}}_n^{LS})^H$. Les pilotes suivent la distribution en quinconce du standard, donc une interpolation spline est utilisée en complément de l'estimateur LS. Pour toutes les courbes de la figure r.7, aucun codage canal n'a été effectué.

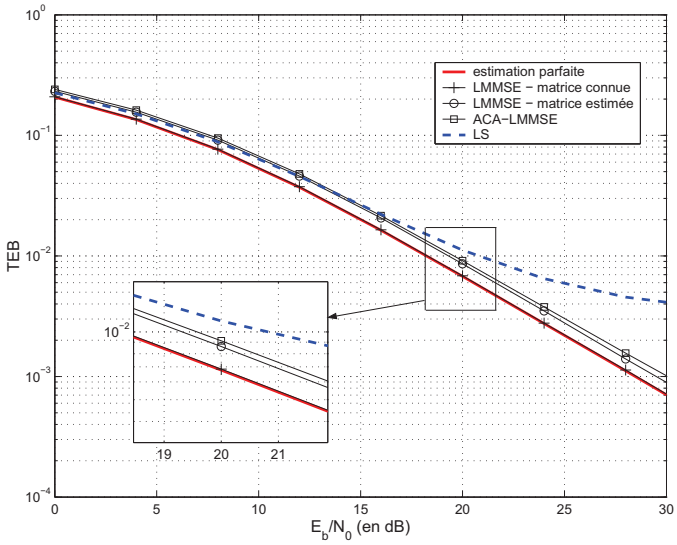

FIGURE r.7 – TEB de ACA-LMMSE comparé à LMMSE et LS en fonction de E_b/N_0.

On remarque que LMMSE et ACA-LMMSE surpassent LS et que contrairement à LS, leurs courbes n'atteignent pas de borne inférieure d'erreur (dans la plage de E_b/N_0 considérée). Ce phénomène de seuil d'erreur sera étudié plus en détail dans la partie r.5, mais on peut déjà dire qu'il est dû à l'interpolation. La figure r.7 permet de vérifier que LMMSE atteint l'optimum quand elle est effectuée avec une matrice de covariance parfaitement connue. On observe aussi que ACA-LMMSE est à moins de 2 dB du TEB de l'estimation parfaite et que l'écart de TEB entre ACA-LMMSE et LMMSE effectuée avec $\underline{\tilde{\mathbf{R}}}_H$ est de moins de 0,2 dB. On conclut qu'à performance équivalente, ACA-LMMSE nécessite moins de calculs que LMMSE, et n'a pas besoin de la matrice de covariance du canal physique.

r.3.5 Conclusion et perspectives

On a vu que l'estimation de canal proposée, appelée ACA-LMMSE, atteint des résultats proches de l'estimateur optimal, et sans avoir besoin de la connaissance *a priori* de la matrice de covariance fréquentielle du canal. De plus, comparée à un cas plus réaliste LMMSE où cette matrice est estimée et mise à jour, on a montré que ACA-LMMSE nécessite moins de calculs, dans un environnement où le canal de transmission varie au cours du temps. En effet, grâce à l'effet de masquage du canal, l'inversion et la multiplication matricielles nécessaires à LMMSE ne sont calculées qu'une seule fois en début de transmission. Bien que ce ne soit pas montré dans cette partie, il est aussi possible d'utiliser ACA-LMMSE pour adapter certains algorithmes à un canal variable dans le temps. Un exemple est développé dans la partie 3.5.3,

où l'algorithme RISIC [36] permettant la suppression d'ISI dans des canaux quasi-statiques est adapté aux canaux variant rapidement dans le temps.

r.4 Estimation conjointe du RSB et du canal

Dans la partie précédente, l'estimation ACA-LMMSE a été proposée comme solution pour utiliser LMMSE sans connaissance *a priori* de la matrice de covariance du canal, tout en réduisant le nombre de calculs nécessaires dans le cas de canaux variant dans le temps. Cependant, la variance du bruit nécessaire à LMMSE (r.20) ou ACA-LMMSE (r.29) est supposée connue du récepteur. En pratique, ce paramètre est aussi à estimer.

Dans cette partie, on propose une méthode pour estimer conjointement le canal et le rapport signal-à-bruit (RSB). Pour obtenir une estimation précise, on base l'estimation sur le critère MMSE pour les deux paramètres. En utilisant l'estimateur MMSE, la valeur de chacune des inconnues (canal ou bruit) est nécessaire pour estimer l'autre. En conséquence, l'algorithme proposé est itératif. Le principe de la méthode a été présenté dans [37] pour un cas théorique, où la matrice de covariance du canal était supposée connue. Un cas plus réaliste, où cette matrice doit être estimée, a été publié dans [38, 39]. C'est cette version de l'algorithme qui est présenté dans cette partie.

r.4.1 Présentation de l'algorithme

r.4.1.1 Estimation de la variance du bruit et du RSB

Dans cette partie, on suppose que les estimations du canal et du bruit sont effectuées sur un préambule, *i.e.* toutes les porteuses d'un symbole OFDM sont dédiées à l'estimation. Pour estimer la variance du bruit σ^2, on utilise le critère de l'erreur quadratique moyenne :

$$\begin{aligned}\hat{\sigma}^2 &= \frac{1}{M} E\{||\mathbf{U}\mathbf{C}^{-1} - \hat{\mathbf{H}}||_F^2\} \\ &= \frac{1}{M} E\{||\hat{\mathbf{H}}^{LS} - \hat{\mathbf{H}}||_F^2\}. \end{aligned} \quad \text{(r.33)}$$

On remarque dans (r.33) que l'estimation de la variance du bruit dépend de la qualité de l'estimateur de canal. Ainsi, une estimation LS mène à une estimation $\hat{\sigma}^2$ nulle. C'est pourquoi on propose dans la suite d'utiliser l'estimateur de canal optimal selon le critère MMSE.

Le RSB, noté ρ est alors estimé en utilisant le moment d'ordre deux du signal reçu noté M_2 :

$$\begin{aligned} M_2 &= E\{|\mathbf{U}|^2\} = P_s + \sigma^2 \\ \Rightarrow \hat{\rho} &= \frac{M_2}{\hat{\sigma}^2} - 1, \end{aligned} \quad \text{(r.34)}$$

où P_s est la puissance du signal reçu.

r.4.1.2 Description de l'algorithme itératif

Dans un scénario réaliste, la matrice de covariance du canal $\underline{\mathbf{R}}_H$ est inconnue du récepteur, et doit être estimée. On notera $\underline{\tilde{\mathbf{R}}}_H$ cette matrice estimée. L'algorithme, dont les étapes sont détaillées ci-après, est décrit par la figure r.8. On notera i l'indice de l'itération.

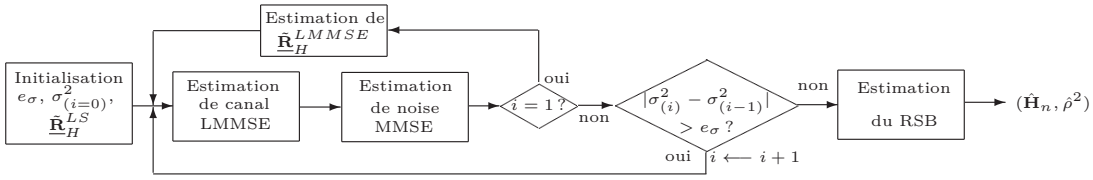

FIGURE r.8 – Schéma-bloc de l'algorithme proposé dans un cas réaliste.

1. A l'itération $(i = 0)$, seule l'estimation LS du canal est disponible. On estime donc la matrice de covariance par $\underline{\tilde{\mathbf{R}}}_H^{LS} = \hat{\mathbf{H}}^{LS}(\hat{\mathbf{H}}^{LS})^H$. De plus, on fixe un critère d'arrêt, noté e_σ, et on initialise la variance du bruit $\hat{\sigma}^2_{(i=0)}$.

2. A l'étape $(i = 1)$, on effectue l'estimation LMMSE avec la matrice $\underline{\tilde{\mathbf{R}}}_H^{LS}$:

$$\hat{\mathbf{H}}_{(i=1)}^{LMMSE} = \underline{\tilde{\mathbf{R}}}_H^{LS}(\underline{\tilde{\mathbf{R}}}_H^{LS} + \hat{\sigma}^2_{(i=0)}\underline{\mathbf{I}})^{-1}\hat{\mathbf{H}}^{LS}, \tag{r.35}$$

3. A partir de (r.33), la variance du bruit est estimée :

$$\hat{\sigma}^2_{(i=1)} = \frac{1}{M}E\{||\hat{\mathbf{H}}^{LS} - \hat{\mathbf{H}}_{(i=1)}^{LMMSE}||^2\}. \tag{r.36}$$

   Si les étapes suivantes de l'algorithme sont effectuées avec $\underline{\tilde{\mathbf{R}}}_H^{LS}$, on montre dans [38] et dans l'annexe B.1 que l'algorithme converge vers zéro. C'est dû au fait que $\underline{\tilde{\mathbf{R}}}_H^{LS}$ est une matrice bruitée. Pour obtenir une matrice de covariance du canal plus proche de la matrice exacte, on peut alors utiliser $\hat{\mathbf{H}}_{(i=1)}^{LMMSE}$, tel que :

$$\underline{\tilde{\mathbf{R}}}_H^{LMMSE} = \hat{\mathbf{H}}_{(i=1)}^{LMMSE}(\hat{\mathbf{H}}_{(i=1)}^{LMMSE})^H. \tag{r.37}$$

4. Pour $i \geq 2$, on effectue les estimations (r.35) et (r.36) en utilisant $\underline{\tilde{\mathbf{R}}}_H^{LMMSE}$:

$$\hat{\mathbf{H}}_{(i)}^{LMMSE} = \underline{\tilde{\mathbf{R}}}_H^{LMMSE}(\underline{\tilde{\mathbf{R}}}_H^{LMMSE} + \hat{\sigma}^2_{(i-1)}\underline{\mathbf{I}})^{-1}\hat{\mathbf{H}}^{LS}, \tag{r.38}$$

$$\hat{\sigma}^2_{(i)} = \frac{1}{M}E\{||\hat{\mathbf{H}}^{LS} - \hat{\mathbf{H}}_{(i)}^{LMMSE}||^2\}. \tag{r.39}$$

5. Tant que $|\hat{\sigma}^2_{(i)} - \hat{\sigma}^2_{(i-1)}| > e_\sigma$, on retourne à l'étape 4 avec $i \leftarrow i+1$, sinon, on passe à l'étape 6.

6. La dernière itération est notée i_0, alors on estime le RSB en utilisant (r.34) :

$$\hat{\rho} = \frac{\hat{M}_2}{\hat{\sigma}^2_{(i_0)}} - 1. \tag{r.40}$$

7. fin de l'algorithme.

A chaque itération de l'algorithme, les estimations du canal et du bruit se rapprochent d'une valeur finale $(\hat{\mathbf{H}}_{i_0}, \hat{\sigma}^2_{i_0})$ dont la précision sera évaluée par simulation. On va aussi montrer que la valeur de l'initialisation joue un rôle dans la convergence de l'algorithme.

r.4.2 Convergence de l'algorithme

Les étapes prouvant la convergence de l'algorithme vers une valeur non nulle sont résumées dans cette partie. Pour cela, on montre que l'estimation de la variance du bruit $\hat{\sigma}^2_{(i)}$ converge vers une valeur non-nulle. Alors, logiquement, à partir de (r.38) et (r.40), on conclut que l'estimation de canal et le RSB convergent.

r.4.2.1 Expression scalaire de l'algorithme

A partir de (r.39), il est possible d'obtenir une version scalaire de l'expression de la variance du bruit, comme il est montré dans [38] ou dans le chapitre 4. On montre alors que $(\hat{\sigma}^2_{(i)})$ est une suite construite à partir d'une fonction $\hat{\sigma}^2_{(i+1)} = f_{r2}(\hat{\sigma}^2_{(i)})$. Plus précisément, en posant $x = \hat{\sigma}^2_{(i)}$, on obtient :

$$f_{r2}(x) = \frac{x^2}{M} \sum_{m=0}^{M-1} \frac{\lambda_m + \sigma^2}{(\frac{(\lambda_m+\sigma^2)^3}{(\lambda_m+\sigma^2+\hat{\sigma}^2_{(i=0)})^2} + x)^2}. \tag{r.41}$$

On remarque que l'initialisation $\hat{\sigma}^2_{(i=0)}$ apparaît dans (r.41). Elle joue donc un rôle fondamental dans la convergence de l'algorithme.

r.4.2.2 Conditions de convergence

On remarque aisément que f_{r2} est croissante sur $\mathbb{R}^+$ et que $f_{r2}([0, M_2]) \subset [0, M_2]$. Donc, en utilisant le théorème du point fixe, on déduit que f_{r2} a au moins un point fixe, que $(\hat{\sigma}^2_{(i)})$ est monotone et donc qu'elle converge vers un des points fixes de f_{r2}. Un point fixe, *i.e.* une solution de $f_{r2}(x) = x$, est évident, car $f_{r2}(0) = 0$. Or, on souhaite une convergence vers une autre valeur que zéro. On peut alors donner des conditions (voir [38] pour plus de précisions) sur $\hat{\sigma}^2_{(i=0)}$ pour assurer une convergence de $(\hat{\sigma}^2_{(i)})$ vers une autre valeur que zéro.

- A partir de la dérivée seconde de f_{r2}, une condition nécessaire est déduite :

$$\hat{\sigma}^2_{(i=0)} \geq (\sqrt{\frac{27}{8}} - 1)M_2. \tag{r.42}$$

- On peut alors montrer qu'une condition suffisante existe si $\hat{\sigma}^2_{(i=0)} = \Lambda M_2$, avec $\Lambda >> 1$, mais sans plus de précision sur Λ et sur la valeur finale de l'estimation de la variance du bruit $\hat{\sigma}^2_{i_0}$.
- Un choix optimal de $\hat{\sigma}^2_{(i=0)}$ peut être fait si, à chaque symbole pilote on résout

$$\frac{\hat{\sigma}^4}{M} \sum_{m=0}^{M-1} \frac{\lambda_m + \hat{\sigma}^2}{(\frac{(\lambda_m+\hat{\sigma}^2)^3}{(\lambda_m+\hat{\sigma}^2+\hat{\sigma}^2_{(i=0),opt})^2} + \hat{\sigma}^2)^2} - \hat{\sigma}^2 = 0. \tag{r.43}$$

  en fonction de $\hat{\sigma}^2_{(i=0),opt}$. Les valeurs $\hat{\sigma}^2$ et λ_m sont les variables estimées grâce au symbole pilote précédent.

r.4.3 Résultats de simulations

r.4.3.1 Estimation du RSB

Dans un premier temps, on évalue la performance de l'algorithme sur l'estimation du rapport signal-à-bruit. Pour cela, on va le comparer à trois méthodes de la littérature :

– La méthode de Ren [40] est spécifiquement adaptée aux systèmes OFDM. En effet, elle nécessite un préambule composé de deux symboles OFDM pilotes. De plus, le canal est supposé invariant pendant deux symboles consécutifs. Alors la variance du bruit est estimée par :

$$\begin{aligned}\hat{\sigma}^2 &= \frac{1}{2M} E\{||\mathbf{U}_n - \mathbf{U}_{n+1}||_F^2\} \\ &= \frac{1}{2M} E\{||\mathbf{W}_n - \mathbf{W}_{n+1}||_F^2\}. \end{aligned} \tag{r.44}$$

– La méthode de Xu [41] se base sur les sous-espaces de la matrice de corrélation estimée du canal $\underline{\tilde{\mathbf{R}}}_H$. Le moment d'ordre deux du signal reçu est estimé sur le sous espace des valeurs propres non-nulles du canal, tandis que le niveau du bruit est estimé sur l'espace complémentaire, où les valeurs propres du canal sont nulles.
– La méthode M_2M_4 est utilisable pour toute forme d'onde [42]. Son principe est d'estimer le moment d'ordre deux (r.34) et le moment d'ordre quatre $M_4 = \frac{1}{M} E\{||\mathbf{U}\mathbf{U}^H||_F^2\} = P_s^2 + 4P_s\sigma^2 + 2\sigma^4$. On déduit alors la puissance du signal et la variance du bruit par :

$$\begin{aligned}\hat{P}_s &= \sqrt{2M_2^2 - M_4} \\ \hat{\sigma}^2 &= M_2 - \sqrt{2M_2^2 - M_4},\end{aligned}$$

puis le RSB $\hat{\rho} = \hat{P}_s/\hat{\sigma}^2$.

De plus, on compare l'algorithme proposé (dans le cas réaliste) avec le cas théorique où la matrice de covariance est supposée connue [37]. La figure r.9 représente l'erreur quadratique moyenne normalisée (ou NMSE en anglais) de l'estimation du RSB $NMSE = E\{|\hat{\rho} - \rho|^2/\rho^2\}$ en fonction du RSB. L'algorithme proposé est comparé avec les méthodes précédemment présentées.

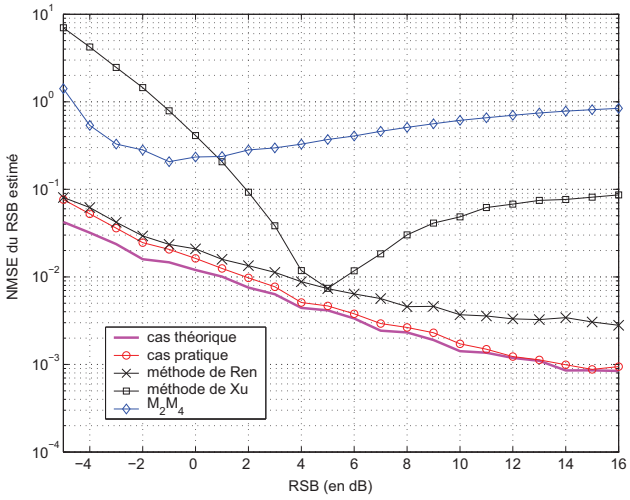

FIGURE r.9 – NMSE de l'estimation du RSB en fonction de ρ.

On observe que la méthode proposée dans un scénario réaliste atteint presque les performances du cas optimal. De plus, l'algorithme itératif surpasse les autres méthodes de la

littérature. Comparée à la méthode de Ren, le bénéfice est double, car pour une meilleure performance, la technique proposée n'utilise qu'un symbole OFDM pilote par préambule, contre deux pour la méthode de Ren.

r.4.3.2 Estimation de canal

On montre sur la figure r.10 la performance de l'estimation de canal de la méthode proposée par le taux d'erreur binaire en fonction de ρ et pour différentes valeurs du nombre d'itérations. Une comparaison avec l'estimation LS et le cas théorique est proposée. La constellation utilisée est une MAQ-16, et le canal de transmission est similaire à celui utilisé dans la partie r.3.

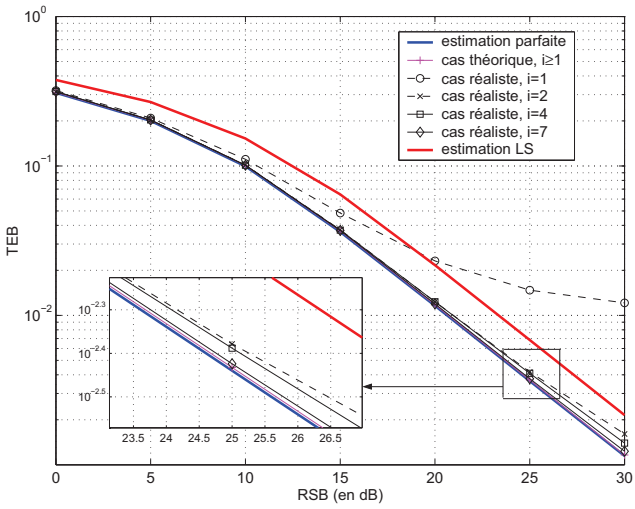

FIGURE r.10 – Taux d'erreur binaire (TEB) de la méthode proposée en fonction du RSB, comparaison avec des méthodes existantes.

On observe qu'à partir de $i = 2$, la méthode proposée surpasse les performances de l'estimateur LS. La figure r.10 montre que l'estimation de canal converge, et qu'elle converge vers une limite proche de l'estimation parfaite, puisque l'écart en les deux courbes est inférieur à 0.2 dB.

r.4.4 Conclusion et perspectives

Dans cette partie, on a présenté un algorithme itératif pour l'estimation conjointe du RSB et du canal. Comme l'estimation se base sur le critère MMSE, celle-ci est très performante pour chacun des paramètres, ce qui a été vérifié par simulation. De plus, on suppose un cas réaliste, où la matrice de covariance du canal est *a priori* inconnue. Cet algorithme permet donc une application pratique de LMMSE, où ses paramètres statistiques sont estimés itérativement.

La suite des travaux concernant cette méthode est son application à la détection de bande libre dans le cadre de la radio intelligente. En effet on peut montrer que, sans changer la structure de l'algorithme, il converge aussi si du bruit seul est présent en entrée à la place du signal, comme c'était le cas dans cette partie. On peut alors détecter la présence ou non d'un utilisateur dans la bande considérée. Cette application est présentée dans la partie 4.5.

r.5 Étude des interpolations sur les performances de l'estimation d'un canal de Rayleigh

Dans cette partie, on s'intéresse aux erreurs d'estimation dues aux interpolations, nécessaires quand on considère une distribution des pilotes différente d'un préambule en fréquence. On va montrer qu'il est possible de caractériser ces erreurs en calculant analytiquement la limite atteinte par le TEB. Les premiers résultats de cette étude ont été publiés dans [43].

r.5.1 Modèle

Dans toute cette partie, on va considérer des interpolations effectuées selon l'axe fréquentiel. On utilisera de manière équivalente le formalisme continu ou discret pour décrire le canal :

$$H(f) = \sum_{l=0}^{L-1} h_l e^{-2j\pi f \tau_l} \Longleftrightarrow H_m = \sum_{l=0}^{L-1} h_l e^{-2j\pi \frac{\beta_l m}{M}}, \tag{r.45}$$

Dans le formalisme discret, on définit δ_p (correspondant à δ_f en continu) l'écart fréquentiel entre deux pilotes consécutifs, comme l'illustre la figure r.11. Dans la suite, on considèrera $\delta_p \in \{2, 3, 4\}$. De plus, on suppose que les pilotes sont uniformément répartis dans chaque symbole OFDM.

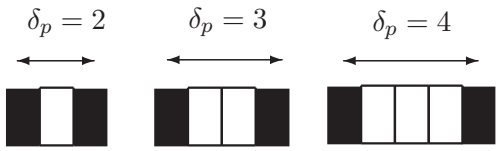

FIGURE r.11 – Illustration de la distribution des pilotes pour différentes valeurs de δ_p.

Pour faciliter les simulations, chaque symbole OFDM sera composé de $M = 241$ porteuses : pour tout $\delta_p \in \{2, 3, 4\}$, 240 est divisible par δ_p. Pour valider les développements qui vont suivre, on simulera deux canaux de Rayleigh $\mathcal{H}_1$ et $\mathcal{H}_2$, dont les paramètres (retards et gain) sont :

- $\mathcal{H}_1 : \beta_l \in \{0\ 6\ 13\ 16\}$ et $\sigma_l^2 = \{1\ 0,5\ 0,4\ 0,2\}$,
- $\mathcal{H}_2 : \beta_l = \{0\ 4\ 9\ 14\ 16\ 18\ 21\}$ et $\sigma_l^2 = \{1\ 0,5\ 0,4\ 0,3\ 0,3\ 0,2\ 0,1\}$.

r.5.2 Statistique des erreurs d'interpolation

r.5.2.1 Expression des erreurs

On va s'intéresser ici aux interpolations nearest neighbor (NN) et linéaire. Dans un premier temps, on s'intéresse aux erreurs uniquement dues aux interpolations, donc on suppose un bruit nul $\sigma^2 = 0$. On note e_h l'erreur d'interpolation $\hat{H}(f) - H(f)$ et ξ son module. A partir des expressions des interpolations NN (r.24) et linéaire (r.25), on donne les erreurs ξ_{NN} et ξ_{li} :

$$\xi_{NN} = |\hat{H}(f) - H(f)| = |H(f_p) - H(f)| \tag{r.46}$$

$$\xi_{li} = |H(f) - \hat{H}(f)| = \frac{1}{2}|(f_{p+\delta_p} - f)(f_p - f)| \times |H''(\alpha)|, \tag{r.47}$$

où H'' est la dérivée seconde de la réponse fréquentielle (on voit dans (r.45) que H est visiblement $\mathcal{C}^2$) canal et $\alpha \in [f_p, f_{p+\delta_p}]$. L'expression de ξ_{NN} est triviale en utilisant (r.24). Celle de ξ_{li} se déduit simplement de la formule de Taylor en f_p et $f_{p+\delta_p}$, comme il est montré dans l'annexe C. A partir de (r.47), on peut déjà déduire que si $|H(f)|$ suit une loi de Rayleigh, alors ξ_{NN} et ξ_{li} suivent aussi une distribution de Rayleigh, dont les variances seront données plus loin. De plus, comme les erreurs sont fonctions de $H(f)$ (ou de sa dérivée seconde), ξ et $|H(f)|$ sont corrélés.

r.5.2.2 Paramètres statistiques des erreurs

A partir des expressions des erreurs (r.47) et de la réponse fréquentielle du canal (r.45), sans le démontrer ici, on déduit les expressions des variances σ_ξ^2 dans le formalisme discret. On note k une porteuse donnée se situant entre deux positions pilote p et $p+\delta_p$. On exprime alors σ_ξ^2 pour les deux interpolations considérées :

$$\sigma^2_{\xi_{k,NN}} = \sum_{l=0}^{L-1} \sigma_l^2 (2 - 2\cos(2\pi \frac{k\beta_l}{M})) \tag{r.48}$$

$$\sigma^2_{\xi_{k,li}} = |\frac{(\delta_p - k)k}{M^2}|^2 4\pi^4 \sum_{l=1}^{L-1} \beta_l^4 \sigma_l^2. \tag{r.49}$$

On remarque que ces valeurs dépendent de la distance à un pilote. Physiquement, cela se traduit par le fait que plus on considère une valeur interpolée écartée d'une position d'un pilote, plus l'erreur d'estimation est grande, statistiquement.

On calcule aussi le coefficient de corrélation entre l'erreur d'estimation e_h et le canal $H(f)$. On note $\rho_{r\xi}$ ce coefficient, qui s'exprime $\rho_{r\xi} = \frac{|E\{H(f)e_h^*\}|}{\sigma_h \sigma_\xi}$. Plus précisément, on obtient :

$$\rho_{r\xi_k,NN} = \frac{|\sum_{l=0}^{L-1} \sigma_l^2 (e^{-2j\pi \frac{\beta_l k}{M}} - 1)|}{\sigma_h \sigma_{\xi_{k,NN}}} \tag{r.50}$$

$$\rho_{r\xi_k,li} = \frac{|\frac{(\delta_p - k)k}{M^2}| 2\pi^2 \sum_{l=1}^{L-1} \beta_l^2 \sigma_l^2}{\sigma_r \sigma_{\xi_{k,li}}}. \tag{r.51}$$

Plus de précisions sur l'obtention des expressions (r.49) et (r.51) sont données dans le chapitre 5. Comme ξ et $|H(f)|$ sont de processus de Rayleigh corrélés, on peut déduire une expression de leur densité de probabilité conjointe $p_{r,\xi}(r,\xi)$ [44, 45], où $r = |H(f)|$:

$$p_{r,\xi}(r,\xi) = \frac{r\xi}{\sigma_r^2 \sigma_\xi^2 (1-\rho_{r\xi}^2)} \exp\left(-\frac{\sigma_\xi^2 r^2 + \sigma_r^2 \xi^2}{2\sigma_r^2 \sigma_\xi^2 (1-\rho_{r\xi}^2)}\right) I_0\left(\frac{r\xi\rho_{r\xi}}{\sigma_r \sigma_\xi (1-\rho_{r\xi}^2)}\right), \tag{r.52}$$

où $I_0(.)$ est la fonction de Bessel modifiée de première espèce et d'ordre zéro.

r.5.3 Considérations géométriques

r.5.3.1 Modèle

On va maintenant étudier l'impact des erreurs d'interpolation sur la détection des symboles de constellation. Naturellement, l'impact des erreurs diffère selon la taille et la géométrie des

constellations. Dans cette partie, on va étudier une BPSK (Binary Phase Shift Keying) et une 4-QAM (Quadrature Amplitude Modulation) avec un codage de Gray, comme l'illustre la figure r.12, où d est une valeur de normalisation.

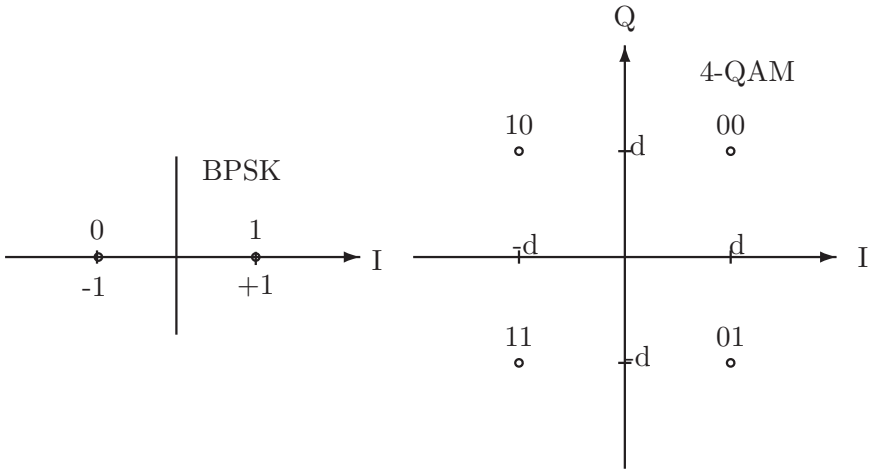

FIGURE r.12 – BPSK et 4-QAM avec un codage de Gray.

La détection des symboles est effectuée par un égaliseur zero forcing. Comme on suppose ici un bruit nul, le symbole estimé $\hat{C}$ s'écrit :

$$\hat{C} = \frac{H(f)}{\hat{H}(f)}C = \frac{H(f)}{H(f)+e_h}C. \tag{r.53}$$

Dans la suite, on va utiliser les notations complexes suivantes : $H(f) = re^{j\Theta_H}$, $e_h = \xi e^{j\Theta_\xi}$, et on définit aussi $\Theta = \Theta_H - \Theta_\xi$.

r.5.3.2 BPSK

Pour une BPSK ($C \in \{-1, +1\}$), les domaines de décisions sont symétriques, il est donc équivalent de raisonner sur $C =^{+}_{-} 1$. On va choisir $C = 1$ dans la suite. La probabilité d'erreur de détection, qu'on note P_e^{BPSK}, est alors donnée par :

$$P_e^{BPSK} = P\left(\mathfrak{Re}\{\hat{C}\} < 0 | C = 1\right). \tag{r.54}$$

Après un calcul simple mais fastidieux, la résolution de (r.54) donne :

$$\begin{aligned} P_e^{BPSK} &= P\left(\mathfrak{Re}\{\frac{H(f)}{H(f)+e_h} \times 1\} < 0\right) \\ \Rightarrow P_e^{BPSK} &= P\left(\frac{r^2 + r\xi\cos(\Theta)}{|H(f)+e_h|^2} < 0\right), \end{aligned} \tag{r.55}$$

puis

$$P_e^{BPSK} = \begin{cases} 0 & \text{if } \xi \leq r \\ 1 - \frac{\arccos(-\frac{r}{\xi})}{\pi} & \text{if } \xi \geq r \end{cases}. \tag{r.56}$$

r.5.3.3 4-QAM

De la même manière pour une $4-QAM$, comme il est mentionné dans [46], les domaines de décision sont symétriques par rapport aux axes I et Q pour les bits de poids forts (ou MSB en anglais) et les bits de poids faibles (ou LSB). On peut donc arbitrairement raisonner sur $C = +d + jd$ dans la suite. Dans ce cas, la probabilité d'erreur de décision P_e^{4QAM} pour le MSB (égale pour les MSB et les LSB) s'écrit

$$P_e^{4QAM} = P\left(\mathfrak{Re}\{\hat{C}\} < 0 | C = d + jd\right). \tag{r.57}$$

On développe (r.57) pour obtenir :

$$\begin{aligned} P_e^{4QAM} &= P\left(\mathfrak{Re}\{\frac{H(f)}{H(f)+e_h}(d+jd)\} < 0\right) \\ \Rightarrow P_e^{4QAM} &= P\left(r + \xi(\cos(\Theta) - \sin(\Theta)) < 0\right), \end{aligned} \tag{r.58}$$

puis finalement

$$P_e^{4QAM} = \begin{cases} 0, \text{ if } 0 \leq \xi \leq \frac{r}{\sqrt{2}} \\ \frac{\arctan(t_2^+) - \arctan(t_{2-})}{\pi}, \text{ if } \frac{r}{\sqrt{2}} \leq \xi \leq r \\ (1 + \frac{\arctan(t_{3-}) - \arctan(t_3^+)}{\pi}), \text{ if } r \leq \xi \end{cases}, \tag{r.59}$$

où $t_{2-}^+ = t_{3+}^- = \frac{2\xi_-^+\sqrt{\Delta_p}}{2(r-\xi)}$, avec $\Delta_Q = 4\xi^2 - 4(r^2 - \xi^2)$.

r.5.3.4 Expression de la valeur seuil du TEB

La borne inférieure atteinte par le taux d'erreur binaire, que l'on note TEB^{seuil} se calcule en intégrant P_e^{const} que multiplie la ddp conjointe $p_{r,\xi}(r,\xi)$:

$$TEB^{seuil} = \int_0^{+\infty}\int_0^{+\infty} P_e^{const} p_{r,\xi}(r,\xi) d\xi dr, \tag{r.60}$$

où l'exposant *const* dépend de la constellation considérée.

r.5.4 Résultats de simulations

Pour valider les résultats analytiques, la figure r.13 compare les courbes de TEB simulées et les valeurs de seuils obtenues analytiquement en fonction du RSB. Pour chaque sous-figure, deux écarts $\delta_p \in \{2, 4\}$ et les deux constellations sont représentées. Sur la figure r.13 (a), les courbes sont obtenues pour le canal $\mathcal{H}_{(1)}$ et l'interpolation NN, et la figure r.13 (b), les courbes sont obtenues pour le canal $\mathcal{H}_{(2)}$ et l'interpolation linéaire. Les valeurs des seuils de TEB sont obtenues en utilisant r.60. Pour plus de précisions sur les valeurs des paramètres de simulations σ_ξ^2 et $\rho_{r\xi}$, on peut consulter la section 5.6.

Un grand nombre de cas avec des paramètres différents sont représentés, afin de couvrir le plus de scénarios possibles. On remarque que chaque valeur analytique du TEB correspond effectivement à la limite atteinte par chacune des courbes. Les développements théoriques sont donc validés. On remarque aussi que, naturellement, l'interpolation linéaire est plus

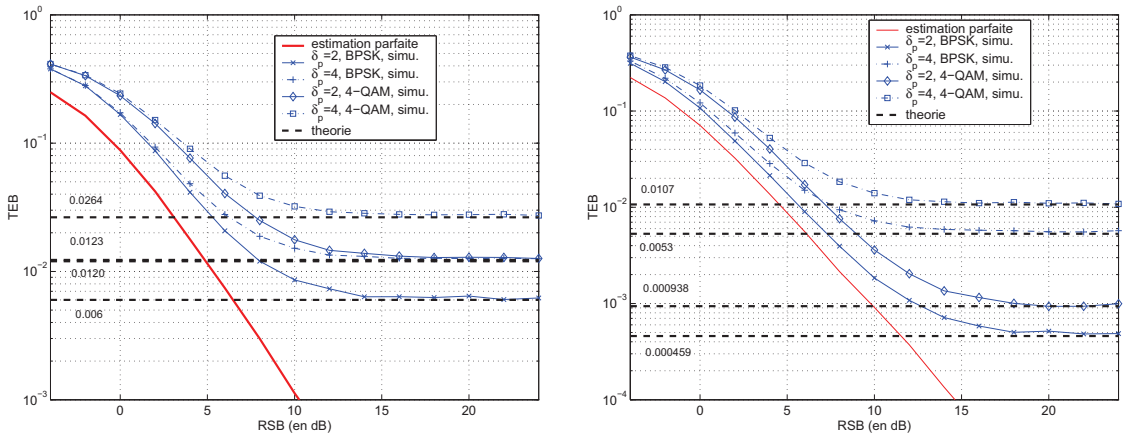

(a) Canal $\mathcal{H}_{(1)}$, interpolation NN.

(b) Canal $\mathcal{H}_{(2)}$, interpolation linéaire.

FIGURE r.13 – Courbes de TEB simulées comparées aux seuils calculés analytiquement.

performante que l'interpolation NN. De plus, on vérifie que les résultats se dégradent avec l'augmentation de δ_p. La très légère différence pouvant être visible entre les limites théoriques et les courbes de simulations peut s'expliquer par le fait que la double intégrale dans (r.60) s'approxime en réalité par une double somme.

r.5.5 Conclusion et perspectives

Dans cette partie, on a présenté une étude sur les erreurs d'estimation dues aux interpolations. Une analyse statistique permet de caractériser ces erreurs, en fonction de la méthode d'interpolation et de l'espacement fréquentiel entre pilotes. Cette étude associée à une analyse géométrique dépendant de la constellation, il est alors possible de prédire la borne inférieure atteinte par les courbes de TEB. Dans le chapitre 5, on montre qu'il est aussi possible de donner une expression analytique du MSE en fonction du RSB. Une suite logique à ces travaux sera d'étendre l'étude à des constellations de plus grandes tailles et à d'autres types d'interpolations. De plus, on peut envisager d'utiliser la même étude pour caractériser les interpolations en traitement d'image.

r.6 Application de la diversité de délai cyclique à un SFN

Dans cette partie est présentée la diversité de délai cyclique (ou CDD en anglais) appliquée à un SFN (Single Frequency Network) utilisant la norme DRM/DRM+. Cette étude et le résultat de la contribution de l'ECAM Rennes au Projet OCEAN (Optimisation d'une Chaîne d'Emission-réception pour la rAdio Numérique terrestre), et a été publiée dans [47].

r.6.1 Modèle

r.6.1.1 Réception d'un signal dans un SFN

Dans cette partie, on considère un récepteur mobile Rx se situant dans la zone de recouvrement entre deux cellules d'un réseau SFN (pour Single Frequency Network, en anglais), comme l'illustre la figure r.14 (a). Dans ce type de réseau, le signal est émis à la même

fréquence quelle que soit l'antenne d'émission Tx. Suivant ce modèle, les évanouissements fréquentiels du canal peuvent affecter toute la bande passante d'un signal donné. Dans ce cas, la diversité fréquentielle de l'OFDM devient inutile, même si un codage canal est utilisé.

Du point de vue du récepteur dans la zone de recouvrement, la réponse fréquentielle du canal est la somme des contributions du signal provenant de Tx_1 et Tx_2. Pour tout $m = 0, 1, ..., M-1$, on a alors :

$$\begin{aligned} H_m &= \sum_{l_1=0}^{L_1-1} h_{l_1} e^{-2j\pi \frac{m\beta_{l_1}}{M}} + \sum_{l_2=0}^{L_2-1} h_{l_2} e^{-2j\pi \frac{m\beta_{l_2}}{M}} \\ &= \sum_{l=0}^{L-1} h_l e^{-2j\pi \frac{m\beta_l}{M}}, \end{aligned} \tag{r.61}$$

où h_l, h_{l_1}, h_{l_2} sont les coefficients et $\beta_l, \beta_{l_1}, \beta_{l_2}$ les retards échantillonnés des trajets. L_1 et L_2 sont le nombre de trajets provenant de Tx_1 et Tx_2, et on suppose que $L \leq L_1 + L_2$, sans perte de généralité. De plus, on suppose que le délai maximum du canal est très court. Dans cette condition, les gains $|H_m|$ peuvent être fortement atténués, et sur une large plage de fréquence, comme l'illustre la représentation temps-fréquence de la réponse fréquentielle du canal sur la figure r.14 (b).

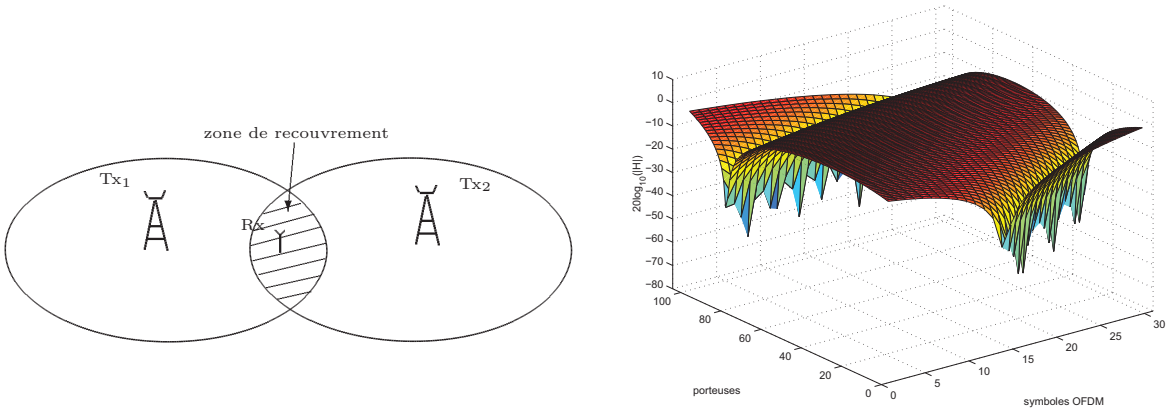

(a) Réseau SFN simplifié à 2 Tx.

(b) Réponse fréquentielle du canal équivalent, sans diversité.

FIGURE r.14 – Réseau SFN simplifié et réponse fréquentielle du canal vu de la zone de recouvrement.

Quand toute la totalité des porteuses est affectée par un évanouissement, le gain de la diversité fréquentielle apporté par l'OFDM devient nul, et un grand nombre d'erreurs apparaissent dans le signal reçu, et cela même si un codage de canal est utilisé.

r.6.1.2 Paramètres de simulations

Le signal utilisé tout au long de cette partie suit les paramètres donnés par le mode de robustesse B de la norme DRM/DRM+ [1]. On va considérer un signal de largeur en fréquence $B = 5$ kHz, composé de 103 porteuses mappées par une 4-QAM (dont une nulle au centre)

et une trame composée de 15 symboles OFDM. Chaque symbole a une durée $T_s = 21.33$ ms et un préfixe cyclique (CP) de durée $T_{CP} = 5.33$ ms. Un code de Reed-Solomon [48] de rendement 0,5 est appliqué. Les paramètres de simulations sont résumés dans le tableau r.3.

TABLE r.3 – Paramètres de simulations.

Robustness B	
Durée d'un symbole T_s	21.33 ms
Durée du CP T_{CP}	5.33 ms
Durée d'une trame	400 ms
Nombre de porteuses M	103
Largeur de bande B	5 kHz
Constellation	4-QAM
Rendement du code RS	0.5

r.6.2 Diversité de délai cyclique

Le principe de la diversité de délai cyclique (ou CDD, en anglais), décrite dans [49], est d'augmenter artificiellement la sélectivité fréquentielle du canal pour retrouver l'avantage de la diversité fréquentielle de l'OFDM. Pour obtenir ce résultat, on opère un décalage cyclique k_Φ sur les échantillons des symboles émis sur une des deux antennes Tx_1 ou Tx_2, tel que, si on note $u_{k,div}$ le k^{ème} échantillon du nouveau symbole, alors on obtient :

$$u_{k,div} = u_{k-k_\Phi(modM)} = \sum_{m=0}^{M-1} (C_m e^{-2j\pi k_\Phi m/M}) e^{2j\pi km/M}, \tag{r.62}$$

où *mod* signifie modulo. De manière équivalente, cela revient à ajouter une phase $\Phi_m = -2\pi k_\Phi m/M$, avec $m = 0, 1, ..., M-1$ avant l'IFFT au signal émis sur une des deux antennes. Cette méthode est alors appelée diversité de phase [49]. Comme les deux antennes jouent un rôle symétrique, on supposera que la phase additionnelle est ajoutée sur Tx_2. Alors, du point de vue du récepteur, le nouveau canal équivalent est donné par :

$$\begin{aligned} H_m &= \sum_{l_1=0}^{L_1-1} h_{l_1} e^{-2j\pi \frac{m\beta_{l_1}}{M}} + \sum_{l_2=0}^{L_2-1} h_{l_2} e^{-2j\pi \frac{m\beta_{l_2}}{M}} e^{\Phi_m} \\ &= \sum_{l_1=0}^{L_1-1} h_{l_1} e^{-2j\pi \frac{m\beta_{l_1}}{M}} + \sum_{l_2=0}^{L_2-1} h_{l_2} e^{-2j\pi \frac{m(\beta_{l_2}+k_\Phi)}{M}}. \end{aligned} \tag{r.63}$$

Bien qu'il y ait équivalence entre la diversité de phase et la CDD, on remarque que la mise en œuvre de la CDD nécessite seulement un décalage des échantillons dans le domaine temporel, tandis que la diversité de phase nécessite M multiplication. La CDD est donc moins complexe que la diversité de phase. Comme il est mentionné dans [50], l'augmentation de la sélectivité est effective si $k_\Phi > 2$. La figure r.15 montre la nouvelle réponse fréquentielle du canal pour une CDD avec $k_\Phi = 6$. Comparativement à r.14 (b), on remarque bien l'augmentation de la sélectivité fréquentielle du canal. Dans ces conditions, on retrouve l'avantage de l'OFDM codé.

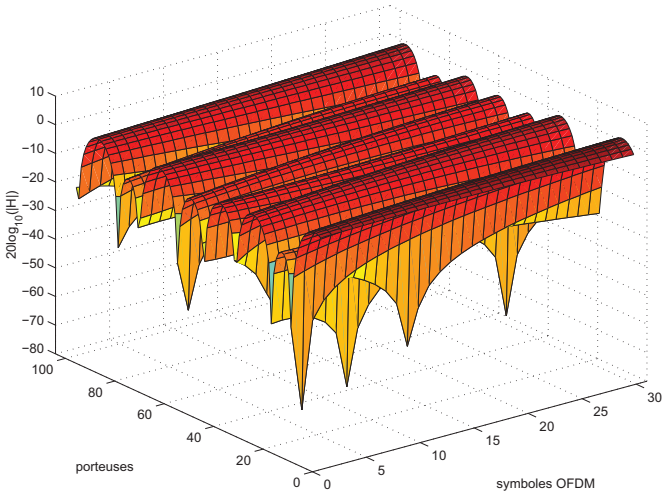

FIGURE r.15 – Réponse fréquentielle du canal avec diversité de délai cyclique.

r.6.3 Résultat de simulation

Dans cette partie, on caractérise les performances de la CDD en prenant en compte le système plus globalement par le taux d'erreur binaire (TEB). Ainsi, à la réception, une estimation LS est effectuée au niveau des pilotes, puis une interpolation spline permet d'obtenir la réponse du canal sur tout le réseau temps-fréquence.

La figure r.16 montre le TEB en fonction des symboles OFDM, sur une durée de 11,20 s (soit 420 symboles). Deux processus indépendants sont affichés (1 pour chaque fenêtre), pour lesquels une transmission sans CDD et une transmission avec CDD sont comparées. Le délai vaut $k_\Phi = 6$, et le rapport signal-à-bruit vaut 10 dB. Pour chaque processus, les observations sont faites sur un temps correspondant à dix fois le temps de cohérence, ce qui est suffisant pour tirer des conclusions statistiques.

Quel que soit le processus, on remarque que le nombre d'échantillons (ici, un échantillon est un symbole OFDM) dont le TEB est non-nul décroît quand la CDD est utilisée, comparativement à une transmission sans CDD. Ainsi, on peut remarquer sur la fenêtre du haut que la durée correspondant à un BER non-nul pour la transmission sans CDD est environ égale à 1,5 s, tandis que le TEB est nul pendant toute la transmission pour la transmission avec CDD. Sur la fenêtre du bas, on remarque que des symboles à TEB non-nul pour une transmission avec CDD peuvent aussi apparaître, mais de manière ponctuelle. Si on considère une transmission radio, on déduit alors que la CDD permet d'obtenir des erreurs quasi-inaudibles, tandis que les erreurs dans une transmission sans CDD peuvent gêner l'écoute.

La figure r.17 (a) donne les courbes de TEB en fonction du RSB pour une une transmission sans CDD et pour une transmission avec CDD avec $k_\Phi = 3$ et $k_\Phi = 6$. La courbe d'une transmission avec seulement du bruit additif gaussien est tracée comme référence, celle-ci étant la borne inférieure du TEB. On observe clairement le gain apporté par la CDD : à TEB=10^{-3}, le gain en RSB pour $k_\Phi = 3$ est de 2 dB et de 3 dB pour $k_\Phi = 6$. La conclusion concernant la baisse du nombre d'erreurs tirée de la figure r.16 est donc confirmée statistiquement.

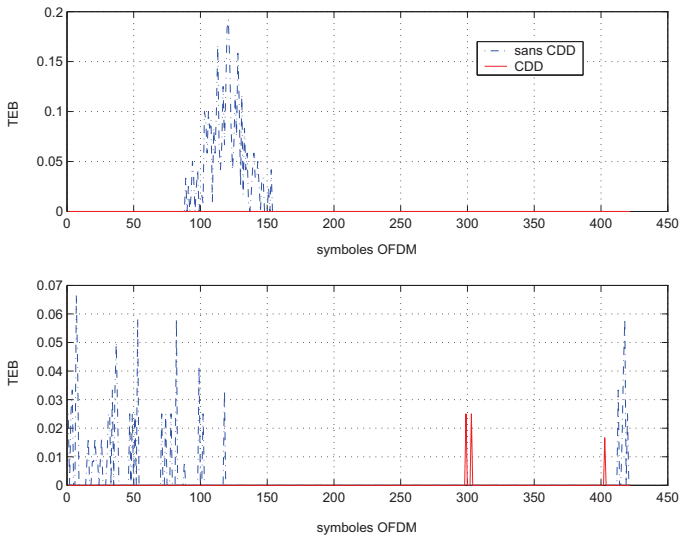

FIGURE r.16 – TEB en fonction des symboles OFDM, pour deux processus indépendants.

La figure r.17 (b) montre les même courbes que la r.17 (a), exceptée la courbe de transmission sans CDD, et celles-ci sont comparées avec les courbes d'une estimation effectuée par une interpolation linéaire. Cela permet d'étudier l'effet de la CDD sur la performance plus globale du système. L'interpolation spline nécessite une complexité de l'ordre de $\mathcal{O}(M^2)$ et l'interpolation linéaire $\mathcal{O}(M)$, mais l'interpolation spline est plus précise que la linéaire, notamment si les fonctions varient rapidement.

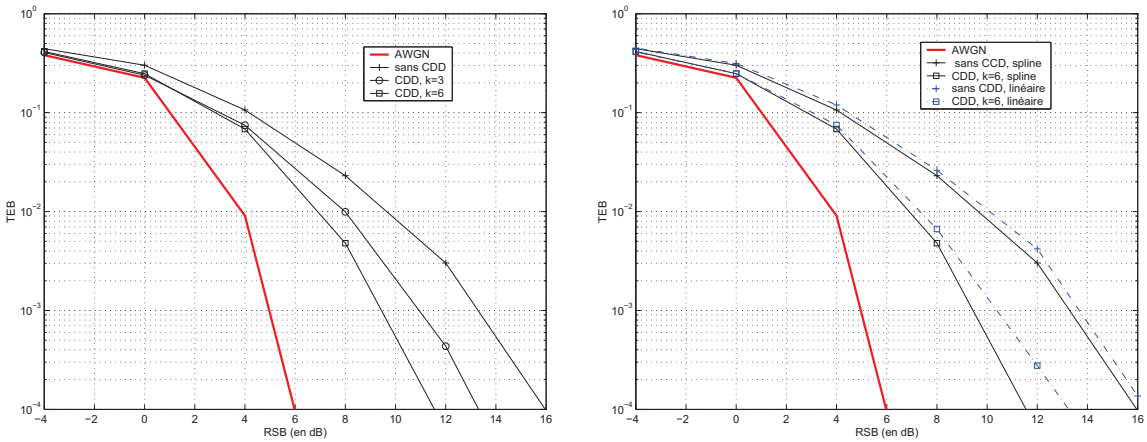

(a) Effet de la CDD sur le TEB.

(b) Effet de la CDD sur l'estimation de canal.

FIGURE r.17 – TEB en fonction du RSB, pour une transmission avec et sans CDD, et pour deux types d'interpolation.

C'est ce qui est vérifié sur la figure r.17 (b). En effet, on observe que l'interpolation spline offre de meilleures performances que l'interpolation linéaire. Cependant, on remarque que pour TEB=10^{-4}, la différence de RSB entre les courbes d'une interpolation spline et linéaire est de 1 dB pour $k_\Phi = 3$, et cette différence vaut 2 dB pour $k_\Phi = 6$. Ainsi, plus le canal est sélectif, plus l'interpolation spline est précise, comparativement à l'interpolation linéaire. On

déduit que pour atteindre une valeur de TEB pour un RSB donné, la seule augmentation de la valeur k_Φ ne suffit pas, car celle-ci influe sur l'estimation de canal. Ainsi, une augmentation artificielle de la sélectivité peut engendrer une augmentation de la complexité de l'estimateur en réception.

Pour conclure, l'estimation de canal doit être prise en compte dans la performance globale du système quand la CDD est utilisée. Un compromis entre l'augmentation de la phase k_Φ et la complexité du récepteur est alors nécessaire.

Conclusion

Ce résumé a couvert les différents travaux et thématiques de la thèse, et les principaux résultats ont été présentés. Après avoir rappelé les éléments de base concernant les canaux de transmissions, notamment les canaux WSSUS, ainsi que la transmission et les propriétés d'un signal OFDM, un état de l'art des techniques usuelles d'estimation de canal a été fait. Parmi celles-ci, les études effectuées au cours de la thèse se sont orientées vers les méthodes LS, LMMSE (pour Least Square et Linear-Minimum Mean Square Error, respectivement) et les techniques d'interpolation basées sur des polynômes interpolateurs.

La méthode ACA-LMMSE (pour Artificial Channel Aided-LMMSE) permet d'approcher les performances optimales de LMMSE en évitant deux de ses inconvénients. Ainsi, ni la connaissance *a priori* de la matrice de covariance du canal, ni son estimation ne sont nécessaires au récepteur. De plus, dans un environnement variant rapidement, aucune mise à jour des coefficients de cette matrice ne doit être effectuée. Pour cela, on place en récepteur un filtre connu agissant comme un canal artificiel masquant le canal physique. Grâce à un choix adapté des paramètres du filtre, on peut estimer la somme des canaux physique et artificiel en utilisant uniquement la matrice de covariance du canal artificiel. Le canal physique est ensuite estimé par soustraction des coefficients du filtre à l'estimation de la somme. Le choix des paramètres du filtre permet aussi de rendre la méthode indépendante des variations physiques ou statistiques du canal.

Dans ACA-LMMSE, la variance du bruit est supposée connue, ce qui est rarement le cas en pratique. Une autre méthode proposée dans la thèse consiste à supposer le canal et le bruit inconnus, et de les estimer itérativement grâce au critère MMSE. Ainsi, à chaque itération, l'estimation d'un paramètre permet l'estimation de l'autre. Il est montré, que par un choix adapté de l'initialisation, cet algorithme converge vers des valeurs de bruit et de canal proches des valeurs exactes. Cette méthode permet donc une estimation performante du canal, du bruit et du rapport signal-à-bruit, et peut même être utilisé pour la détection de bande libre dans un contexte de radio intelligente.

Quand les pilotes sont dispersés dans la trame OFDM, il est nécessaire d'effectuer une interpolation pour obtenir l'estimation des coefficients fréquentiels sur tout le réseau temps-fréquence. Ces interpolations ont une erreur résiduelle, qui engendre alors des erreurs sur le signal reçu. On a montré qu'on peut caractériser statistiquement ces erreurs, et cela de manière analytique, en fonction de la technique d'interpolation, de l'écart entre pilotes et de la constellation choisie. Des mesures de performance théoriques, comme l'erreur quadratique moyenne ou le seuil de taux d'erreur binaire, ont été déduites. Celles-ci sont validées par comparaison avec les valeurs obtenues par simulations.

Enfin, une application de la diversité de délai cyclique (ou CDD) à un SFN (pour Single Frequency Network) a été accomplie dans le standard DRM/DRM+. Dans ce type de réseau, il arrive que le récepteur se trouvant dans une zone de recouvrement de deux antennes perde la totalité du signal. Ceci est dû à un type de canal à trajets courts, dont la conséquence est l'apparition d'évanouissements fréquentiels affectant la totalité de la bande du signal. Dans ce cas, même l'OFDM codé ne suffit pas à recouvrer l'information utile. La solution est donc d'augmenter artificiellement la sélectivité fréquentielle du canal grâce à la CDD. Cependant, on a montré que quand les pilotes sont dispersés dans la trame OFDM, cette augmentation de sélectivité impacte la qualité d'estimation. Il faut alors faire un compromis entre le gain apporté par la CDD et la complexité de l'estimateur. Cette étude a été menée dans le contexte du projet OCEAN, visant à l'optimisation d'une chaîne d'émission réception pour la radio numérique terrestre.

Abstract

In wireless communications systems, the transmission channel between the transmitter and the receiver antennas may disrupt the signal. Indeed, the channel can be frequency selective due to the multipath, and time selective if any element of the propagation environment is in motion. The multicarrier modulations, such as the orthogonal frequency division multiplexing (OFDM), are very robust against the multipath effect, and allow to recover the transmitted signal with a low error rate, when it is combined with a channel encoding. Furthermore, it is usual to consider that the channel frequency response is constant on each subcarrier, so the equalization is simply performed by a per subcarrier division. The channel estimation then plays a key role in the performance of the communications systems. For this reason, a great number of papers that propose various methods have been published for many years. Among them, we interest to the pilot aided techniques that use pilot tones to estimate the channel on some time and frequency positions. To do so, a lot of techniques are based on the least square (LS) and the minimum mean square error (MMSE) criteria. The LS is simple, but is sensitive to the noise level, and an interpolation is required if the pilot tone are scattered in the OFDM frame. The MMSE is optimal, but is much more complex than LS, and requires the a priori knowledge of the second order moment of the channel and the noise.

In this manuscript, two methods that allow to reach a performance close to the one of LMMSE while getting around its drawback are investigated. Thus, the proposed method called artificial channel aided-LMMSE (ACA-LMMSE) does not require the a priori knowledge of the channel covariance matrix nor its estimation. Moreover, this method is independent of the physical or statistical variations of the channel, so it reduces the complexity, since the covariance matrix just has to be computed once during the transmission. However, ACA-LMMSE supposes that the noise level is known at the receiver side. A second method then proposes to perform the joint estimation of the noise and the channel by means of the MMSE criterion. Consequently, as the estimation of each parameter requires the estimation of the other one, the proposed algorithm is iterative. In another way, a third part of this dissertation investigates the errors of estimation due to the interpolations. By combining a statistical and a geometrical study of the errors of interpolation, it is possible to derive an analytical expression of the mean square error (MSE) of the estimation and a theoretical expression of the lower bound of the bit error rate (BER) curves. Finally, a application of the cyclic delay diversity to a single frequency network (SFN) using the DRM/DRM+ standard is presented. The consequence of the increase of the frequency selectivity on the channel estimation is shown.

Introduction

Since the invention of the telegraph by Samuel Morse in 1832, we observed an extraordinary development of systems allowing data transmission between two distant points. As these systems became more and more popular, higher and higher data rates were required, then leading to more and more complex systems. This is the reason why the signal processing domain has met different major breakthroughs during its short history life. For instance, one can name the digital signal processing that allowed a great decrease of the size and the complexity of the telecommunications systems, the channel turbo-decoding for quasi-error free transmissions at low signal-to-noise ratios and, more recently, the standardization of multicarrier modulation for high data rate transmissions over severe channels.

Indeed, in the case of data transmission in a dense environment, like an urban transmission for instance the transmitted signal may be disrupted by several effects like reflection or diffusion. As a consequence, the received signal may be seen as a sum of delayed and attenuated versions of the transmitted signal: the transmission is then made over a multipath fading channel. These channels can be very frequency selective, i.e. deep fading may be observed in some frequency bands. For applications requiring low data rates (i.e. a transmission over a narrow bandwidth), the effect of the multipath channel is limited and classical monocarrier modulations are quite appropriate. But for transmission on larger bandwidth, another scheme has to be considered.

The multicarrier modulations, and particularly the orthogonal frequency division multiplexing (OFDM), have shown to be adapted for transmissions in multipath channels. The OFDM signal can be seen as a parallel data transmission over narrower frequency bands. This property then makes the OFDM modulation robust against the frequency selective channels. Coupled with an efficient channel code, the resulting system called coded OFDM (COFDM) has proved its efficiency as it is now part of several telecommunications standards for different applications:

- Wired communication systems: xDSL technology, PLC, etc.
- Wireless systems: WiFi [51] or WiMax, etc.
- Television: DVB-T [52], DTMB, ISBD, etc.
- Radio: DAB [53], DRM [1], etc.

As for the DVB standards that were proposed in order to replace the analog television in the frequency bands between 470 and 862 MHz, DAB and DRM are standards for the digital radio broadcasting:

- The digital audio broadcasting (DAB) [53] uses the band III or the band L.
- The digital radio mondiale (DRM/DRM+) [1] is designed for the radio broadcasting in the current AM and FM bands.

Contrarily to the industrialized countries where the AM/FM network is deeply established, this technology seems to be very attractive for emerging countries. In addition, the urban environments in these countries are also becoming denser and denser which may cause some transmission problems, even with an OFDM-based standard.

In the context of the digital radio broadcasting in the DRM/DRM+ standard, the study made in this thesis is especially focused on the transmission channel estimation. Indeed, the channel estimation is a key function in the transmission chain in order to limit the transmission errors. This is particularly relevant in the DRM channels, because the channels are naturally frequency selective due to the multipath effect, but also time selective as the receiver may be mobile. Furthermore, in radio broadcasting, there is no feedback of data via an uplink from the mobile station (MS) to the base station (BS), so the receiver does not have any a priori information on the channel.

The literature is very extensive about the channel estimation techniques. In this dissertation, two methods are proposed to approach the optimal estimator by avoiding its drawbacks. The channel is also studied in particular cases, i.e. when the path delays are very short or, on the contrary, when they are overlong. Furthermore, an analytical study of the channel estimation, when performed by means of interpolations techniques, is proposed. It is shown that the different methods and studies proposed in this report are not limited to the framework of the DRM standard, but can be applied in the general context of the transmission of any OFDM signal over multipath channels.

The organization of this dissertation is depicted on Fig. 18. For an better reading of the thesis, the links between the different chapters are highlighted by arrows. The content of the chapters are presented hereafter.

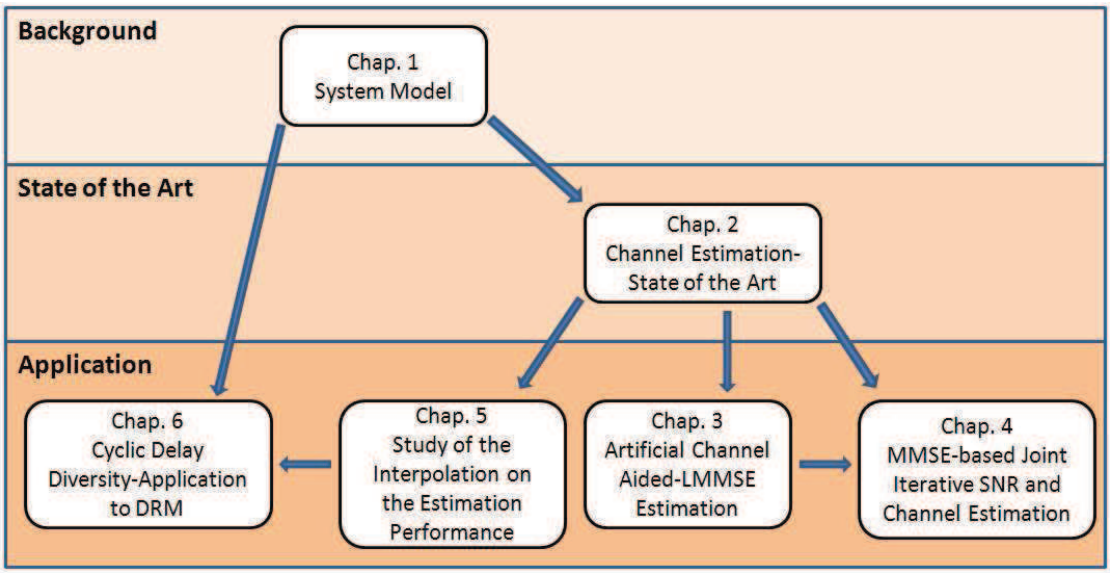

FIGURE 18 – Plan of the thesis dissertation.

Chapter 1 presents the system model used all along the dissertation. The different statistical properties and the characterizations of the transmission channel are recalled. The model

of the OFDM transmission over a multipath channel is formalized, and the different features of such a multi-carrier transmission are reminded.

Chapter 2 presents the main techniques of channel estimation. After having skated over the blind methods and the methods with knowledge of the channel, we focus on the semi-blind techniques, also called pilot symbol aided modulation (PSAM) in the literature. The pilot subcarriers are essentially used for the synchronization and, in our context, the channel estimation. Different pilot arrangements in an OFDM frame are presented, according to the time and/or frequency selectivity of the propagation channel. The two main estimation criteria least square (LS) and minimum mean square error (MMSE) are detailed, and a new expression of the MMSE is proposed. Then, some usual methods of the literature are presented, with their advantages and weaknesses.

In Chapter 3, a channel estimation method called artificial channel aided - linear MMSE (ACA-LMMSE) is proposed. Although the LMMSE channel estimation is optimal according to the MMSE criterion, it has two main drawbacks. The first one is its complexity, especially in a mobile environment, since the channel variations must be tracked. The second one lies in the fact that LMMSE requires an a priori knowledge of both the channel statistics via the channel covariance matrix and the noise level. The proposed technique allows to reduce the complexity of LMMSE in the case of a time-varying channel, and avoid the a priori knowledge or the estimation of the channel covariance matrix. Furthermore, the performance of ACA-LMMSE is close to the one of the theoretical LMMSE. In addition, it is shown that ACA-LMMSE can be combined with the residual intersymbol interference cancellation (RISIC) algorithm to mitigate the interference in a mobile environment.

Chapter 4 also deals with the LMMSE estimator, but with a different point of view from the previous chapter. Here, a joint and iterative method for both signal to noise ratio (SNR) and channel frequency response is proposed. Contrary to ACA-LMMSE, the receiver does not have any knowledge of the noise level, in addition to the transmission channel. In order to get a very good channel estimation, both parameters are estimated by means of the MMSE criterion. As the MMSE estimation of the noise variance requires the channel knowledge and the LMMSE channel estimation requires the noise level, an iterative algorithm is proposed, in which each estimation feeds the other one. The chapter is divided into three part: in the first one, a theoretical approach of the algorithm is presented. Here, the channel covariance matrix is supposed to be known, which is not the case in practice. Thus, in a second part, the receiver does not have any knowledge of the channel statistics, and the channel covariance matrix is estimated. It is theoretically proved that the algorithm converges in both scenarios. In the third part, an application of the algorithm to spectrum sensing is presented. The performance of the joint estimation is compared to several techniques of the literature, and simulations show that it is very close to the optimal one. Applied to spectrum sensing, the methods turns out to have a high detection probability, even for low SNR values. Thus, the proposed algorithm is able to achieve the detection of a hole in the spectrum, and the joint estimation of the channel and the SNR. The method comes then within the scope of cognitive radio.

After having studied the LMMSE channel estimation, Chapter 5 focuses on the error of interpolation in the context of the channel estimation. It is usual to consider sparsely distributed pilot tones in the OFDM frame, so an interpolation is required to get the estimation over

the whole time-frequency lattice. However, these interpolations are responsible of estimation errors, which result in the appearance of an error floor on the bit error rate (BER) curves. In this chapter, we propose to analytically evaluate this error floor value, according to the considered interpolation method and constellation type. Thus, the analysis is split into two parts: a statistical analysis of the errors, according to the interpolation, and a geometrical analysis, according to the chosen constellation. The study is carried out for two different interpolation methods: nearest neighbor (NN) and linear, and for two constellation sizes: binary phase shift keying (BPSK) and 4-quadrature amplitude modulation (4-QAM). Furthermore, an theoretical expression of the mean square error of the channel estimation performed with different kinds of interpolation is proposed.

Finally, Chapter 6 presents an application of the cyclic delay diversity (CDD) to the digital radio mondiale DRM/DRM+ standard [1] and its impact on the channel estimation. In single frequency networks (SFNs), it may happen that flat fading affects the whole transmission channel when the receiver is situated in the overlapping area between two cells. In that case, the benefit of OFDM in frequency selective environments is lost, and the whole signal may be lost, even if a channel code is used. In order to keep the advantage of OFDM, one solution is to artificially increase the frequency selectivity of the channel by increasing its maximum delay. This technique is then called delay diversity. In this chapter, the benefit of DD is shown, and the effect of the increase of the frequency selectivity on the choice of the estimation method is studied.

Within the framework of the radio transmission in the standard DRM/DRM+, the collaborative project called OCEAN, for Optimisation d'une Chaine Emission-Réception pour la rAdio Numérique terrestre, aims at the study and the optimization of the radio transmission chain. This thesis comes whithin the scope of this project. Started in 2010 and ended in 2013, it has grouped four industrial and academic partners together, all four located in Brittany, France:

- Digidia and Kenta, two SMEs which manufacture devices for the digital broadcasting and the implementation of the network,
- ECAM Rennes and Télécom Bretagne, two engineering schools.

This project has been funded by the Brittany region and by Rennes métropole. Fig. 19 shows the logos of the four partners and the financiers.

FIGURE 19 – Partners and financiers of the OCEAN project.

Chapter 1

System, Models, Basic Elements

1.1 Introduction

This chapter reminds some fundamentals about the propagation channel and the OFDM transmission chain. A topic about the transmission channel and its modeling is firstly covered. Then a description of the statistical tools that are used to characterize it is proposed. Second, the OFDM transmission chain, and in particular the OFDM signal, its properties and its benefits in a multipath environment is presented.

1.2 The Transmission Channel

As a large number of expressions are used to qualify the channels (static, wide sense stationary, deterministic etc.), we propose in this section our definitions of the basic elements that identify a transmission channel. These definitions are thus suggested to avoid some confusions and will be used in the rest of this manuscript.

The transmission channel defines the environment situated between the emission and the reception antennas. The signal, transmitted over the channel, suffers from some perturbations of different kinds: reflection, diffraction or diffusion. These phenomena are due to obstacles in the environment of propagation, like an hilly landscape, buildings or the change of temperature with the altitude. Furthermore, the transmitter, the obstacles or the receiver can be in motion. The consequence is a time variation of the channel that also causes a Doppler effect. The simple picture of Fig. 1.1 illustrates different causes of the signal perturbations.

1.2.1 The Multipath Channel

Some transmission networks only involve one fixed transmitter and one fixed receiver both being in line of sight. It is then simple to shape directional antennas to get a radio beam. In such conditions, the signal is generally weakly degraded. In mobile radio transmissions, antennas are isotropic, and the signal takes several paths before reaching the reception antenna. This propagation environment is called multipath channel. For example, Wi-Fi waveforms [51] are reflected on the walls, on the floor and on the ceiling of a building. At other wavelengths, the obstacles (TV waveforms in DVB-T standard [52] for example) are building and the ones at FM wavelength [1] are hilly landscapes or mountains.

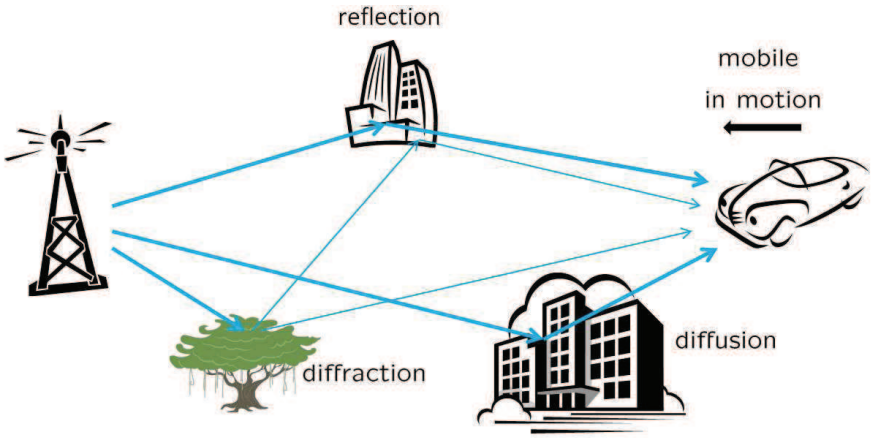

FIGURE 1.1 – Illustration of effects of the transmission channel.

In most transmission schemes, the transmitting antennas do not need to be necessarily in line of sight (LOS), i.e. in direct visibility. Thanks to multiple reflections, the signal can bypass the obstacles and be received in buildings, in a dense urbanization etc. This kind of multipath channel is qualified as Non- Line Of Sight (NLOS). On the other hand, a signal processing is required in order to limit the degradations due to the multipath effect.

The impulse response of a multipath channel can be characterized by three parameters:

- the number L of paths of the channel,
- the complex gain of each path, noted h_l
- the delay of each path, noted τ_l, with $l = 0, 1, ..., L-1$.

Considering a mobile channel, these three parameters can be time varying, and noted $L(t)$, $h_l(t)$ and $\tau_l(t)$. In this general model, the impulse response of the channel, function of the time t and of the delay τ, is given by

$$h(t,\tau) = \sum_{l=0}^{L(t)-1} h_l(t)\delta(\tau - \tau_l(t)), \tag{1.1}$$

where $\delta(\tau)$ is the Dirac impulse.

The nature of the channel depends on the sizing of the signal, i.e. the modulation. Thus, if we denote T the reference time of the modulation (i.e. the symbole duration), then, we distinguish four kinds of channels:

- Static channel: the channel is time-invariant.
- Quasi-static channel: the channel can be considered as time-invariant during a significant time $>> T$.
- Dynamic channel: the channel is constant during a symbol, but varies from a symbol to another .
- Fast-varying channel: the channel may vary during a data symbol.

The writing of (1.1) tallies with fast-varying channel. In the rest of this document, we will be interested only by quasi-static and dynamic channel models. Furthermore, in the majority of cases, we will assume that the number of path L and the delays τ_l are constant during the transmission, which simplifies the writing to

$$h(t,\tau) = \sum_{l=0}^{L-1} h_l(t)\delta(\tau - \tau_l). \tag{1.2}$$

1.2.2 Channel Models

In order to limit the degradations caused by the channel, the knowledge of $h(t,\tau)$ is required. However, a transmission channel is very complex. It depends on the wavelength, the environment, the arrangements of the transmitter and the receiver, the movements of the transmitters etc. Two models are then available to describe the channel at best: the deterministic model and the statistical model.

1.2.2.1 Deterministic Model

A simple method to determine the channel profile is to measure its impulse response at different points on a given area [54], [55]. This method leads to an empirical model of the channel. It is usually used in the planning of a network, in order to optimize the ratio between the installations cost and the size of the covered area. However, it requires a laborious measures campaign. Furthermore, this method does not specify the characteristic of the channel, as the number of paths, the delays etc.

With the improvement of the computation capacity of the computers, the ray tracing technique has been developed, as depicted in [56], [57]. The method is based on the same principle as the geometrical optics, considering the light waves as rays following geometrical propagations. In this case, the electromagnetic waves of the signal is seen as a ray having linear propagation in a known environment (thanks to a map, a building plan etc.). It is then possible to determine the signal trajectories. This method gives a better description of the physical reality of the channel than the empirical model, but requires a greater computational complexity.

These two methods are very useful to plan a network and to provide an a priori state of the propagation channel for the user in a given environment. However, it is sensitive to the random variation of the channel.

1.2.2.2 Statistical Model

As a great number of natural phenomena, the transmission channel is subject to random variations. The deterministic model then becomes insufficient to characterize its statistical properties. In this model, $h(t,\tau)$ is seen as a random variable, characterized by statistic functions, as developed in subsection 1.2.3. The statistical model is commonly used in the theoretical studies of the channel and for simulations. This model is also used in this report.

1.2.3 Channel Statistics

In this section, we define the channel model that is used in this report. Thus, we introduce the Wide Sense Stationary Uncorrelated Scattering channel model. Furthermore, from Bello's model [2], we derive the statistical functions as the channel intensity profile, the correlation function, the channel Doppler spectrum and the scattering function.

1.2.3.1 Probability Density Function of the Amplitude and the Phase of $h(t,\tau)$

In an NLOS transmission, the antennas being considered as isotropic, the signal is supposed to be received from all possible directions at the reception antenna. In first approximation, the channel $h(t)$ can be seen as a sum of K independent components $h(t)^{(\kappa)}$ (with $\kappa = 0, 1, ..., K$) coming from all directions, with $K \to +\infty$. The components $h(t)^{(\kappa)}$ are complex random variables, with a mean m_κ and with a variance σ_κ^2. By applying the central limit theorem, $h(t)$ is then a zero-mean Gaussian complex process whose gain $|h(t)|$ follows a Rayleigh distribution [3], noted $p_{r,Ray}(r)$. Its variance, noted σ_h^2, is equal to $E\{|h(t)|^2\}$. $p_{r,Ray}(r)$ is written as

$$p_{r,Ray}(r) = \frac{r}{\sigma_h^2} e^{\frac{-r^2}{2\sigma_h^2}}, \tag{1.3}$$

where r is a positive real value. The probability density function (pdf) of the phase of a Rayleigh process follows a constant distribution, noted $p_{\phi_{h_{ray}}}(\theta)$ as

$$\forall \theta \in [-\pi, \pi],\ p_{\phi_{h_{ray}}}(\theta) = \frac{1}{2\pi}, \tag{1.4}$$

For a LOS transmission, a line of sight component is added to the previous model. The corresponding probability density function follows the Rice distribution (given in [58]), noted $p_{r,Rice}(r)$ as

$$p_{r,Rice}(r) = \frac{r}{\sigma_h^2} e^{-\frac{r^2+\rho^2}{2\sigma_h^2}} I_0(\frac{r\rho}{\sigma_h^2}), \tag{1.5}$$

where $I_0(.)$ is the modified Bessel function of the first kind with order zero, r is a positive real value, ρ^2 is the variance of the line of sight path, and σ_h^2 the variance of the scattered components. We define the Rice factor $\mathcal{C}_R = \frac{\rho^2}{\sigma_h^2}$ as the ratio between the power of the LOS received signal component and all the NLOS components. The probability density function of the phase $p_{\phi_{h_{rice}}}$ is given by

$$p_{\phi_{h_{rice}}}(\theta) = \frac{e^{-\frac{\rho^2}{\sigma_h^2}}}{2\pi} \left(1 + \sqrt{\frac{\pi\rho^2}{\sigma_h^2}} \cos(\theta - \theta_\rho) e^{\frac{\rho^2 \cos^2(\theta-\theta_\rho)}{\sigma_h^2}} \left(1 + \text{erf}(\frac{\rho\cos(\theta-\theta_\rho)}{\sigma_h})\right)\right), \tag{1.6}$$

where erf(.) is the error function and θ_ρ is the phase of the LOS path. For $x \geq 0$, the error function is defined as $\text{erf}(x) = \frac{2}{\pi}\int_0^x e^{-t^2} dt$. θ is defined as $-\pi < \theta \leq \pi$. We remark in (1.5) and (1.6) that if $\rho^2 \longrightarrow 0$, we naturally get the Rayleigh model that has been previously described. Fig. 1.2 depict the probability density functions of the amplitude (a) and phase (b) in Rayleigh and Rice cases, for $\sigma_h^2 = 1$ and $\theta_\rho = 0$.

Although Rayleigh and Rice models are the most frequently used channel models, some other ones exist. Thus, the Weibull model [4] is close to real measured channels. Nakagami model [5], later generalized in [6] by the $\kappa - \mu$ distribution, is a general model in which Rayleigh's and Rice's are particular cases.

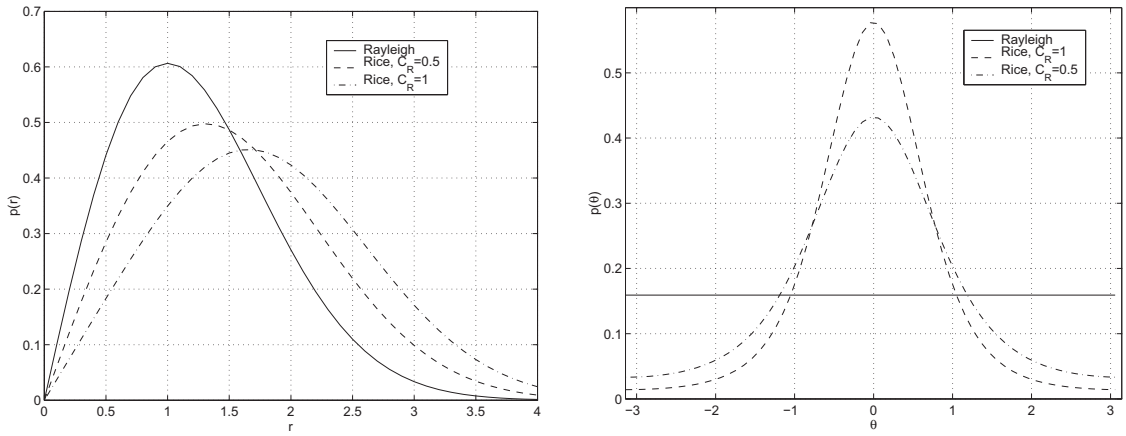

(a) Amplitude (b) Phase

FIGURE 1.2 – Probability Density Function of the Amplitude and the Phase of $h(t, \tau)$.

1.2.3.2 Time-Frequency Correlation Function and Power spectra in WSSUS Model

Based on Bello's work [2], and thanks to the theoretical developments in [3] and [59], we define in this part the different statistical functions allowing to describe the channel. Illustrations will clarify the different relationships between the following functions.

a. Impulse Response and Frequency Response The impulse response $h(t, \tau)$ given by (1.2) and the frequency response $H(t, f)$ (1.7) of the channel are mutually linked by a Fourier Transform relation noted FT_τ. The subscript in $FT_{(.)}$ denote the variable on which the Fourier Transform is processed.

$$\begin{aligned} H &= FT_\tau(h) \\ \Rightarrow H(t,f) &= \int_{-\infty}^{+\infty} h(t,\tau) e^{-2j\pi f\tau} d\tau \\ H(t,f) &= \sum_{l=0}^{L-1} h_l(t) e^{-2j\pi f\tau_l}. \end{aligned} \tag{1.7}$$

Fig. 1.3 illustrates this relationship ((a): $h(t, \tau)$, and (b): $H(t, f)$). We notice that the FT is made on the delays τ, which makes the frequency response $H(t, f)$ a time-varying function. As far as Fig. 1.3 is only an illustration of the impulse and frequency responses of a channel, the axes scales have been only defined for simulations purpose of $h(t, \tau)$ and $H(t, f)$.

b. WSSUS Channel Model From [2], we highlight the acronym WSSUS:

– WSS, for wide sense stationary: each path $h_l(t)$ in (1.2) is a zero mean Gaussian complex process, so $E\{h_l(t)\} = 0$, $\forall t$, with $E\{.\}$ the statistical expectation, and then the mean of each path is independent of the time variations. Furthermore, the time correlation function $r_{h_l}(t_1, t_2) = E\{h_l(t_1)h_l^*(t_2)\}$ can be only written with the difference $\Delta_t = t_1 - t_2$, i.e.

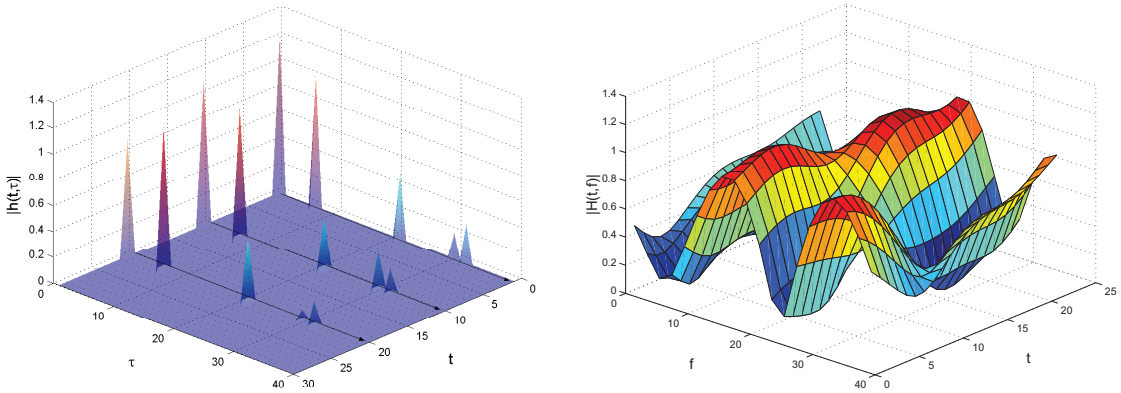

(a) Impulse response $h(t, \tau)$ (b) Frequency response $H(t, f)$

FIGURE 1.3 – Illustration of time-varying impulse and frequency responses of a channel.

$$r_{h_l}(t_1, t_2) = r_{h_l}(\Delta_t). \tag{1.8}$$

Each path $h_l(t)$ of the channel is then wide sense stationary.

– US, for uncorrelated scattering: the paths are uncorrelated, so for $l_1 \neq l_2$

$$E\{h_{l_1}(t)h^*_{l_2}(t)\} = 0. \tag{1.9}$$

c. Time-Frequency Correlation Function and Channel Doppler Spectrum Since the channel follows the WSSUS model, its time-frequency correlation function, noted R_H and defined by $R_H(t_1, t_2, f_1, f_2) = E\{H(t_1, f_1)H^*(t_2, f_2)\}$ has the following property:

$$R_H(t_1, t_2, f_1, f_2) = R_H(\Delta_t, \Delta_f), \tag{1.10}$$

where $\Delta_f = f_1 - f_2$. To generalize, all the statistical functions are written with the variables Δ_t and Δ_f that are independent of the time t and the frequency f.

A useful and usual function describing the channel is the power spectral density (PSD), also called channel Doppler spectrum. Considering a two-dimensional plane for the signal scattering, isotropic antennas, an homogeneous transmission environment and a Rayleigh-distributed channel response, it is shown that the PSD follows the Jakes' model [60] also called spectrum in "U". However, Clarke was the first to propose this PSD in [61]. The PSD, noted $S_H(\nu, \Delta_f)$ is defined as the Fourier Transform of the time correlation function $R_H(\Delta_t, \Delta_f)$ for $\Delta_f = 0$. We then restrict the correlation function (1.10) to its time component, and according to the notations, we adopt a small letter writing, i.e. $R_H(\Delta_t, \Delta_f = 0) = r_h(\Delta_t)$ for the time correlation function. Furthermore, we note $S_H(\nu, \Delta_f = 0) = S_H(\nu)$. We then get:

$$S_H(\nu) = FT_{\Delta_t}(r_h(\Delta_t)). \tag{1.11}$$

Basically, the Jakes' PSD is given by

$$S_H(\nu) = \begin{cases} \frac{\sigma_h^2}{\pi \nu_{D_{max}} \sqrt{1-(\frac{\nu}{\nu_{D_{max}}})^2}} & \text{if } |\nu| \leq \nu_{D_{max}} \\ 0 & \text{else} \end{cases}, \tag{1.12}$$

where $\nu_{D_{max}}$ is called maximum Doppler frequency, and represents the time variation of the mobile channel. In first approximation, $\nu_{D_{max}}$ can be seen as the ratio between the velocity v_M of the received mobile or surrounding objects on the wavelength λ_s of the transmitted signal, $\nu_{D_{max}} = \mathrm{v}_M/\lambda_s$.

Thanks to the developments given in [3], the time correlation function $r_h(\Delta_t)$ is the inverse Fourier transform (noted $FT_\nu^{-1}(.)$) of $S_H(\nu)$

$$\begin{aligned} r_h &= FT_\nu^{-1}(S_H) \\ \Rightarrow r_h(\Delta_t) &= \sigma_h^2 J_0(2\pi\nu_{D_{max}}\Delta_t), \end{aligned} \tag{1.13}$$

where J_0 is the Bessel function of the first kind with order zero. Fig. 1.4 depicts the Jakes' PSD and the tallying time-correlation function for $\sigma_h^2 = 1$, considering a mobile receiver of speed 100 km.s^{-1} and a signal transmitted at 108 MHz. The maximum Doppler frequency is then equal to $\nu_{D_{max}} = 10$ Hz.

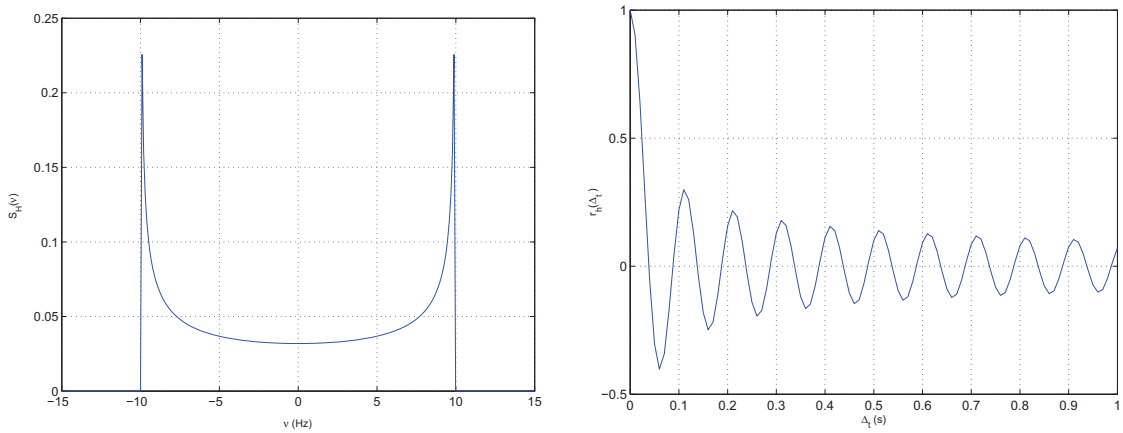

(a) Channel Doppler Spectrum (b) Time Correlation Function

FIGURE 1.4 – Link between the Jakes PSD and the time correlation spectrum.

However, the Jakes' PSD is not the only model for describing transmissions. It is shown in [62], [63] that in the presence of far echoes in the propagation, the Doppler PSD turns to Gaussian shape. It tallies with HF transmissions, with paths reflected on the ionosphere. Thus, it is for example the PSD used in the DMR standard [1] for broadcasting tallying with the AM bands. Furthermore, the same model is used in aeronautical propagations [64], as transmission between airplanes and satellites.

The function $S_H(\nu)$ is usually given in the following form:

$$S_H(\nu) = \frac{\sigma_h^2}{\sqrt{2\pi\sigma_D^2}} e^{-\frac{(\nu - f_D)^2}{2\sigma_D^2}}, \tag{1.14}$$

where σ_D^2 is the Doppler spread and f_D the Doppler shift. The Gaussian function is centered on its mean f_D. The time correlation function is then derived, following the expression given in [65]:

$$r_h(\Delta_t) = \sigma_h^2 e^{(2j\pi f_D \Delta_t)} e^{-\frac{1}{2}(2\pi\sigma_D\Delta_t)^2}. \tag{1.15}$$

It is noticeable that $r_h(\Delta_t)$ is a complex function, as $S_H(\nu)$ is centered on f_D. Indeed, when $S_H(\nu)$ is even (i.e. $f_D = 0$), then $r_h(\Delta_t)$ is a real function. Fig. 1.5 depicts (1.14) and (1.15), with $f_D = 0$, $\sigma_h^2 = 2$ and $\sigma_D^2 = 2$. These parameters are typically the ones of HF propagations with ionospheric scattering [1].

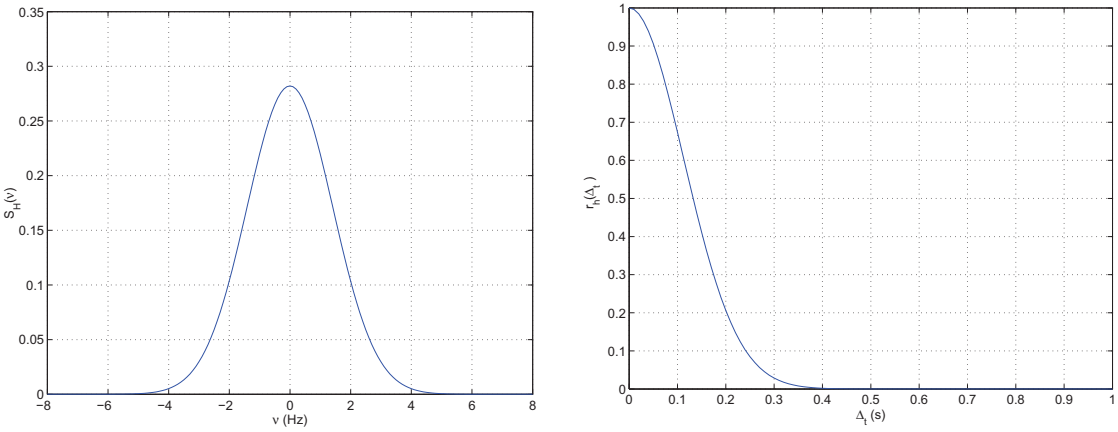

(a) Channel Doppler Spectrum (b) Time Correlation Function

FIGURE 1.5 – Link between the Gaussian PSD and the time correlation function.

As already mentioned, Jakes and Gaussian Doppler PSD are based on a 2-D scattering model with isotropic propagation. More realistic models have been developed. Thus, [66] shows that 3-D scattering model (i.e. the received signal has a solid angle of 4π steradian) have an uniform PSD. In [67], a generalization of the PSD is developed in the case of non-isotropic propagations, i.e. the signal is not received uniformly on the antenna.

d. Time-Frequency Correlation Function and Channel Intensity Profile We here give the relation between the frequency correlation function and the channel intensity profile. We restrict the correlation function (1.10) to its frequency part, i.e. the function $R_H(\Delta_t, \Delta_f)$ for $\Delta_t = 0$, that we note $R_H(\Delta_f)$. The channel intensity profile, function of the variable τ, is noted $\Gamma(\Delta_t, \tau)$. We here simplify the writing to $\Gamma(\Delta_t = 0, \tau) = \Gamma(\tau)$. The frequency correlation function and the channel intensity profile are linked by a Fourier transform relation as

$$\begin{aligned} \Gamma &= FT_{\Delta_f}^{-1}(R_H) \\ \Leftrightarrow R_H &= FT_{\tau}(\Gamma). \end{aligned} \tag{1.16}$$

As the channel is supposed to follow a WSSUS channel model, the paths are uncorrelated, then $\Gamma(\tau)$ can be expressed as the sum of the intensity profile of each path $\Gamma_l(\tau)$, as done in [7] and detailed in Appendix A.1. Thus, from [59] and [7], we give in (1.17) the expression of $R_H(\Delta_f)$:

$$R_H(\Delta_f) = \sum_{l=0}^{L-1} \int_0^{\tau_{max}} \Gamma_l(\tau) e^{(-2j\pi\Delta_f\tau)} d\tau. \tag{1.17}$$

Mathematically, the only constraint on $\Gamma_l(\tau)$ is its integrability. Physically, as seen in [7–9], most of the models for the channel intensity is the decreasing exponential profile

$$\Gamma(\tau) = \begin{cases} Ce^{\frac{-\tau}{\tau_{max}}} & \text{, if } \tau \in [0, \tau_{max}] \\ 0, & \text{else,} \end{cases} \tag{1.18}$$

where C is a normalization constant whose value is defined afterward. The frequency correlation function is then derived, as done in [7]:

$$\begin{aligned} R_H(\Delta_f) &= \sum_{l=0}^{L-1} \int_0^{\tau_{max}} Ce^{\frac{-\tau}{\tau_{max}}} e^{-2j\pi\Delta_f\tau} d\tau \\ &= \sum_{l=0}^{L-1} C. \left(\frac{e^{-\tau_{max}(\frac{1}{\tau_{max}}+2j\pi\Delta_f)} - 1}{-\tau_{max}(\frac{1}{\tau_{max}} + 2j\pi\Delta_f)} \right) \\ &= LC. \frac{1 - e^{-2j\pi\Delta_f\tau_{max}}e^{-1}}{1 + 2j\pi\Delta_f\tau_{max}}. \end{aligned} \tag{1.19}$$

We find $R_H(\Delta_f = 0) = LC(1 - e^{-1})$. In order to get $R_H(\Delta_f = 0) = 1$ (property of the correlation functions), the normalized constant is then fixed $C = 1/(L(1 - e^{-1}))$. Fig. 1.6 depicts the decreasing intensity profile and the real and imaginary parts of the frequency correlation function. The arbitrary chosen parameters are $\tau_{max} = 0.7$ ms and $L = 4$.

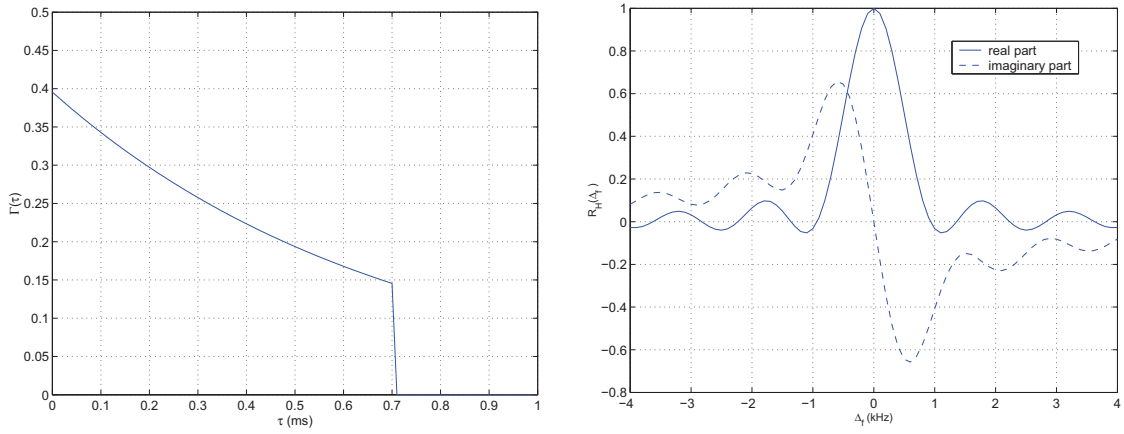

(a) Channel Intensity profile

(b) Frequency Correlation Function

FIGURE 1.6 – Link between the channel intensity profile and the frequency correlation function.

e. Scattering function The fourth statistical function that is used to describe the channel is the scattering function, noted S_h, and function of the variables ν and τ. Determining $S_h(\nu, \tau)$ is in most cases not necessary as it can be easily derived from the previously defined functions with the following relations

$$\begin{aligned} S_h &= TF_{\Delta_t}(\Gamma) \\ S_h &= TF^{-1}_{\Delta_f}(S_H). \end{aligned} \tag{1.20}$$

Nevertheless it is interesting, because the study of $S_h(\nu, \tau)$ is sufficient to characterize the channel scattering. Indeed, the shape of $S_h(\nu, \tau = 0)$ (i.e. the Doppler spectrum) characterizes the channel variation speed, and the shape of $S_h(\nu = 0, \tau)$ (i.e. channel intensity profile) determines the length and gain of the paths. Fig. 1.7 depicts the 3D scattering function. Note that the scales on X and Y axes are defined for simulation purpose and do not reflect any physical reality.

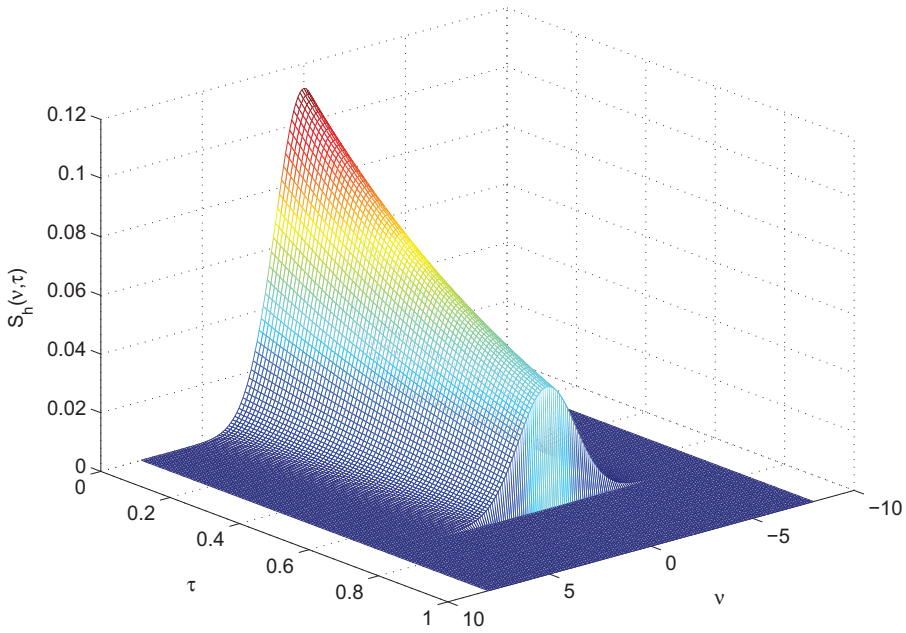

FIGURE 1.7 – Scattering function $S_h(\nu, \tau)$.

As the channel is time-varying, it is very difficult to obtain a dynamic knowledge of its characteristics. Furthermore, it becomes impossible to get a perfect knowledge if some additive noise is considered. However, its statistic properties are well described by the functions $R_H(\Delta_t, \Delta_f)$, $S_H(\nu, \Delta_f)$, $\Gamma(\Delta_t, \tau)$ and $S_h(\nu, \tau)$. Indeed, by a priori approximations, empirical model or measurements, it is possible to use these functions in order to design a given transmitted signal. For instance, knowing the number of paths, their delays and the channel variation speed is crucial to determine:

- the choice of the modulation to use (single/multicarrier),
- the design of the equivalent receiver (channel estimation, echo cancellation etc.),
- the possible data rate that can be reached.

The design of the transmitter/receiver is also facilitated by the knowing of the coherence time noted T_C and the coherence bandwidth noted B_C. It is considered that the channel is invariant during the time duration T_C and frequency bandwidth B_C. In first approximation, proposed in [68], T_C and B_C can be given by

$$T_C \propto \frac{1}{\nu_{D_{max}}} \tag{1.21}$$

$$B_C \propto \frac{1}{\tau_{max}} \tag{1.22}$$

The statistical functions and the links between them are often summarized in literature by the diagram given in Fig. 1.8, as Bello presented it in [2].

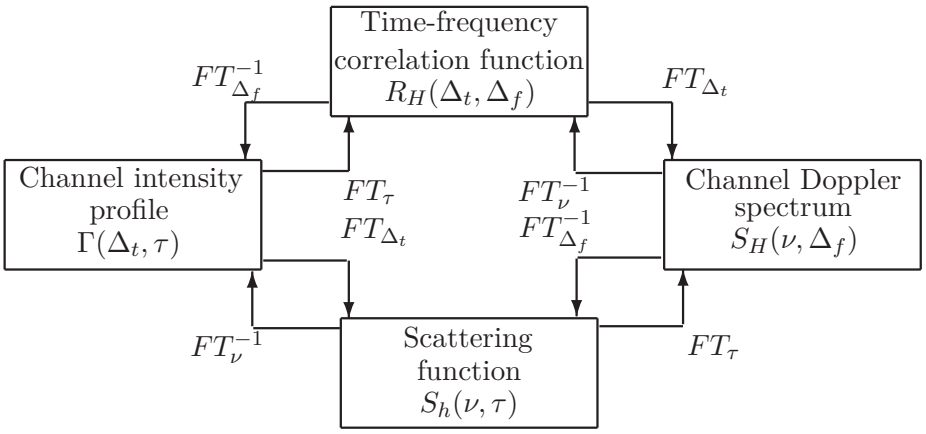

FIGURE 1.8 – Diagram summarizing the links between the different statistical channel functions.

1.3 The OFDM Signal and the Transmission Chain

1.3.1 History

As it is described in [69, 70], the transmission of the data using a frequency multiplexing is very robust against the frequency selectivity of the channel, when it is combined with a channel coding. As mentioned in [70, 71], the first techniques of frequency multiplexing with orthogonal carriers appeared in the mid 50's for military applications. In the 60's and 70's, the analog modulation and demodulation by means of the Fourier transform as been developed, but it was prohibitive in terms of calculation load for a massive deployment of this technology. The OFDM acronym appeared in the 80's, when the evolution of the technology of semi-conductor allowed a great development of the implementation of complex algorithms, especially the ones based on FFT/IFFT of large size. This kind of modulation is now used in a large number of wired and wireless transmission standards.

1.3.2 Modelisation of the OFDM Signal

In this section, we describe the mathematical expression of the OFDM signal in a time-continuous formalism. In baseband, the n^{th} OFDM symbol noted $s_n(t)$, composed of M subcarriers, is given by:

$$s_n(t) = \sqrt{\frac{1}{T_s}} \sum_{m=0}^{M-1} C_{m,n} \Pi(t - nT_s) e^{2j\pi m F_s t}, \tag{1.23}$$

whith $\Pi(t)$ the rectangular function of duration T_s as

$$\Pi(t) = \begin{cases} 1 & \text{if } -\frac{T_s}{2} \leq t < \frac{T_s}{2} \\ 0 & \text{else,} \end{cases} \tag{1.24}$$

where T_s is the OFDM symbol duration, $F_s = \frac{1}{T_s}$ is the subcarrier spacing and $C_{m,n}$, $m = 0, 1, ..., M-1$ are the information symbols coming from a set Ω of a given constellation. For example, for a QPSK, we have the set $\Omega = \{1+j, 1-j, -1+j, -1-j\}$. The orthogonal frequency multiplexing can be written with the family of functions $\phi_m(t)$, defined by

$$\phi_{m,n}(t) = \sqrt{\frac{1}{T_s}}\Pi(t - nT_s)e^{2j\pi mF_s t}. \tag{1.25}$$

This family of functions is known to satisfy the orthonormal property for the usual complex scalar product:

$$\begin{aligned} \left\langle \phi_{m,n}, \phi_{m',n'} \right\rangle &= \int_{-\infty}^{+\infty} \phi_{m,n}(t)\phi^*_{m',n'}(t)dt \\ &= \delta_{m,m'}\delta_{n,n'}, \end{aligned} \tag{1.26}$$

where δ is the Kronecker delta symbol

$$\delta_{m,n} = \begin{cases} 1 & \text{if } m = n, \\ 0 & \text{else} \end{cases}. \tag{1.27}$$

The signal at the transmitter is composed of an infinity of OFDM symbol, for $n \in \mathbb{Z}$:

$$s(t) = \sqrt{\frac{1}{T_s}} \sum_{n\in\mathbb{Z}} \sum_{m=0}^{M-1} C_{m,n}\Pi(t - nT_s)e^{2j\pi mF_s t}. \tag{1.28}$$

From the expression of the OFDM signal (1.28) and the orthogonality relation (1.26), the demodulation of the signal amounts to a simple scalar product:

$$\hat{C}_{m,n} = \left\langle \phi_{m,n}, s \right\rangle. \tag{1.29}$$

1.3.3 Transmission of the OFDM Signal

The signal $s(t)$ is transmitted over the multipath channel $h(t, \tau)$ (1.2). An additive white Gaussian noise (AWGN) $w(t)$ is added at the receiver side. The received signal $u(t)$ is expressed by

$$\begin{aligned} u(t) &= (h \star s)(t) + w(t) \\ &= \int_0^{\tau_{max}} h(t, \tau)s(t - \tau)d\tau + w(t), \end{aligned} \tag{1.30}$$

where $\star$ is the convolution product. In practice, if the OFDM signal were simply transmitted following (1.28), the channel with delayed multipath would create intersymbol interferences (ISI), as depicted in Fig 1.9. In order to avoid this effect, a guard interval (GI) is added to each OFDM symbol. The GI can be of several kinds [72]:

– zero-padding: a signal equal to zero is introduced at the beginning of each symbol,
– known-sample-padding: a known signal is introduced at the beginning of each symbol,
– cyclic prefix (CP): the end of the symbol of length T_{CP} is copied out at its beginning. We will consider CP for the rest of the report. The addition of the CP is depicted in Fig 1.10.

In the three cases, the GI does not include useful information, so this technique reduces the useful data rate. The CP duration is chosen so that T_{CP} is at least equal to the maximum channel delay. The effective transmitted signal is then of duration $T'_s = T_s + T_{CP}$. We consider in the transmission model (1.30) that the CP has been removed. In the following, we will justify that the use of CP allows to simplify the mathematical expression of the received signal, thanks to the cyclic property of the CP.

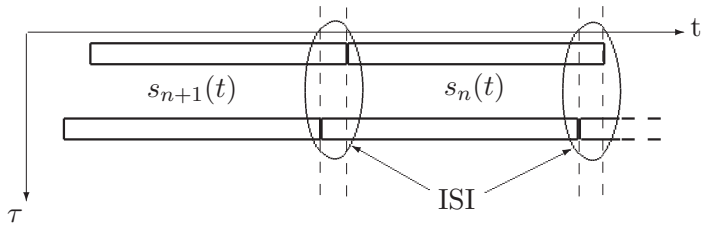

FIGURE 1.9 – ISI due to delayed multipath channel.

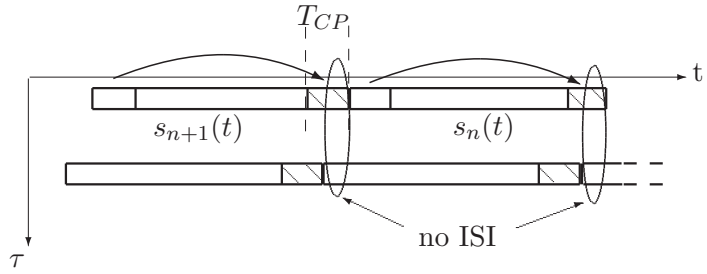

FIGURE 1.10 – ISI cancellation by means of the CP.

The OFDM signal, combined with a cyclic prefix, is a robust modulation against the multipath channel as it efficiently limits ISI. In frequency domain, the effects of the multipath channel are the fading in some parts of the frequency bandwidth B of the considered signal. Equation (1.31) gives the received signal $U(f)$ in frequency after the Fourier Transform:

$$\begin{aligned} U &= FT_t(u) \\ &= FT_t((h \star s) + w) \\ \Rightarrow U(f) &= H(f).C(f) + W(f). \end{aligned} \tag{1.31}$$

where $C(f)$ is the FT of $s(t)$. The use of orthogonal carriers in frequency domain amounts to consider the bandwidth B as M parallel subchannels of width $B_M = \frac{B}{M}$. The signal is well dimensioned thanks to coherence bandwidth B_C if $\frac{B}{M} << B_C$ (see section 1.2). In this condition, each subchannel can be seen as a Gaussian channel, i.e. only a flat channel

with AWGN. Knowing the channel, it is straightforward to recover the information symbols $C_{m,n}$ thanks to a one-tap equalization, i.e. a simple division. Fig. 1.11 depicts this OFDM property: the signal $C(f)$ and the frequency channel response $H(f)$ can be locally (on the bandwidth B/M) seen as constant. A simple per subcarrier equalization is then performed. This representation of parallel subchannels also leads to a simple discrete model of the OFDM signal, developed in section 1.3.4.

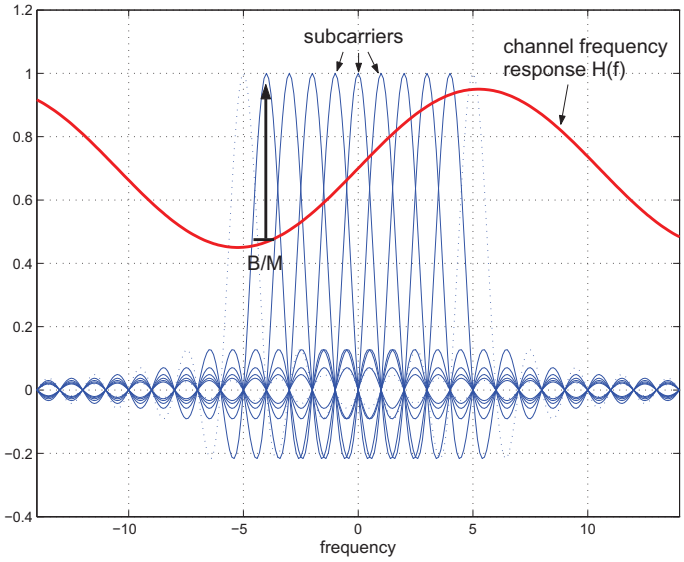

FIGURE 1.11 – Illustration of the OFDM principle and the frequency effect of multipath channel.

However, the attenuations can be locally strong, i.e. $H(f) \approx 0$ for a given value of f. In this case, the demodulation (1.29) operation recovers only noise due to $W(f)$, and errors may appear. As a consequence, the sole OFDM modulation is insufficient to fight against these perturbations. However, by combining the OFDM with channel coding is a very efficient solution [73]. The coded-OFDM (COFDM) is used nowadays in all the OFDM transmission systems. The coding operation is made at the binary information level. The principle is to create redundancy in the transmitted message in a way that the errors can be corrected thanks to the additional information. Reed-Solomon code (RS) [48] or convolutive codes, proposed in 1955 in [74] and [75] are two frequently used kinds of code. The convolutive codes allow to correct the independent errors in the frame, and RS code the error packets. Furthermore, in order to limit the length of these packets, a bit interleaving is operated on the bit frame, which allows to separate the error chains in reception.

Fig. 1.12 depicts a simplified transmission chain including the interleaving, channel encoding, mapping, modulation at the transmitter side and their reverse blocks at the receiver side. Some blocks such as "pilots insertion" or "IDFT" will be explained afterward in the dissertation.

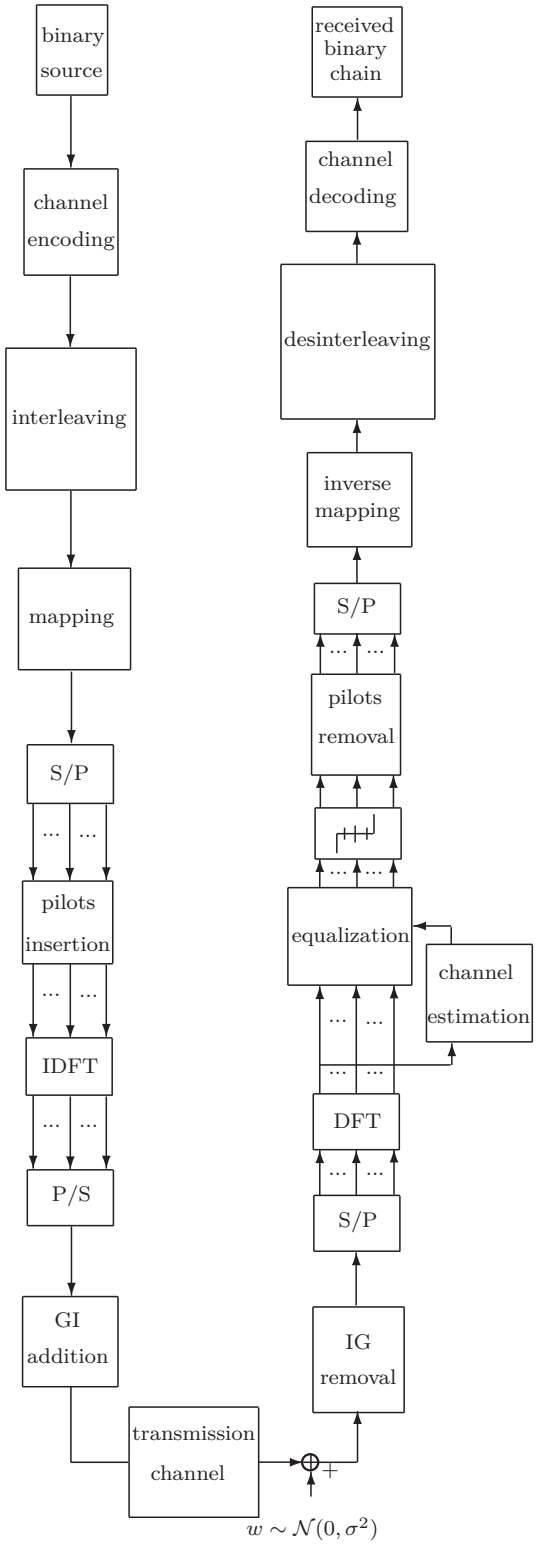

FIGURE 1.12 – Simplified diagram of the transmission chain of an OFDM signal.

1.3.4 Discrete Model of the OFDM Transmission

Most of the time, the design of analog modulators and demodulators is hard to implement as it requires very specific technologies that are sometimes reproducible with difficulty. This is even more the case for OFDM signal modulation as it can be seen as M parallel monocarrier modulators. In addition to the fact that M can be very large, the perfect synchronization of the M modulators becomes an insuperable problem. This is the reason why for such modulations, the signal digitalization is unavoidable as it allows the use of digital processors like ASICs, FPGAs or DSPs whose chip is very reproducible. Moreover, as further seen in this paragraph, we show that the sampled OFDM signal can be generated by (I)DFT, and (I)FFT in some particular cases. Indeed, in the case where $M = 2^p$ (with p an integer), the (I)DFT can be computed by an (I)FFT algorithm that reduces the IDFT computation.

We note τ_s the sampling time. According to the Shannon theorem, τ_s is defined for the rest of the report as

$$\tau_s = \frac{T_s}{M}. \tag{1.32}$$

From (1.23), we derive the expression of the OFDM symbol samples $s_n[k]$ in the discrete time, noted $s_{k,n}$ for more readibility:

$$\begin{aligned} s_{k,n} &= s_n(t = k\tau_s) \\ &= \sqrt{\frac{1}{M}} \sum_{m=0}^{M-1} C_{m,n} e^{2j\pi m F_s k \tau_s} \\ &= \sqrt{\frac{1}{M}} \sum_{m=0}^{M-1} C_{m,n} e^{2j\pi m \frac{k}{M}}, \end{aligned} \tag{1.33}$$

with $k = 0, 1, ..., M-1$. The complex vector $\mathbf{s}_n = (s_{0,n}, s_{1,n}, ..., s_{M-1,n})^T$ of size $M \times 1$ represents the n^{th} OFDM symbol sampled at the frequency $f_s = 1/\tau_s$. From (1.33), we notice that the samples $s_{k,n}$ are obtained by the inverse discrete Fourier transform (IDFT) of the constellation symbols $C_{m,n}$. We define the vector $\mathbf{C}_n = (C_{0,n}, C_{1,n}, ..., C_{M-1,n})^T$ of size $M \times 1$ in the frequency domain, composed of the M elements $C_{m,n}$ transmitted at the n^{th} time slot. In the same way, each component $C_{m,n}$ of $\mathbf{C}_n$ is the discrete Fourier transform (DFT) of the samples $s_{k,n}$:

$$C_{m,n} = \sqrt{\frac{1}{M}} \sum_{k=0}^{M-1} s_{k,n} e^{-2j\pi m \frac{k}{M}}. \tag{1.34}$$

Eqs. (1.33) and (1.34) can be rewritten in a vectorial formulation:

$$\mathbf{s}_n = \underline{\mathcal{F}}^{-1} \mathbf{C}_n, \tag{1.35}$$

$$\mathbf{C}_n = \underline{\mathcal{F}} \mathbf{s}_n, \tag{1.36}$$

where $\underline{\mathcal{F}}$ is the $M \times M$ Fourier matrix defined by

$$\underline{\mathcal{F}} = \frac{1}{\sqrt{M}} \begin{pmatrix} 1 & 1 & 1 & \cdots & 1 \\ 1 & \omega & \omega^2 & \cdots & \omega^{(M-1)} \\ 1 & \omega^2 & \omega^4 & \cdots & \omega^{2(M-1)} \\ \vdots & \vdots & \vdots & \ddots & \vdots \\ 1 & \omega^{(M-1)} & \omega^{2(M-1)} & \cdots & \omega^{(M-1)^2} \end{pmatrix}, \tag{1.37}$$

with $\omega = e^{-\frac{2j\pi}{M}}$. The Fourier matrix verifies the orthonormality condition $\underline{\mathcal{F}}\underline{\mathcal{F}}^H = \underline{\mathbf{I}}$, $\underline{\mathbf{I}}$ being the identity matrix. We also deduce that $\underline{\mathcal{F}}^H = \underline{\mathcal{F}}^{-1}$. $\mathbf{s}_n$ and $\mathbf{C}_n$ are the representations of an OFDM symbol in the time and frequency domains, respectively.

The discrete-time impulse response of the channel is derived from (1.2). Considering the channel to be invariant during an OFDM symbol, we rewrite the expression of each path gain as $h_l(t) = h_{l,n}$. Furthermore, each path delay is sampled as $\tau_l = \beta_l \tau_s$, with $\beta_l \in \mathbb{N}$. Equation (1.2) then becomes:

$$h(\tau) = \sum_{l=0}^{L-1} h_{l,n} \delta(\tau - \beta_l \tau_s). \tag{1.38}$$

In its vectorial form, the channel impulse response (CIR) (1.38) is the $M \times 1$ vector $\mathbf{h}_n = (h_{0,n}, h_{1,n}, ..., h_{l,n}, ..., h_{L-1,n}, 0, ..., 0)^T$. In the literature, we usually find two models of channel impulse response (IR): a dense CIR, where $h_{l,n}$ is non-null whatever l and a sparse CIR, where some $h_{l,n}$ values are null. The model used in this thesis report is a sparse CIR, as shown in the following.

The corresponding frequency response is obtained by applying a M-points DFT on (1.38). Thus, we obtain the following expression of the frequency response of the channel at the frequencies $f_m = \frac{m}{M\tau_s}$:

$$\begin{aligned} H_{m,n} &= \sum_{l=0}^{L-1} h_{l,n} e^{-2j\pi f_m \beta_l \tau_s} \\ &= \sum_{l=0}^{L-1} h_{l,n} e^{-2j\pi \frac{m}{M} \beta_l}. \end{aligned} \tag{1.39}$$

1.3.4.1 Cyclic Properties

Inspired from the work in [76], we develop the steps of the transmission in the discrete model. We show that the use of the cyclic prefix allows to simplify the equations. Indeed, as it has been proved in [10], the cyclic extension of the OFDM symbol transforms the linear convolution $h_{m,n} \star s_{m,n}$ into a cyclic convolution, which allows to get a simple per carrier discrete multiplication $H_{m,n}C_{m,n}$ after the DFT. Furthermore, we justify that the CP does not appear in the transmission expression (1.30). The convolution is performed by means of the circulant channel matrix built with the vector $\mathbf{h}_n$.

We note M_{CP} the number of samples in the cyclic prefix, so that $M_{CP} = T_{CP}/\tau s$. From $\mathbf{s}_n$, we built $\mathbf{s}'_n$ by adding the CP: $\mathbf{s}'_n = (s_{N-M_{CP},n}, ..., s_{N-1,n}, s_{0,n}, ..., s_{N-1,n})^T$. $\mathbf{s}'_n$ is then a complex vector of size $(M + M_{CP}) \times 1$. The complex channel matrix of size $(M + M_{CP}) \times (M + M_{CP})$, noted $\underline{\mathbf{h}}'_n$ is a Toeplitz circulant matrix given by

$$\underline{\mathbf{h}}'_n = \begin{pmatrix} h_{L-1,n} & \cdots & h_{1,n} & h_{0,n} & 0 & & \cdots \\ 0 & \ddots & \ddots & \ddots & \ddots & \ddots & \\ & \ddots & \ddots & \ddots & \ddots & \ddots & 0 \\ \cdots & & 0 & h_{L-1,n} & \cdots & h_{1,n} & h_{0,n} \end{pmatrix}. \tag{1.40}$$

The received signal $\mathbf{u}'_n$ is the contribution of the symbol $\mathbf{s}'_n$ and last L samples of the previous symbol $\mathbf{s}'_{n-1}$, as depicted in Fig. 1.10. The expression of $\mathbf{u}'_n$ is detailed as follows:

$$\begin{aligned} \mathbf{u}'_n = & \begin{pmatrix} h_{L-1,n} & \cdots & h_{1,n} & h_{0,n} & 0 & & \cdots \\ 0 & \ddots & \ddots & \ddots & \ddots & \ddots & \\ & \ddots & \ddots & \ddots & \ddots & \ddots & 0 \\ \cdots & & 0 & h_{L-1,n} & \cdots & h_{1,n} & h_{0,n} \end{pmatrix} \begin{pmatrix} s_{M-M_{CP},n} \\ \vdots \\ s_{M-1,n} \\ s_{0,n} \\ \vdots \\ s_{M-1,n} \end{pmatrix} \\ & + \begin{pmatrix} 0 & \cdots & 0 & h_{L-1,n-1} & \cdots & & h_{0,n-1} \\ \vdots & \ddots & & 0 & \ddots & & \vdots \\ \vdots & & & & \ddots & & h_{L-1,n-1} \\ 0 & \cdots & & \ddots & & \cdots & 0 \\ \vdots & & & & & \ddots & \vdots \\ 0 & \cdots & & \cdots & & \cdots & 0 \end{pmatrix} \begin{pmatrix} s_{M-M_{CP},n-1} \\ \vdots \\ s_{M-1,n-1} \\ s_{0,n-1} \\ \vdots \\ s_{M-1,n-1} \end{pmatrix} + \mathbf{w}'_n, \end{aligned} \tag{1.41}$$

$$\mathbf{u}'_n = \underline{\mathbf{h}}'_n \mathbf{s}'_n + \underline{\mathbf{h}}^{ISI'}_{n-1} \mathbf{s}'_{n-1} + \mathbf{w}'_n, \tag{1.42}$$

where $\mathbf{w}'_n$ is the $(M + M_{CP}) \times 1$ complex vector representing the Gaussian noise. The cyclic prefix is supposed to be well dimensioned, i.e. $M_{CP} \geq L$. The $M \times 1$ received signal vector $\mathbf{u}_n$ is obtained after the CP removal in (1.41). In a practical way, it tallies with the suppression of the M_{CP} first samples of the transmitted signal vector and of $\mathbf{w}'_n$, and the removal of the M_{CP} up rows of $\underline{\mathbf{h}}'_n$ and $\underline{\mathbf{h}}^{ISI'}_{n-1}$ (in the second line of the expression (1.41)). We remark that the matrix $\underline{\mathbf{h}}^{ISI'}_{n-1}$ then becomes null, which results in the ISI cancellation. The expression of $\mathbf{u}_n$ is detailed as follows:

$$\mathbf{u}_n = \begin{pmatrix} 0 & \cdots & h_{L-1,n} & \cdots & h_{1,n} & h_{0,n} & 0 & & \cdots \\ \vdots & \ddots & 0 & \ddots & \ddots & \ddots & \ddots & \ddots & \\ \vdots & \ddots & & \ddots & \ddots & \ddots & \ddots & \ddots & 0 \\ 0 & \cdots & \cdots & & 0 & h_{L-1,n} & \cdots & h_{1,n} & h_{0,n} \end{pmatrix} \begin{pmatrix} s_{M-M_{CP},n} \\ \vdots \\ s_{0,n} \\ \vdots \\ s_{M-1,n} \end{pmatrix} + \mathbf{w}_n. \tag{1.43}$$

Thanks to the cyclic character of the $(M + M_{CP}) \times M$ channel matrix in (1.43) and of the vector $(s_{M-M_{CP}}, ..., s_{M-1,n}, s_{0,n}, ..., s_{M-1,n})^T$, we rewrite (1.43) so as to highlight the desired vector $\mathbf{s}_n$:

$$\mathbf{u}_n = \begin{pmatrix} h_{0,n} & 0 & \cdots & \cdots & h_{L-1,n} & \cdots & h_{1,n} \\ h_{1,n} & h_{0,n} & 0 & \ddots & \ddots & \ddots & \vdots \\ \vdots & \ddots & \ddots & & \ddots & \ddots & h_{L-1,n} \\ h_{L-1,n} & \ddots & \ddots & h_{0,n} & 0 & \ddots & 0 \\ 0 & \ddots & \ddots & & \ddots & \ddots & \vdots \\ \vdots & \ddots & \ddots & & \ddots & \ddots & 0 \\ 0 & \cdots & 0 & h_{L-1,n} & \cdots & h_{1,n} & h_{0,n} \end{pmatrix} \begin{pmatrix} s_{0,n} \\ s_{1,n} \\ \vdots \\ \vdots \\ s_{M-1,n} \end{pmatrix} + \mathbf{w}_n. \tag{1.44}$$

The $M \times M$ circulant matrix of the channel is noted $\underline{\mathbf{h}}_n$. (1.44) is simply written as

$$\mathbf{u}_n = \underline{\mathbf{h}}_n \mathbf{s}_n + \mathbf{w}_n. \tag{1.45}$$

This is the discrete version of the convolution (1.30). This demonstration proves that the equation of transmission can be considered after removal of the CP, when it respects the condition $M_{CP} \geq L$. The scenario $M_{CP} < L$ will be studied afterward, in Chapter 3. We obtain the equivalent transmission equation in the frequency domain by multiplying by the Fourier matrix as

$$\begin{aligned} \mathbf{U}_n &= \underline{\mathcal{F}}\mathbf{u}_n \\ &= \underline{\mathcal{F}\mathbf{h}}_n \mathbf{s}_n + \underline{\mathcal{F}}\mathbf{w}_n. \end{aligned} \tag{1.46}$$

We note $\mathbf{W}_n = \underline{\mathcal{F}}\mathbf{w}_n$ the contribution of the noise is the frequency domain. Due to $\underline{\mathcal{F}\mathcal{F}}^H = \underline{\mathbf{I}}$, we develop (1.46):

$$\begin{aligned} \mathbf{U}_n &= \underline{\mathcal{F}\mathbf{h}}_n \underline{\mathcal{F}}^H \underline{\mathcal{F}}\mathbf{s}_n + \mathbf{W}_n \\ &= \underline{\mathcal{F}\mathbf{h}}_n \underline{\mathcal{F}}^H \mathbf{C}_n + \mathbf{W}_n \\ &= \underline{\mathbf{H}}_n \mathbf{C}_n + \mathbf{W}_n. \end{aligned} \tag{1.47}$$

We note $\underline{\mathbf{H}}_n = \underline{\mathcal{F}}\mathbf{h}_n\underline{\mathcal{F}}^H$ the channel matrix in the frequency domain. Since $\underline{\mathbf{h}}_n$ is a circulant matrix, then $\underline{\mathbf{H}}_n$ is diagonal, as shown in (1.48). Indeed, every circulant matrix is diagonalizable in a Fourier basis [11]. The proof of the property is given in Appendix A.2, or in [12].

$$\underline{\mathbf{H}}_n = \begin{pmatrix} H_{0,n} & 0 & \cdots & 0 \\ 0 & \ddots & \ddots & \vdots \\ \vdots & \ddots & \ddots & 0 \\ 0 & \cdots & 0 & H_{M-1,n} \end{pmatrix} \tag{1.48}$$

Since $\underline{\mathbf{H}}_n$ is diagonal, (1.47) can be written in an equivalent form:

$$\begin{aligned} &\mathbf{U}_n = \underline{\mathbf{H}}_n \mathbf{C}_n + \mathbf{W}_n \\ \Leftrightarrow\ &\mathbf{U}_n = \underline{\mathbf{C}}_n \mathbf{H}_n + \mathbf{W}_n, \end{aligned} \tag{1.49}$$

where $\underline{\mathbf{C}}_n$ is the $M \times M$ diagonal matrix whose diagonal elements are the ones of the vector $\mathbf{C}_n$, $\mathbf{H}_n$ is the channel frequency response vector composed of the diagonal elements of $\underline{\mathbf{H}}_n$. Consequently, whatever $m = 0, 1, .., M-1$, the samples of $\mathbf{U}_n$ are simply expressed by

$$U_{m,n} = H_{m,n}C_{m,n} + W_{m,n}. \tag{1.50}$$

This shows that if the CP is well sized, it fully cancels the ISI and each transmitted symbol $C_{m,n}$ is only corrupted by the channel frequency coefficient $H_{m,n}$ and the noise $W_{m,n}$. This expression is widely exploited for the channel estimation, which will be discussed further in this document.

1.3.5 Frequency Covariance and Correlation Matrix

The frequency covariance matrix is very important to describe the statistical properties of the channel in the discrete domain. In the rest of the report, we will see that it is particularly useful in several estimation methods. We note $\underline{\mathbf{R}}_H$ this $M \times M$ complex matrix defined as

$$\underline{\mathbf{R}}_H = E\{\mathbf{H}_n \mathbf{H}_n^H\}. \tag{1.51}$$

As the expectation is a linear operator, each sample (u, v) of the matrix (u^{th} row, v^{th} column) is given by

$$(\underline{\mathbf{R}}_H)_{u,v} = E\{\mathbf{H}_{u,n}\mathbf{H}_{v,n}^H\}. \tag{1.52}$$

From the expression of the frequency correlation function (1.19), we get the covariance matrix by sampling the variables $\Delta_f = (u-v)/\tau_s$ and $\tau = \beta\tau_s$ such as

$$(\underline{\mathbf{R}}_H)_{u,v} = \sum_{l=0}^{L-1} \int_0^{\beta_{max}} \Gamma_l(\beta) e^{-2j\pi\frac{(u-v)}{M}\beta} d\beta, \tag{1.53}$$

where β_{max} is equal to τ_{max}/τ_s. From (1.53), it is obvious that $(\underline{\mathbf{R}}_H)_{u,v} = (\underline{\mathbf{R}}_H)^*_{v,u}$, that is in matrix form: $\underline{\mathbf{R}}_H = \underline{\mathbf{R}}_H^H$. Furthermore, we notice that $(\underline{\mathbf{R}}_H)_{u+1,v+1} = (\underline{\mathbf{R}}_H)_{v,u}$, so $\underline{\mathbf{R}}_H$ is Toeplitz matrix. The frequency covariance matrix is then a Toeplitz and Hermitian matrix. The covariance matrix is called correlation matrix if this one is normalized, i.e. $(\underline{\mathbf{R}}_H)_{u,v} = 1$. The correlation matrix is noted $\underline{\mathcal{R}}_H$ and is linked to the covariance matrix by the relation:

$$\underline{\mathcal{R}}_H = \frac{1}{\sigma_h^2}\underline{\mathbf{R}}_H, \tag{1.54}$$

where σ_h^2 is the variance of the channel, defined in the discrete domain by

$$\sigma_h^2 = \sum_{l=0}^{L-1} E\{|h_{l,n}|^2\}. \tag{1.55}$$

We also define $\sigma_{l,h}^2$ as the variance of each path of the channel given by $\sigma_{l,h}^2 = E\{|h_{l,n}|^2\}$. In order to directly obtain a correlation matrix, it is possible, in a simulation process to create a normalized channel. In this case, each path variance is directly given by $\sigma_{l,h}^2/\sigma_h^2$. In this report, we will mainly use non-normalized channels in simulations.

If the channel is static, we get:

$$\underline{\mathbf{R}}_H = E\{\mathbf{H}_n \mathbf{H}_n^H\} = \mathbf{H}_n \mathbf{H}_n^H, \tag{1.56}$$

as the channel is deterministic, in such a case. This exact form can also be used in the case of quasi-static channels, but the covariance channel matrix $\underline{\mathbf{R}}_H$ must be regularly updated.

1.4 Simulation of the Transmission Channel

In this section, we describe a usual method to design the transmission channel by simulation, called "filter method". Other techniques are presented in [3], but the most common one is the filter method. Additional descriptions are given in [1], [3] or [77]. Due to the WSSUS model, each tap can be independently created. The principle is to generate each zero mean complex process $h_{l,n}$ thanks to a white Gaussian Noise (WGN) process filtered by the square root of the path Doppler spectrum as (1.12) or (1.14). The method is summarized as follows, and the diagram in Fig. 1.13 depicts it.

Filter Method

For each path $l = 0, 1, ..., L-1$, and for a process of size N:

1. create a Gaussian process $\xi_{\mathbf{l}} \sim \mathcal{N}(\mathbf{0}, \sigma^{\mathbf{2}}_{\mathbf{l,h}})$ of size N.
2. Make an DFT of $\xi_{\mathbf{l}}$.
3. Filter by the square root of the desired N-sampled Doppler spectrum $\sqrt{S_H(\nu)}$. Each path has its own variance $\sigma^2_{l,h}$, Doppler spread σ^2_D and Doppler shift f_D linked to the attenuation and the speed of the channel variations.
4. Make an IDFT to obtain the vector $\mathbf{h_{l,n}}$

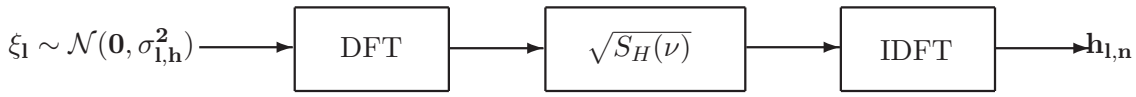

FIGURE 1.13 – Block-diagram of the filter method.

Fig. 1.14 illustrates the time-varying path gains $10\log(|h_{l,n}|^2)$ of a four paths channel. We summarize in Table 1.1 the parameters of the four-paths (non-null paths) channel model given in the DRM standard [1] called *US Consortium*. The Doppler spectrum of each path is Gaussian.

TABLE 1.1 – *US Consortium* channel parameters.

Path number l	1	2	3	4
Delay (τ_l) (in ms)	0	0,7	1,5	2,2
Variance ($\sigma^2_{l,h}$)	1	0,7	0,5	0,25
Doppler shift (f_D) (in Hz)	0,1	0,2	0,5	1,0
Doppler spread (σ^2_D) (in Hz)	0,1	0,5	1,0	2,0

We observe on Fig. 1.14 the gain variations of the four paths of the *US Consortium* channel separately. On the Y axis, we sampled the variations on 170 consecutive OFDM

symbol. Each path varies independently from the others, and we observe that the speed of variation increases in the same way than the Doppler spread value. The global transmission channel is finally the sum of these paths. An illustration of the frequency response of the *US Consortium* channel varying with time can be seen by clicking on the following link:

`http://www.youtube.com/watch?v=NIVx1Mqks9Q`

It has been simulated with the filter method previously described. The time dimension is on the X-axis, frequency on the Y-axis, and the gain $10\log(|H(t,f)|^2)$ on the Z-axis. This is the same representation as Fig. 1.3 (a), although in Fig. 1.14, the impulse response is depicted on 200 OFDM symbols, which makes it continuous from the observer point of view.

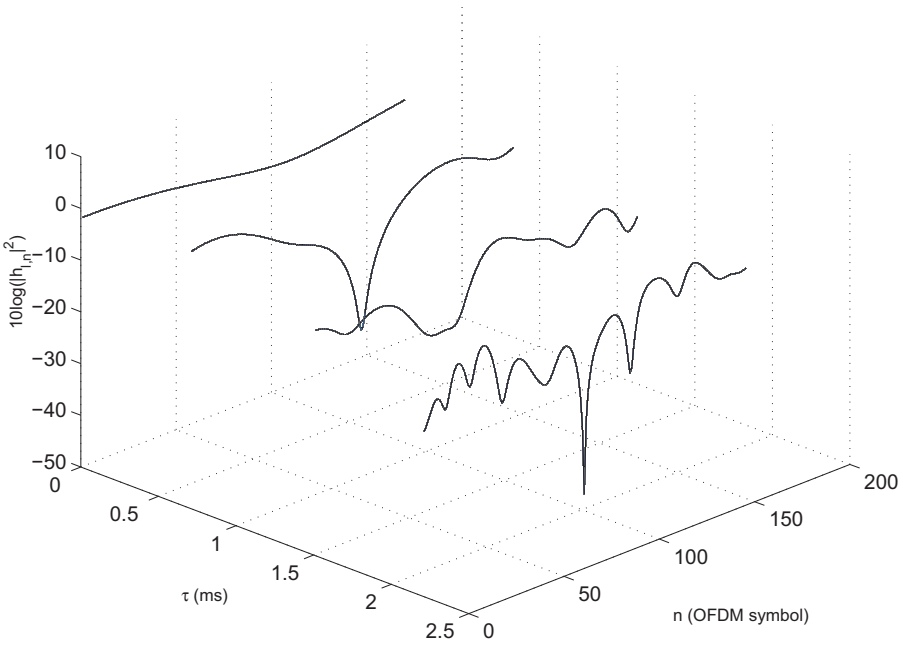

FIGURE 1.14 – Time variations of the four paths of the *US Consortium* channel.

1.5 Conclusion

This chapter presented the system model which will be used throughout the next chapters. The OFDM modulation and the cyclic property of the OFDM signal with CP have been covered. It also described the transmission channel: the statistical functions (the correlations functions, the intensity profile etc.) and the relations linking them. Furthermore, it provides the way to simulate the channel, by means of a Monte Carlo method.

Chapter 2

Channel Estimation Methods

2.1 Introduction

The multipath channel is one of the main sources of distortions in wireless communications systems. Consequently, a channel estimation is required in order to compensate the channel effects and limit the loss of useful data. In OFDM systems, a simple per carrier equalization can be performed to recover the transmitted information. The error rate at the receiver is then directly linked to the channel estimation performance.

The literature about channel estimation is very extensive, and describes a very wide range of methods, so we will not make an exhaustive list of these techniques in this chapter. In order to highlight the field of interest of this thesis, we propose to classify them according to two main parameters : the formalism (time or frequency), and the degree of knowledge of the channel at the receiver. Some other classification parameters such as the complexity or the adaptativity of the methods could be used, but this classification offers a simple overview of this vast domain of study. Furthermore, we focus on the methods used in ODFM context, although some of the techniques are useable for single and multicarrier systems.

2.1.1 Time or Frequency Domain Estimation

As shown in Chapter 1, the structure of the OFDM modulation is adapted to the frequency domain estimation. Indeed, if the channel is supposed to be constant on each subcarrier, a simple one-tap equalization can be performed to cancel the fading due to multipath channels (see Fig. 1.11). Some time domain estimation techniques are proposed in the literature. Generally, these methods have exactly the same formulations in time or frequency domains. Thus, [78–80] refer to the usual minimum mean square error (MMSE), maximum likelihood (ML) and least square estimators. The description of these methods in the frequency domain are given in Section 2.4.

Several other alternative solutions have been described. In [81], the authors proposed to combine a frequency and a time domain MMSE estimation, and show that the performance is improved compared to the same method performed in a single domain. In [82], an hybrid domain LS and MMSE estimation is presented. From (1.50), the hybrid domain formulation of the m^{th} received carrier is given by

$$\begin{aligned} U_{m,n} &= H_{m,n}C_{m,n} + W_{m,n} \\ &= \sum_{l=0}^{L-1} h_{l,n}(e^{-2j\pi\frac{ml}{M}}C_{m,n}) + W_{m,n}. \end{aligned} \tag{2.1}$$

We observe in (2.1) the contribution of elements in time domain $h_{l,n}$ and in frequency domain $C_{m,n}$. This scheme is called hybrid domain. In the rest of the thesis report, we will focus on frequency domain estimation methods.

2.1.2 Blind Estimation

The blind estimation methods implies that the receiver has no information about the channel. The advantage is the high spectral efficiency of these transmission schemes, since all the bandwidth is used to carry data only. However, blind estimation suffers from a computational high complexity or a low efficiency. The principle of a large number of methods is based on second-order moment of the received signal, as depicted in [83]. Thus, if we note $\underline{\tilde{\mathbf{u}}}$ the $M \times N$ matrix composed of N received OFDM symbols $\tilde{\mathbf{u}}_n = \underline{\mathbf{h}}_n \mathbf{s}_n$ without noise, we get the following eigendecomposition

$$\underline{\tilde{\mathbf{u}}}\underline{\tilde{\mathbf{u}}}^H = (\underline{\bar{\mathbf{q}}}\ \underline{\tilde{\mathbf{q}}}) \begin{pmatrix} \underline{\mathbf{A}}_{P\times P} & \underline{\mathbf{0}}_{P\times L} \\ \underline{\mathbf{0}}_{L\times P} & \underline{\mathbf{0}}_{L\times L} \end{pmatrix} \begin{pmatrix} \underline{\bar{\mathbf{q}}}^H \\ \underline{\tilde{\mathbf{q}}}^H \end{pmatrix}, \tag{2.2}$$

where $P = M - L$ and $\underline{\tilde{\mathbf{q}}}$ is the $M \times L$ matrix whose columns span the null space of $\underline{\tilde{\mathbf{u}}}$. We note $\tilde{\mathbf{q}}_l$ the l^{th} column of $\underline{\tilde{\mathbf{q}}}$. From (2.2), it is proved in [83] that, with the orthogonal spaces property, the equation

$$\mathfrak{h}^H(\underline{\mathfrak{q}}_0, ..., \underline{\mathfrak{q}}_{L-1}) = \underline{\mathbf{0}} \tag{2.3}$$

has a unique nontrivial solution $\mathfrak{h}$, where $\mathfrak{h} = (h_0, h_1, ..., h_l, ..., h_{L-1})^T$. The matrice $\underline{\mathfrak{q}}_l$, with $l = 0, 1, ..., L-1$ is given by

$$\underline{\mathfrak{q}}_l = \begin{pmatrix} \tilde{q}_{l,0} & \tilde{q}_{l,1} & \cdots & \tilde{q}_{l,P-1} \\ \tilde{q}_{l,1} & \tilde{q}_{l,2} & \cdots & \tilde{q}_{l,P} \\ \vdots & \vdots & \vdots & \vdots \\ \tilde{q}_{l,L-1} & \tilde{q}_{l,L} & \cdots & \tilde{q}_{l,M-1} \end{pmatrix}. \tag{2.4}$$

As noticed in [83], $\underline{\tilde{\mathbf{u}}}$ is replaced by $\mathbf{u}_n$ in practice. The channel estimation $\hat{\mathfrak{h}}$ is then obtained in the least square sense by minimizing the cost function

$$J = |\mathfrak{h}(\underline{\mathfrak{q}}_0, ..., \underline{\mathfrak{q}}_{L-1})|^2. \tag{2.5}$$

In [84, 85], the same property of orthogonal spaces is used according to some characteristics of OFDM modulation, such as the virtual carriers or zero padding guard interval. The blind channel estimation is then performed in the frequency domain.

2.1.3 Transmission Methods with a Known Channel State Information

Contrary to the blind estimation, some techniques consider the channel as perfectly known at the receiver and/or the transmitter sides. In that case, we can not strictly talk about channel estimation, but we present the simple principle of methods using the channel information. As described in [86] and in Fig. 2.1, the diagram of the transmission chain with known channel remains the same as before, except that some filters can be added at the receiver and/or the transmitter sides.

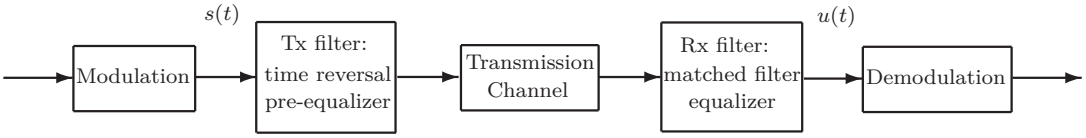

FIGURE 2.1 – Transmission scheme exploiting the knowledge of the channel state information.

Whatever the considered domain (time or frequency), the filters, inserted at the transmitter and/or the receiver side, allow cancelling the channel distortion. These filters then act as perfect equalizers. For instance, we can cite the matched filter [87] at the receiver, or the time reversal method [88], when the channel information is used at the transmitter side. The two methods being equivalent, we express the received signal if time reversal is used. In that case, the T_x filter is $h^*(-t)$ and then

$$\begin{aligned} u(t) &= (s(t) \star h^*(-t) \star h(t)) + w(t) \\ &= (s(t) \star R_h(t)) + w(t), \end{aligned} \tag{2.6}$$

where $R_h(t)$ is the channel autocorrelation function. As mentioned in [88], in the ideal case, $R_h(t) = \delta(t)$, and then the received signal is given by $u(t) = s(t)+w(t)$. Obviously, in practice, $h(t)$ is not perfectly known, and it turns to a usual problem of channel estimation.

2.1.4 Semi-blind Estimation

In the majority of cases, the transmission channel is unknown at the receiver, but extrinsic information is transmitted to perform the channel estimation. This kind of signal called pilot is multiplexed with the useful data, and its physical characteristics are known by both transmitter and receiver, as detailed in the next section.

In the rest of the chapter, we will focus on semi-blind estimation methods, also called pilot-aided estimation or pilot symbol aided modulation (PSAM). Fig. 2.2 offers a simple overview of where is the field of study among all the channel estimation methods. First, we describe the different arrangement of the pilots in an OFDM frame in Section 2.2. Second, we express the two usual criterions (LS and MMSE) used for the channel estimation in section 2.2, and then we propose a state of the art of the main pilot-aided estimation methods in Section 2.4.

2.2 The Pilots in the OFDM Frame

The pilots, noted $C = \alpha e^{j\phi}$, are subcarriers whose gain α, phase ϕ and arrangement in the time-frequency lattice are known by both the transmitter and the receiver. They do

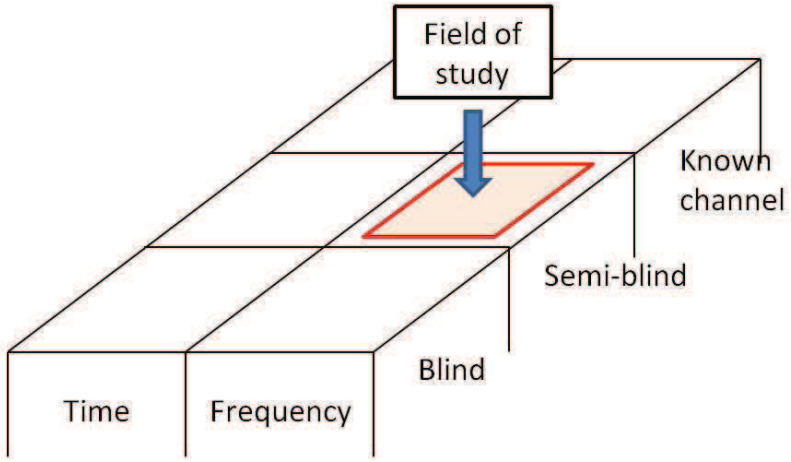

FIGURE 2.2 – Classification of the estimation methods.

not carry any useful data, but are dedicated in the OFDM frame to the time and frequency synchronization, as well as the SNR and the channel estimation. In order to reduce their sensivity to the noise, the gain is usually higher than the other subcarriers carrying useful data (usually normalized to one). For instance, the DRM/DRM+ [1] specifies a gain $\alpha = \sqrt{2}$, and $\alpha = 2$ for the boosted pilots which are on the edge of the spectrum. Fig. 2.3 illustrates four different pilots arrangements in the OFDM frame.

The choice of the pilot pattern depends on the selectivity of the channel, which is characterized by B_C and T_C. The block-type arrangement (a), also called time preamble, is adapted to quasi-static channels with high frequency selectivity. On the contrary, the comb-type arrangement (b) is used when the channel is time selective and with a low frequency selectivity. In the case of time and frequency selective channels, the rectangular (c) or staggered rows (d) patterns can be used. Consequently, an interpolation will be needed to estimate the channel frequency response over the time-frequency plan. The literature describes some other arrangements such as the hexagonal pattern or even an irregular distribution [14].

We define δ_f and δ_n the gaps between two consecutive pilot subcarriers along the frequency and the time axis, respectively. As reminded in [13], in order to perform an efficient channel estimation, these gap must respect the sampling theorem:

$$\delta_f \leq \frac{B_C}{2} \tag{2.7}$$

$$\delta_n \leq \frac{T_C}{2}. \tag{2.8}$$

The choice of the pilots arrangement not only depends on the considered channel, but is also a trade-off between the specified BER at the receiver and the expected data rate. Indeed, the higher the number of pilots, the lower the BER, but at the same time the lower the data rate. If the number of pilots is reduced, the BER may increase, and targeting a required BER value may involve that the channel estimation method becomes more complex.

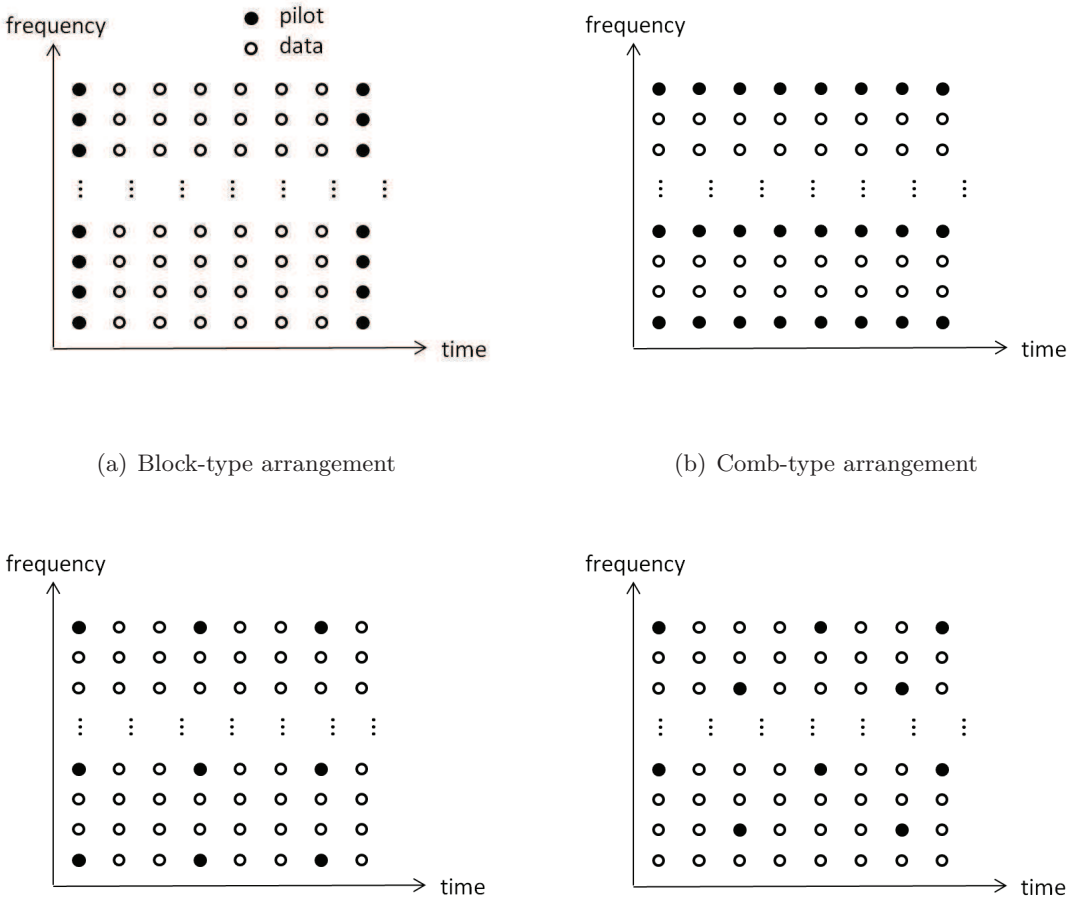

(a) Block-type arrangement

(b) Comb-type arrangement

(c) Rectangular pattern

(d) Staggered rows pattern

FIGURE 2.3 – Four possible pilot arrangements in the OFDM frame.

2.3 LS and MMSE Criteria

In this section, we consider a preamble scheme (see Fig. 2.3 (a)) to make the developments. However, we will see that they are also valid if the pilot tones are sparsely distributed (such as the rectangular or the staggered rows pattern) in the OFDM frame.

2.3.1 Principle of LS Estimation

2.3.1.1 Expression of LS Estimation

The least square criterion aims at minimizing the cost function J defined as the square norm of an error vector. This vector is the difference between the vector of the received signal $\mathbf{U}$ and the product of the transmitted signal vector $\mathbf{C}$ by a diagonal matrix $\underline{\mathbf{D}}$ whose coefficients have to be optimized. We then get the estimation $\hat{\mathbf{H}}^{LS} = \underline{\mathbf{D}}_{opt}$. The cost function is first expressed as

$$J_{LS} = |\mathbf{U} - \underline{\mathbf{D}}\mathbf{C}|^2, \tag{2.9}$$

By developing (2.9), we get

$$J_{LS} = \sum_{m=0}^{M-1} |U_m - D_m C_m|^2. \tag{2.10}$$

Minimizing J_{LS} amounts to solve $\nabla_{\underline{\mathbf{D}}} J_{LS} = 0$ with

$$\nabla_{\underline{\mathbf{D}}} J_{LS} = \begin{pmatrix} \frac{\partial}{\partial D_0}(|U_0 - D_{0,opt}C_0|^2) \\ \vdots \\ \frac{\partial}{\partial D_m}(|U_m - D_{m,opt}C_m|^2) \\ \vdots \\ \frac{\partial}{\partial D_{M-1}}(|U_{M-1} - D_{M-1,opt}C_{M-1}|^2) \end{pmatrix}. \tag{2.11}$$

For all $m = 0, 1, .., M-1$, we simply get

$$-2C_m(U_m - D_{m,opt}C_m) = 0, \tag{2.12}$$

and from $\hat{\underline{\mathbf{H}}}^{LS} = \underline{\mathbf{D}}_{opt}$ we deduce

$$\hat{H}_m^{LS} = \frac{U_m}{C_m} = H_m + \frac{W_m}{C_m}. \tag{2.13}$$

We notice that the LS estimation can be performed on each carrier individually. It can then be applied in the case of sparse pilot carriers in the OFDM frame. In the case of a pilot preamble, from (1.49) we give the vectorial form of the expression (2.13):

$$\hat{\mathbf{H}}^{LS} = \mathbf{U}\underline{\mathbf{C}}^{-1} = \mathbf{H} + \mathbf{W}\underline{\mathbf{C}}^{-1}. \tag{2.14}$$

From (2.14), it can be seen that the LS estimation is very sensitive to the noise level. In order to reduce the sensitivity to the noise, [15] proposes the scaled LS (SLS) estimator, in which $\hat{\mathbf{H}}^{LS}$ is multiplied by a coefficient γ, which is chosen such as the mean square error $E\{||\mathbf{H} - \gamma\hat{\mathbf{H}}^{LS}||_F^2\}$ is minimized. In the same way, [16] presents the generalized form of SLS, called shifted SLS (SSLS), in which $\hat{\mathbf{H}}^{LS}$ is replaced by $\gamma\hat{\mathbf{H}}^{LS} + \mathbf{x}$, where γ and $\mathbf{x}$ are to be optimized.

2.3.1.2 Characteristics of the LS Estimation

From (2.14), we derive the bias and the minimum mean square error of LS estimation. Since the noise is zero-mean, the bias B is obviously equal to zero:

$$B(\hat{\mathbf{H}}^{LS}) = E\{\hat{\mathbf{H}}^{LS} - \mathbf{H}\} = E\{\mathbf{W}\underline{\mathbf{C}}^{-1}\} = 0. \tag{2.15}$$

For the minimum mean square error (noted $MMSE_{LS}$), we use the same development as in [15, 17, 18], i.e. we minimize the error function $J_{\hat{\mathbf{H}}^{LS}}$:

$$J_{\hat{\mathbf{H}}^{LS}} = \frac{1}{M}E\{||\hat{\mathbf{H}}^{LS} - \mathbf{H}||_F^2\} = \frac{1}{M}E\{||\mathbf{W}\underline{\mathbf{C}}^{-1}||_F^2\}, \tag{2.16}$$

conditionally to $C_m C_m^* = \mathcal{P}$, $\mathcal{P}$ being the power of the pilots. We denote by $||.||_F$ the Frobenius norm [1]. Therefore, the $MMSE_{LS}$ is simply given by

$$\begin{aligned} MMSE_{LS} &= \frac{1}{M} E\{tr(\mathbf{W}\underline{\mathbf{C}}^{-1}(\mathbf{W}\underline{\mathbf{C}}^{-1})^H)\} \\ &= \frac{1}{M}\sum_{m=0}^{M-1}\frac{E\{W_m W_m^*\}}{C_m C_m^*} \\ MMSE_{LS} &= \frac{\sigma^2}{\mathcal{P}}. \end{aligned} \tag{2.17}$$

We recognize the result given in [17]. The minimum mean square error of LS estimation is then equivalent to the inverse of the SNR. We will show in Chapter 5 that it is also possible to derive an analytical mean square error of the LS estimation in the case of sparsely distributed pilots in the frame. In this scenario, the interpolation method has to be taken into account.

2.3.2 Principle of Linear-MMSE Estimation

2.3.2.1 Expression of LMMSE Estimation

The MMSE aims at minimizing cost function defined by the mean square error of the error vector $\mathbf{H} - \underline{\mathbf{D}}\mathbf{U}$, as shown in [19]:

$$J_{MMSE} = E\{||\mathbf{H} - \underline{\mathbf{D}}\mathbf{U}||_F^2\}, \tag{2.18}$$

where $\underline{\mathbf{D}}$ is the matrix whose coefficients have to be optimized. The channel estimation is then given by $\hat{\mathbf{H}}^{LMMSE} = \underline{\mathbf{D}}_{opt}\mathbf{U}$. As mentioned in [7,32], the term *linear* in LMMSE is valid when the channel is supposed to be flat over each tone, which is the case in our model. We develop (2.18) as

$$\begin{aligned} J_{MMSE} &= E\{tr\left((\mathbf{H} - \underline{\mathbf{D}}\mathbf{U})(\mathbf{H} - \underline{\mathbf{D}}\mathbf{U})^H\right)\} \\ &= tr\left(E\{\mathbf{H}\mathbf{H}^H - \mathbf{H}\mathbf{U}^H\underline{\mathbf{D}}^H - \underline{\mathbf{D}}\mathbf{U}\mathbf{H}^H + \underline{\mathbf{D}}\mathbf{U}\mathbf{U}^H\underline{\mathbf{D}}^H\}\right). \end{aligned} \tag{2.19}$$

We remind that $\mathbf{U} = \mathbf{H}\underline{\mathbf{C}}+\mathbf{W}$, and we consider that $\mathbf{H}$ and $\mathbf{W}$ are two uncorrelated zero-mean vectors, so we get:

$$\begin{aligned} J_{MMSE} &= tr\left(\underline{\mathbf{R}}_H - \underline{\mathbf{R}}_H\underline{\mathbf{C}}^H\underline{\mathbf{D}}^H - \underline{\mathbf{D}}\underline{\mathbf{C}}\underline{\mathbf{R}}_H + \underline{\mathbf{D}}(\underline{\mathbf{C}}\underline{\mathbf{R}}_H\underline{\mathbf{C}}^H + \sigma^2\underline{\mathbf{I}})\underline{\mathbf{D}}^H\right) \\ &= tr(\underline{\mathbf{R}}_H) - tr(\underline{\mathbf{R}}_H\underline{\mathbf{C}}^H\underline{\mathbf{D}}^H) - tr(\underline{\mathbf{D}}\underline{\mathbf{C}}\underline{\mathbf{R}}_H) \\ &\quad + tr(\underline{\mathbf{D}}(\underline{\mathbf{C}}\underline{\mathbf{R}}_H\underline{\mathbf{C}}^H + \sigma^2\underline{\mathbf{I}})\underline{\mathbf{D}}^H). \end{aligned} \tag{2.20}$$

We derivate the expression (2.20) to find $\underline{\mathbf{D}}_{opt}$ satisfying $\partial J_{MMSE}/\partial\underline{\mathbf{D}} = 0$. To this end, we use the matrix derivative form [89]:

$$\frac{\partial J_{MMSE}}{\partial\underline{\mathbf{D}}} = 0 - \underline{\mathbf{R}}_H\mathbf{C}^H - (\underline{\mathbf{C}}\underline{\mathbf{R}}_H)^H + 2\underline{\mathbf{D}}(\underline{\mathbf{C}}\underline{\mathbf{R}}_H\underline{\mathbf{C}}^H + \sigma^2\underline{\mathbf{I}}) = 0. \tag{2.21}$$

1. The Frobenius norm of a matrix $\underline{\mathbf{A}}$ is given by $||\underline{\mathbf{A}}||_F = \sqrt{tr(\underline{\mathbf{A}}\underline{\mathbf{A}}^H)}$.

Since the channel covariance matrix $\underline{\mathbf{R}}_H$ is Hermitian, it is equal to its conjugate transform $\underline{\mathbf{R}}_H^H = \underline{\mathbf{R}}_H$ [11]. We then express the optimal matrix $\underline{\mathbf{D}}_{opt}$ as

$$\begin{aligned}\underline{\mathbf{D}}_{opt} &= \underline{\mathbf{R}}_H \mathbf{C}^H (\underline{\mathbf{C}}\underline{\mathbf{R}}_H \underline{\mathbf{C}}^H + \sigma^2 \underline{\mathbf{I}})^{-1} \\ &= \underline{\mathbf{R}}_H (\underline{\mathbf{R}}_H + (\underline{\mathbf{C}}\underline{\mathbf{C}}^H)^{-1}\sigma^2 \underline{\mathbf{I}})^{-1} \underline{\mathbf{C}}^{-1}. \end{aligned} \tag{2.22}$$

We finally deduce the expression of the LMMSE channel estimation:

$$\begin{aligned}\hat{\mathbf{H}}^{LMMSE} &= \underline{\mathbf{D}}_{opt}\mathbf{U} \\ &= \underline{\mathbf{R}}_H (\underline{\mathbf{R}}_H + (\underline{\mathbf{C}}\underline{\mathbf{C}}^H)^{-1}\sigma^2 \underline{\mathbf{I}})^{-1} \underline{\mathbf{C}}^{-1}\mathbf{U} \\ \hat{\mathbf{H}}^{LMMSE} &= \underline{\mathbf{R}}_H (\underline{\mathbf{R}}_H + (\underline{\mathbf{C}}\underline{\mathbf{C}}^H)^{-1}\sigma^2 \underline{\mathbf{I}})^{-1} \hat{\mathbf{H}}^{LS}. \end{aligned} \tag{2.23}$$

In order to lighten the writing, the matrix $\underline{\mathbf{R}}_H (\underline{\mathbf{R}}_H + (\underline{\mathbf{C}}\underline{\mathbf{C}}^H)^{-1}\sigma^2 \underline{\mathbf{I}})^{-1}$ will be noted $\underline{\mathbf{B}}$. Eq. (2.23) is the usual expression of the LMMSE estimation. We notice that it requires more operations to be performed than LS, due to the matrix inversion and the multiplication. However, it is less sensitive to the noise than LS, as shown in Section 2.3.2.2. This is due to the LMMSE estimator is based on the mean square error, and the considered Gaussian noise has a mean equal to zero. Furthermore, LMMSE can play the role of interpolator, as shown in Section 2.4.2, so it can be used in the case of pilots which are sparsely distributed in the frame.

2.3.2.2 Characteristics of the LMMSE Estimation

From (2.23), we derive the bias and the minimum mean square error of LMMSE estimation. Since $\mathbf{H}$ and $\mathbf{W}$ are zero-mean processes, we simply express the bias B as

$$\begin{aligned} B(\hat{\mathbf{H}}^{LMMSE}) &= E\{\hat{\mathbf{H}}^{LMMSE} - \mathbf{H}\} \\ &= E\{(\underline{\mathbf{R}}_H (\underline{\mathbf{R}}_H + (\underline{\mathbf{C}}\underline{\mathbf{C}}^H)^{-1}\sigma^2 \underline{\mathbf{I}})^{-1} - \underline{\mathbf{I}})\mathbf{H} \\ &\quad + \underline{\mathbf{R}}_H (\underline{\mathbf{R}}_H + (\underline{\mathbf{C}}\underline{\mathbf{C}}^H)^{-1}\sigma^2 \underline{\mathbf{I}})^{-1} \mathbf{W} \underline{\mathbf{C}}^{-1}\} \\ &= 0. \end{aligned} \tag{2.24}$$

We observe that LMMSE is also an unbiased estimator. We now express the MMSE of the LMMSE estimation, noted $MMSE_{LMMSE}$, based on the developments proposed in [15, 19]. To this end, we define the error function $J_{\hat{\mathbf{H}}^{LMMSE}}$ that must be minimized:

$$J_{\hat{\mathbf{H}}^{LMMSE}} = \frac{1}{M} E\{||\mathbf{H} - \hat{\mathbf{H}}^{LMMSE}||_F^2\}. \tag{2.25}$$

The development of the minimization given in [15, 19] requires the chain differentiation rule for traces of matrices [89,90] in order to solve $\partial(J_{\hat{\mathbf{H}}^{LMMSE}})/\partial C_m^* = 0$. However, this is valid for MIMO systems, where the channel covariance matrix is supposed to be invertible. Indeed, [15] expresses $MMSE_{LMMSE}$ by

$$MMSE_{LMMSE} = \frac{M\sigma^2}{M\mathcal{P}/\sigma^2 + tr(\underline{\mathbf{R}}_H^{-1})}. \tag{2.26}$$

In Chapter 1, we noticed that in the SISO case, the $M \times M$ matrix $\underline{\mathbf{R}}_H$ has rank L, with $L < M$, so $\underline{\mathbf{R}}_H$ is not invertible. The formula (2.26) is then not valid, and must be reconsidered for the SISO systems.

2.3.2.3 Expression of the Minimum Mean Square Error of LMMSE in the SISO Case

a. Scalar Expression of $J_{\hat{\mathbf{H}}^{LMMSE}}$

In this part, we propose a new development based on the one in [15] to make it suitable with non invertible channel covariance matrices. To this end, we first express a scalar expression of the mean square error, and we derive the $MMSE_{LMMSE}$ by considering a minimization under constraint problem. This new approach has been proposed in [20].

From (2.23), we derive the mean square error function J_{LMMSE}:

$$\begin{aligned} J_{\hat{\mathbf{H}}^{LMMSE}} &= \frac{1}{M} E\{||\mathbf{H} - \hat{\mathbf{H}}^{LMMSE}||_F^2\} \\ &= \frac{1}{M} E\{tr((\mathbf{H} - \hat{\mathbf{H}}^{LMMSE})(\mathbf{H} - \hat{\mathbf{H}}^{LMMSE})^H)\} \\ &= \frac{1}{M} tr(E\{(\mathbf{H} - \hat{\mathbf{H}}^{LMMSE})\mathbf{H}^H\} - E\{(\mathbf{H} - \hat{\mathbf{H}}^{LMMSE})(\hat{\mathbf{H}}^{LMMSE})^H\}). \end{aligned} \tag{2.27}$$

Using the orthogonality principle [91], the second term in the right part of (2.27) is equal to zero. Since $\mathbf{H}$ and $\mathbf{W}$ are uncorrelated zero mean processes, we have $E\{\mathbf{H}\mathbf{W}^H = 0\}$. We then develop (2.27) to get

$$\begin{aligned} J_{\hat{\mathbf{H}}^{LMMSE}} &= \frac{1}{M} tr(E\{\mathbf{H}\mathbf{H}^H\} - E\{\underline{\mathbf{R}}_H(\underline{\mathbf{R}}_H + \sigma^2(\underline{\mathbf{C}}\underline{\mathbf{C}}^H)^{-1})^{-1}\hat{\mathbf{H}}^{LS}\mathbf{H}^H\}) \\ &= \frac{1}{M} tr(\underline{\mathbf{R}}_H - \underline{\mathbf{R}}_H(\underline{\mathbf{R}}_H + \sigma^2(\underline{\mathbf{C}}\underline{\mathbf{C}}^H)^{-1})^{-1}\underline{\mathbf{R}}_H). \end{aligned} \tag{2.28}$$

As one can remark that $\underline{\mathbf{R}}_H = \underline{\mathbf{R}}_H + \sigma^2(\underline{\mathbf{C}}\underline{\mathbf{C}}^H)^{-1} - \sigma^2(\underline{\mathbf{C}}\underline{\mathbf{C}}^H)^{-1}$, (2.28) simplifies to

$$\begin{aligned} J_{\hat{\mathbf{H}}^{LMMSE}} &= \frac{1}{M} tr(\underline{\mathbf{R}}_H(\underline{\mathbf{R}}_H + \sigma^2(\underline{\mathbf{C}}\underline{\mathbf{C}}^H)^{-1})^{-1}\sigma^2(\underline{\mathbf{C}}\underline{\mathbf{C}}^H)^{-1}) \\ &= \frac{1}{M} tr(\underline{\mathbf{R}}_H(\frac{1}{\sigma^2}\underline{\mathbf{R}}_H(\underline{\mathbf{C}}\underline{\mathbf{C}}^H) + \underline{\mathbf{I}})^{-1}), \end{aligned} \tag{2.29}$$

where $\underline{\mathbf{I}}$ is the identity matrix. Since $\underline{\mathbf{R}}_H$ is an Hermitian and positive-semidefinite matrix, and as $(\underline{\mathbf{C}}\underline{\mathbf{C}}^H)$ is a multiple of the identity matrix, $\frac{1}{\sigma^2}\underline{\mathbf{R}}_H(\underline{\mathbf{C}}\underline{\mathbf{C}}^H) + \underline{\mathbf{I}}$ is also an Hermitian and positive-semidefinite matrix having the same eigendecomposition basis as $\underline{\mathbf{R}}_H$. We can then write

$$\begin{aligned} \underline{\mathbf{R}}_H &= \underline{\mathbf{Q}}\underline{\mathbf{D}}_H\underline{\mathbf{Q}}^H \\ \frac{1}{\sigma^2}\underline{\mathbf{R}}_H(\underline{\mathbf{C}}\underline{\mathbf{C}}^H) + \underline{\mathbf{I}} &= \underline{\mathbf{Q}}\underline{\mathbf{D}}\underline{\mathbf{Q}}^H, \end{aligned} \tag{2.30}$$

where $\underline{\mathbf{Q}}$ is an unitary matrix. The m^{th} components of $\underline{\mathbf{D}}_H$ and $\underline{\mathbf{D}}$ are λ_m and $1/(\frac{C_m C_m^* \lambda_m}{\sigma^2}+1)$ respectively. Inserting (2.30) into (2.29) and remembering that $\lambda_m = 0$ for $m = L, L+1, ..., M-1$, we finally get the scalar expression of the error function

$$J_{\hat{\mathbf{H}}^{LMMSE}} = \frac{1}{M}\sum_{m=0}^{L-1}\frac{\lambda_m \sigma^2}{\lambda_m C_m C_m^* + \sigma^2}. \tag{2.31}$$

b. Minimizing $J_{\hat{\mathbf{H}}^{LMMSE}}$

From (2.31), we may reason on the L variables C_m. Thus, we notice that if $L = M$ (i.e. $\underline{\mathbf{R}}_H$ has full rank), the problem remain the same as in [15]. We minimize the error function (2.31) subject to the power constraint $\frac{1}{L}\sum_{m=0}^{L-1} C_m C_m^* = \mathcal{P}$. To this end, we use the Lagrange multipliers method so that the problem can be rewritten as

$$\mathcal{L} = \frac{1}{M}\sum_{m=0}^{L-1}\frac{\lambda_m \sigma^2}{\lambda_m C_m C_m^* + \sigma^2} + \mu(\frac{1}{L}\sum_{m=0}^{L-1} C_m C_m^* - \mathcal{P}), \tag{2.32}$$

where μ is the Langrange multiplier. Whatever $m = 0, 1, ...L-1$, the partial derivatives of the gradient $\nabla\mathcal{L}$ must satisfy

$$\frac{\partial \mathcal{L}}{\partial C_m^*} = -\frac{\lambda_m^2 \sigma^2 C_m}{(\lambda_m C_m C_m^* + \sigma^2)^2} + \frac{\mu C_m}{L} = 0. \tag{2.33}$$

We deduce that $C_m C_m^* = \sqrt{\frac{\sigma^2 L}{\mu M}} - \frac{\sigma^2}{\lambda_m}$, and using the constraint $\frac{1}{L}\sum_{m=0}^{L-1} C_m C_m^* = \mathcal{P}$, we obtain

$$\sqrt{\frac{\sigma^2 L}{\mu M}} = \mathcal{P} + \frac{1}{L}\sum_{m=0}^{L-1}\frac{\sigma^2}{\lambda_m}, \tag{2.34}$$

and then

$$C_m C_m^* = \mathcal{P} + \frac{1}{L}\sum_{m'=0}^{L-1}\frac{\sigma^2}{\lambda_{m'}} - \frac{\sigma^2}{\lambda_m}. \tag{2.35}$$

Inserting (2.35) into (2.31), we finally get the expression of the MMSE of the LMMSE channel estimation:

$$MMSE_{LMMSE} = \frac{1}{M}.\frac{L^2\sigma^2}{L\mathcal{P} + \sum_{m=0}^{L-1}\frac{\sigma^2}{\lambda_m}}. \tag{2.36}$$

We can see that if $L = M$ (i.e. $\underline{\mathbf{R}}_H$ has full rank), then (2.36) is identical to (2.26). It then validates the proposed expression of $MMSE_{LMMSE}$. Furthermore, we recognize the characteristics given in [15, 18]: $MMSE_{LMMSE} < MMSE_{LS}$, in particular for high σ^2 values, and $MMSE_{LMMSE} = \frac{L}{M} MMSE_{LS}$ for low σ^2 values. Fig. 2.4 displays the shape of $MMSE_{LMMSE}$ got by simulations and by using the analytical expression (2.36). In addition, it compares $MMSE_{LMMSE}$ to $MMSE_{LS}$ (2.17). For the simulations, we used a FFT size $M = 128$, and a channel of length $L = 32$ with a decreasing intensity profile. Furthermore, the pilot power is normalized, that is $\mathcal{P} = 1$.

We observe that the theoretical curve $MMSE_{LMMSE}$ and the one plotted by simulation matches. It validates the proposed expression (2.36). Moreover, we verify the inequality $MMSE_{LMMSE} < MMSE_{LS}$ whatever the value of the ratio $\mathcal{P}/\sigma^2$.

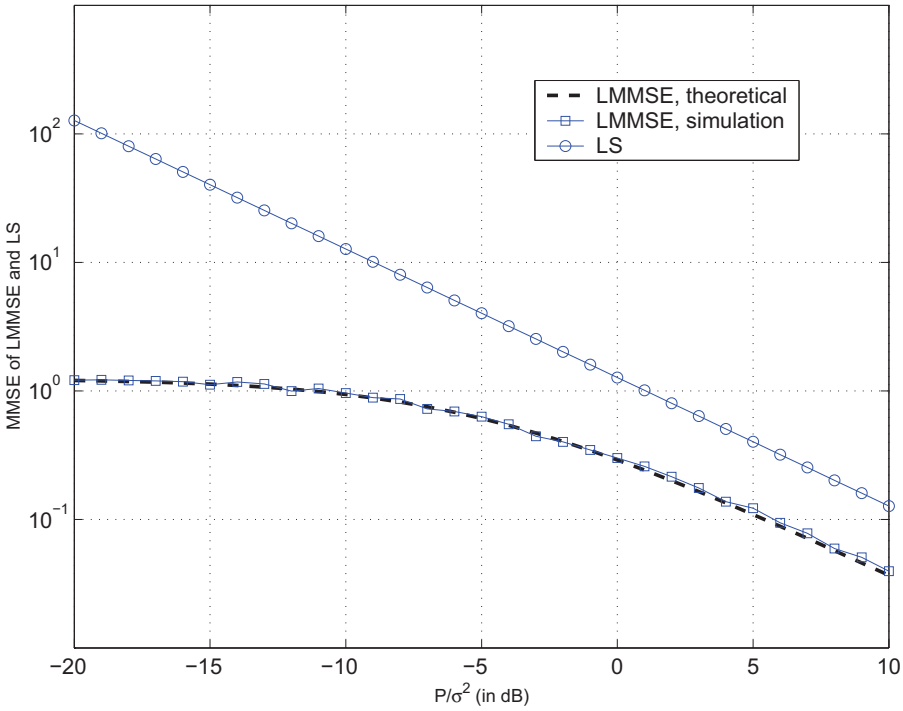

FIGURE 2.4 – MMSE of LMMSE and LS estimations versus $\mathcal{P}/\sigma^2$.

2.4 Pilot-Aided Estimation Methods

In this section are presented some important and usual channel estimation methods, which are precisely described in the literature, in particular in [22–27]. The basic principle of PSAM is to estimate the channel on the pilot tones, and to extend this knowledge by means of some interpolation techniques to the complete time-frequency carriers set, in order to perform equalization afterward. We classify them in three groups according to three main criteria:

- The methods require some physical and/or statistical knowledge about the channel.
- The methods are only based on interpolation techniques.
- The methods use a feedback from the transmission chain in order to get information on the transmitted signal.

2.4.1 Methods with Knowledge of Some Properties of the Channel

2.4.1.1 Wiener Filter

The Wiener filter is an MMSE criterion-based channel estimation method described in [28]. As mentioned in [7, 13, 28], it is an optimal technique according to the MSE criterion. Let us consider $P \times N_p$ sparse pilot tones in an OFDM frame, as depicted on Fig. 2.5. The Wiener filter performing the estimation on the data subcarriers is

$$\hat{H}_{m,n} = \sum_{p=0}^{P-1} \sum_{n_p=0}^{N_p-1} w(m,n,p,n_p) \hat{H}^{LS}_{p,n_p}, \tag{2.37}$$

where the optimal filter minimizes the mean square error as

$$w(m,n) = \min_{\hat{H}_{m,n}} \left(E\{|H_{m,n} - \hat{H}_{m,n}|^2\} \right). \tag{2.38}$$

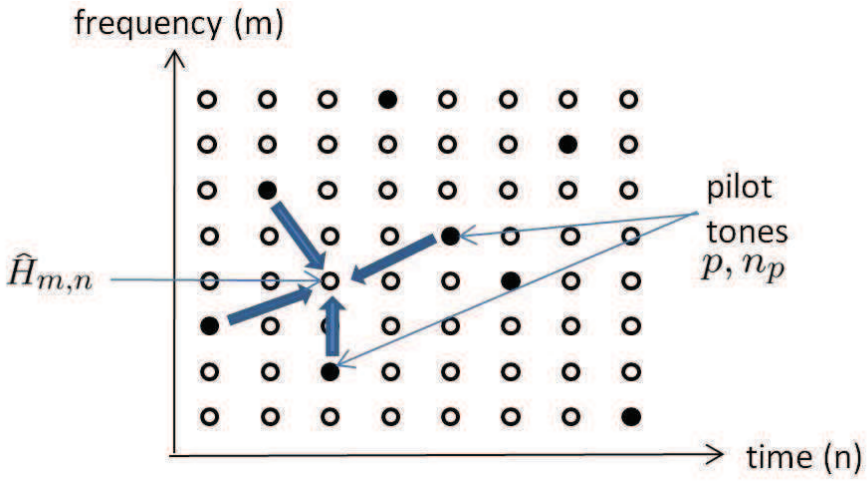

FIGURE 2.5 – Illustration of the Wiener filtering.

Since it uses a filter function of the time and the frequency directions, it is called 2-D Wiener filter. This method is very complex [13, 92], and it is usual to find methods in which the 2-D filter is split into two filters, one along the frequency axis, and the other one along the time axis. The frequency filter is the one given in (2.23) and the frequency channel covariance matrix is expressed in (1.53). However, a pilot preamble is considered in (2.23). Here, the pilot subcarriers are sparse in the OFDM symbol. In that case, the LMMSE estimator plays the role of interpolator [7]. Let us assume P pilots per OFDM symbol, thus we note $\underline{\mathcal{R}}_H$ the $M \times P$ matrix built from $\underline{\mathbf{R}}_H$ and whose columns are restricted to the pilots positions. In the same way, we note $\underline{\tilde{\mathcal{R}}}_H$ the $P \times P$ frequency covariance matrix, $\underline{\mathcal{C}}_n$ and $\hat{\mathcal{H}}_n^{LS}$ the vectors containing the pilot subcarriers and the LS estimation of the channel on these pilots positions respectively. Then, the LMMSE estimation (interpolation) along the frequency axis is given by

$$\hat{\mathbf{H}}^{LMMSE} = \underline{\mathcal{R}}_H (\underline{\tilde{\mathcal{R}}}_H + (\underline{\mathcal{C}}_n \underline{\mathcal{C}}_n^H)^{-1} \sigma^2 \underline{\mathbf{I}})^{-1} \hat{\mathcal{H}}_n^{LS}. \tag{2.39}$$

In order to perform an interpolation along the time axis, we firstly built the time correlation matrix. As proposed in [92], we consider for instance a Jakes model or a uniform Doppler spectrum. The time correlation is the Fourier transform of the Doppler spectrum (see chap. 1), so we obtain

$$\begin{aligned} (\underline{\mathbf{R}}_H^{time})_{u,v} &= \sigma_h^2 J_0(2\pi \nu_{D_{max}}(u-v)) \\ (\underline{\mathbf{R}}_H^{time})_{u,v} &= \frac{\sin(2\pi \sigma_{D_{max}}^2 (u-v) T_s)}{2\pi \nu_{D_{max}}^2 (u-v) T_s}, \end{aligned} \tag{2.40}$$

for the Jakes and the uniform spectrum, respectively, where $\nu_{D_{max}}$ is the maximum Doppler frequency. At last, in the literature, the mainly used pilot positioning are the preamble and the

comb-type arrangement. In the following, we will also use these patterns in the simulations, and we will only consider a frequency filtering. In (2.39), we observe that the interpolating filter $\underline{\mathcal{R}}_H(\tilde{\mathcal{R}}_H + (\underline{\mathcal{C}}_n\underline{\mathcal{C}}_n^H)^{-1}\sigma^2\underline{\mathbf{I}})^{-1}$ requires a $P \times P$ matrix inversion and a $(M \times P) \times (P \times P)$ matrix multiplication. The LMMSE channel estimation then requires a complexity [2] equal to $\mathcal{O}(P^3 + MP^2)$ [93]. To sum up, the Wiener (or LMMSE) estimation is an optimal method, but requires the knowledge of the matrix $\underline{\mathbf{R}}_H$ and the noise variance σ^2, and has a high complexity, particularly if a preamble scheme is considered.

2.4.1.2 iFFT Estimation

The principle of iFFT (for interpolated fast Fourier transform) is described in [13, 29] and depicted on Fig. 2.6. After having performed the LS estimation on the pilot subcarriers, a P-sized IDFT is made to recover the channel impulse response (supposing that the number of pilots is greater than the length of the channel). Then, $M - P$ samples equal to zeros are added at the end of the estimated IR vector (zero padding). Finally, a M-sized DFT is applied to obtain the estimation of the complete channel frequency response. The window which appears on Fig. 2.6 is simply the rectangular window of the OFDM signal, as seen in (1.23).

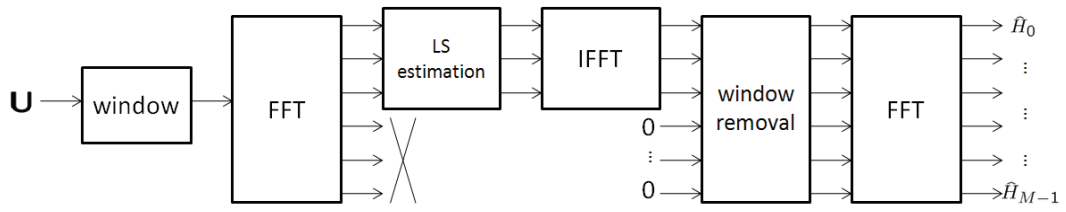

FIGURE 2.6 – Illustration of the interpolated fast Fourier transform Estimation.

As mentioned in [29], the iFFT channel estimation has two drawbacks. First, the signal must be periodic and M must be an integer multiple of P to recover the correct spectrum. Second, as a window is used, it is well known that the estimated spectrum leaks on the adjacent channel. This phenomenon is called leakage. However, in order to reduce the leakage, some kinds of windows have been proposed, as in [29, 94]. For instance in Fig. 2.7, we give the frequency response of the Hanning window compared to the rectangular one. We actually observe that the leakage is lower when the Hanning window is used instead of the rectangular one.

a. Complexity of the iFFT estimation: If the iFFT estimation is performed using the DFT matrix $\underline{\mathcal{F}}$ (A.15) (for any M), the complexity of the method is $\mathcal{O}(P^2 + M^2)$ operations. Indeed, the IDFT and the DFT require $\mathcal{O}(P^2)$ and $\mathcal{O}(M^2)$ multiplications, respectively. However, it is known that with some algorithms using the Hermitian property of $\underline{\mathcal{F}}$, the complexity can be reduced to $\mathcal{O}(P\ln(P) + M\ln(M))$, and even, if M is a power of two, the complexity can be reduced to $\mathcal{O}(P\log_2(P) + M\log_2(M))$ by means of the Cooley-Tukey algorithm. This estimator is obviously less complex than LMMSE. To summarize, iFFT is a low complexity estimation method, but needs that M is an integer multiple of P. Moreover, due to the win-

2. given in number of elementary multiplications

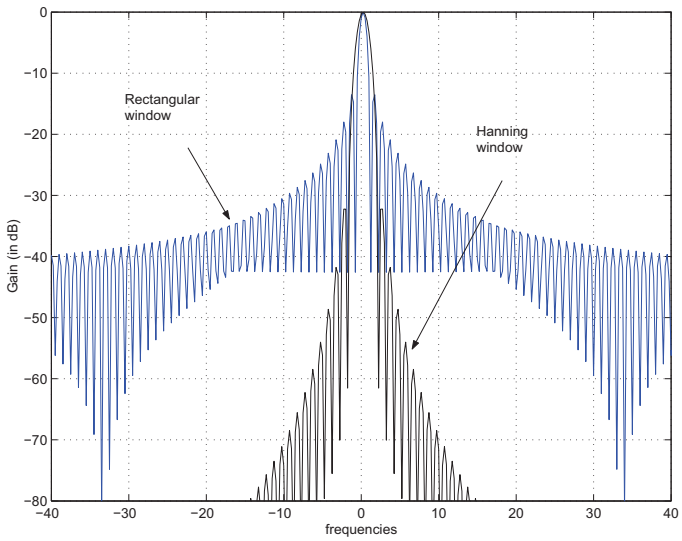

FIGURE 2.7 – Frequency responses of the Hanning and the rectangular windows.

dowing, the estimated spectrum leaks on the adjacent ones, which is a drawback when the nearby channels are used by other users or applications.

2.4.1.3 Maximum Likelihood Estimation

In this section, the maximum likelihood estimation and the expectation-maximization algorithms are presented. Since the additive noise is considered as a zero mean Gaussian process, each received symbol $U_m = H_m C_m + W_m$ is a also a Gaussian process of mean $H_m C_m$ and variance σ^2, whatever $m = 0, 1, ...M-1$. Furthermore, as $\mathbf{H}_n$ and $\mathbf{W}_n$ are uncorrelated, and the elements of the noise vector are independent, the conditional probability density function of the received signal is given by (see [30, 31] for more precisions):

$$p(\mathbf{U}_n|\mathbf{H}_n, \underline{\mathbf{C}}_n, \sigma^2) = \frac{1}{(2\pi\sigma^2)^{P/2}} \exp\Big(-\frac{1}{2\sigma^2} \sum_{m=0}^{P-1} |U_m - H_m C_m|^2\Big). \tag{2.41}$$

The joint maximum Likelihood estimation of $\hat{\mathbf{H}}_n$ and $\hat{\underline{\mathbf{C}}}_n$ is performed by means of

$$(\hat{\mathbf{H}}_n, \hat{\underline{\mathbf{C}}}_n) = \max_{\mathbf{H}_n, \underline{\mathbf{C}}_n} \Big(\ln(p(\mathbf{U}_n|\mathbf{H}_n, \underline{\mathbf{C}}_n, \sigma^2))\Big). \tag{2.42}$$

If $\underline{\mathbf{C}}_n$ is a pilot symbol, it becomes obvious that the ML estimation (2.42) is equivalent to the LS one, as mentioned in [95]. Indeed, maximizing the logarithm of $p(\mathbf{U}_n|\mathbf{H}_n, \underline{\mathbf{C}}_n, \sigma^2)$ is exactly equivalent to minimizing J_{LS} in (2.9). The interest of ML appears when the matrix $\underline{\mathbf{C}}_n$ is composed of pilots and data, as when a comb-type pilot scheme is used, for instance. In that case, let us denote $\tilde{\underline{\mathbf{C}}}_n$ and $\bar{\underline{\mathbf{C}}}_n$ the matrices containing the pilots and the data, respectively, such as the complete OFDM symbol is $\underline{\mathbf{C}}_n = \{\tilde{\underline{\mathbf{C}}}_n, \bar{\underline{\mathbf{C}}}_n\}$. $\tilde{\underline{\mathbf{C}}}_n$ and $\bar{\underline{\mathbf{C}}}_n\}$ are usually named observed information and additional information, and their size is $P \times P$ and $(M - P) \times (M - P)$, respectively. The direct solving of (2.42) thanks to the incomplete observation $\tilde{\underline{\mathbf{C}}}_n$ necessitates a prohibitive calculation cost. In order to make it feasible in practice, the expectation-maximization (EM) has been developed in 1977 by A. P. Dempster *et al* in [96].

Several equivalent formulations of the EM algorithm have been proposed in literature [97–99]. As indicated by its name, the EM algorithm is composed of two steps. Let us denote i the number of the iteration. The general formulation of EM is

– 1. Expectation step:

$$\mathcal{Q}(\mathbf{H}_n|\hat{\mathbf{H}}_{n,(i-1)}) = E\{\ln(p(\mathbf{U}_n|\mathbf{H}_n))|\underline{\tilde{\mathbf{C}}}_n, \hat{\mathbf{H}}_{n,(i-1)}\}. \tag{2.43}$$

– 2. Maximization step:

$$\hat{\mathbf{H}}_{n,(i)} = \arg\max_{\mathbf{H}_n} \left(\mathcal{Q}(\mathbf{H}_n|\hat{\mathbf{H}}_{n,(i-1)})\right). \tag{2.44}$$

The EM algorithm allows reaching the ML performance when i tends to infinity. References [97, 98] discuss the initialization value $\hat{\mathbf{H}}_{n,(i=0)}$, and a detailed expression of the function $\mathcal{Q}(\mathbf{H}_n|\hat{\mathbf{H}}_{n,(i-1)})$ is developed in [100].

2.4.2 Methods without Knowledge of the Channel Properties

This section briefly describes usual interpolation techniques which do not require any channel or noise properties as the aforementioned ones, but are only based on different kinds of interpolations. These methods are also described in [23, 27]. Furthermore, Chapter 5 is partially dedicated to the statistical characterization of these interpolations. These interpolations are used when a comb-type pilot scheme, a rectangular or a staggered rows pattern is considered.

2.4.2.1 Nearest-Neighbor Interpolation

The nearest-neighbor (NN) interpolation is a simple method to get an estimation of the channel frequency response between the pilot subcarriers. Let us denote f_p the frequency position of a pilot, and δ_f the frequency gap between two consecutive pilots. In the following, we also note δ_p the frequency gap corresponding to δ_f in the discrete formalism. We also suppose a regular pilot arrangement ..., $f_{p-\delta_f}, f_p, f_{p+\delta_f}$, ... Furthermore, we denote f_{p^-} and f_{p^+} the centers of the intervals $[f_{p-\delta_f}, f_p]$ and $[f_p, f_{p+\delta_f}]$ respectively. As illustrated on Fig. 2.8, whatever $f \in [f_{p^-}, f_{p^+}]$, the channel estimation on this interval is

$$\hat{H}(f) = \hat{H}(f_p), \tag{2.45}$$

where $\hat{H}(f_p)$ is the LS estimation performed on the position f_p. In the discrete formalism, whatever $p - \delta_p/2 \leq m \leq p + \delta_p/2$, the expression (2.45) becomes

$$\hat{H}_m = \hat{H}_p. \tag{2.46}$$

Although its simplicity, it is obvious that this interpolation is only adapted to very weakly selective channels.

2.4.2.2 Linear and Second Order Interpolation

The linear interpolation is also a simple method, which consists, for a given value $f \in [f_p, f_{p+\delta_f}]$, of taking the mean of the values $\hat{H}(f_p)$ and $\hat{H}(f_{p+\delta_f})$, weighted by the inverse of the distance $f_{p+\delta_f} - f_p$. More precisely, $\hat{H}(f)$ is obtained by

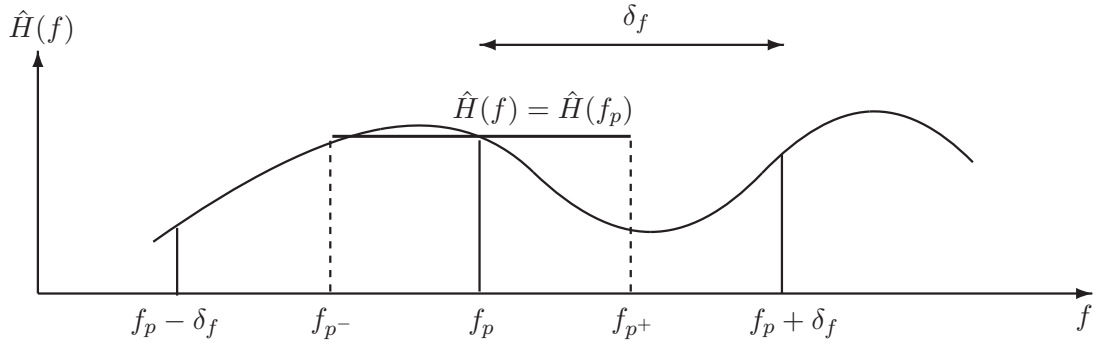

FIGURE 2.8 – Illustration of nearest-neighbor interpolation.

$$\hat{H}(f) = \hat{H}(f_p) + (f - f_p)\frac{\hat{H}(f_{p+\delta_f}) - \hat{H}(f_p)}{f_{p+\delta_f} - f_p}. \tag{2.47}$$

Equivalently, in the discrete formalism, we get

$$\hat{H}_m = \hat{H}_p + (m - p)\frac{\hat{H}_{p+\delta_p} - \hat{H}_p}{\delta_p}. \tag{2.48}$$

Fig. 2.9 illustrates the principle of the linear interpolation. In the same way as the NN interpolation, this method offers bad results when the channel is highly frequency selective.

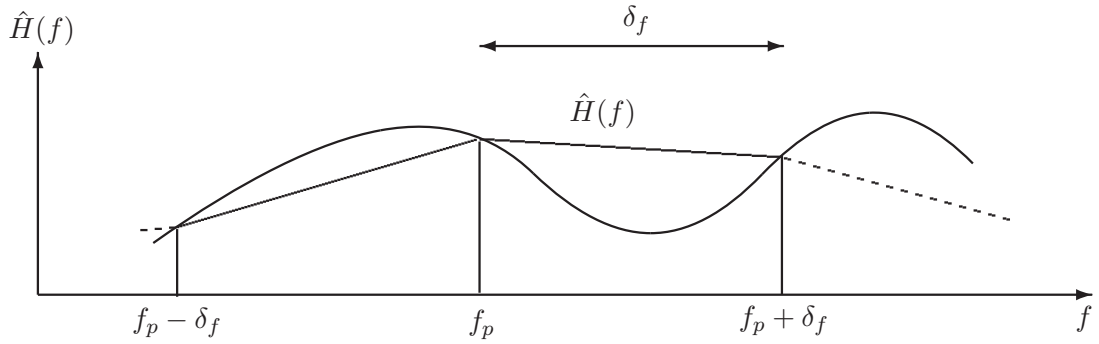

FIGURE 2.9 – Illustration of the linear interpolation.

As described in [101], the second order interpolation is similar to the linear one, but uses three pilots instead of two. Thus, for a given subcarrier m between the pilot positions p and $p + \delta_p$, the second order interpolation $\hat{H}_m$ is given by

$$\hat{H}_m = c_{p-\delta_p}\hat{H}_{p-\delta_p} + c_p\hat{H}_p + c_{p+\delta_p}\hat{H}_{p+\delta_p}, \tag{2.49}$$

where the coefficients $c_{p-\delta_p}$, c_p and $c_{p+\delta_p}$ are equal to

$$\begin{cases} c_{p-\delta_p} = \frac{1}{2}(a(a-\delta_p)) \\ c_p = -(a-\delta_p)(a+\delta_p) \\ c_{p+\delta_p} = \frac{1}{2}(a(a+\delta_p)) \\ a = \frac{\delta_p}{m-p}. \end{cases} \tag{2.50}$$

It is shown in [101] that the second order interpolation is only slightly more efficient than the linear one. In the rest of the report, we will only take interest in the linear interpolation.

2.4.2.3 Polynomial Interpolation

The polynomial interpolation consists in the approximation of $H(f)$ by a polynomial of degree $P-1$ noted χ which verifies: for the pilot positions f_p, $p = 0, 1, ..., P-1$, χ takes the values $\hat{H}(f_p)$. Thus, we get $\hat{H}(f) = \chi(f)$. Since the following methods are based on mathematical considerations, the developments are made in the continuous formalism. Obviously, the results remain valid after sampling (on the expected subcarriers for instance). As shown in Fig. 2.10, the pilots can be evenly distributed or not. The usual way to build χ is to use the Lagrange basis of the functions $\mathcal{L}_0, \mathcal{L}_1, ..., \mathcal{L}_{P-1}$ defined, for $p = 0, ..., P-1$ by

$$\mathcal{L}_p(f) = \prod_{\substack{k=0 \\ k\neq p}}^{P-1} \frac{f - f_k}{f_p - f_k} = \frac{(f-f_0)(f-f_1)...(f-f_{P-1})}{(f_p-f_0)(f_p-f_1)...(f_p-f_{P-1})}, \tag{2.51}$$

and such as

$$\chi(f) = \sum_{p=0}^{P-1} \mathcal{L}_p(f)\chi(f_p) = \sum_{p=0}^{P-1} \mathcal{L}_p(f)\hat{H}(f_p). \tag{2.52}$$

This is the only polynomial of degree $P-1$ verifying the conditions $\chi(f_p) = \hat{H}(f_p)$, as shown in [21]. The main drawback of the Lagrange polynomial interpolation is the Runge effect. It results in fluctuations of $\chi(f)$ between the nodes, and especially near the end points f_0 and f_p. It occurs in particular when P is large, and when the control points f_p (the pilot positions in our case) are evenly distributed. The error of interpolation even tends to infinity when P tends to infinity.

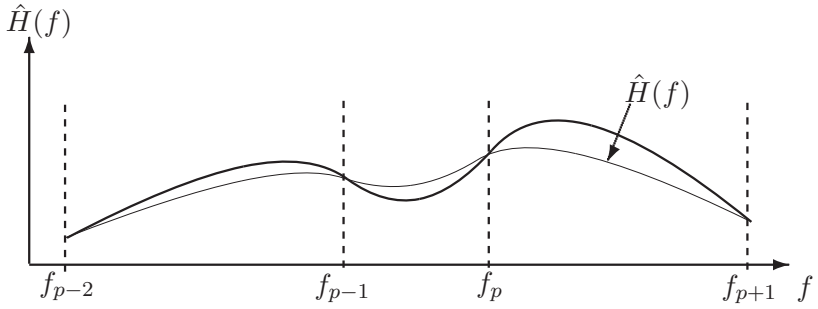

FIGURE 2.10 – Illustration of polynomial interpolation.

Piecewise Cubic Interpolation

In order to limit the Runge effect, a method consists in cutting the interval of $H(f)$ (the bandwidth of the channel) into several shorter intervals $[f_0, f_3], [f_3, f_6], ..., [f_{P-4}, f_{P-1}]$, and

performing a cubic interpolation on each on them. Considering for instance the first interval $[f_0, f_3]$, the Lagrange's (2.51) basis simplifies to

$$\begin{aligned}
\mathcal{L}_0(f) &= \frac{f-f_1}{f_0-f_1} \times \frac{f-f_2}{f_0-f_2} \times \frac{f-f_3}{f_0-f_3} \\
\mathcal{L}_1(f) &= \frac{f-f_0}{f_1-f_0} \times \frac{f-f_2}{f_1-f_2} \times \frac{f-f_3}{f_1-f_3} \\
\mathcal{L}_2(f) &= \frac{f-f_0}{f_2-f_0} \times \frac{f-f_1}{f_2-f_1} \times \frac{f-f_3}{f_2-f_3} \\
\mathcal{L}_3(f) &= \frac{f-f_0}{f_3-f_0} \times \frac{f-f_1}{f_3-f_1} \times \frac{f-f_2}{f_3-f_2},
\end{aligned} \tag{2.53}$$

In the following, we assume that the pilots are evenly distributed. However, in that case, the Runge effect is limited because of the poor value of the polynomial. Since the polynomials are independently built, we notice that the curve is discontinuous on the interval $[f_0, f_{P-1}]$. In order to make the interpolating curve continuous on the complete interval, it is usual to use the cubic Hermite interpolation and the cubic spline interpolation, as described in the following.

2.4.2.4 Cubic Spline Interpolation

The cubic spline interpolation uses the Hermite polynomials basis, and ensures the continuity of the interpolating curve on each control point by adding a condition on the derivative of the curve on these point. Another difference with the Lagrange cubic interpolation is that a polynomial of degree three is built between each node. On the interval $[0, 1]$, the Hermite basis is the following:

$$\begin{aligned}
\eta_0(f) &= (1+2f)(1-f)^2 \\
\eta_1(f) &= f^2(3-2f) \\
\kappa_0(f) &= f(1-f)^2 \\
\kappa_1(f) &= f^2(f-1).
\end{aligned} \tag{2.54}$$

Now, considering some interval $[f_p, f_{p+1}]$, we derive the spline cubic polynomial χ_s as

$$\begin{aligned}
\chi_s(f) = \quad & \eta_0\left(\frac{f-f_p}{f_{p+1}-f_p}\right)H(f_p) + \eta_1\left(\frac{f-f_p}{f_{p+1}-f_p}\right)H(f_{p+1}) \\
& + \kappa_0\left(\frac{f-f_p}{f_{p+1}-f_p}\right)(f_{p+1}-f_p)H'(f_p) + \kappa_1\left(\frac{f-f_p}{f_{p+1}-f_p}\right)(f_{p+1}-f_p)H'(f_{p+1}),
\end{aligned} \tag{2.55}$$

where $H'(f)$ is the derivative of H on the point f. As shown in [102], it would be easy to show that $\chi_s(f)$ is the single polynomial satisfying $\chi_s(f_p) = H(f_p)$, $\chi_s(f_{p+1}) = H(f_{p+1})$, $\chi'_s(f_p) = H'(f_p)$ and $\chi'_s(f_{p+1}) = H'(f_{p+1})$. When these conditions are used for the derivative of $\chi'_s(f_p)$, the interpolation is called clamped cubic spline. A second usual choice is to take null derivative $\chi'_s(f_p) = 0$ and $\chi'_s(f_{p+1}) = 0$. In that case, the interpolation is called natural cubic spline.

2.4.2.5 Other Interpolations

It would remain a wide range of interpolation methods to be described. References [27,103] cover around twenty of the most classical techniques. For the most of them, the principle is to filter the pilots in order to get the missing information. The general formulation for these techniques is

$$\hat{H}(f) = \int_{-\infty}^{+\infty} g_i(f-\nu)\hat{H}_p(\nu)d\nu, \tag{2.56}$$

where g_i is the interpolating function, and $\hat{H}_p(\nu)$ is the function which takes the value $H(f_p)$ for $\nu = f_p$ and zero elsewhere. Obviously, the observation is not infinite (limited to the pilots), and the system is discrete. After sampling, we can then rewrite (2.56) as

$$\hat{H}_m = \sum_{k=0}^{P-1} g_{i,m-k}\hat{H}_{p,k}. \tag{2.57}$$

From (2.56), we notice that the interpolation method only depends on the function g_i. The moving average interpolation usually requires decreasing functions g_i as the inverse function, or the decreasing exponential. Another very usual interpolation is based on the Nyquist-Shannon sampling theorem (1949) and on Whittaker's work (1935). This method is based on the properties of the sinc function and is then called Shannon-Whittaker interpolation or sinc interpolation. It is expressed by

$$\hat{H}_m = \sum_{k=0}^{P-1} \hat{H}_{p,k}\text{sinc}\left(\frac{m-k\delta_p}{\delta_p}\right). \tag{2.58}$$

2.4.3 Iterative and Recursive Channel Estimation

2.4.3.1 Iterative Channel Estimation, Equalization and Data Detection

The class of the iterative estimation methods allows getting both channel and data estimations. The principle, clearly described in [104] and in Fig. 2.11 is to use the estimated data (and the channel respectively) to feed the channel estimator block (the data detection block resp.). The steps are summarized in the following:

- Initialization: A channel estimation $\hat{H}_{p,(0)}$ is performed on the pilot tones p at iteration $i = 0$. The complete channel estimation $\hat{\mathbf{H}}_{(0)}$ is derived.
- The data subcarriers $\hat{C}_{m,(0)}$ are estimated.
- For $i \geq 0$, the data $\hat{C}_{m,(i)}$ is used as virtual pilot tones to estimate $\hat{H}_{m,(i)}$, and $\hat{H}_{m,(i)}$ is used for the equalization.

As indicated in [104], although detection errors ($\hat{C}_{m,(i)} \neq C_m$) may occur, if the error probability is low enough, the channel estimation $\hat{\mathbf{H}}_{(i)}$ is more accurate from an iteration i to the next one. In order to reduce the errors in detections, the system can include a channel decoder, as presented in [105,106]. In that case, the channel estimation is made conditionally to the estimated bits, and is called estimation with hard decision.

The channel estimation can be performed thanks to any aforementioned techniques. The complexity of the iterative techniques then depends on the estimation and equalization methods. For instance, [107] proposes an LS-based one, the authors of [108] base their method on the EM algorithm and LMMSE is used in [105].

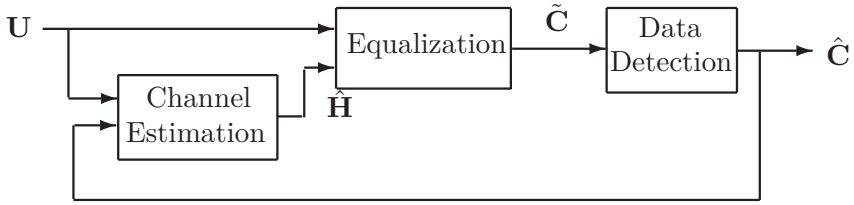

FIGURE 2.11 – Block-diagram of the iterative channel estimation with feedback from the data detection.

2.4.3.2 Recursive Channel Estimation

The principle of recursive channel estimation is to use an adaptive filter to perform the estimation. Thus, contrary to iterative methods, in which the estimation is done l times on the same symbol, the recursive techniques require not only the n^{th} OFDM symbol, but also the k previous ones. The most used estimator is the recursive least square (RLS), whose principle is explained in [109]. We denote J_n^{RLS} the cost function to minimize:

$$J_n^{RLS} = \sum_{k=0}^{n} \lambda^{n-k} ||\mathbf{e}_k||^2, \tag{2.59}$$

where λ is the forgetting factor such as $0 < \lambda \leq 1$, and $\mathbf{e}_k$ is the error vector given by

$$\mathbf{e}_k = \mathbf{U}_k - \hat{\mathbf{H}}_k \underline{\mathbf{C}}_k. \tag{2.60}$$

$\hat{\mathbf{H}}_k$ is the vector which minimizes the cost function J_n^{RLS}, that is

$$\nabla_{\hat{\mathbf{H}}_k} J_n^{RLS} = \begin{pmatrix} \frac{\partial}{\partial \hat{H}_{0,k}} (\sum_{k=0}^{n} \lambda^{n-k} ||\mathbf{e}_k||^2) \\ \vdots \\ \frac{\partial}{\partial \hat{H}_{m,k}} (\sum_{k=0}^{n} \lambda^{n-k} ||\mathbf{e}_k||^2) \\ \vdots \\ \frac{\partial}{\partial \hat{H}_{M-1,k}} (\sum_{k=0}^{n} \lambda^{n-k} ||\mathbf{e}_k||^2) \end{pmatrix} = (0). \tag{2.61}$$

Whatever $m = 0, ..., M-1$, by solving (2.61) we find

$$\hat{H}_{m,n} = \frac{\sum_{k=0}^{n} \lambda^{n-k} U_{m,k} C_{m,k}^*}{\sum_{k=0}^{n} \lambda^{n-k} |C_{m,k}|^2}, \tag{2.62}$$

hence, if we rewrite (2.62), we get the update equation (see [109] for more details)

$$\hat{H}_{m,n} = \hat{H}_{m,n-1} + \frac{C_{m,k}^*}{\sum_{k=0}^{n} \lambda^{n-k} |C_{m,k}|^2} (U_{m,n} - \hat{H}_{m,n-1} C_{m,n}). \tag{2.63}$$

Similarly to RLS, the authors of [110] propose the recursive MMSE (RMMSE). This method is slightly more complex than RLS. Indeed, in addition to the channel, the channel covariance matrix $\underline{\mathbf{R}}_H$ and the noise variance σ^2 must be updated in function of the forgetting factor λ. Furthermore, if the statistics of the channel vary, [109] naturally advises to perform an update of λ.

2.5 Conclusion

In this chapter, a state of the art about the most important channel estimation methods used in OFDM systems has been presented. These methods differ from one to another by the optimization criterion that is used, the complexity, and the need of the a priori knowledge of some channel characteristics. The performance of LS and LMMSE has been characterized, via the MMSE. In this chapter, the contribution of the thesis is the derivation of a new expression of the minimum mean square error of the LMMSE estimator in SISO context. This expression can be seen as a generalization of the MMSE to the systems in which the channel correlation matrix is not invertible.

Chapters 3 and 4 focus on the LMMSE estimation, and propose new methods to avoid the a priori knowledge of the channel covariance matrix and/or the noise level. Chapter 5 focuses on the interpolation methods, and studies the error of estimation that they cause. Thus, the following three Chapters will mainly refer to Sections 2.3 and 2.4.2.

Chapter 3

Artificial Channel Aided-LMMSE Channel Estimation

3.1 Introduction

In Chapter 2, the LMMSE channel estimator has been presented in detail. Although it is the optimal estimator according to the MMSE criterion, two main drawbacks limit its practical implementation. First, from (2.23), we notice that the LMMSE estimator requires the channel covariance matrix $\underline{\mathbf{R}}_H$ and the noise variance σ^2. In this chapter, $\underline{\mathbf{R}}_H$ is a priori unknown by the receiver. Second, the matrix inversion and multiplication require $\mathcal{O}(M^3)$ operations, where M is the DFT size. For instance, let us consider the transmission of a signal built with the 2K-mode of the DVB-T standard [52]. In that case, each ODFM symbol is composed of 1705 useful carriers, so the LMMSE estimation requires about $8.5.10^9$ operations. This complexity still increases when the channel is time-varying. Indeed, if the channel impulse response (CIR) $\mathbf{h}_n$ changes from one OFDM symbol to another, the matrices $\underline{\mathbf{R}}_H$ and $\underline{\mathbf{B}} = \underline{\mathbf{R}}_H(\underline{\mathbf{R}}_H + (\underline{\mathbf{C}}\underline{\mathbf{C}}^H)^{-1}\sigma^2\underline{\mathbf{I}})^{-1}$ have to be accordingly updated.

In order to avoid the a priori knowledge of the channel covariance matrix and/or reduce the complexity of LMMSE, the literature proposes several approaches. In [7,111], a singular value decomposition of $\underline{\mathbf{B}}$ is used to perform a low rank estimation, which reduces the complexity of LMMSE with a negligible loss of the performance. In [18], the authors propose the relaxed MMSE (RMMSE), in which the matrix $\underline{\mathbf{R}}_H$ is replaced by a diagonal matrix $\alpha\underline{\mathbf{I}}$. The coefficient α is optimized to reduce the MMSE of the estimator. In the same way, in [112], $\underline{\mathbf{B}}$ is also replaced by a diagonal matrix $\beta\underline{\mathbf{I}}$, and a double optimization on α and β is performed to reduce the MMSE. This method is called dual diagonal LMMSE (DD-LMMSE). Both techniques reduce a lot the complexity of the LMMSE estimator, but to the detriment of the efficiency. Following another way, the authors of [33] use the symmetry property of the covariance matrix combined with a fast algorithm for the Toeplitz matrix inversion [113] to reduce the complexity.

In this chapter, we propose a LMMSE-based method in which the knowledge of the channel covariance matrix is not necessary. To this end, a perfectly tunable filter acting like an artificial channel is added at the receiver side. An LMMSE estimation of the sum of this artificial channel and the physical channel is then performed by using the sole covariance matrix of the artificial channel, and the physical channel estimation is finally obtained by subtracting

the frequency coefficients of the added filter. This method, called artificial channel aided-LMMSE (ACA-LMMSE) published in [34, 35], also reduces the complexity of LMMSE, since the matrix $\underline{\mathbf{B}}$ has to be computed only once. Furthermore, this chapter presents in Section 3.5 an application of the proposed method in the context of channels with delays longer than the CP durations. Combined with the algorithm called RISIC [36], the technique also allows to perform the channel estimation and the ISI cancellation in the case of fast varying channels. In this chapter, since we consider that the channel response can vary from one OFDM symbol to another, the subscript n is adopted to point out the OFDM symbol index.

3.2 Description of the Method

3.2.1 Principle of the Method

In most of transmission models, the receiver does not have any knowledge of the CSI nor of the statistics of the channel. This is particularly the case in broadcast systems. In the LMMSE techniques described in the literature, the covariance matrix $\underline{\mathbf{R}}_H$ is considered to be known, or must be estimated. Thus, this matrix must be regularly updated in order to track the channel variations.

The solution proposed in this chapter and described in Figs. 3.1 and 3.2 avoids the a priori knowledge of $\underline{\mathbf{R}}_H$. To this end, an artificial signal (composed of pilots only) is transmitted through a filter $\mathcal{G}$ and added to the received signal. Actually, the filter $\mathcal{G}$ plays the role of an artificial channel, whose parameters (coefficients, paths delays etc.) are perfectly known and tunable by the receiver. The statistics of the filter $\mathcal{G}$ is chosen in order to match a WSSUS channel. The coefficients of the filter $\mathcal{G}$ are randomly varying like an artificial channel. Consequently, we use a channel terminology to describe $\mathcal{G}$. To do so, we note $g_n(\tau)$ and $G_{m,n}$ the impulse response and the samples of the frequency response of the artificial channel, respectively. They are expressed by

$$g_n(\tau) = \sum_{d=0}^{D-1} g_{d,n}\delta(\tau - \beta_d\tau_s), \tag{3.1}$$

$$G_{m,n} = \sum_{d=0}^{D-1} g_{d,n}e^{-2j\pi\frac{m\beta_d}{M}}, \tag{3.2}$$

where $g_{d,n}$ are complex zero mean Gaussian processes and D is the number of paths of the artificial channel. We assume that the physical channel $h_n(\tau)$ and the artificial one $g_n(\tau)$ are uncorrelated. The pilot tones of the artificial signal are supposed to have exactly the same arrangement in the frame than the pilots in the OFDM received signal. The positions matching with the data carriers in the OFDM signal are replaced by zeros in the artificial signal. Furthermore, we assume that the artificial signal is perfectly synchronized with the received signal. From the receiver point of view, the pilots are distorted by the sum of the physical channel and the artificial channel. For a given pilot $C_{m,n}$, if we note $\tilde{U}_{m,n}$ the artificial received signal, it yields

$$\tilde{U}_{m,n} = (H_{m,n} + G_{m,n})C_{m,n} + W_{m,n}. \tag{3.3}$$

The resulting channel, noted $\mathcal{K} = \mathcal{H} + \mathcal{G}$, is called hybrid channel afterward. Its channel impulse response $\kappa_n(\tau)$ is the sum of the ones of the physical and the artificial channels:

$$\kappa_n(\tau) = \sum_{l=0}^{L-1} h_{l,n}\delta(\tau - \beta_l\tau_s) + \sum_{d=0}^{D-1} g_{d,n}\delta(\tau - \beta_d\tau_s)$$
$$= \sum_{l_K=0}^{L_K-1} \kappa_{l_K,n}\delta(\tau - \beta_{l_k}\tau_s). \quad (3.4)$$

$L_K \leq L + D$ is the number of paths of the hybrid channel and $\kappa_{l_K,n}$ its path coefficients. As it is possible to get $\beta_l = \beta_d$, it explains the inequality $L_K \leq L + D$. Fig. 3.1 illustrates via a simple diagram the masking effect of the physical channel $h_n(\tau)$ by the artificial one $g_n(\tau)$. The shape and the length of the impulse response of the artificial channel will be discussed afterward.

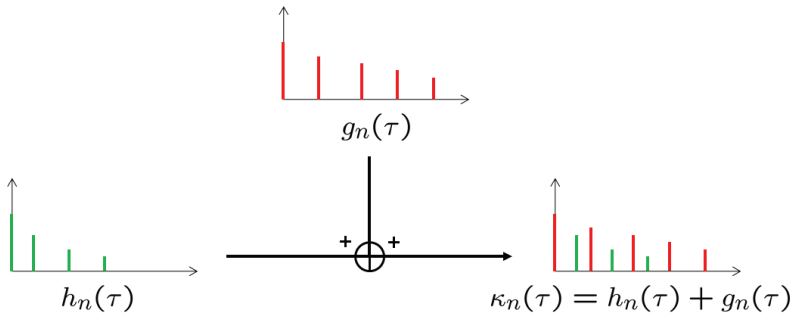

FIGURE 3.1 – Illustration of the masking effect of $\mathcal{H}$ by $\mathcal{G}$.

The goal of the proposed method is to perform an LMMSE channel estimation of $\mathbf{K}_n = \mathbf{G}_n + \mathbf{H}_n$ without any knowledge of the statistics of $\mathbf{H}_n$. We then propose a way to design the filter $\mathcal{G}$ such that the hybrid channel covariance matrix $\underline{\mathbf{R}}_K$ used in the LMMSE estimation of the hybrid channel can be entirely computed using the parameters of $\mathcal{G}$. In this way, we will justify the covariance matrix approximation $\underline{\mathbf{R}}_K \approx \underline{\mathbf{R}}_G$. The filter $\mathcal{G}$ must then play the role of "mask" for $\mathcal{H}$. This result will be obtained thanks to a relevant choice of the filter parameters, as described in Section 3.3. Finally, as $\mathcal{G}$ is perfectly known, we retrieve the estimation of $\mathcal{H}$ by subtracting $\mathcal{G}$ from the LMMSE estimation of the hybrid channel $\mathcal{K}$. As we make an LMMSE-based estimation of the physical channel with the help of an artificial channel $\mathcal{G}$, we refer the proposed method as artificial channel aided-LMMSE (ACA-LMMSE) in the rest of the chapter.

3.2.2 ACA-LMMSE channel Estimation

We now develop the mathematical expression of the proposed estimation method. In order to simplify the writing, let us consider that the pilots are arranged in a preamble scheme in the following. However, the result remains also valid in the case of pilot tones that are sparsely distributed in the OFDM frame, since LMMSE is based on Wiener interpolator filter (see Section 2.4.1). The hybrid channel vector $\mathbf{K}_n = \mathbf{H}_n + \mathbf{G}_n$ is estimated by means of the LMMSE estimator as

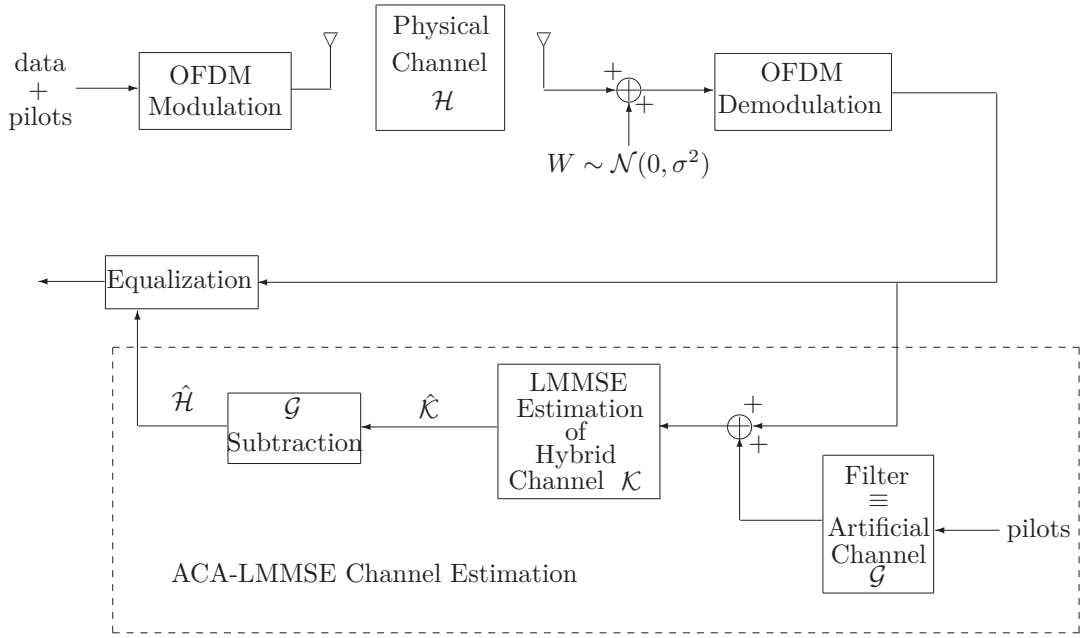

FIGURE 3.2 – Diagram of the ACA-LMMSE estimation in a simplified transmission-reception chain.

$$\begin{aligned}\hat{\mathbf{K}}_n^{LMMSE} &= \underline{\mathbf{R}}_K(\underline{\mathbf{R}}_K + \sigma^2(\underline{\mathbf{C}}_n\underline{\mathbf{C}}_n^H)^{-1})^{-1}\hat{\mathbf{K}}_n^{LS} \\ &= \underline{\mathbf{R}}_K(\underline{\mathbf{R}}_K + \frac{\sigma^2}{\mathcal{P}}\underline{\mathbf{I}})^{-1}\hat{\mathbf{K}}_n^{LS}, \end{aligned} \tag{3.5}$$

where $\hat{\mathbf{K}}_n^{LS}$ is the vector containing the LS estimated samples $\tilde{U}_{m,n}/C_{m,n}$, $m = 0, 1, .., M-1$, and $\underline{\mathbf{R}}_K$ is the $M \times M$ complex covariance matrix of $\mathcal{K}$, whose elements $(\underline{\mathbf{R}}_K)_{u,v}$ are expressed similarly to (1.53):

$$(\underline{\mathbf{R}}_K)_{u,v} = \sum_{l_K=0}^{L_K-1} \int_0^{\beta_{max}} \Gamma_{l_K}(\beta) e^{-2j\pi\frac{(u-v)}{M}\beta} d\beta. \tag{3.6}$$

In (3.6), β_{max} is the maximum delay of $\mathcal{K}$, i.e. the one of $\mathcal{H}$ or the one of $\mathcal{G}$. Let us assume that the noise variance is known or estimated with an algorithm adapted for OFDM transmissions [40], [41], [37]. In order to perform the LMMSE estimation of the hybrid channel in (3.5), the covariance matrix $\underline{\mathbf{R}}_K = \underline{\mathbf{R}}_{H+G}$ has to be calculated. However $\underline{\mathbf{R}}_K$ is unknown, as the statistics of $\mathcal{H}$ are supposed to be unknown. The proposed solution aims to mask $\mathcal{H}$ thanks to the filter $\mathcal{G}$, that is to set the statistics of $\mathcal{G}$ (recalling that these statistics are fixed by the user) leading to the approximation $\underline{\mathbf{R}}_K \approx \underline{\mathbf{R}}_G$. If this condition is verified, (3.5) remains valid whatever the variations of the physical channel $\hat{\mathbf{H}}_n$, and even if its statistics change (i.e. if $\underline{\mathbf{R}}_H$ changes). Thus, the covariance matrix $\underline{\mathbf{R}}_G$ has to be computed only once during all the transmission. ACA-LMMSE is then less complex compared to the methods in which $\underline{\mathbf{R}}_H$ and $\underline{\mathbf{B}}$ have to be updated. From (3.5), we get an estimation of the physical channel noted $\hat{\mathbf{H}}_n^{ACA}$ as

$$\hat{\mathbf{H}}_n^{ACA} = \hat{\mathbf{K}}_n^{LMMSE} - \mathbf{G}_n. \tag{3.7}$$

Although the coefficients $g_{d,n}$ of $\mathcal{G}$ are randomly generated (by means of a known statistic and the filter method described in Section 1.4), they can be stored in a memory after their generation so that $\mathbf{G}_n$ can be completely accessible for the estimation step of (3.7). In order to avoid the need of a memory, simulations will show that a simple filter with fixed coefficient can replace the artificial varying channel. The proposed solution can then be simply implemented in practice.

3.2.3 Characteristics of ACA-LMMSE

From (3.7), we derive the bias of the ACA-LMMSE estimation. Since $\mathbf{H}_n$ and $\mathbf{G}_n$ are zero mean processes, it is obvious that $\mathbf{K}_n = \mathbf{H}_n + \mathbf{G}_n$ is also a zero-mean process. Thus, by analogy with (2.24), we express the bias $B(\hat{\mathbf{H}}_n^{ACA})$ of ACA-LMMSE as

$$\begin{aligned} B(\hat{\mathbf{H}}_n^{ACA}) &= E\{\hat{\mathbf{H}}_n^{ACA} - \mathbf{H}_n\} \\ &= E\{\hat{\mathbf{K}}_n^{LMMSE} - \mathbf{G}_n\} - E\{\mathbf{H}_n\} \\ &= E\{\underline{\mathbf{R}}_K(\underline{\mathbf{R}}_K + \frac{\sigma^2}{\mathcal{P}}\underline{\mathbf{I}})^{-1}\hat{\mathbf{K}}_n^{LS}\} - E\{\mathbf{G}_n\} \\ &= 0. \end{aligned} \tag{3.8}$$

Eq. (3.8) shows that ACA-LMMSE is an unbiased estimator. Since we consider a SISO system, we now express the MMSE of the ACA-LMMSE estimation, noted $MMSE_{ACA}$, based on the developments proposed of Section 2.3.2.3. To this end, we define the error function $J_{\hat{\mathbf{H}}^{ACA}}$ which must be minimized. From (3.7), it yields

$$\begin{aligned} J_{\hat{\mathbf{H}}^{ACA}} &= \frac{1}{M}E\{||\mathbf{H}_n - \hat{\mathbf{H}}_n^{ACA}||_F^2\} \\ &= \frac{1}{M}E\{||\mathbf{H}_n - (\hat{\mathbf{K}}_n^{LMMSE} - \mathbf{G}_n)||_F^2\} \\ &= \frac{1}{M}E\{||\mathbf{K}_n - \hat{\mathbf{K}}_n^{LMMSE}||_F^2\}. \end{aligned} \tag{3.9}$$

By replacing $\mathbf{H}_n$ by $\mathbf{K}_n$, we notice that (3.9) is equivalent to (2.27). We directly deduce the expression of $MMSE_{ACA}$ from Section 2.3.2.3 and [20]:

$$MMSE_{ACA} = \frac{1}{M}.\frac{L_K^2\sigma^2}{L_K\mathcal{P} + \sum_{l_K=0}^{L_K-1}\frac{\sigma^2}{\lambda_{K,l_K}}}, \tag{3.10}$$

where λ_{K,l_K} are the eigenvalues of the hybrid channel. We observe that the MMSE of ACA-LMMSE has the same form as the one of LMMSE, but with the eigenvalues of $\underline{\mathbf{R}}_K$. It then theoretically proves the efficiency of the ACA-LMMSE estimation. Furthermore, since $\mathcal{K}$ is unknown, if the approximation $\underline{\mathbf{R}}_K \approx \underline{\mathbf{R}}_G$ is verified, (3.10) proves that the performance of ACA-LMMSE is driven by an appropriate choice of $\mathcal{G}$. As LMMSE plays the role of an interpolator (see Section 2.4.1), the proposed technique is also valid when the pilot tones are sparse in each OFDM symbol, as when a comb-type pilot scheme is used. Although the closed form of MMSE is impossible to derive in this case, simulations will compare the proposed solution with the LMMSE and LS Section 3.4.

3.2.4 Complexity Comparison with Standard LMMSE

3.2.4.1 Computation of the Channel Covariance Matrix

Without taking into account the characteristics of the channel covariance matrix, the number of operations required to compute $\underline{\mathbf{R}}_H = E\{\mathbf{H}_n\mathbf{H}_n^H\}$ is equal to M^2. However, as it is mentioned in Section 1.3.5, $\underline{\mathbf{R}}_H$ is a Toeplitz and Hermitian matrix. As a consequence, with $m = 0, 1, .., M-1$, it is sufficient to compute M multiplications $H_m H_1^*$ to deduce the M^2 elements of $\underline{\mathbf{R}}_H$.

The main drawback of the LMMSE estimator is that $\underline{\mathbf{R}}_H$ is a priori unknown. An usual solution to get around this problem [7] is to compute an estimated covariance matrix that we note $\underline{\tilde{\mathbf{R}}}_H$ by means of the LS estimate of the channel frequency response $\mathbf{H}_n^{LS}$:

$$\underline{\tilde{\mathbf{R}}}_H = \hat{\mathbf{H}}_n^{LS}(\hat{\mathbf{H}}_n^{LS})^H. \tag{3.11}$$

Unlike $\underline{\mathbf{R}}_H$, $\underline{\tilde{\mathbf{R}}}_H$ is "only" an Hermitian matrix. Thus, it is necessary to compute all the elements of the lower or upper triangle of $\underline{\tilde{\mathbf{R}}}_H$ to deduce the others. In that case, the number of multiplications is equal to $\frac{M(M+1)}{2}$. However, since we here consider a time varying channel, $\underline{\tilde{\mathbf{R}}}_H$ has to be regularly updated in order to track the channel variations. If we note N the number of required updates, the total complexity (computation of $\underline{\tilde{\mathbf{R}}}_H$ + update) is then equal to $N\frac{M(M+1)}{2}$. Whatever the frequency of the updates (every OFDM symbol, OFDM frame, 2 frames etc.), the value of N becomes huge as the transmission duration increases. Furthermore, even if $\underline{\mathbf{R}}_H$ can be computed, it is possible that the statistics of the channel change, and then the covariance matrix must also be updated.

In the case of the ACA-LMMSE estimation, it is assumed that the approximation $\underline{\mathbf{R}}_K \approx \underline{\mathbf{R}}_G$ is verified (see next section). Since $\mathcal{G}$ is perfectly known, $\underline{\mathbf{R}}_G$ is computed using (3.6), so we know that this covariance matrix is a Toeplitz and Hermitian matrix. As a consequence, its computation only requires M elementary operations. Furthermore, the filter $\mathcal{G}$ is designed in order to always mask the physical channel $\mathcal{H}$, so ACA-LMMSE is independent of the variations of the channel gain and statistics. At last, $\underline{\mathbf{R}}_G$ requires M multiplications and must be computed only once during the transmission.

3.2.4.2 Computation of the matrix $\underline{\mathbf{B}}$

The computation of $\underline{\mathbf{B}} = \underline{\mathbf{R}}_H(\underline{\mathbf{R}}_H + (\underline{\mathbf{C}}\underline{\mathbf{C}}^H)^{-1}\sigma^2\underline{\mathbf{I}})^{-1}$ requires a complexity equal to M^3 for the matrix inversion, and M^3 for the matrix multiplication, namely $2M^3$ multiplications. When LMMSE is performed with $\underline{\tilde{\mathbf{R}}}_H$, the computation of $\underline{\mathbf{B}}$ must be done N times during the transmission in order to track the channel variations. The total complexity is then $2NM^3$.

Once more, by using ACA-LMMSE, $\underline{\mathbf{B}}$ is computed only once at the beginning of the transmission and does not require any update. It is also possible to reduce the complexity of LMMSE (or ACA-LMMSE) by using the singular value decomposition (SVD) of the channel covariance matrix, while keeping the same performance, as proposed in [7]. In that case, the complexity is reduced to $2NLM^2$ for the LMMSE estimator and $2L_KM^2$ for ACA-LMMSE. Table 3.1 summarizes the complexity of the proposed ACA-LMMSE compared to the usual LMMSE. The exponent ^{1} indicates that the methods are simplified by means of the matrix characteristics and the SVD method for the computation of $\underline{\mathbf{B}}$ [7]. We notice that the complexity of each operation has the same order of magnitude for both techniques. It means that ACA-LMMSE is much simpler than the usual LMMSE estimation because the operations of

ACA-LMMSE have to be performed only once during all the transmission duration, unlike LMMSE which requires updates. It is all the more the case if the channel quickly varies and if the transmission duration is long.

TABLE 3.1 – Complexity comparison between ACA-LMMSE and usual LMMSE. The exponent [1] points out the simplified methods.

Operations	$\underline{\mathbf{B}}$	$\tilde{\mathbf{R}}_H$ or $\underline{\mathbf{R}}_K$	update	Total
usual LMMSE	$2M^3$	M^2	N	$N(2M^3+M^2)$
ACA-LMMSE	$2M^3$	M^2	-	$2M^3+M^2$
usual LMMSE [1]	$2LM^2$	$\frac{M(M+1)}{2}$	N	$N(2LM^2+\frac{M(M+1)}{2})$
ACA-LMMSE [1]	$2L_KM^2$	M	-	$2L_KM^2+M$

3.3 Choice of Filter $\mathcal{G}$ Parameters

The aim of this section is to justify the approximation $\underline{\mathbf{R}}_K \approx \underline{\mathbf{R}}_G$. To this end, we use the practical *US Consortium* channel model coming from the Digital Radio Mondiale (DRM) standard [1] and whose parameters are given in Table 1.1. Although we use a practical model from DRM standard in this section, we will extend the method for any WSSUS model in Section 3.4. The transmitted OFDM signal is composed of 148 independent carriers, according to robustness Mode C of the standard. Keep in mind that the training symbols are in staggered rows in the OFDM frame. Table 3.2 summarizes the parameters used for the simulations.

TABLE 3.2 – Parameters of Robustness C mode.

Robustness C	
Symbol duration	14.66 ms
CP duration	5.33 ms
Frame duration	400 ms
Number of carriers	148
Signal bandwidth	10 kHz
Signal constellation	64-QAM

The physical channel $\mathcal{H}$ being unknown, the exact statistical parameters of $\mathcal{K}$ are unknown. Thus, we can not use the covariance matrix $\underline{\mathbf{R}}_K$ given by (3.6). We then perform the LMMSE estimation of the hybrid channel using the covariance matrix of $\mathcal{G}$, whose parameters are perfectly known and controllable, and defined by

$$(\underline{\mathbf{R}}_G)_{u,v} = \sum_{d=0}^{D-1} \int_0^{\beta_{max}^{(G)}} \Gamma_d(\beta) e^{-2j\pi \frac{(u-v)}{M}\beta} d\beta, \tag{3.12}$$

where $\beta_{max}^{(G)}$ is the maximum delay of the artificial channel. Equation (3.12) highlights three parameters which have an influence on the covariance matrix $\underline{\mathbf{R}}_G$: the number of paths D of the artificial channel, the maximum delay $\beta_{max}^{(G)}$ (or equivalently $\tau_{max}^{(G)}$ in the continuous formalism) and the intensity delay profile $\Gamma_d(\beta)$. The following subsections characterize these

three parameters in order to get the approximation $\underline{\mathbf{R}}_K \approx \underline{\mathbf{R}}_G$, i.e. to make (3.12) as close as possible to (3.6).

3.3.1 Discussion on the Choice of the Parameters

We now focus on the choice of the parameters D, $\beta_{max}^{(G)}$ (or $\tau_{max}^{(G)}$) and $\Gamma_d(\beta)$ to make (3.12) as close as possible to (3.6). Firstly, our choice is driven by using some basic features about OFDM. Thus, since the system is supposed to be well designed, we have $\beta_{max}^{(H)}\tau_s \leq T_{CP}$. As a consequence, choosing $\beta_{max}^{(G)}\tau_s = T_{CP}$ ensures $\beta_{max} = \beta_{max}^{(G)}$ in (3.6).

The goal of the artificial channel is to mask the physical one. As a consequence, the number of artificial paths D must be chosen larger than L. However, as L is unknown, we must fix an arbitrary large D value. Due to the discrete time formulation, the length of the impulse response (limited by $\beta max^{(G)}$) of the filter is finite. We can then fix an upper limit to the number D equal to $\tau_{max}^{(G)}/\tau_s$.

The multipath intensity profile $\Gamma(\beta_b)$ can be a priori chosen in an infinite set of functions. Nevertheless, the choice is only limited by a practical consideration: expression (3.12) must be integrable. However, the decreasing exponential shape is commonly used ([7], [8] and [9]) in a large number of channel models, so we will use this shape. These a priori choice for D, $\beta_{max}^{(G)}$ and $\Gamma_d(\beta)$ will be confirmed in the next sections.

3.3.2 Discussion on the Choice of the Maximum Delay $\tau_{max}^{(G)}$

Here, the validity of ACA-LMMSE is verified for any value of the maximum delay $\beta_{max} = \beta_{max}^{(G)} \geq \beta_{max}^{(H)}$, with $\beta_{max}^{(G)} \in [\beta_{max}^{(H)}, T_{CP}/\tau_s]$. Figure 3.3 depicts the 3-D curve of the bit error rate (BER) of the ACA-LMMSE estimation versus $\beta_{max}^{(G)}/\beta_{max}^{(H)}$ and E_b/N_0 on the X and Y axes, respectively. According to the aforementioned recommendations, the number of paths D is set to 20 paths and $\Gamma_d(\beta)$ follows a decreasing exponential profile.

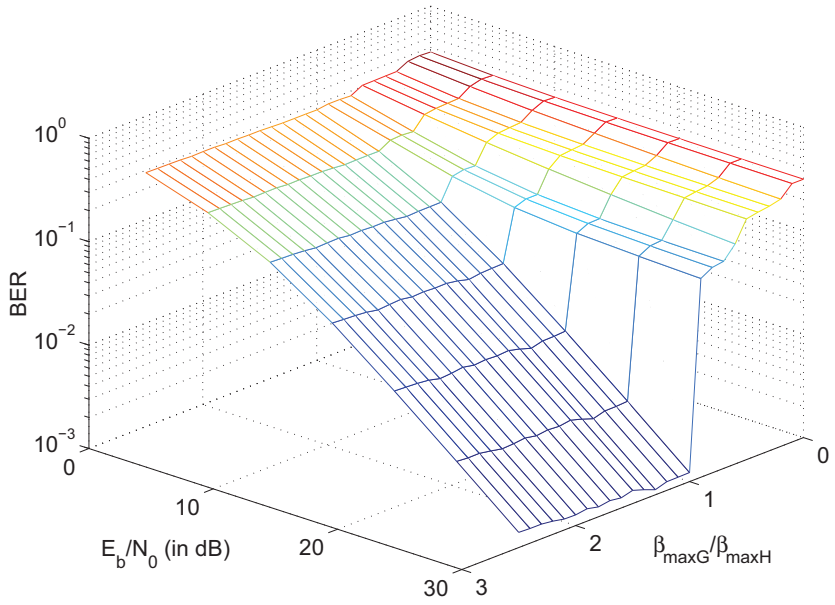

FIGURE 3.3 – BER curve versus $\beta_{max}^{(G)}/\beta_{max}^{(H)}$ and E_b/N_0.

Two zones in the BER curve are clearly noticeable. For $\beta_{max}^{(G)}/\beta_{max}^{(H)} \leq 1$, the error floor of the BER is larger than 0.1, for any considered value of E_b/N_0. The error floor of the zone $\beta_{max}^{(G)}/\beta_{max}^{(H)} \leq 1$ is due to a bad LMMSE hybrid channel estimation. Indeed, LMMSE method requires a correctly sized covariance matrix, i.e. the rank of the covariance matrix must be equal to the length of the channel path delay, according to [7]. In the case $\beta_{max}^{(G)}/\beta_{max}^{(H)} \leq 1$, the length of the hybrid channel $\mathcal{K} = \mathcal{H} + \mathcal{G}$ is equal to that of the physical channel $\mathcal{H}$, so the rank of the covariance matrix $\underline{\mathbf{R}}_G$ is lower than the length of the hybrid channel. In these conditions, the LMMSE method does not perform an efficient hybrid channel estimation, and so the channel $\mathcal{H}$ can not be efficiently estimated.

For $\beta_{max}^{(G)}/\beta_{max}^{(H)} \geq 1$, the BER does not reach any error floor for the considered E_b/N_0 values, according to an efficient channel estimation. $\mathcal{H}$ being unknown, $\underline{\mathbf{R}}_G$ is used to perform the estimation, and the rank of $\underline{\mathbf{R}}_G$ is equal to the length of the artificial channel $\mathcal{G}$. In the case $\beta_{max}^{(G)}/\beta_{max}^{(H)} \geq 1$, the condition on the rank of the covariance matrix $\underline{\mathbf{R}}_G$ equal to the length of the hybrid channel is respected. Indeed, the length of the hybrid channel $\mathcal{K} = \mathcal{H}+\mathcal{G}$ is equal to that of the artificial channel $\mathcal{G}$. $\mathcal{K}$ is then well estimated with LMMSE method and the channel estimation is efficiently performed with ACA-LMMSE. One can also observe that for $\beta_{max}^{(G)} \in [\beta_{max}^{(H)}, T_{CP}]$ (i.e. $\beta_{max}^{(G)}/\beta_{max}^{(H)} \in [1, T_{CP}/\beta_{max}^{(H)}]$), the BER reaches the same value for a given E_b/N_0. Assuming $\beta_{max}^{(H)}$ to be unknown, it is then shown that $\beta_{max}^{(G)}$ can be chosen equal to T_{CP} without degradation of performance. It justifies the first a priori choice $\beta_{max}^{(G)} = T_{CP}$.

3.3.3 Discussion on the Choice of the Number of Paths of the Artificial Channel

In this section, the effect of the number of paths D of the artificial channel is studied, assuming that the parameters β_{max} and $\Gamma_d(\beta)$ are chosen according to the previous recommendations. By hypothesis, the number of paths L of the physical channel is unknown, thus, L_K is also unknown in (3.6). The LMMSE estimation of the hybrid channel $\mathcal{K}$ is then performed by means of the covariance matrix $\underline{\mathbf{R}}_G$ defined by (3.12). Recalling that $L_K \leq L + D$, the larger D compared to L, the less the error between D and L_K. The physical consequence is that the gain of the channel becomes negligible in comparison to the one of the added filter, which justifies the masking effect.

On one hand, the channel is characterized by the non-null eigenvalues of its covariance matrix [114]. On the other hand, as the channel covariance matrices are Hermitian, comparing the eigenvalues of two covariance matrices is equivalent to comparing the matrices themselves [115]. In order to justify the approximation $\underline{\mathbf{R}}_K \approx \underline{\mathbf{R}}_G$, the eigenvalues of the matrices $\underline{\mathbf{R}}_K$ and $\underline{\mathbf{R}}_G$ are compared. For $m = 0, ..., M-1$ we define $\lambda_m^{(K)}$ and $\lambda_m^{(G)}$ the eigenvalues of $\underline{\mathbf{R}}_K$ and $\underline{\mathbf{R}}_G$ respectively. Figure 3.4 depicts the normalized error noted ε_m as a function of m and defined by

$$\varepsilon_m = \frac{|\lambda_m^{(K)} - \lambda_m^{(G)}|}{\max\limits_m(\lambda_m^{(G)})}, \tag{3.13}$$

where $\max\limits_m(\lambda_m^{(G)})$ is the largest eigenvalue of the matrix $\underline{\mathbf{R}}_G$. Four curves of error are considered, corresponding to $D = 5, 10, 20$ and 40 paths. The eigenvalues are stored in the ascending

order $\lambda_m^{(G)} \leq \lambda_{m+1}^{(G)}$ and $\lambda_m^{(K)} \leq \lambda_{m+1}^{(K)}$.

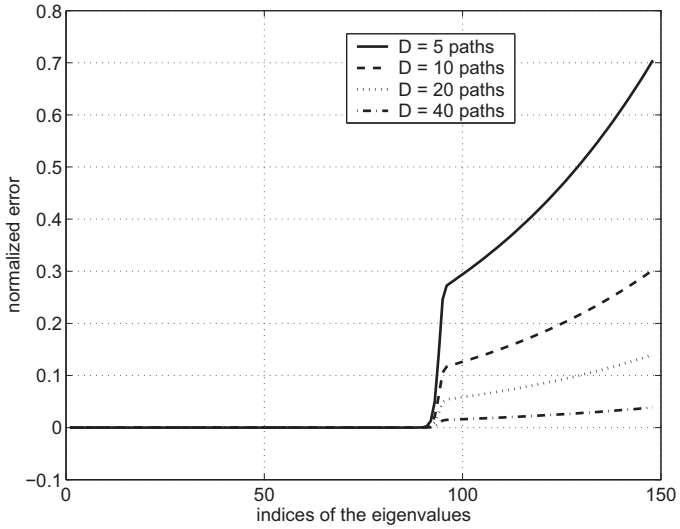

FIGURE 3.4 – Normalized error ε_m between the eigenvalues of $\underline{\mathbf{R}}_K$ and $\underline{\mathbf{R}}_G$.

Two parts are noticeable in Fig. 3.4. For $m = 0$ to 93, the error ε_m is null and for $m = 94$ to 147, the error ε_m is non-null. This is because the channel gain is contained in the last eigenvalues, tallying with the length of the impulse response (IR). Fig. 3.4 also highlights that the larger the number of paths D, the lower the normalized error ε_m. Indeed, for $D = 40$, the error ε_m is less than 0.05 for $m = 0, ..., M-1$. From Fig. 3.4, we can fix an arbitrary value D equal to 1/3 or 1/2 of the upper limit $\tau_{max}^{(G)}/\tau_s$. Indeed, for sufficiently large D, the matrices $\underline{\mathbf{R}}_G$ and $\underline{\mathbf{R}}_K$ have their eigenvalues almost equal, i.e. for $m = 0, ..., M-1$ we have $\lambda_m^{(G)} \approx \lambda_m^{(K)}$. It then justifies the approximation $\underline{\mathbf{R}}_G \approx \underline{\mathbf{R}}_K$.

3.3.4 Discussion on the Choice of the Multipath Intensity Profile

In this section, the effects of the multipath intensity profile $\Gamma_d(\beta)$ on the estimation efficiency is studied. The parameters $\tau_{max}^{(G)}$ and D are chosen according to the previous recommendations. As already stated, since $\mathcal{K}$ is unknown, the function $\Gamma_{l_K}(\beta)$ of the hybrid channel is approximated by the one of the artificial channel $\mathcal{G}$, which is chosen by the user. Since a decreasing exponential profile is an usual model for the gain of the multipath channels, it is logic to suppose that it is the best profile for $\Gamma_d(\beta)$ to guarantee the masking effect.

Although all integrable functions can be used in (3.12), three shapes are simulated for the multipath intensity profile: a decreasing exponential profile (d.e.p.) (noted $\Gamma_{dep}(\beta)$), a constant profile (c.p.) (noted $\Gamma_{cp}(\beta)$) and a growing exponential profile (g.e.p.) (noted $\Gamma_{gep}(\beta)$), and whose shapes are depicted in Fig. 3.5.

$$\Gamma_{dep}(\beta) = \begin{cases} Ce^{\frac{-\beta}{\beta max}} & \text{if } \beta \in [0, \beta_{max}] \\ 0, & \text{else,} \end{cases} \tag{3.14}$$

$$\Gamma_{cp}(\beta) = \begin{cases} C & \text{if } \beta \in [0, \beta_{max}] \\ 0, & \text{else,} \end{cases} \tag{3.15}$$

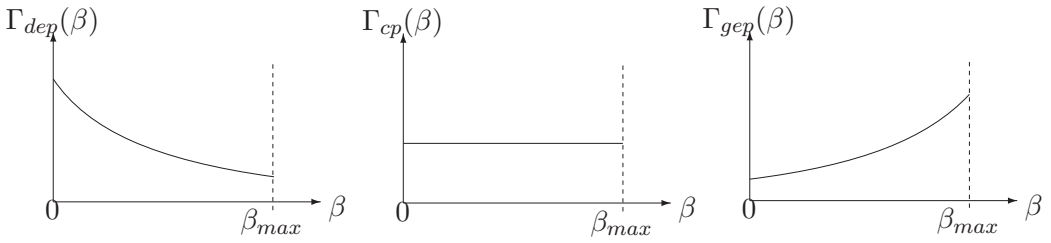

(a) Decreasing exponential profile (b) Constant profile (c) Growing exponential profile

FIGURE 3.5 – Three profiles for $\Gamma(\beta)$.

$$\Gamma_{gep}(\beta) = \begin{cases} Ce^{\frac{\beta}{\beta max}} & \text{if } \beta \in [0, \beta_{max}] \\ 0, & \text{else,} \end{cases} \tag{3.16}$$

where C is a normalization constant. Here, since the channel is not normalized, $C = 1$. Inserting (3.14) to (3.16) into (3.12) yields

$$(\underline{\mathbf{R}}_G)^{dep}_{u,v} = DC.\frac{1 - e^{-2j\pi\frac{(u-v)}{M}\beta_{max}}e^{-1}}{1 + 2j\pi\frac{(u-v)}{M}\beta_{max}}, \tag{3.17}$$

$$(\underline{\mathbf{R}}_G)^{cp}_{u,v} = DC.\frac{1 - e^{-2j\pi\frac{(u-v)}{M}\beta_{max}}}{2j\pi\frac{(u-v)}{M}\beta_{max}}, \tag{3.18}$$

$$(\underline{\mathbf{R}}_G)^{gep}_{u,v} = DC.\frac{1 - e^{-2j\pi\frac{(u-v)}{M}\beta_{max}+1}}{1 - 2j\pi\frac{(u-v)}{M}\beta_{max}}. \tag{3.19}$$

It is noticeable that the decreasing exponential profile (3.17) has the same the expression than (1.17), but in the discrete formalism.

Fig. 3.6 compares the BER curves versus E_b/N_0 of the theoretical LMMSE estimation (with the known matrix $\underline{\mathbf{R}}_H$) and the ACA-LMMSE using the three proposed multipath intensity profiles. To get a perfect control of $\underline{\mathbf{R}}_G$, we fix $\beta^{(G)}_{max}\tau_s = T_{CP}$ and $D = 20$ paths. Simulations show that the proposed solution is really close to the LMMSE estimation performance. There is only a 2 dB E_b/N_0 loss between ACA-LMMSE and the LMMSE estimator. Furthermore, in the ACA-LMMSE case, the statistics of the physical channel are unknown, contrary to the theoretical LMMSE estimator. This 2 dB loss comes from the approximation of the multipath intensity profile of the hybrid channel $\mathcal{K}$ by $\mathcal{G}$. In addition, Fig. 3.6 shows that the shape of the intensity profile do not have a significant impact on the BER performance. Indeed, the decreasing exponential profile leads to only slightly better results than the other two profiles. This is due to the shape of the considered channel, which has also a decreasing intensity profile. In that case, the filter $\mathcal{G}$ better matches with the physical channel. Nevertheless, with a sufficiently large D value, $\mathcal{G}$ acts like a mask for $\mathcal{H}$. The ACA-LMMSE method then leads to good estimations for any choice of $\Gamma_d(\beta)$. Thus, the choice of the shape of $\Gamma_d(\beta)$ is not a necessary condition for the feasibility of the proposed method.

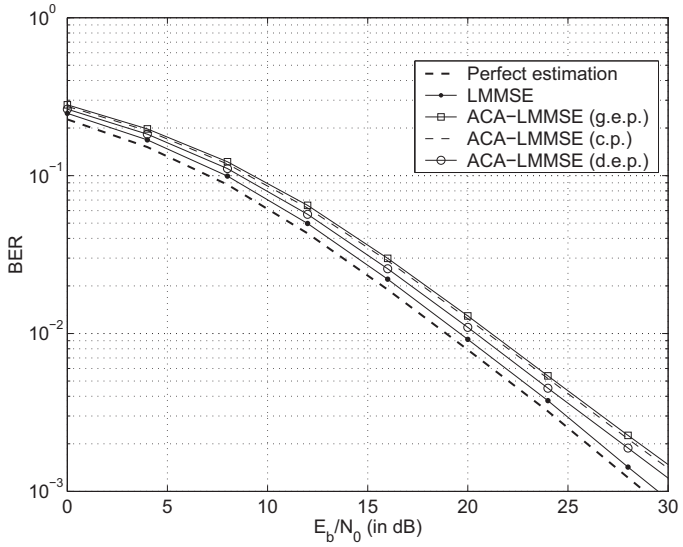

FIGURE 3.6 – BER of the ACA-LMMSE estimator for three different intensity profiles.

3.4 Simulations Results

3.4.1 Mean Square Error of ACA-LMMSE

The performance of the ACA-LMMSE estimator is first evaluated by means of the minimum means square error MMSE, estimated by the value $E\{\frac{1}{M}\sum_{m=0}^{M-1}|H_m - \hat{H}_m|^2\}$. The simulations parameters remain the same as in the previous section. Two pilot distributions are considered: a preamble scheme (noted PB), according to the analytical developments given in this chapter, and a distribution in staggered row (noted SP), according to the DRM standard. In Figs. 3.7 and 3.8, the ACA-LMMSE estimator is compared with the usual LMMSE and LS ones. In the SP case, LS is combined with the polynomial interpolation in order to get the estimation over the entire time and frequency lattice. According to robustness C (see [1], Appendix L), the pilot tones are placed every 4 carriers along the frequency axis and 1 pilot every 2 carriers along the time axis. The filter $\mathcal{G}$ has the following parameters: D = 15, $\tau_{max}^{(G)} = T_{CP} = 5.33$ ms and the delay profile follows a decreasing exponential profile. This configuration is coherent regarding the previous requirements.

For both PB and SP cases and whatever the SNR, the MMSE of the ACA-LMMSE estimator reaches a value 2 dB higher than the theoretical LMMSE. The ACA-LMMSE performance is slightly degraded compared to LMMSE, as the proposed estimator uses the covariance matrix $\underline{\mathbf{R}}_G$ which is naturally different from $\underline{\mathbf{R}}_H$. This phenomenon can be explained by comparing the theoretical expressions of the MMSE of the usual LMMSE (2.26) and ACA-LMMSE (3.10). Indeed, $MMSE$ is a growing function with respect to the value L (or L_K in (3.10)). Yet, L_K is set in order to get $L_K \geq L$, so $MMSE_{ACA} \geq MMSE_{LMMSE}$. Now comparing ACA-LMMSE with LS, it clearly outperforms LS as it offers an MMSE gain around 10 dB. This result is valid for both SP and PB distributions. Note then that the differences between the SP and PB cases are due to the interpolation technique that inevitably degrades the estimation quality.

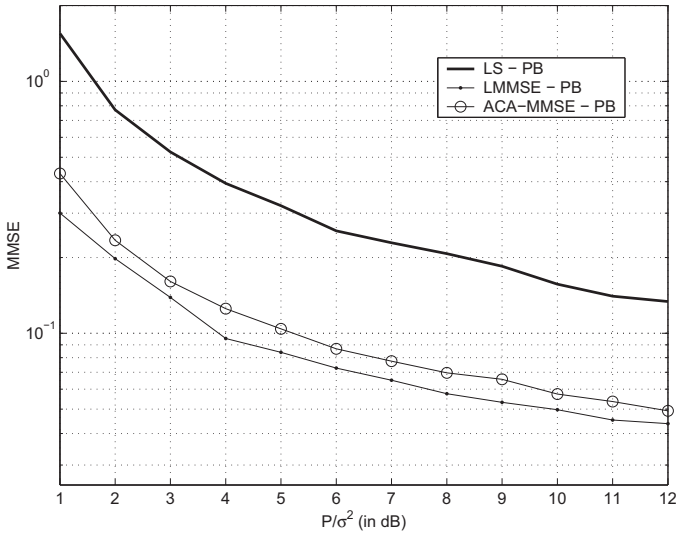

FIGURE 3.7 – Evolution of MMSE of ACA-LMMSE compared to LS and LMMSE as function of $\frac{P}{\sigma^2}$ for PB distribution.

3.4.2 Comparison with other methods

For all the BER curves in this chapter, no channel encoding is considered. Fig. 3.9 displays the BER curves versus E_b/N_0 of the ACA-LMMSE estimator, compared to LS, LMMSE and the perfect estimation. Two cases are considered for the LMMSE estimation: one performed with the exact channel covariance matrix $\underline{\mathbf{R}}_H = \mathbf{H}_n\mathbf{H}_n^H$ on one hand, and one performed with the estimated one $\underline{\tilde{\mathbf{R}}}_H$ (3.11) on the other hand. LS is performed with a polynomial interpolation. For all the E_b/N_0 values, the BER is obtained by making a mean on 10^6 bits.

We observe on Fig. 3.9, for $E_b/N_0 \geq 15$ dB, that both LMMSE and ACA-LMMSE curves converge to zero while the LS curve reaches an error floor. This error floor, equal to 4.10^{-2}, is due to the interpolation and will be characterized in Chapter 5. According to [7], when performed with $\underline{\mathbf{R}}_H$, LMMSE is optimal and almost reaches the perfect estimation. ACA-LMMSE and usual LMMSE performed with $\underline{\tilde{\mathbf{R}}}_H$ almost reach the same performance, the E_b/N_0 gap between the two curves being less than 0.2 dB. Furthermore, the error between these estimations and the perfect one is less than 2 dB. In both cases, the gap is due to the approximation of the covariance matrix $\underline{\tilde{\mathbf{R}}}_H$ instead of $\underline{\mathbf{R}}_H$, or $\underline{\mathbf{R}}_G \approx \underline{\mathbf{R}}_K$. We conclude that the LMMSE estimation performed with $\underline{\tilde{\mathbf{R}}}_H$ and ACA-LMMSE allows to avoid the knowledge of $\mathcal{H}$, but for similar performance, ACA-LMMSE is N times less complex than LMMSE, as shown in Section 3.2.4.

3.4.3 Suitability of ACA-LMMSE in general WSSUS Channel Models

In order to show that the ACA-LMMSE is suitable to all WSSUS-based models, the physical channels used to simulate Fig. 3.10 have been randomly generated. To this end L and $\tau_{max}^{(H)}$ are random variables and $\Gamma_l(\beta)$ is a random function. More precisely, for each simulation run, the random parameters L, $\tau_{max}^{(H)}$ and $\Gamma_l(\beta)$ follow these statistics:

– L is evenly distributed on $[\![2, 14]\!]$.
– $\tau_{max}^{(H)}$ is also uniformly distributed between 1 and 4 ms.

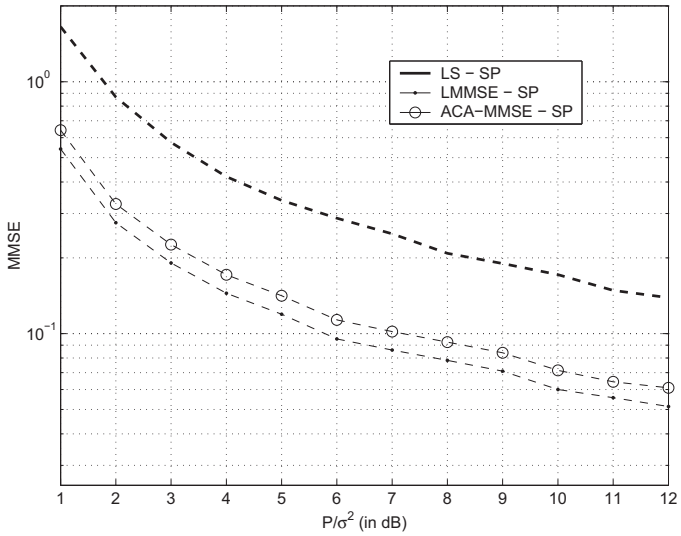

FIGURE 3.8 – Evolution of MMSE of ACA-LMMSE compared to LS and LMMSE as function of $\frac{P}{\sigma^2}$ for SP distribution.

– $\Gamma_l(\beta)$ follows the d.e.p., the g.e.p. or the c.p. with a probability equal to 1/3.

The BER is averaged over 30 simulation runs of 70 frames, which is equivalent to 4×10^6 bits. At each run, all the parameters change according to the previous recommendations. Fig. 3.10 compares the BER performance of the LMMSE and ACA-LMMSE estimations for these random physical channels. It is considered a theoretical LMMSE, in which the channel parameters at each run are supposed to be known. The parameters of the artificial channel for the ACA-LMMSE estimation are the same as mentioned previously: $D = 20$ paths, $\tau_{max}^{(G)} = T_{CP} = 5.33$ ms and $\Gamma_d(\beta)$ follows a decreasing exponential profile.

Fig. 3.10 shows that the E_b/N_0 gap between the BER curves of LMMSE and ACA-LMMSE is less than 0.5 dB. Furthermore, the difference of the BER between the ACA-LMMSE curve and the perfect estimation one is about 1 dB. These results match with the ones obtained with the *US Consortium* channel. It shows that the proposed method can be adapted for all channels based on the WSSUS model, and has a performance close to the theoretical LMMSE.

3.4.4 Reduction of Implementation Complexity

In this section, it is shown that a practical application of the ACA-LMMSE method can be simply performed by means of a constant filter $\mathcal{G}$. Indeed, we noted in Section 3.2.2 that the coefficient $g_{d,n}$ have to be generated and stored in a memory. By following the steps to generate the coefficients described in 1.4, the three stages FFT, filtering and IFFT have a cumulative complexity equal to $N(\log_2(N) + 1)$ for each coefficient $g_{d,n}$. In order to avoid these calculations, it is proposed to consider a filter $\mathcal{G}$ with constant coefficients such as its impulse response is

$$g(\tau) = \sum_{d=0}^{D-1} g_d \delta(\tau - \beta_d \tau_s). \tag{3.20}$$

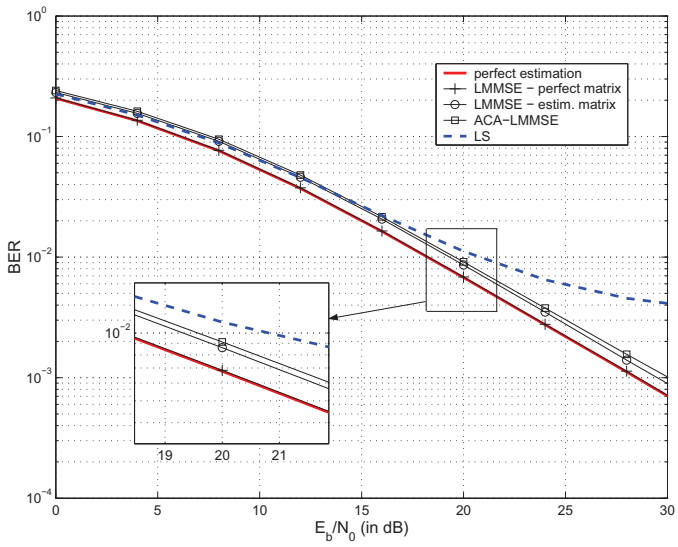

FIGURE 3.9 – BER of ACA-LMMSE compared to LMMSE and LS for *US Consortium* Channel.

Such a filter can be simply designed with only delay lines, as described in Fig. 3.11 . We notice that the coefficients g_d are fixed whatever the value of n. It then makes the method applicable with a low cost of implementation. In order to keep the masking effect of $\mathcal{G}$ on $\mathcal{H}$ on one hand, and the same covariance matrix (3.17) as previously on the other hand, the parameters $\tau_{max}^{(G)}$ and D are fixed such as $\tau_{max}^{(G)} = T_{CP}$, $D = 20$ paths. In order to approach the multipath intensity profile $\Gamma_d(\tau)$, we impose that the coefficient gains $|g_d|^2$ follow a decreasing exponential profile. The D paths are equally spaced on the interval $[0, \tau_{max}^{(G)}]$, with g_0 corresponding to $\tau = 0$ and g_{D-1} corresponding to $\tau = \tau_{max}^{(G)} = T_{CP}$. The phase $\phi(g_d)$ of each path coefficient is randomly chosen, following a uniformly distribution on $[0, 2\pi]$.

Fig. 3.12 compares the BER performance of the theoretical LMMSE and the ACA-LMMSE estimation when performed with the fixed filter depicted in (3.20) and Fig. 3.11. In order to generalize the method, the same WSSUS-based model with the varying parameters as in Section 3.4.3 is used.

Figs. 3.10 and 3.12 are quite similar, i.e. the difference between the BER curves of LMMSE and ACA-LMMSE is less than 0.5 dB. This result shows that the performance of the method is the same with a time-varying and a static filter $\mathcal{G}$. This method can then be performed in practice with a low cost of implementation.

3.5 Application to Intersymbol Interference Cancellation

In this section, let us now assume a very disrupted transmission, in which the channel is supposed to be fast varying and its delay spread is longer than the cyclic prefix. In these conditions, intersymbol interference (ISI) and intercarrier interference (ICI) occur. The transmission model under these constraints will be detailed in Section 3.5.1.

The literature proposes a wide panel of methods for the ISI and ICI cancellation. The two main methods for the interferences mitigation is the equalization and the cancellation. The

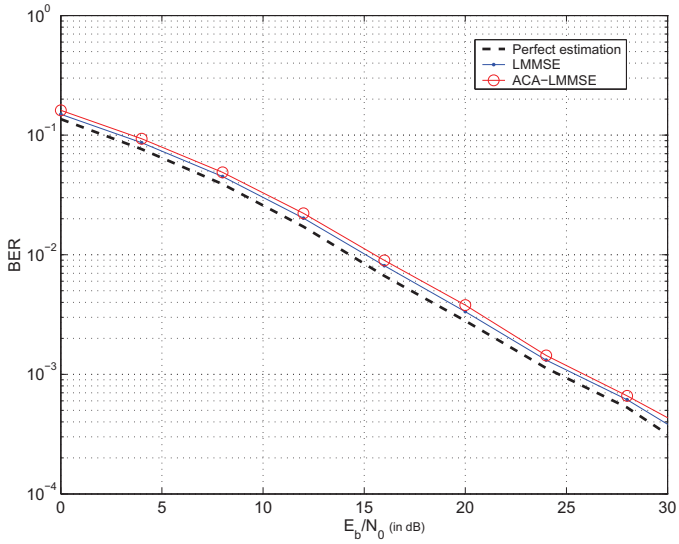

FIGURE 3.10 – BER curve of the ACA-LMMSE estimator compared to the LMMSE for a general channel model.

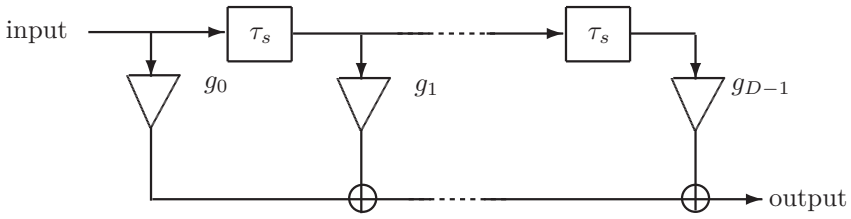

FIGURE 3.11 – Diagram of the constant filter $\mathcal{G}$ simply represented by delay lines and constant coefficients.

first one rather acts on the received signal whereas the second one rather acts on the transmission channel. For instance, it is shown in [116,117] that the turbo-equalizer suppresses the interferences and even allows the BER to reach the theoretical lowest bound. Its principle is to iteratively estimate the data $\mathbf{s}_n$ by means of a succession of steps: equalization, desinterleaving, symbol-to-binary conversion, channel decoding, binary-to-symbol conversion and interleaver. At each iteration, the equalizer is updated according to the mean square error $E\{|\mathbf{s}_n^{(e)} - \mathbf{s}_n|^2\}$, where $\mathbf{s}_n^{(e)}$ is the output of the equalizer. Although the turbo-equalizer allows the BER to reach the lowest bound, this method is complex, as each stage requires several operations. Furthermore, the convergence is not ensured in the presence of highly frequency selective channels.

The usual technique for both ISI and ICI cancellation is called residual ISI cancellation (RISIC) [36]. This time-domain cancellation (TDC) is the iterative version of the previously proposed multitone echo canceller algorithm (MTEC) [118]. The RISIC algorithm, whose principle is detailed afterward, allows to suppress ISI and mitigates ICI by making the transmission channel matrix cyclic. However, RISIC is efficient if the channel is supposed to be static or quasi static, since its performance is degraded in varying channels. Indeed, the channel is estimated on a preamble and is assumed to be invariant over several OFDM symbols.

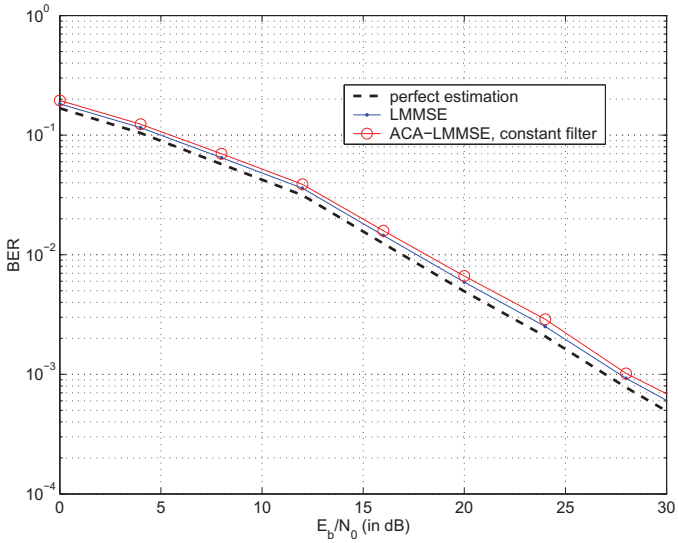

FIGURE 3.12 – BER curve versus E_b/N_0 of the ACA-LMMSE when performed with a constant filter. Comparison to the theoretical LMMSE.

In order to make the RISIC algorithm suitable for time varying channels, it is proposed to combine it with the ACA-LMMSE estimator. Indeed, the ACA-LMMSE performance is close to the optimal one, and this method is particularly adapted to varying channels. In the following, the model of the ISI channel is derived from the model developed in Chapter 1. The RISIC algorithm is presented and its combination with ACA-LMMSE is proposed.

3.5.1 Model of ISI Channel

By analogy with the transmission model described from (1.41) to (1.44) in Chapter 1, we derive the model in which the channel response is longer than the CP, that is $L > M_{CP}$. The CP removal corresponds to the removal of the M_{CP} rows in (1.41). Since $L > M_{CP}$, it yields

$$\mathbf{u}_n = \underline{\mathbf{h}}_n \mathbf{s}_n + \underline{\mathbf{h}}_{n-1}^{ISI} \mathbf{s}_{n-1} + \mathbf{w}_n, \tag{3.21}$$

where $\underline{\mathbf{h}}_n$ is the $M \times M$ channel matrix

$$\underline{\mathbf{h}}_n = \begin{pmatrix} h_{0,n} & 0 & \cdots & & 0 & h_{M_{CP}-1,n} & \cdots & h_{1,n} \\ h_{1,n} & h_{0,n} & 0 & & 0 & \ddots & \ddots & \vdots \\ & & & \ddots & h_{L-1,n} & & & \\ \vdots & & & \ddots & \ddots & & & \vdots \\ & \ddots & \ddots & & & & \ddots & h_{L-1,n} \\ h_{L-1,n} & \ddots & \ddots & & & \ddots & \ddots & 0 \\ \vdots & \ddots & \ddots & & & \ddots & \ddots & \vdots \\ 0 & \cdots & h_{L-1,n} & & & \ddots & h_{1,n} & h_{0,n} \end{pmatrix}, \tag{3.22}$$

and $\underline{\mathbf{h}}_{n-1}^{ISI}$ is the $M \times M$ contribution of the $n-1^{th}$ time slot such as

$$\underline{\mathbf{h}}_{n-1}^{ISI} = \begin{pmatrix} 0 & \cdots & 0 & h_{L-1,n-1} & \cdots & & h_{M_{CP},n-1} \\ \vdots & \ddots & & 0 & \ddots & & \vdots \\ \vdots & & & & \ddots & & h_{L-1,n-1} \\ 0 & \cdots & & \ddots & & \cdots & 0 \\ \vdots & & & & & \ddots & \vdots \\ 0 & \cdots & & \cdots & & \cdots & 0 \end{pmatrix}. \tag{3.23}$$

We notice in the top left corner of (3.22) that the channel matrix is not cyclic, which causes intercarrier interferences (ICI). We note $\underline{\mathfrak{h}}_n$ the complementary matrix of $\underline{\mathbf{h}}_n$ such as $\underline{\mathbf{h}}_n + \underline{\mathfrak{h}}_n$ is the cyclic matrix of the channel. The second term in (3.21) is the ISI contribution, whose channel matrix is $\underline{\mathbf{h}}_{n-1}^{ISI}$. The subscript n is used in order to highlight the fact that the channel is time varying. The received carriers U_m, $m = 0, .., M-1$ are obtained by applying an M-point FFT to (3.21), such as

$$\begin{aligned} \mathbf{U}_n &= FFT\{\mathbf{u}_n\} = FFT\{\underline{\mathbf{h}}_n \mathbf{s}_n\} + FFT\{\underline{\mathbf{h}}_{n-1}^{ISI} \mathbf{s}_{n-1}\} + FFT\{\mathbf{w}_n\} \\ &= \mathbf{U}_n^u + \mathbf{U}_n^{ICI} + \mathbf{U}_n^{ISI} + \mathbf{W}_n. \end{aligned} \tag{3.24}$$

The exponent u in the first term means useful. We define $\mathcal{U}(.)$ the Heaviside step function as

$$\mathcal{U}(x) = \begin{cases} 0, & \text{if } x < 0 \\ 1, & \text{if } x \geq 0 \end{cases}. \tag{3.25}$$

For all $0 \leq m \leq M-1$, the samples of the three vectors $\mathbf{U}_n^u$, $\mathbf{U}_n^{ICI}$ and $\mathbf{U}_n^{ISI}$ in (3.24) can be expressed as it is made in [36, 119, 120]:

$$\begin{aligned} U_{m,n}^u = C_{m,n} \Bigg[& \sum_{l=0}^{L-1} h_{l,n} \exp\left(\frac{-2j\pi lm}{M}\right) \\ & - \frac{1}{M} \sum_{l=M_{CP}}^{L-1} \sum_{i=0}^{M-1} h_{l,n} \exp\left(\frac{2j\pi m(M-l)}{M}\right) \mathcal{U}(l-i-M_{CP}) \Bigg], \end{aligned} \tag{3.26}$$

$$U_{m,n}^{ICI} = -\frac{1}{M} \sum_{l=M_{CP}}^{L-1} h_{l,n} \sum_{i=0}^{M-1} \sum_{\substack{\nu=0 \\ \nu \neq m}}^{M-1} C_{\nu,n} \exp\left(2j\pi \frac{\nu(M-l+i) - im}{M}\right) \mathcal{U}(l-i-M_{CP}), \tag{3.27}$$

$$U_{m,n-1}^{ISI} = \frac{1}{M} \sum_{l=M_{CP}}^{L-1} h_{l,n-1} \sum_{i=0}^{M-1} \sum_{\nu=0}^{M-1} C_{\nu,n-1} \exp\left(2j\pi \frac{\nu(M'-l+i) - im}{M}\right) .\mathcal{U}(l-i-M_{CP}), \tag{3.28}$$

with $M' = M + M_{CP} - 1$. The RISIC algorithm, presented afterward, allows to mitigate the two sources of interferences given in (3.27) and (3.28).

3.5.2 RISIC Algorithm

The principle of the RISIC algorithm holds in two main steps: the ISI $\underline{\mathbf{h}}_{n-1}^{ISI}\mathbf{s}_{n-1}$ is cancelled, and the ICI is cancelled by means of the cyclic reconstruction of the channel matrix. The steps are summarized as follows, assuming that the n^{th} OFDM symbol is received. The iterations are noted by means of the exponent (I).

1. An estimation of the channel $\hat{\underline{\mathbf{h}}}$ is performed only once thanks to a preamble, and valid for the transmission duration. The estimated matrices $\hat{\underline{\mathbf{h}}}^{ISI}$ and $\hat{\underline{\mathfrak{h}}}_n$ are deduced from $\hat{\underline{\mathbf{h}}}$.
2. Thanks to the estimation of the previous symbol $\hat{\mathbf{s}}_{n-1}^{(I-1)}$, the ISI is mitigated thanks to
$$\mathbf{u}_n^{(I)} - \hat{\underline{\mathbf{h}}}^{ISI}\hat{\mathbf{s}}_{n-1}^{(I-1)}. \tag{3.29}$$
3. An estimation of the current symbol $\hat{\mathbf{s}}_n^{(I)}$ is achieved,
4. The cyclic reconstruction is performed such as $\mathbf{u}_n^{(I)} - \hat{\underline{\mathbf{h}}}^{ISI}\hat{\mathbf{s}}_{n-1}^{(I-1)} + \hat{\underline{\mathfrak{h}}}_n\hat{\mathbf{s}}_n^{(I)}$.

The two last steps are iteratively performed, with $I \leftarrow I+1$. It is shown in [36] that this algorithm has a good performance. However, it can not be used in the case of time varying channels, as $\underline{\mathbf{h}}$ varies. Nevertheless, the next section proposes to apply ACA-LMMSE with RISIC in the case of fast-varying channels.

3.5.3 ACA-LMMSE with RISIC Algorithm

Let us now consider a time-varying channel. In this context, an adapted pilot pattern must be chosen (see Chapter 2, Section 2.2). According to the DRM/DRM+ standard, let us assume pilot tones in staggered row in the OFDM frame. It has been shown that the ACA-LMMSE is a good estimator, and is particularly adapted in the time-varying channel case, since its complexity does not increase in this context. The channel used for the simulations is based on the *US Consortium* model, whose parameters are given in Table 1.1. The signal is the same as the one used in Section 3.3. In order to simulate a transmission with ISI, we add a fifth path whose delay is up to $T_{CP} = 5.33\ ms$. Its variance $E\{h_{5,n}\}/2$ is set equal to 0.1. Being limited by the number of samples of the signal, we suppose that this delay noted $\tau_{max}^{(H)}$ is strictly lower than $T_u/2$. Thus we define $5.33 < \tau_{max} \leq 6\ ms$.

In order to apply ACA-LMMSE by supposing that the channel parameters are a priori unknown, the ones of the artificial channel $\mathcal{G}$ are set such as:

- $D = 15$ paths,
- $\Gamma_l(\beta)$ follows a decreasing exponential profile,
- $\tau_{max}^{(G)} = 7$ ms. For simulations purposes, this value is limited by $T_u/2 = 7.33$ ms.

The RISIC algorithm combined with the ACA-LMMSE channel estimation is summarized as follows:

1. Perform ISI cancellation such as
$$\tilde{\mathbf{u}}_n^{(0)} = \mathbf{u}_n - \hat{\underline{\mathbf{h}}}_{n-1}^{ISI}\hat{\mathbf{s}}_{n-1}. \tag{3.30}$$
For $n = 0$, it is assumed that $\mathbf{s}_0$ is the first transmitted OFDM symbol, i.e. no ISI occurs. In that case, the algorithm is simply a ACA-LMMSE estimation. Thus, (3.30) becomes valid from $n = 1$.

2. Obtain the symbol $\tilde{\mathbf{U}}_n^{(0)}$ in frequency domain by applying an M-point DFT to $\tilde{\mathbf{u}}_n^{(0)}$. Achieve the ACA-LMMSE channel estimation $\hat{\mathbf{H}}_n^{(0)}$ as done in (3.5) and (3.7). A simple one-tap equalization is performed and a decision is made to get the data $\hat{C}_{m,n}^{(0)}$, and after the IDFT, $\hat{\mathbf{s}}_n^{(0)}$ is obtained. Furthermore, from $\hat{\mathbf{H}}_n^{(0)}$, estimate the channel impulse response $[\hat{h}_{0,n}^{(0)}, \hat{h}_{1,n}^{(0)}, ..., \hat{h}_{L-1,n}^{(0)}, 0, ..., 0]^T$ and deduce the estimated matrix $\underline{\hat{\mathfrak{h}}}_n^{(0)}$.
3. From the iteration $I = 1$, perform the cyclic reconstruction by applying

$$\tilde{\mathbf{u}}_n^{(I)} = \tilde{\mathbf{u}}_n^{(0)} + \underline{\hat{\mathfrak{h}}}_n^{(I-1)} \hat{\mathbf{s}}_n^{(I-1)}. \tag{3.31}$$

4. Obtain the symbol $\tilde{\mathbf{U}}_n^{(I)}$ in frequency domain by applying an M-point DFT to $\tilde{\mathbf{u}}_n^{(I)}$. Perform the ACA-LMMSE channel estimation $\hat{\mathbf{H}}_n^{(I)}$ and deduce $\underline{\hat{\mathfrak{h}}}_n^{(I)}$. The equalization and decision are made to get $\hat{C}_{m,n}^{(I)}$ and $\hat{\mathbf{s}}_n^{(I)}$.
5. Go back to step 3 and perform steps 3 and 4, with $I \leftarrow I - 1$.
6. End of the algorithm.

In order to complete the RISIC algorithm as described in [36], we propose to add a stopping criterion. Thus, we note e_r the threshold such as

$$\text{if } ||\tilde{\mathbf{u}}_n^{(I)} - \tilde{\mathbf{u}}_n^{(I-1)}||_F < e_r, \tag{3.32}$$

then the algorithm stops. Finally, the proposed algorithm is summed up by Algorithm 1.

begin
  Initialization: e_r, ;
  $I \leftarrow 0$;
  if $n = 0$ **then**
    Estimate $\hat{\mathbf{H}}_0^{(0)}$
  else
    Perform ISI cancellation

$$\tilde{\mathbf{u}}_n^{(0)} = \mathbf{u}_n - \underline{\hat{\mathbf{h}}}_{n-1}^{ISI} \hat{\mathbf{s}}_{n-1}. \tag{3.33}$$

    $I \leftarrow 1$;
    while $||\tilde{\boldsymbol{u}}_n^{(I)} - \tilde{\boldsymbol{u}}_n^{(I-1)}||_F > e_r$ **do**
      Perform the cyclic reconstruction by applying

$$\tilde{\mathbf{u}}_n^{(I)} = \tilde{\mathbf{u}}_n^{(0)} + \underline{\hat{\mathfrak{h}}}_n^{(I-1)} \hat{\mathbf{s}}_n^{(I-1)}. \tag{3.34}$$

      Obtain the symbol $\tilde{\mathbf{U}}_n^{(I)}$;
      Perform the ACA-LMMSE channel estimation $\hat{\mathbf{H}}_n^{(I)}$ and deduce $\underline{\hat{\mathfrak{h}}}_n^{(I)}$;
      Obtain $\hat{C}_{m,n}^{(I)}$ and $\hat{\mathbf{s}}_n^{(I)}$;
      $I \leftarrow I + 1$;
    end
  end
end

Algorithm 1: RISIC algorithm combined with ACA-LMMSE channel estimation.

3.5.4 Simulations Results for RISIC combined with ACA-LMMSE

Fig. 3.13 shows the impulse responses of the physical and the artificial channels versus τ/T_s. It illustrates the principle of the ACA-LMMSE applied to the RISIC algorithm. The simulations are made using the aforementioned parameters.

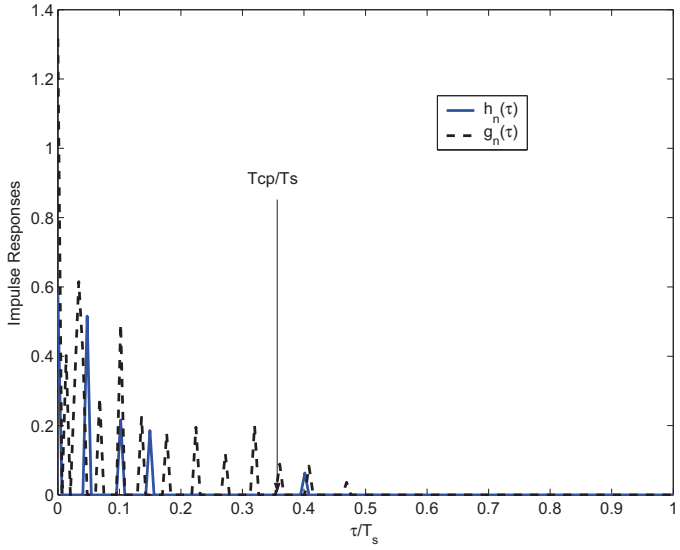

FIGURE 3.13 – Impulse responses of the physical channel $h_n(\tau)$ and the artificial channel $g_n(\tau)$.

Fig. 3.13 indeed shows that the fifth path of $h_n(\tau)$ has a delay higher than T_{CP}, which causes ISI and ICI. Moreover, the mask effect of $\mathcal{H}$ by $\mathcal{G}$ is observable through $D > L$ and $\tau_{max}^{(G)} > \tau_{max}^{(H)}$. This figure is a snapshot of the IR of $\mathcal{H}$ and $\mathcal{G}$ at a given time. Nevertheless, all the paths are time-varying, according to the model.

Fig. 3.14 depicts the BER curves of the proposed method versus E_b/N_0, for different values of the iteration number. They are compared to the curve of the transmission without ACA-LMMSE and RISIC. In that case, only the ACA-LMMSE channel estimation is performed at the receiver. No channel code is used in the simulations.

When the proposed method is not used, the BER curve reaches an error floor equal to 0.1 for high values of E_b/N_0. This high error rate is due to the interferences. Indeed, we observe that the iterative mitigation of the ISI and ICI by means of the RISIC algorithm allows to reduce a lot the BER limit. Thus, for $I = 4$, the limit is equal to 3×10^{-3}. The use of RISIC allows to divide the bit errors rate by a value greater than 30. The use of a channel code can then allows to reduce more the BER and to get a good transmission quality.

Fig. 3.15 displays the value $||\tilde{\mathbf{u}}_n^{(I)} - \tilde{\mathbf{u}}_n^{(I-1)}||_F$ versus the iteration number from $I = 1$ to $I = 4$. The curve of $||\tilde{\mathbf{u}}_n^{(I)} - \tilde{\mathbf{u}}_n^{(I-1)}||_F$ decreases and converges to zero. Thus, the threshold e_r can be chosen as small as possible, according to the expected precision. It validates the proposed possibility of using a stopping criterion to complete the RISIC algorithm [36], in addition to the combination with ACA-LMMSE.

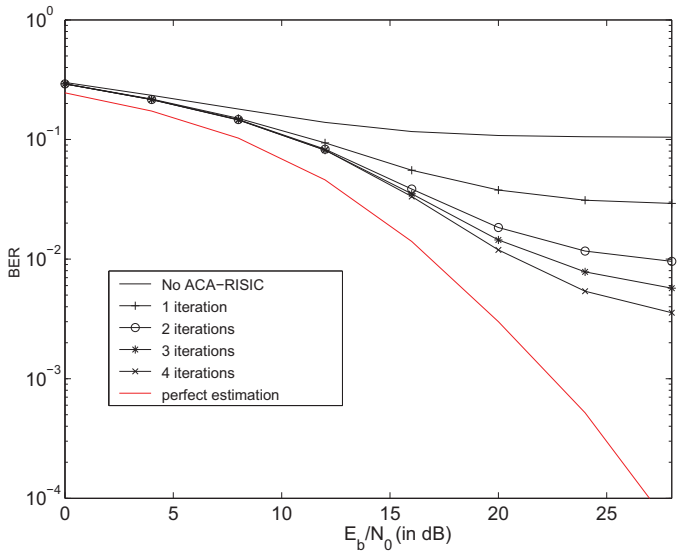

FIGURE 3.14 – BER versus E_b/N_0 of ACA-LMMSE and RISIC method.

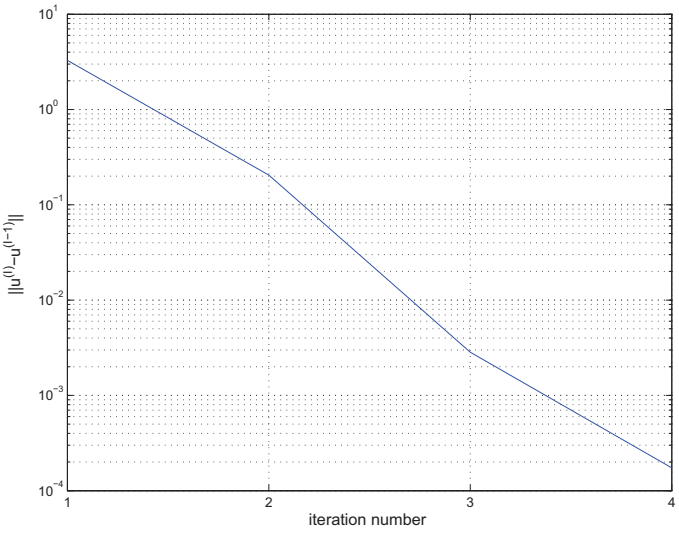

FIGURE 3.15 – $||\tilde{\mathbf{u}}_n^{(I)} - \tilde{\mathbf{u}}_n^{(I-1)}||_F$ versus the iteration number.

3.6 Conclusion

In this chapter, a channel estimation method called ACA-LMMSE has been presented [34, 35]. Its principle is to mask the impulse response of the physical channel by a filter acting like an artificial channel, in order to apply the LMMSE estimator to this hybrid channel. The artificial channel being known, it is subtracted to the hybrid channel estimation in order to keep only the physical channel estimation. This method has two advantages, compared to the usual LMMSE. First, it allows to perform an efficient estimation without any knowledge of the channel covariance matrix, nor its estimation. Indeed, the hybrid channel

LMMSE estimation can be performed by using the sole statistics of the artificial filter. Second, in a mobile environment, the complexity is reduced. Indeed, due to the variations of the channel, the covariance matrix must be updated and a matrix inversion is regularly required, which is very complex. With ACA-LMMSE, the channel covariance matrix and the matrix inversion are computed only once during the transmission. It has been shown that the practical implementation of the method can be performed by means of a simple delay line filter. Furthermore, since the estimator is independent of the channel variations, it can be used for the implementation of methods as RISIC which supposed quasi static channel. In this chapter, an ISI and ICI cancellation method is proposed. It is based on the RISIC algorithm [36], which is combined with ACA-LMMSE to make it valid in very time selective channels. In the next chapter, an other MMSE based method is presented. It differs from ACA-LMMSE in the sense that the channel covariance matrix and the noise level are supposed to be unknown, and are estimated.

Chapter 4

MMSE-based Joint Iterative SNR and Channel Estimation

4.1 Introduction

In Chapter 3, the ACA-LMMSE channel estimation method has been presented. It almost reaches the performance of LMMSE, and does not require the a priori knowledge of the channel covariance matrix. However, the noise level was supposed to be known at the receiver side. In practice, the noise variance is obviously unknown and must be estimated. In this chapter, a MMSE-based method is proposed for the joint estimation of the noise and the channel.

In addition to the multipath channel, the additive noise is another source of disturbance in wireless communications. Most of the time, the noise level is characterized by comparison with the signal power by means of the signal to noise ratio (SNR). The knowledge of the noise power is very useful in order to design the transmitter and/or the receiver. For instance, at the transmitter side, the knowledge of the SNR allows to perform adaptive modulations. As summarized in [121], the principle is to adjust the constellation in terms of kind and size, according to the SNR level. At the receiver side, the noise level is used in several algorithm, such as turbo-decoding [122], or LMMSE channel estimation [7, 15]. For this particular example, it is often assumed that the noise level is a priori known, or well estimated thanks to an existing method of the literature. We also supposed this for the ACA-LMMSE estimation presented in the last chapter. In this chapter, a method for the estimation of both SNR and channel estimation is proposed. The SNR is estimated thanks to the MMSE criterion that requires an estimation of the frequency selective channel, as it is presented afterward. Since the noise variance is required for the LMMSE channel estimation (see Chapters 2 and 3), we then notice that one estimation may be used for the other one. Thus, it seems natural to propose an iterative algorithm.

First, a simple case will be presented, in which the channel covariance matrix is supposed to be known. The solution will then be extended to a more realistic case, in which the covariance matrix has to be estimated. Finally, an application of this algorithm to the free band detection will be proposed.

4.2 SNR Estimation: State of the Art

The SNR estimation methods are all based on the same elementary scheme:

1. The noise variance estimation $\hat{\sigma}^2$ is first performed,
2. An estimation of the transmitted signal power $\hat{P}_s$ is achieved,
3. The SNR, noted ρ is finally obtained by $\hat{\rho} = \hat{P}_s/\hat{\sigma}^2$.

Alternatively, the steps 2. and 3. are sometimes replaced by the following processing:

2. The second order-moment of the received signal is estimated $\hat{M}_2 = \hat{P}_s + \hat{\sigma}^2$,
3. the SNR is estimated by $\hat{\rho} = \hat{M}_2/\hat{\sigma}^2 - 1$.

The main difference between the techniques of the literature lies in the way to estimate σ^2. A wide range of usual methods are described in [123–125]. Among them, the second- and forth-order moment (M_2M_4) estimator, is firstly mentioned in [126]. Its principle is to estimate the second order moment of the received signal U_m $M_2 = E\{U_m U_m^*\} = P_s + \sigma^2$ on one hand, and the forth order moment $M_4 = E\{(U_m U_m^*)^2\} = P_s^2 + 4P_s\sigma^2 + 2\sigma^4$ on the other hand. Then, the signal and the noise powers estimations are deduced by

$$\hat{P}_s = \sqrt{2M_2^2 - M_4} \tag{4.1}$$

$$\hat{\sigma}^2 = M_2 - \sqrt{2M_2^2 - M_4}. \tag{4.2}$$

In [125], an alternative M_2M_4 method is proposed, using a new definition of the forth order moment $M_4' = E\{(\mathfrak{Re}(U_m)^2 + \mathfrak{Im}(U_m)^2)^2\}$, where $\mathfrak{Re}(.)$ and $\mathfrak{Im}(.)$ denote the real part and the imaginary part of a complex number, respectively. The advantages of the M_2M_4 lie in the facts that it does not require any channel estimation and that it has a low complexity. However, its efficiency is degraded in the presence of frequency selective channels.

The maximum likelihood estimator (ML), whose developments are given in [19], suppose the channel to be known, or requires a high complexity, as shown in Section 2.4.1.3. In order to reduce the complexity of the ML, the expectation maximization (EM) algorithm given in [96, 99] and summarized in 2.4.1.3 is adapted for the joint channel and noise estimation in [127, 128].

The minimum mean square error (MMSE) estimator, from which the method proposed in this chapter is derived, also requires the estimation of the transmission channel. Thus, the performance of the MMSE estimation depends on the channel estimation. References such as [42, 123, 129] only derive a theoretical expression of the MMSE in which the channel is supposed to be known, but the authors do not propose any practical solution to reach it.

These usual methods can be derived in the OFDM context, as it is done by the authors of [42]. If, in addition, a frequency selective channel is considered, the literature proposes two strategies for the SNR estimation. The first one uses the previously cited methods, and requires a channel estimation. In the second one, the estimation of the channel frequency response is avoided [40, 129]. In [129], the author proposes a method for a 2×2 Multi Input Multi Output (MIMO) configuration that features a two pilot-symbols preamble and assumes that the channel coefficients are invariant over two consecutive carriers. Following a similar scheme, [40] also proposes a preamble-based method featuring two pilot symbols for the estimation of the noise variance. The received symbols in the preamble are then expressed by $\mathbf{U}_n = \underline{\mathbf{C}}_n\mathbf{H}_n + \mathbf{W}_n$ and $\mathbf{U}_{n+1} = \underline{\mathbf{C}}_{n+1}\mathbf{H}_{n+1} + \mathbf{W}_{=1}$, where $\underline{\mathbf{C}}_{n+1}\mathbf{H}_{n+1}$ is supposed to be

equal to $\underline{\mathbf{C}}_n\mathbf{H}_n$. Thus, the channel estimation is avoided because the noise variance is simply estimated by

$$\hat{\sigma}^2 = \frac{1}{2}E\{||\mathbf{U}_n - \mathbf{U}_{n+1}||^2\}. \tag{4.3}$$

Although it is an efficient method, its main drawback is the loss of data rate due to the need of a preamble composed of two pilots. This is especially the case if a preamble must be regularly inserted, as in the case of time-varying channels. In [41], the SNR is estimated by means of the properties of the channel covariance matrix. As presented in Chapter 1, the channel has a length L. Thus, its covariance matrix has L non-null eigenvalues from which M_2 is estimated and $M-L$ null eigenvalues from which σ^2 is estimated. This method is limited by the channel insufficient statistics, which degrades the estimation performance.

4.3 First Approach of the Method in a Simple Context

In this part, a theoretical approach of the algorithm is presented. In that case, the covariance matrix of the channel is supposed to be known at the receiver. This work has been published in [37]. Second, a more realistic approach, in which the channel covariance matrix is estimated, is derived in Section 4.4. This case has been covered in detail in [38,39]. Third, in a cognitive radio context, an application of this algorithm for free bands detection is presented in Section 4.5.

4.3.1 System Model

4.3.1.1 Channel Model

In the following, and unlike the channel model of Chapter 3, let us here assume a quasi static multipath channel. Thus, the pilots tones in the frame follow a block-type arrangement, as depicted in Fig. 2.3 (a). In this section, the channel covariance matrix is considered to be known at the receiver. Furthermore, two cases are taken into account:

- $\underline{\mathbf{R}}_H$ is the covariance matrix in the perfect case (called "case 1"), that is when computed by means of (1.56), i.e. $\underline{\mathbf{R}}_H = \mathbf{H}\mathbf{H}^H$,
- $\breve{\underline{\mathbf{R}}}_H$ is the covariance matrix computed by means of the statistics of the channel (1.53):

$$(\breve{\underline{\mathbf{R}}}_H)_{u,v} = \sum_{l=0}^{L-1} \int_0^{\tau_{max}} \Gamma_l(\tau) e^{-2j\pi\frac{(u-v)}{M}\tau} d\tau.$$

  This case is called "case 2". Fig. 4.1 displays the shape of a channel intensity profile, simulated according to the Robustness C parameters ($M = 148$) and for a decreasing intensity profile with $\tau_{max} = 2.2$ ms. We remind that the shape of $\Gamma(\tau)$ is also the one following by the eigenvalues of the channel when taken in the decreasing order. In that case, the $M-L$ last eigenvalues of $\breve{\underline{\mathbf{R}}}_H$ are null.

Without loss of generality, the pilots and the channel are normalized, i.e. for all pilot tones $m = 0, .., M-1$, $\mathcal{P} = C_m C_m^* = 1$, and remembering that λ_m is an eigenvalue of the channel, $\frac{1}{M}\sum_{m=0}^{M-1}\lambda_m = 1$.

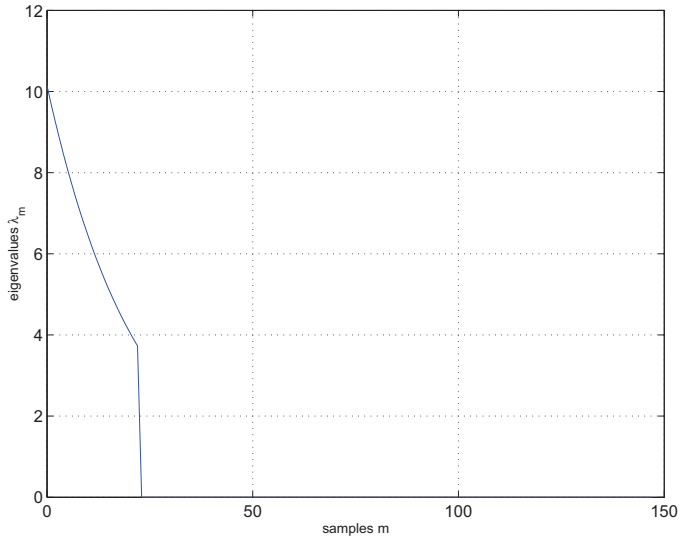

FIGURE 4.1 – Profile of the eigenvalues λ_m of the channel, with $M = 148$ and $\tau_{max} = 2.2ms$.

4.3.1.2 MMSE Noise Variance Estimation

The noise variance estimation, performed on a pilot symbol, is given by:

$$\begin{aligned}\hat{\sigma}^2 &= E\{|U_m - C_m\hat{H}_m|^2\} \\ &= \frac{1}{M}E\{||\mathbf{U} - \mathbf{C}\hat{\mathbf{H}}||_F^2\}.\end{aligned} \tag{4.4}$$

The two expressions in (4.4) are strctly equivalent, since the first line is the scalar version of the estimator and the second one is its matrix expression. As it is assumed that $\mathcal{P} = 1$, then (4.4) can be rewritten as

$$\begin{aligned}\hat{\sigma}^2 &= \frac{1}{M}E\{||\mathbf{U}\mathbf{C}^{-1} - \hat{\mathbf{H}}||_F^2\} \\ &= \frac{1}{M}E\{||\hat{\mathbf{H}}^{LS} - \hat{\mathbf{H}}||_F^2\}.\end{aligned} \tag{4.5}$$

In a more general case where $\mathcal{P} = \alpha$, we find $\hat{\sigma}^2$ from (4.5) by simply multiplying the right part of the equality by α. From the same equation, we can affirm that the more accurate the channel estimation (i.e. $\hat{\mathbf{H}}$ becoming similar to $\mathbf{H}$), the better the noise variance estimation.

4.3.2 Proposed Algorithm - Theoretical Case

4.3.2.1 Description of the Algorithm

Since the performance of the MMSE noise variance estimation in (4.5) requires an accurate channel estimation, it is proposed in [37] to use the LMMSE estimator. At the same time, the noise variance is required in this channel estimation (2.23). As the noise variance estimation feeds the channel estimation and vice versa, an iterative technique allowing a joint estimation

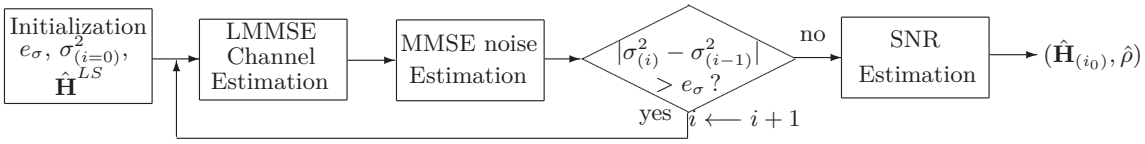

FIGURE 4.2 – Block diagram of the proposed iterative algorithm.

of the noise variance and the channel frequency response is proposed. The principle of the algorithm is depicted in Fig. 4.2.

The steps of the algorithm are given as follows and summarized by Algorithm 2. We note i the iteration index. The algorithm can be performed with the matrix $\underline{\mathbf{R}}_H$ as with $\breve{\underline{\mathbf{R}}}_H$ as well. Moreover, it is assumed that a LS estimation of the channel is performed on the preamble.

1. Initialize the noise variance so that $\hat{\sigma}^2_{(i=0)} > 0$. The inequality is strict because if the initialization $\hat{\sigma}^2_{(i=0)}$ were equal to zero, the LMMSE channel estimation would be equivalent to the LS one. If LS channel estimation were chosen to perform noise variance one in (4.5), it would lead to $\hat{\sigma}^2_{(i=1)} = 0$. In this condition, the algorithm would enter an endless loop. Furthermore, fix a stopping criterion e_σ.
   For $i \geq 1$:
2. Perform an LMMSE estimation of the channel by using
$$\hat{\mathbf{H}}^{LMMSE}_{(i)} = \underline{\mathbf{R}}_H(\underline{\mathbf{R}}_H + \hat{\sigma}^2_{(i-1)}\underline{\mathbf{I}})^{-1}\hat{\mathbf{H}}^{LS}. \tag{4.6}$$
3. For $i \geq 1$, perform the MMSE noise variance estimation $\hat{\sigma}^2_{(i)}$ with
$$\hat{\sigma}^2_{(i)} = \frac{1}{M}E\{||\hat{\mathbf{H}}^{LS} - \hat{\mathbf{H}}^{LMMSE}_{(i)}||^2\}. \tag{4.7}$$
4. While $|\hat{\sigma}^2_{(i)} - \hat{\sigma}^2_{(i-1)}| > e_\sigma$, go back to step 3 with $i \leftarrow i+1$, otherwise go to step 6.
5. Estimate the SNR $\hat{\rho}$ from the final noise variance estimation noted $\hat{\sigma}^2_{(i_0)}$:
$$\hat{\rho} = \frac{\hat{M}_2}{\hat{\sigma}^2_{(i_0)}} - 1, \tag{4.8}$$
   where (i_0) indicates the index of the last iteration.
6. End of the algorithm.

4.3.2.2 Convergence of the Algorithm

In this section, it is shown that the proposed algorithm converges, i.e. the noise variance $\hat{\sigma}^2_{(i)}$ and the channel frequency response $\hat{\mathbf{H}}^{LMMSE}_{n(i)}$ estimations converge. From (4.6), it is obvious that if $(\hat{\sigma}^2_{(i)})$ admits a limit, then $\hat{\mathbf{H}}^{LMMSE}_{(i)}$ converges to a given channel estimation. In the following, a scalar recursive expression of $\hat{\sigma}^2_{(i)}$ is derived, then the proof of the convergence of this sequence is given.

a. Scalar Expression of the Sequence $(\hat{\sigma}^2_{(i)})$

begin
  Initialization: $e_\sigma > 0$, $\hat{\sigma}^2_{(i=0)}$;
  $i \leftarrow 1$;
  while $|\hat{\sigma}^2_{(i)} - \hat{\sigma}^2_{(i-1)}| > e_\sigma$ **do**
    Perform an LMMSE channel estimation (4.6) ;
    Perform the noise variance estimation (4.7) ;
    $i \leftarrow i + 1$;
  end
  Estimate the SNR $\hat{\rho}$ (4.8) with $\hat{\sigma}^2_{(i_0)}$;
end

Algorithm 2: MMSE-based joint estimation of channel and SNR, theoretical case.

In the following, the different mathematical formulations are based on the covariance matrix $\underline{\mathbf{R}}_H$. However, the developments remain valid with $\breve{\underline{\mathbf{R}}}_H$ since it is also an Hermitian matrix. Since $\mathcal{P} = 1$, we have $\underline{\mathbf{C}}\underline{\mathbf{C}}^H = \underline{\mathbf{I}}$, and then the development of (4.7) yields

$$\begin{aligned}\hat{\sigma}^2_{(i+1)} &= \frac{1}{M} E\{||\hat{\mathbf{H}}^{LS} - \hat{\mathbf{H}}^{LMMSE}_{(i+1)}||^2_F\} \\ &= \frac{1}{M} E\{||\hat{\mathbf{H}}^{LS} - \underline{\mathbf{R}}_H(\underline{\mathbf{R}}_H + \hat{\sigma}^2_{(i)}(\underline{\mathbf{C}}\underline{\mathbf{C}}^H)^{-1})^{-1}\hat{\mathbf{H}}^{LS}||^2_F\} \\ &= \frac{1}{M} E\{||\hat{\mathbf{H}}^{LS} - \underline{\mathbf{R}}_H(\underline{\mathbf{R}}_H + \hat{\sigma}^2_{(i)}\underline{\mathbf{I}})^{-1}\hat{\mathbf{H}}^{LS}||^2_F\}. \end{aligned} \tag{4.9}$$

By noticing that $\underline{\mathbf{R}}_H = (\underline{\mathbf{R}}_H + \hat{\sigma}^2_{(i)}\underline{\mathbf{I}}) - \hat{\sigma}^2_{(i)}\underline{\mathbf{I}}$, the factorized form of (4.9) is obtained:

$$\begin{aligned}\hat{\sigma}^2_{(i+1)} &= \frac{1}{M} E\{||(\hat{\sigma}^2_{(i)}\underline{\mathbf{I}}(\underline{\mathbf{R}}_H + \hat{\sigma}^2_{(i)}\underline{\mathbf{I}})^{-1})\hat{\mathbf{H}}^{LS}||^2_F\} \\ &= \frac{1}{M} tr\left(E\{(\hat{\sigma}^2_{(i)}(\underline{\mathbf{R}}_H + \hat{\sigma}^2_{(i)}\underline{\mathbf{I}})^{-1}\hat{\mathbf{H}}^{LS})(\hat{\sigma}^2_{(i)}\underline{\mathbf{I}}(\underline{\mathbf{R}}_H + \hat{\sigma}^2_{(i)}\underline{\mathbf{I}})^{-1}\hat{\mathbf{H}}^{LS})^H\}\right). \end{aligned} \tag{4.10}$$

The sole random variable remaining in (4.10) is $\hat{\mathbf{H}}^{LS}$, so we get

$$\begin{aligned}\hat{\sigma}^2_{(i+1)} &= \frac{1}{M} tr\left((\hat{\sigma}^2_{(i)}(\underline{\mathbf{R}}_H + \hat{\sigma}^2_{(i)}\underline{\mathbf{I}})^{-1})E\{(\hat{\mathbf{H}}^{LS}(\hat{\mathbf{H}}^{LS})^H)\}(\hat{\sigma}^2_{(i)}\underline{\mathbf{I}}(\underline{\mathbf{R}}_H + \hat{\sigma}^2_{(i)}\underline{\mathbf{I}})^{-1})\right) \\ &= \frac{1}{M} tr\left(\hat{\sigma}^4_{(i)}(\underline{\mathbf{R}}_H + \hat{\sigma}^2_{(i)}\underline{\mathbf{I}})^{-1}(\underline{\mathbf{R}}_H + \sigma^2\underline{\mathbf{I}})(\underline{\mathbf{R}}_H + \hat{\sigma}^2_{(i)}\underline{\mathbf{I}})^{-1}\right). \end{aligned} \tag{4.11}$$

Since $\underline{\mathbf{R}}_H$ is an Hermitian and positive semi-definite matrix, it can be diagonalized by means of a unitary matrix $\underline{\mathbf{Q}}$ [11,15]. Moreover, whatever $\alpha \in \mathbb{C}$, it obvious that the matrix $\underline{\mathbf{R}}_H + \alpha\underline{\mathbf{I}}$ has the same eigendecomposition basis as $\underline{\mathbf{R}}_H$. One can deduce that $\underline{\mathbf{R}}_H + \sigma^2\underline{\mathbf{I}}$ and $\underline{\mathbf{R}}_H + \hat{\sigma}^2_{(i)}\underline{\mathbf{I}}$ are diagonalizable in the same basis, and we note:

$$\begin{aligned}\underline{\mathbf{D}}_H &= \underline{\mathbf{Q}}^H(\underline{\mathbf{R}}_H + \sigma^2\underline{\mathbf{I}})\underline{\mathbf{Q}}, \text{and} \\ \underline{\mathbf{D}}_{H(i)} &= \underline{\mathbf{Q}}^H(\underline{\mathbf{R}}_H + \hat{\sigma}^2_{(i)}\underline{\mathbf{I}})\underline{\mathbf{Q}}, \end{aligned} \tag{4.12}$$

where $\underline{\mathbf{D}}_H$ and $\underline{\mathbf{D}}_{H(i)}$ are diagonal matrices, whose elements are $\lambda_m + \sigma^2$ and $\lambda_m + \hat{\sigma}^2_{(i)}$, respectively. Consequently, (4.11) can be rewritten as follows:

$$\hat{\sigma}^2_{(i+1)} = \frac{1}{M} tr\left(\hat{\sigma}^4_{(i)} \underline{\mathbf{Q}} (\underline{\mathbf{D}}_{H(i)})^{-1} (\underline{\mathbf{D}}_H) (\underline{\mathbf{D}}_{H(i)})^{-1} \underline{\mathbf{Q}}^{-1}\right). \tag{4.13}$$

From (4.13), we obtain a recursive formulation of $\hat{\sigma}^2_{(i+1)}$:

$$\hat{\sigma}^2_{(i+1)} = \frac{\hat{\sigma}^4_{(i)}}{M} \sum_{m=0}^{M-1} \frac{\lambda_m + \sigma^2}{(\lambda_m + \hat{\sigma}^2_{(i)})^2}. \tag{4.14}$$

From (4.14), we notice that the sequence $(\hat{\sigma}^2_{(i+1)})$ is defined by a function f_t such as, if we set $x = \hat{\sigma}^2_{(i)}$, we have

$$f_t(x) = \frac{x^2}{M} \sum_{m=0}^{M-1} \frac{\lambda_m + \sigma^2}{(\lambda_m + x)^2}. \tag{4.15}$$

It can be seen that f_t is not defined for $x = 0$, because the minimum value of the eigenvalues is zero. Thus, f_t is defined whatever $x \in]0, +\infty]$. Furthermore, since $\sigma^2_{i=0}$ does not appear in (4.14), the sequence is independent of the initialization value.

b. Proof of Convergence

The proof of the convergence of the sequence $(\hat{\sigma}^2_{(i)})$ is based on the fixed-point theorem. It is known that the sequence $(\hat{\sigma}^2_{(i+1)})$ converges if the equation

$$f_t(x) = x \tag{4.16}$$

has at least one solution, this solution being one of the fixed point of f_t. Yet, it is known that f_t has at least a fixed point on a closed interval $[a, b]$ (a and b are defined afterward) if $f_t([a, b]) \subset [a, b]$. Moreover, the sequence $(\hat{\sigma}^2_{(i)})$ converges to one of the fixed points of f_t if it is bounded and monotonous.

We first prove that $f_t([a, b]) \subset [a, b]$. To this end, we remind that, as the channel has a length L and its covariance matrix is positive semidefinite, its eigenvalues are positive or null according to the value of m:

$$\begin{cases} \lambda_m \geq 0, & \text{if } m = 0, .., L-1 \\ \lambda_m = 0, & \text{if } m = L, .., M-1 \end{cases}. \tag{4.17}$$

From (4.15), we deduce the limits of f_t:

$$\lim_{x \to +\infty} f_t(x) = \frac{1}{M} \sum_{m=0}^{M-1} \lambda_m + \sigma^2 = M_2, \tag{4.18}$$

and

$$\lim_{x \to 0^+} f_t(x) = \frac{1}{M} \sum_{m=L}^{M-1} \sigma^2 = \frac{M-L}{M} \sigma^2. \tag{4.19}$$

As a consequence, (4.19) ensures the existence of a strictly positive value ϵ such as $\epsilon \in]0, \frac{M-L}{M}\sigma^2]$ and that verifies $f_t(\epsilon) \geq \epsilon$. Furthermore, whatever $x > 0$ the second derivative of f_t, defined by

$$f_t'(x) = \frac{2}{M} \sum_{m=0}^{M-1} \frac{\lambda_m(\lambda_m + \sigma^2)x}{(\lambda_m + x)^3}, \tag{4.20}$$

is positive, so f_t is a strictly growing function. From (4.18) and (4.19), we easily obtain that $f_t([\epsilon, +\infty[) \subset [\epsilon, M_2]$. In addition, as f_t is a strictly growing function that is upper bounded by M_2, it justifies the following inclusion:

$$f_t([\epsilon, M_2]) \subset [\epsilon, M_2], \tag{4.21}$$

proving then that f_t has at least one fixed point on the closed interval $[\epsilon, M_2]$. As it has been previously shown that f_t is strictly growing on the interval $[\epsilon, +\infty[$, the sequence $(\hat{\sigma}^2_{(i)})$ is consequently monotonous. From (4.18) and (4.19), the sequence $(\hat{\sigma}^2_{(i)})$ is also lower bounded by ϵ and upper bounded by M_2. Finally, from the fixed-point theorem, $(\hat{\sigma}^2_{(i)})$ converges to one of the fixed point of f_t. Fig. 4.3 displays the shape of f_t for three values of σ^2, and is compared to $y = x$. The eigenvalues are the ones described by Fig. 4.1. Intuitively, it seems on Fig. 4.3 that f_t has a unique fixed point, which is proportional to σ^2. In the following section, a proof of this is proposed.

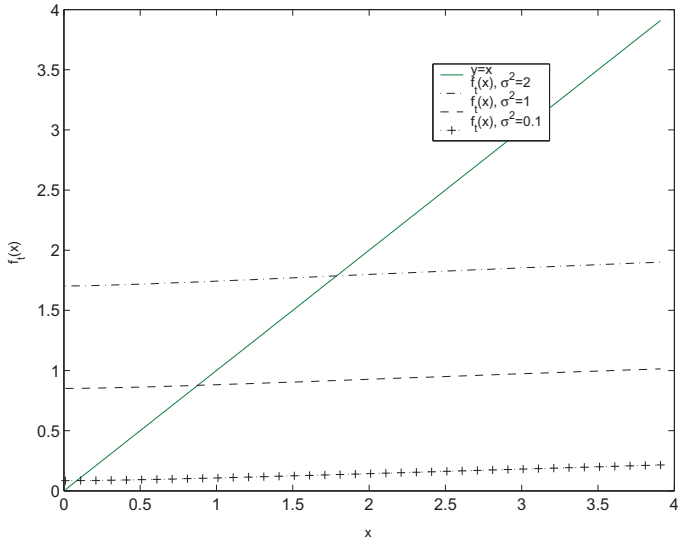

FIGURE 4.3 – Shape of $f_t(x)$ for three different values of σ^2, comparison with $y = x$.

4.3.2.3 Uniqueness of the Solution - Proof by Contradiction

a. Polynomial Expression of the Problem to Solve

In this section, we study f_t in order to prove the uniqueness of the fixed point. A proof by contradiction is used to show the uniqueness of this solution. To this end, we define the function g_t by

$$g_t(x) = f_t(x) - x. \tag{4.22}$$

Let us now assume that g_t has at least two distinct solutions for the equation $g_t(x) = 0$, written down x_1 and x_2, both in $[\epsilon, M_2]$. x_1 being different from x_2, we can fix $x_2 > x_1$.

Therefore, the equality $g_t(x_2) = g_t(x_1) = 0$ can be developed as

$$
\begin{aligned}
& g_t(x_2) = g_t(x_1) = 0 && (4.23)\\
\Leftrightarrow\ & f_t(x_2) - f_t(x_1) - (x_2 - x_1) = 0 \\
\Leftrightarrow\ & \frac{x_2^2}{M}\sum_{m=0}^{M-1}\frac{\lambda_m+\sigma^2}{(\lambda_m+x_2)^2} - \frac{x_1^2}{M}\sum_{m=0}^{M-1}\frac{\lambda_m+\sigma^2}{(\lambda_m+x_1)^2} - (x_2-x_1) = 0 \\
\Leftrightarrow\ & \frac{1}{M}\sum_{m=0}^{M-1}\frac{(\lambda_m+\sigma^2)\left(x_2^2(\lambda_m+x_1)^2 - x_1^2(\lambda_m+x_2)^2\right)}{(\lambda_m+x_2)^2(\lambda_m+x_1)^2} - (x_2-x_1) = 0 \\
\Leftrightarrow\ & \frac{1}{M}\sum_{m=0}^{M-1}\frac{(\lambda_m+\sigma^2)\left(x_2(\lambda_m+x_1)+x_1(\lambda_m+x_2)\right)\lambda_m(x_2-x_1)}{(\lambda_m+x_2)^2(\lambda_m+x_1)^2} - (x_2-x_1) = 0. && (4.24)
\end{aligned}
$$

Due to $x_2 \neq x_1$, (4.24) can be simplified to get

$$
\begin{aligned}
& \frac{1}{M}\sum_{m=0}^{M-1}\frac{(\lambda_m+\sigma^2)(x_2(\lambda_m+x_1)+x_1(\lambda_m+x_2))\lambda_m}{(\lambda_m+x_2)^2(\lambda_m+x_1)^2} - 1 = 0 \\
\Leftrightarrow\ & \frac{1}{M}\frac{\sum_{m=0}^{M-1}(\lambda_m+\sigma^2)(x_2(\lambda_m+x_1)+x_1(\lambda_m+x_2))\lambda_m\prod_{\substack{k=0\\k\neq m}}^{M-1}(\lambda_k+x_2)^2(\lambda_k+x_1)^2}{\prod_{m=0}^{M-1}(\lambda_m+x_2)^2(\lambda_m+x_1)^2} \\
& - 1 = 0, && (4.25)
\end{aligned}
$$

and the common denominator expression is obtained as

$$
\begin{aligned}
& \frac{1}{M}\frac{\sum_{m=0}^{M-1}(\lambda_m+\sigma^2)(x_2(\lambda_m+x_1)+x_1(\lambda_m+x_2))\lambda_m\prod_{\substack{k=0\\k\neq m}}^{M-1}(\lambda_k+x_2)^2(\lambda_k+x_1)^2}{\prod_{m=0}^{M-1}(\lambda_m+x_2)^2(\lambda_m+x_1)^2} \\
& - \frac{M\prod_{m=0}^{M-1}(\lambda_m+x_2)^2(\lambda_m+x_1)^2}{M\prod_{m=0}^{M-1}(\lambda_m+x_2)^2(\lambda_m+x_1)^2} = 0. && (4.26)
\end{aligned}
$$

The solutions of (4.26) are the roots of its numerator, so we reduce the study to:

$$
\begin{aligned}
& \sum_{m=0}^{M-1}\lambda_m(\lambda_m+\sigma^2)(x_2(\lambda_m+x_1)+x_1(\lambda_m+x_2))\prod_{\substack{k=0\\k\neq m}}^{M-1}(\lambda_k+x_2)^2(\lambda_k+x_1)^2 \\
& - M\prod_{m=0}^{M-1}(\lambda_m+x_2)^2(\lambda_m+x_1)^2 = 0 \\
\Leftrightarrow\ & \sum_{m=0}^{M-1}\left(\lambda_m(\lambda_m+\sigma^2)(x_2(\lambda_m+x_1)+x_1(\lambda_m+x_2)) - (\lambda_m+x_2)^2(\lambda_m+x_1)^2\right) \\
& \times\prod_{\substack{k=0\\k\neq m}}^{M-1}(\lambda_k+x_2)^2(\lambda_k+x_1)^2 = 0. && (4.27)
\end{aligned}
$$

In order to show that f_t has a sole fixed point, it must be shown that the unique solution of (4.23) is $x_1 = x_2$. Equivalently, we show that Eq. (4.27) has no solution, whatever the values

of x_1, x_2, λ_m and σ^2. To this end, since $\forall m = 0, 1, ..., M-1$, $\prod_{\substack{k=0 \\ k \neq m}}^{M-1} (\lambda_k + x_2)^2 (\lambda_k + x_1)^2$ is strictly positive it is possible to reduce the study to the polynomial form P defined by

$$P(x_1, x_2, \lambda_m, \sigma^2) = \lambda_m(\lambda_m + \sigma^2)(x_2(\lambda_m + x_1) + x_1(\lambda_m + x_2)) - (\lambda_m + x_2)^2(\lambda_m + x_1)^2. \quad (4.28)$$

If it is proved that $P(x_1, x_2, \lambda_m, \sigma^2)$ has the same sign whatever $m = 0, 1, ..., M-1$, then (4.26) has no root. Thus, the only solution in (4.24) would be $x_2 = x_1$, which contradicts the very first assumption $x_1 \neq x_2$. In the following, the sign of the obtained polynomial is derived according to the both possible natures of the channel covariance matrix (see Section 4.3.1.1).

b. Sign of the Polynomial Considering $\underline{\mathbf{R}}_H$

Firstly, let us consider the case 1, i.e. the channel covariance matrix is $\underline{\mathbf{R}}_H = \mathbf{H}\mathbf{H}^H$. The rank of this matrix is the one of the vector $\mathbf{H}$, i.e. its rank is equal to one. As a consequence, the $M-1$ last eigenvalues $\lambda_1, ..., \lambda_{M-1}$ of $\underline{\mathbf{R}}_H$ are null. In this case, for all $m = 1, ..., M-1$, the expression of the polynomial $P(x_1, x_2, 0, \sigma^2)$ is simplified as

$$P(x_1, x_2, 0, \sigma^2) = -x_2^2 x_1^2. \quad (4.29)$$

Since x_1 and x_2 are strictly positive, we deduce that whatever $m = 1, ..., M-1$, the polynomial $P(x_1, x_2, 0, \sigma^2)$ is negative. For the non-null eigenvalue λ_0, we use elementary physical considerations to prove that the polynomial $P(x_1, x_2, \lambda_0, \sigma^2)$ is also negative. Indeed, the channel is normalized so that

$$\frac{1}{M} \sum_{m=0}^{M-1} \lambda_m = \frac{\lambda_0}{M} = 1. \quad (4.30)$$

Therefore, we have $\lambda_0 = M$, and by reminding that M is the DFT size, we have $M >> 1$. Thus, we can reasonably suppose that we consider a range of values of noise variance such as $\sigma^2 << \lambda_0$. In such conditions, we get the equivalence $P(x_1, x_2, \lambda_m, \sigma^2) \sim -\lambda_0^4 = -M^4$. We conclude that whatever $m = 0, ..., M-1$, the polynomial $P(x_1, x_2, \lambda_m, \sigma^2)$ is negative. We finally conclude that the only solution in (4.24) is $x_1 = x_2$, that is f_t has a sole fixed point.

c. Sign of the Polynomial Considering $\breve{\underline{\mathbf{R}}}_H$

In the case 2, the channel covariance matrix $\breve{\underline{\mathbf{R}}}_H$ is considered. The problem is slightly more complex because $\breve{\underline{\mathbf{R}}}_H$ has rank L. The $M-L$ last eigenvalues are null, so we naturally find again $P(x_1, x_2, 0, \sigma^2) = -x_2^2 x_1^2$ for $m = L, .., M-1$. For the L non-null eigenvalues $\lambda_0, .., \lambda_{L-1}$, the proof is based on an empirical observation. For the need of the proof, let us consider the channel described by Fig. 4.1. It appears that one fixed point (x_2 for instance) of f_t is roughly proportional to σ^2, such as we can note $x_2 = \alpha\sigma^2$. Since it is supposed that $x_1 \neq x_2$, and as x_1 and x_2 play the same role in 4.28, two scenarios can be considered: $x_1 < x_2$ or $x_1 > x_2$. These two cases are shown on Fig. 4.4, which displays the polynomial $P(\sigma^2)$ versus the SNR, for $x_2/x_1 = 10$ and $x_2/x_1 = 0.1$, and for a fixed value α equal to 0.9. Furthermore, $P(\sigma^2)$ is drawn for the lowest and the highest eigenvalues of $\breve{\underline{\mathbf{R}}}_H$, that is $\lambda_0 = 10.1$ and $\lambda_{L-1} = 3.71$.

Fig. 4.4 (a) clearly shows that $P(\sigma^2)$ is strictly negative, whatever x_2/x_1 value, and for the two different eigenvalues. It is reasonable to suppose that it is also valid whatever the eigenvalue λ_m, $m = 0, .., L-1$. Despite these empirical assumptions, we can conclude that $P(x_1, x_2, \lambda_m, \sigma^2) < 0$ for all $m = 0, .., L-1$, and then the only solution is $x_1 = x_2$, which

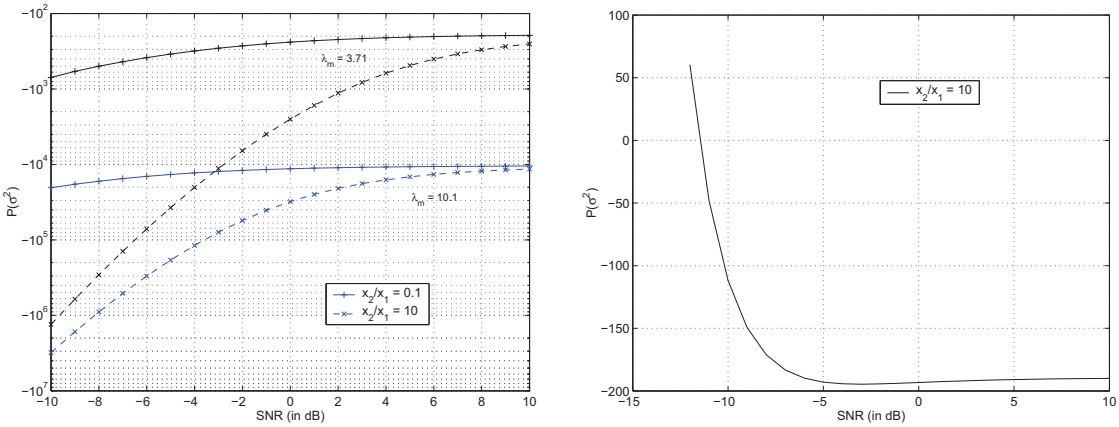

(a) Shape of $P(\sigma^2)$ for two values of x_2/x_1, and for two values of λ_m

(b) Shape of $P(\sigma^2)$ for $x_2 = 0.09$ of $x_2/x_1 = 10$

FIGURE 4.4 – Shapes of $P(\sigma^2)$ in a good and a bad scenario.

proves that the fixed point of f_t is unique. It is nevertheless possible to find scenarios that lead to the opposite observation. For instance, 4.4 (b) displays $P(\sigma^2)$ drawn with $\alpha = 0.09$, $x_2/x_1 = 10$ and $\lambda_m = 3.71$. In that scenario, it is possible to get $P(x_1, x_2, \lambda_m, \sigma^2) = 0$, so it is impossible to prove that the equality (4.27) is not valid. However, it is a very particular case, in which x_1 and x_2 have very low values, which would correspond to a very bad noise variance estimator. Thus, by supposing that the noise estimation is well performed, it naturally leads to the fact that the algorithm converges to a unique solution.

4.3.2.4 Estimation of the Bias of the Noise Estimation

The bias of the noise variance estimation is now derived when the algorithm is performed with the exact covariance matrix $\underline{\mathbf{R}}_H = \mathbf{H}\mathbf{H}^H$. The bias, noted $B(\hat{\sigma}^2)$, is defined by

$$B(\hat{\sigma}^2) = \hat{\sigma}^2 - \sigma^2. \tag{4.31}$$

When the algorithm reaches its limit, i.e. i tends to infinity, we have $\hat{\sigma}^2 = f_t(\hat{\sigma}^2)$. Remembering that the channel covariance matrix $\underline{\mathbf{R}}_H$ has rank one and that $\lambda_0 = M$, (4.31) is expressed by

$$\begin{aligned} B(\hat{\sigma}^2) &= f_t(\hat{\sigma}^2) - \sigma^2 \\ &= \frac{M-1}{M}\sigma^2 + \frac{\hat{\sigma}^4(\lambda_0 + \sigma^2)}{M(\lambda_0 + \hat{\sigma}^2)^2} \\ &= \frac{-\sigma^2(M + \hat{\sigma}^2)^2 + \hat{\sigma}^4(M + \sigma^2)}{M(M + \hat{\sigma}^2)^2}. \end{aligned} \tag{4.32}$$

For a sufficiently large value of M, we can approximate the bias (4.32) by $B(\hat{\sigma}^2) \approx -\frac{\sigma^2}{M}$. One can notice that the larger M, the more accurate the approximation. We will check the accuracy of the approximation $B(\hat{\sigma}^2) \approx -\frac{\sigma^2}{M}$ in the next section.

4.3.3 Simulations Results - Theoretical Approach

The signal parameters used for the simulations are the ones given by Table 3.2 in Chapter 3. However, in this chapter, it is considered a block-type pilot arrangement. The channel is based on the *US Consortium* model of the DRM/DRM+ standard [1], whose path gains are normalized. The channel parameters are summed up in Table 4.1.

TABLE 4.1 – Table of parameters of the channel model.

Channel model				
	path 1	path 2	path 3	path 4
delay	0 ms	0.7 ms	1.5 ms	2.2 ms
gain	0.7448	0.5214	0.3724	0.1862

4.3.3.1 Convergence of the Noise Variance Estimation

Figs. 4.5 (a) and (b) display the noise variance estimations in cases 1 and 2 (for $\underline{\mathbf{R}}_H$ and $\breve{\underline{\mathbf{R}}}_H$, respectively) versus the number of iterations, and compare it to the exact value of the noise variance. The simulations are performed with $\rho = 0$ dB and $\rho = 10$ dB, in order to show the validity of the method for any SNR values. The initialization value is first chosen to be low $\hat{\sigma}^2_{(i=0)} = 0.1$ on Fig. 4.5 (a), and larger $\hat{\sigma}^2_{(i=0)} = 2$ on Fig. 4.5 (b). The curves are obtained after 7000 simulation runs.

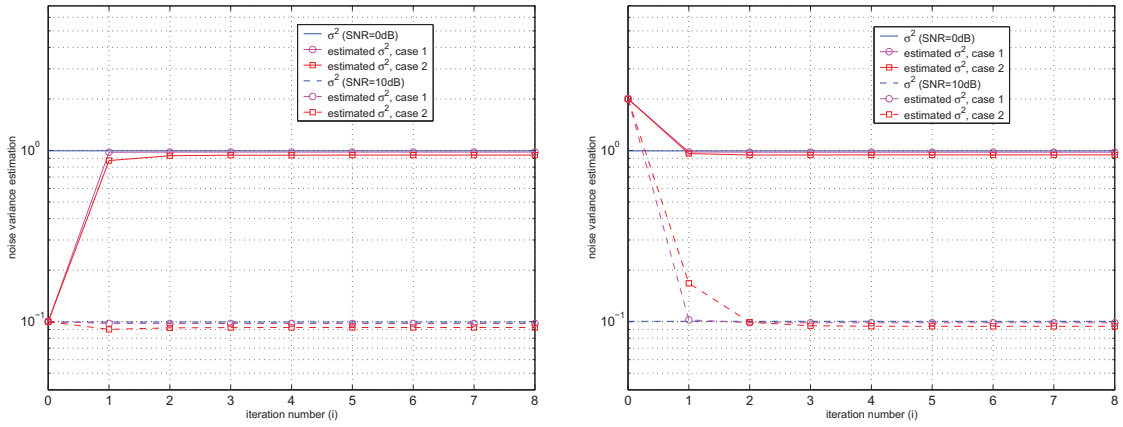

(a) $\sigma^2_{(i=0)} = 0.1$ (b) $\sigma^2_{(i=0)} = 2$

FIGURE 4.5 – Noise variance estimation versus the number of iterations, in cases 1 and 2.

Fig. 4.5 shows the convergence of the noise variance estimation, whatever the SNR and the initialization values. It validates that $(\sigma^2_{(i)})$ is monotonous, independent of the initialization value and converges to a unique solution, close to the exact noise variance.

4.3.3.2 Speed of Convergence of the Algorithm

Fig. 4.6 depicts the absolute difference $|\hat{\sigma}^2_{(i)} - \hat{\sigma}^2_{(i-1)}|$ versus the number of iterations starting from $i = 2$, in cases 1 and 2. Simulations are performed with the parameters $\rho = 10$

dB and the initialization value $\hat{\sigma}^2_{(i=0)} = 2$. These curves allow characterizing the required number of iterations to get an expected threshold value e_σ.

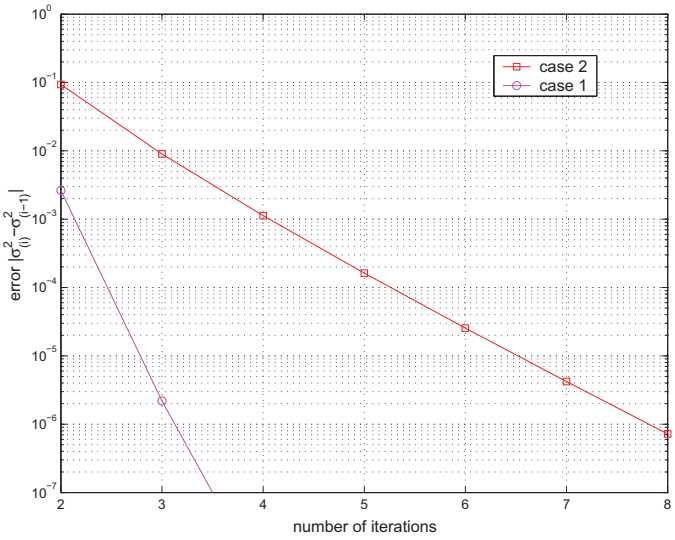

FIGURE 4.6 – Absolute difference between two consecutive noise variance estimations $|\sigma^2_{(i)} - \sigma^2_{(i-1)}|$, for $\rho = 10$ dB and $\hat{\sigma}^2_{(i=0)} = 2$.

The algorithm has a high speed convergence. Indeed, for instance, for a given threshold $e_\sigma = 0.01$, only two iterations are needed in case 1 and three iterations in case 2. Furthermore, we notice in Fig. 4.6 that the value of $|\hat{\sigma}^2_{(i)} - \hat{\sigma}^2_{(i-1)}|$ seems to be almost linear and converges to zero. These results confirm the monotony and the high speed of convergence of the proposed algorithm.

4.3.3.3 Bias of the Noise Variance Estimation

Fig. 4.7 displays the bias of the noise variance estimation $B(\hat{\sigma}^2) = \hat{\sigma}^2 - \sigma^2$ versus the FFT size. We then go beyond the scope of the transmission context described in Table 3.2, since the FFT size varies from $M = 64$ to $M = 1024$. Furthermore, $B(\hat{\sigma}^2)$ is compared to $-\frac{\sigma^2}{M}$ in order to validate the approximation $B(\hat{\sigma}^2) \approx -\frac{\sigma^2}{M}$. The curves are drawn for $\rho = 10$ dB, and the estimated bias values are obtained after averaging out 1000 simulation runs.

We observe that the bias is non null whatever the FFT size. However, the bias has a very low value: above -0.03 for $M = 64$ and until -0.0025 for $M = 1024$. Furthermore, Fig. 4.7 shows that the approximation $B(\hat{\sigma}^2) \approx -\frac{\sigma^2}{M}$ is accurate for high values of M. Indeed, the value of the error $-\frac{\sigma^2}{M} - B(\hat{\sigma}^2)$ is less than 0.025 for $M = 64$ and less than 0.002 for $M = 1024$.

4.3.3.4 Comparison of SNR Estimation to Other Methods

Fig. 4.8 depicts the normalized mean square error (NMSE) of the SNR estimations as a function of the SNR. The proposed algorithm in cases 1 and 2 is compared to Ren's method [40], Xu's method [41] and the usual M_2M_4 method. We remind that Ren's method requires a couple of pilot-symbols in the preamble in order to avoid the effect of the frequency

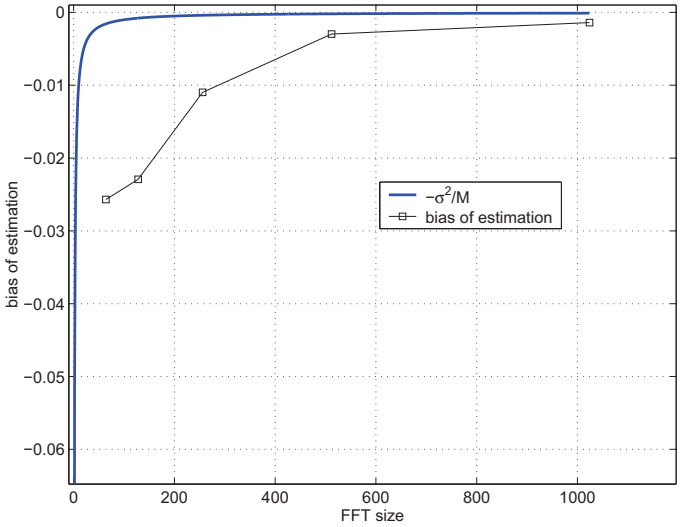

FIGURE 4.7 – Bias of the estimation $B(\hat{\sigma}^2)$ versus the FFT size, compared with $-\frac{\sigma^2}{M}$.

selective channel. Xu's method requires a single pilot-symbol preamble in order to compute the covariance matrix of the channel. The M_2M_4 method directly computes the SNR estimation thanks to the second moment-order M_2 and the fourth moment-order M_4 of the received signal. For a 16-QAM in a Rayleigh fading channel, [42] gives the estimation of the SNR as

$$\hat{\rho} = (\sqrt{M_4 - 2M_2^2})/(0.8M_2^2 - \sqrt{M_4 - 2M_2^2}). \tag{4.33}$$

To get Fig. 4.8, the initialization value is $\hat{\sigma}^2_{(i=0)} = 0.1$ and the algorithm runs until $i = 3$. The NMSE whose expression is $NMSE = E\{|\hat{\rho} - \rho|^2/\rho^2\}$, is approximated by an average on 200000 samples.

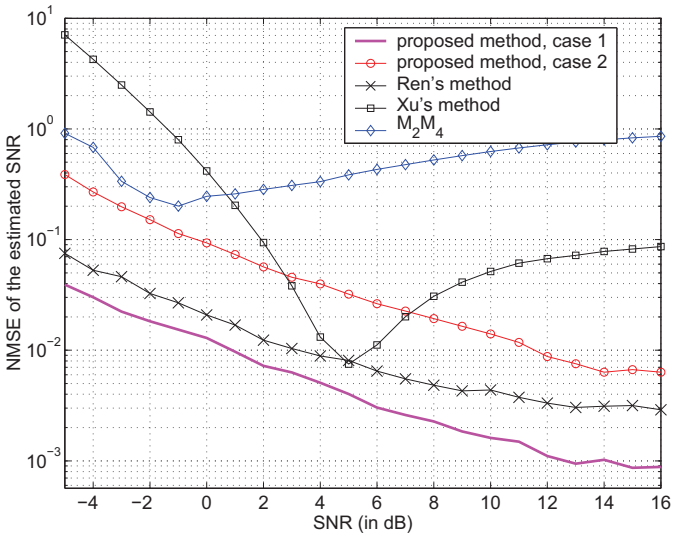

FIGURE 4.8 – NMSE of the SNR estimation of the proposed method compared to three existing methods.

The shapes of the curves of Ren's and Xu's estimation methods match with those in [40]. Furthermore, as mentioned in [42], the performance of the M_2M_4 method is degraded in Rayleigh fading channels, which is also the case here. Then, the proposed method outperforms the usual M_2M_4 for all SNR values. The theoretical case (case 1) has a lower NMSE than Ren's method (that outperforms Xu's method), due to the use of a perfect channel covariance matrix. In case 2, Ren's method has a lower NMSE than the proposed algorithm, due to the approximation of the covariance matrix, but Ren's method requires twice more pilot symbols. On the other hand, the proposed algorithm yields a globally lower NMSE than Xu's method, except for SNR values between 3 and 7 dB. Xu's method as well as the proposed one require only one pilot symbol, so the proposed algorithm is globally more precise for the same useful bit rate. Furthermore, the proposed method also performs a channel estimation, whose efficiency is studied in the next section.

4.3.3.5 Channel Estimation

Fig. 4.9 displays the BER of the proposed method versus the SNR over a relevant span of its values (from 0 to 32 dB). Cases 1 and 2 are considered, and compared to the usual least square and the perfect estimations. The initialization noise value is set like previously, i.e. $\hat{\sigma}^2_{(i=0)} = 0.1$. The BER curves are performed thanks to 2.5×10^6 bits. A zoom is added in order to display in a more precise way the BER curves that may appear as merged.

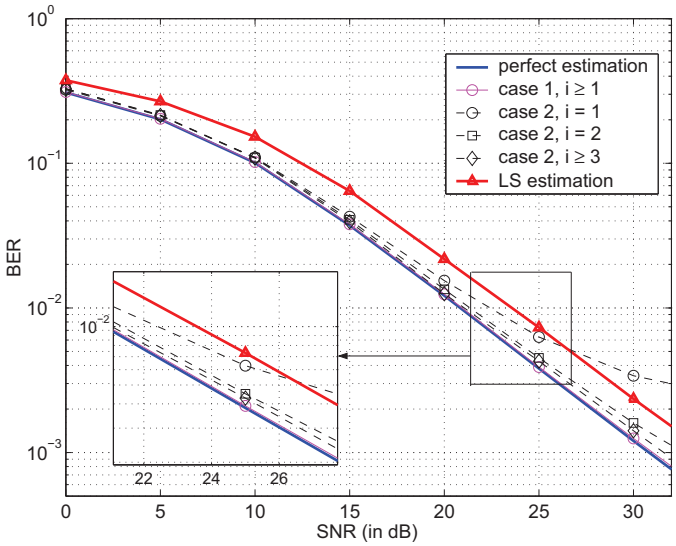

FIGURE 4.9 – BER versus SNR for the proposed method compared with perfect estimation and LS one.

Simulation in Fig. 4.9 show that the channel estimation converges. In case 1, the estimation reaches its limit at the first iteration, which tallies with the convergence speed of the noise variance estimation shown in Fig. 4.8. For a SNR value equal to 25 dB, the error of case 1 compared to the perfect estimation is less than 0.1 dB. For case 2, the channel estimation reaches its limit at $i = 3$, which also tallies with the necessary iterations number to ensure that $(\hat{\sigma}^2_{(i)})$ converges. For a SNR value equal to 25 dB, the error in case 2 compared to the perfect estimation is less than 0.5 dB. Furthermore, the proposed iterative method is more efficient than the regular LS estimation. Indeed, for SNR=25 dB, the error of the LS

estimation compared to the proposed method in case 2 is equal to 2.5 dB. Contrary to the previous chapter, the LS estimation does not reach a BER limit. This is because a pilot preamble arrangement is here used, so no interpolation is required.

4.4 Realistic Approach of the Joint estimation

In this section, a scenario in which the covariance matrix is a priori unknown is considered. As a consequence, this case is called realistic approach, by contrast with the theoretical case of the previous section. The algorithm, performed in this realistic context, has been presented in [38, 39].

4.4.1 Proposed Algorithm - Realistic Case

In the practical case, neither the matrix $\underline{\mathbf{R}}_H$ nor $\breve{\underline{\mathbf{R}}}_H$ is available at the receiver side. Thus, the channel covariance matrix must be estimated, by means of the vector of the estimated channel frequency response. This estimated matrix is noted $\tilde{\underline{\mathbf{R}}}_H$. The algorithm, performed in this realistic case, is described by Fig. 4.10 and its steps are detailed in the following.

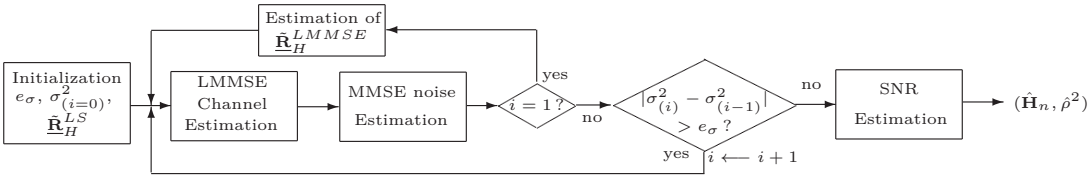

FIGURE 4.10 – Block diagram of the iterative algorithm in the realistic scenario.

1. At the beginning, only the LS channel estimation $\hat{\mathbf{H}}^{LS}$ performed on a pilot preamble is available, so the only way to estimate the covariance matrix denoted $\tilde{\underline{\mathbf{R}}}_H^{LS}$ is

$$\tilde{\underline{\mathbf{R}}}_H^{LS} = \hat{\mathbf{H}}^{LS}(\hat{\mathbf{H}}^{LS})^H. \tag{4.34}$$

   Furthermore, a stopping criterion e_σ is fixed.

2. At the first step ($i = 1$) of the algorithm, the LMMSE channel estimation is performed with $\tilde{\underline{\mathbf{R}}}_H^{LS}$:

$$\hat{\mathbf{H}}_{(i=1)}^{LMMSE} = \tilde{\underline{\mathbf{R}}}_H^{LS}(\tilde{\underline{\mathbf{R}}}_H^{LS} + \hat{\sigma}^2_{(i=0)}\underline{\mathbf{I}})^{-1}\hat{\mathbf{H}}^{LS}, \tag{4.35}$$

   where $\hat{\sigma}^2_{(i=0)}$ still points out the initialization value of the noise variance.

3. The noise variance is then estimated as previously, with $\hat{\mathbf{H}} = \hat{\mathbf{H}}_{(i=1)}^{LMMSE}$. Remembering that the pilots are normalized, $\underline{\mathbf{C}}\underline{\mathbf{C}}^H$ is equal to the identity matrix $\underline{\mathbf{I}}$, so it yields:

$$\begin{aligned}\hat{\sigma}^2_{(i=1)} &= \frac{1}{M}E\{||\mathbf{U} - \underline{\mathbf{C}}\hat{\mathbf{H}}_{(i=1)}^{LMMSE}||^2\} \\ &= \frac{1}{M}E\{||\hat{\mathbf{H}}^{LS} - \hat{\mathbf{H}}_{(i=1)}^{LMMSE}||^2\}.\end{aligned} \tag{4.36}$$

If the algorithm keeps on computing with $\underline{\tilde{\mathbf{R}}}_H^{LS}$, Appendix B.1 proves that $(\hat{\sigma}^2_{(i)})$ converges to zero. Under this condition, the algorithm enters into an endless loop. This is due to the fact that $\underline{\tilde{\mathbf{R}}}_H^{LS}$ is sensitive to the noise. In order to obtain a more accurate channel covariance matrix, it is now possible to use $\hat{\mathbf{H}}_{(i=1)}^{LMMSE}$, such as

$$\underline{\tilde{\mathbf{R}}}_H^{LMMSE} = \hat{\mathbf{H}}_{(i=1)}^{LMMSE}(\hat{\mathbf{H}}_{(i=1)}^{LMMSE})^H. \tag{4.37}$$

4. For $i \geq 2$, the iterative estimation steps (4.35) and (4.37) are performed by using (4.37):

$$\hat{\mathbf{H}}_{(i)}^{LMMSE} = \underline{\tilde{\mathbf{R}}}_H^{LMMSE}(\underline{\tilde{\mathbf{R}}}_H^{LMMSE} + \hat{\sigma}^2_{(i-1)}\underline{\mathbf{I}})^{-1}\hat{\mathbf{H}}^{LS}, \tag{4.38}$$

$$\hat{\sigma}^2_{(i)} = \frac{1}{M}E\{||\hat{\mathbf{H}}^{LS} - \hat{\mathbf{H}}_{(i)}^{LMMSE}||^2\}. \tag{4.39}$$

The characterization of the initialization $\hat{\sigma}^2_{(i=0)}$ will be discussed afterward. However, it is already obvious that $\hat{\sigma}^2_{(i=0)}$ must be strictly positive, otherwise $\hat{\mathbf{H}}_{(i)}^{LMMSE} = \hat{\mathbf{H}}^{LS}$ in (4.38). In that case, $\hat{\sigma}^2_{(i)} = 0$, and the algorithm enters into an endless loop.

5. While $|\hat{\sigma}^2_{(i)} - \hat{\sigma}^2_{(i-1)}| > e_\sigma$, go back to step 4 with $i \leftarrow i+1$, otherwise go to step 6.

6. At last, the final iteration is noted (i_0), and the SNR is estimated from the noise variance thanks to

$$\hat{\rho} = \frac{\hat{M}_2}{\hat{\sigma}^2_{(i_0)}} - 1. \tag{4.40}$$

7. End of the algorithm.

The algorithm derived for the realistic scenario in which an unknown channel covariance matrix is assumed, is summarized in Algorithm 3.

Fig. 4.11 depicts the way our algorithm works. It remains valid for both the theoretical and the realistic scenarios. The joint estimation of the couple $(\hat{\mathbf{H}}_{(i)}, \hat{\sigma}^2_{(i)})$ is depicted on a Cartesian system. From the initialization $\hat{\sigma}^2_{(i=0)}$, the noise variance and channel estimations alternatively feed each other until the algorithm reaches its limit $(\hat{\mathbf{H}}_{i_0}, \hat{\sigma}^2_{i_0})$. Note that this couple is different from the couple $(\mathbf{H}, \sigma^2)$, that characterizes the perfect estimation. This very low bias of estimation will be more precisely measured afterward.

4.4.2 Convergence of the Algorithm

In this section, the convergence of the proposed solution is proved, when an appropriate choice of the initialization $\hat{\sigma}^2_{(i=0)}$ is done. To this end, a necessary and sufficient condition on $\hat{\sigma}^2_{(i=0)}$ is given, and an optimal choice is proposed. As previously explained, if the convergence of the noise variance is proved, it is then obvious that the channel estimation also converges, i.e. the algorithm converges.

begin
- Initialization: $\underline{\tilde{\mathbf{R}}}_H^{LS}$, $e_\sigma > 0$, $\hat{\sigma}^2_{(i=0)}$;
- $i \leftarrow 1$;
- **while** $|\hat{\sigma}^2_{(i)} - \hat{\sigma}^2_{(i-1)}| > e_\sigma$ **do**
  - **if** *i = 1* **then**
    - Perform LMMSE channel estimation (4.35) ;
    - Perform the noise variance estimation (4.36) ;
    - Calculate the matrix $\underline{\tilde{\mathbf{R}}}_H^{LMMSE}$ (4.37) ;
  - **else**
    - Perform an LMMSE channel estimation (4.38) ;
    - Perform the noise variance estimation (4.39) ;
  - **end**
  - $i \leftarrow i + 1$;
- **end**
- Estimate the SNR $\hat{\rho}$ (4.40) with $\hat{\sigma}^2_{(i_0)}$;

end

Algorithm 3: MMSE-based joint estimation of both channel and SNR given in the realistic scenario.

4.4.2.1 Scalar Expression of the Sequence $(\hat{\sigma}^2_{(i)})$

Firstly, as it has been done in the previous section for the theoretical case, a scalar expression of the sequence $(\hat{\sigma}^2_{(i)})$ is derived. Whatever $i \geq 2$, by inserting (4.38) into (4.39), the noise variance estimation is developed as follows

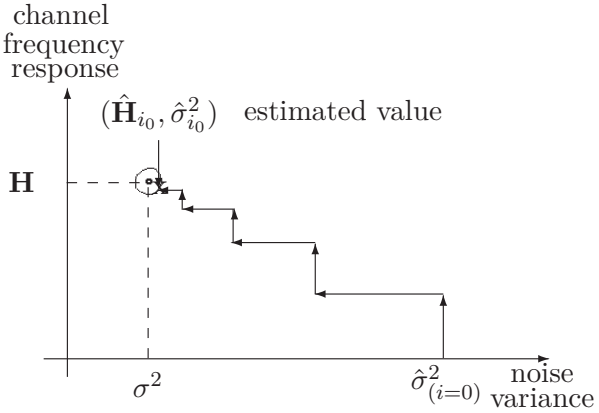

FIGURE 4.11 – Principle of the proposed iterative algorithm.

$$\begin{aligned}\hat{\sigma}^2_{(i+1)} &= \frac{1}{M}E\{||\hat{\mathbf{H}}^{LS} - \hat{\mathbf{H}}^{LMMSE}_{(i+1)}||^2_F\} \\ &= \frac{1}{M}E\{||\hat{\mathbf{H}}^{LS} - \tilde{\underline{\mathbf{R}}}^{LMMSE}_H(\tilde{\underline{\mathbf{R}}}^{LMMSE}_H + \hat{\sigma}^2_{(i-1)}\underline{\mathbf{I}})^{-1}\hat{\mathbf{H}}^{LS}||^2_F\} \\ &= \frac{1}{M}tr\left(\hat{\sigma}^4_{(i)}(\tilde{\underline{\mathbf{R}}}^{LMMSE}_H + \hat{\sigma}^2_{(i)}\underline{\mathbf{I}})^{-1}(\underline{\mathbf{R}}_H + \sigma^2\underline{\mathbf{I}})(\tilde{\underline{\mathbf{R}}}^{LMMSE}_H + \hat{\sigma}^2_{(i)}I)^{-1}\right). \quad (4.41)\end{aligned}$$

The third line of (4.41) is coming from the second one by simply noticing that $\tilde{\underline{\mathbf{R}}}^{LMMSE}_H = (\tilde{\underline{\mathbf{R}}}^{LMMSE}_H + \hat{\sigma}^2_{(i-1)}\underline{\mathbf{I}}) - \hat{\sigma}^2_{(i-1)}\underline{\mathbf{I}}$. The matrix $\tilde{\underline{\mathbf{R}}}^{LMMSE}_H$ is now expressed, assuming that it is computed after the first iteration (4.37), as

$$\begin{aligned}\tilde{\underline{\mathbf{R}}}^{LMMSE}_H &= \frac{1}{M}\hat{\mathbf{H}}^{LMMSE}_{(i=1)}(\hat{\mathbf{H}}^{LMMSE}_{(i=1)})^H \\ &= (\tilde{\underline{\mathbf{R}}}^{LS}_H(\tilde{\underline{\mathbf{R}}}^{LS}_H + \hat{\sigma}^2_{(i=0)}\underline{\mathbf{I}})^{-1}\hat{\mathbf{H}}^{LS})(\tilde{\underline{\mathbf{R}}}^{LS}_H(\tilde{\underline{\mathbf{R}}}^{LS}_H + \hat{\sigma}^2_{(i=0)}\underline{\mathbf{I}})^{-1}\hat{\mathbf{H}}^{LS})^H \\ &= \tilde{\underline{\mathbf{R}}}^{LS}_H(\tilde{\underline{\mathbf{R}}}^{LS}_H + \hat{\sigma}^2_{(i=0)}\underline{\mathbf{I}})^{-1}\hat{\mathbf{H}}^{LS}(\hat{\mathbf{H}}^{LS})^H(\tilde{\underline{\mathbf{R}}}^{LS}_H(\tilde{\underline{\mathbf{R}}}^{LS}_H + \hat{\sigma}^2_{(i=0)}\underline{\mathbf{I}})^{-1})^H. \quad (4.42)\end{aligned}$$

For a sufficiently large value of M, we consider that $\frac{1}{M}tr(\tilde{\underline{\mathbf{R}}}^{LS}_H) = \frac{1}{M}tr(\underline{\mathbf{R}}_H + \sigma^2\underline{\mathbf{I}})$. Since the estimation of the noise variance is calculated thanks to the trace in (4.41), we make the assumption that, as a first approximation:

$$\tilde{\underline{\mathbf{R}}}^{LS}_H = \hat{\mathbf{H}}^{LS}_p(\hat{\mathbf{H}}^{LS}_p)^H \approx \underline{\mathbf{R}}_H + \sigma^2\underline{\mathbf{I}}. \quad (4.43)$$

Finally, the expression of $\tilde{\underline{\mathbf{R}}}^{LMMSE}_H$ is given by inserting (4.43) into (4.42):

$$\tilde{\underline{\mathbf{R}}}^{LMMSE}_H = (\underline{\mathbf{R}}_H+\sigma^2\underline{\mathbf{I}})(\underline{\mathbf{R}}_H+(\sigma^2+\hat{\sigma}^2_{(i=0)})\underline{\mathbf{I}})^{-1}(\underline{\mathbf{R}}_H+\sigma^2\underline{\mathbf{I}})(\underline{\mathbf{R}}_H+(\sigma^2+\hat{\sigma}^2_{(i=0)})\underline{\mathbf{I}})^{-1}(\underline{\mathbf{R}}_H+\sigma^2\underline{\mathbf{I}}). \quad (4.44)$$

Once more, since whatever $\alpha \in \mathbb{C}$, the matrix $\underline{\mathbf{R}}_H + \alpha\underline{\mathbf{I}}$ has the same eigendecomposition basis as $\underline{\mathbf{R}}_H$, one can deduce that $(\underline{\mathbf{R}}_H + \sigma^2\underline{\mathbf{I}})$, $(\underline{\mathbf{R}}_H + \hat{\sigma}^2_{(i)}\underline{\mathbf{I}})$ and $\underline{\mathbf{R}}_H + (\sigma^2 + \hat{\sigma}^2_{(i=0)})\underline{\mathbf{I}}$ are diagonalizable in the same basis:

$$\begin{aligned}\underline{\mathbf{D}}_H &= \underline{\mathbf{Q}}^H(\underline{\mathbf{R}}_H + \sigma^2\underline{\mathbf{I}})\underline{\mathbf{Q}}, \\ \underline{\mathbf{D}}_{H(i)} &= \underline{\mathbf{Q}}^H(\underline{\mathbf{R}}_H + \hat{\sigma}^2_{(i)}\underline{\mathbf{I}})\underline{\mathbf{Q}}, \text{and} \\ \underline{\mathbf{D}}_{H(i=0)} &= \underline{\mathbf{Q}}^H(\underline{\mathbf{R}}_H + (\sigma^2 + \hat{\sigma}^2_{(i=0)})\underline{\mathbf{I}})\underline{\mathbf{Q}}. \quad (4.45)\end{aligned}$$

By replacing (4.45) into (4.44) and (4.41), and after some mathematical developments, the scalar expression of the sequence is

$$\begin{aligned}\hat{\sigma}^2_{(i+1)} &= \frac{\hat{\sigma}^4_{(i)}}{M}\sum_{m=0}^{M-1}\frac{(\lambda_m + \sigma^2 + \hat{\sigma}^2_{(i=0)})^4(\lambda_m + \sigma^2)}{((\lambda_m + \sigma^2)^3 + \hat{\sigma}^2_{(i)}(\lambda_m + \sigma^2 + \hat{\sigma}^2_{(i=0)})^2)^2} \\ \Leftrightarrow \hat{\sigma}^2_{(i+1)} &= \frac{\hat{\sigma}^4_{(i)}}{M}\sum_{m=0}^{M-1}\frac{\lambda_m + \sigma^2}{(\frac{(\lambda_m+\sigma^2)^3}{(\lambda_m+\sigma^2+\hat{\sigma}^2_{(i=0)})^2} + \hat{\sigma}^2_{(i)})^2}. \quad (4.46)\end{aligned}$$

It can be seen that, unlike the theoretical scenario, the initialization $\hat{\sigma}^2_{(i=0)}$ appears in (4.46), and then, has an influence on the convergence of the sequence. Thus, if $\hat{\sigma}^2_{(i=0)}$ is chosen close to zero, the term $\frac{(\lambda_m+\sigma^2)^3}{(\lambda_m+\sigma^2+\hat{\sigma}^2_{(i=0)})^2}$ is then roughly equal to $(\lambda_m + \sigma^2)$. In that case, Appendix B.1 shows that it is equivalent to use the covariance matrix $\underline{\tilde{\mathbf{R}}}_H^{LS}$ and the noise estimation then converges towards zero. The choice of the initialization will be studied in the following.

As previously mentioned, one can notice that the sequence $(\hat{\sigma}^2_{(i+1)})$ is built from a function, that will be noted f_{r2}, and if we set $x = \hat{\sigma}^2_{(i)}$, $f_{r2}(x)$ is expressed by

$$f_{r2}(x) = \frac{x^2}{M} \sum_{m=0}^{M-1} \frac{\lambda_m + \sigma^2}{(\frac{(\lambda_m+\sigma^2)^3}{(\lambda_m+\sigma^2+\hat{\sigma}^2_{(i=0)})^2} + x)^2}. \tag{4.47}$$

4.4.2.2 Necessary Condition for the Convergence of the Sequence $(\hat{\sigma}^2_{(i)})$

In this part, a necessary condition on the initialization value $\hat{\sigma}^2_{(i=0)}$ for the convergence of the sequence $(\hat{\sigma}^2_{(i)})$ is derived. To this end, some properties of f_{r2} are listed as follows:

- Since $\frac{(\lambda_m+\sigma^2)^3}{(\lambda_m+\sigma^2+\hat{\sigma}^2_{(i=0)})^2} > 0$, f_{r2} is continuous on $\mathbb{R}^+$.
- $\forall x \in \mathbb{R}^+$ the derivative

$$f'_{r2}(x) = \frac{2x}{M} \sum_{m=0}^{M-1} \frac{(\lambda_m + \sigma^2)\frac{(\lambda_m+\sigma^2)^3}{(\lambda_m+\sigma^2+\hat{\sigma}^2_{(i=0)})^2}}{(\frac{(\lambda_m+\sigma^2)^3}{(\lambda_m+\sigma^2+\hat{\sigma}^2_{(i=0)})^2} + x)^3} \tag{4.48}$$

  is positive, so f_{r2} is growing on $\mathbb{R}^+$.
- $f_{r2}(0) = 0$.
- $\lim\limits_{x\to\infty} f_{r2}(x) = \sum_{m=0}^{M-1} \lambda_m + \sigma^2 = M_2$.

From these four properties, we deduce the inclusion $f_{r2}([0, M_2]) \subset [0, M_2]$, and since f_{r2} is growing on $\mathbb{R}^+$, we conclude that f_{r2} has at least one fixed point in $[0, M_2]$. From the third item, it is obvious that zero is a fixed point of f_{r2}. Since $f_{r2}(0) = 0$ and f_{r2} is growing on $\mathbb{R}^+$, necessary (but not sufficient) condition for f_{r2} to have other fixed points can be expressed as follows: there exists $x_0 \geq 0$ such as $\max\limits_x(f'_{r2}(x)) = f'_{r2}(x_0) > 1$, which can allow f_2 the possibility to be above the first bisector. Then, $\hat{\sigma}^2_{(i=0)}$ can be adjusted in order to ensure this condition. If we note $f'_{r2_m}(x)$ as the functions extracted from $f'_{r2}(x)$ such as $f'_{r2}(x) = \sum_{m=0}^{M-1} f'_{r2_m}(x)$, we have

$$f'_{r2_m}(x) = \frac{1}{M} \frac{2x(\lambda_m + \sigma^2)\frac{(\lambda_m+\sigma^2)^3}{(\lambda_m+\sigma^2+\hat{\sigma}^2_{(i=0)})^2}}{(\frac{(\lambda_m+\sigma^2)^3}{(\lambda_m+\sigma^2+\hat{\sigma}^2_{(i=0)})^2} + x)^3}. \tag{4.49}$$

Let us note $f'_{r2_{min}}(x)$ the function whose maximum reached for $x = x_{0min}$ is the lowest among all the maxima of the functions f'_{r2_m} in the set $\{f'_{r2_m}\}$, $m = 0, ..., M-1$. If we adjust $\hat{\sigma}^2_{(i=0)}$ so that $f'_{r2_{min}}(x_{0min}) \geq 1$, then we fulfill the necessary condition, $f'_{r2}(x_{0min}) \geq 1$. Indeed, if $f'_{2_{min}}(x_{0min}) \geq 1$, then

$$1 \leq f'_{r2_{min}}(x_{0min}) \leq \frac{1}{M}\sum_{m=0}^{M-1} f'_{r2_m}(x_{0min}) = f'_{r2}(x_{0min}). \tag{4.50}$$

In order to find x_{0min}, we calculate the second derivative $f''_{r2_{min}}$ of $f_{r2_{min}}$:

$$f''_{r2_m}(x) = \frac{1}{M}\frac{2(\lambda_m+\sigma^2)\frac{(\lambda_m+\sigma^2)^3}{(\lambda_m+\sigma^2+\hat{\sigma}^2_{(i=0)})^2}(\frac{(\lambda_m+\sigma^2)^3}{(\lambda_m+\sigma^2+\hat{\sigma}^2_{(i=0)})^2}-2x)}{(\frac{(\lambda_m+\sigma^2)^3}{(\lambda_m+\sigma^2+\hat{\sigma}^2_{(i=0)})^2}+x)^4}. \tag{4.51}$$

The second derivative $f''_{r2_{min}}$ is equal to zero for $x_{0min} = \frac{1}{2}\frac{(\lambda_m+\sigma^2)^3}{(\lambda_m+\sigma^2+\hat{\sigma}^2_{(i=0)})^2}$, so we get the maximum value of $f'_{r2_{min}}$:

$$f'_{r2_{min}}(x_{0min}) = \frac{8}{27}\frac{(\lambda_m+\sigma^2+\hat{\sigma}^2_{(i=0)})^2}{(\lambda_m+\sigma^2)^2}. \tag{4.52}$$

Whatever the values of σ^2 and $\hat{\sigma}^2_{(i=0)}$, $f'_{r2_{min}}(x_{0min})$ is minimum for $\lambda_m = \lambda_{max}$, with λ_{max} the maximum eigenvalue of $\underline{\underline{\mathbf{R}}}_H$, and minimum for $\lambda_m = 0$. We can then minimize $\hat{\sigma}^2_{(i=0)}$:

$$\begin{aligned} &\frac{8}{27}\frac{(\lambda_{max}+\sigma^2+\hat{\sigma}^2_{(i=0)})^2}{(\lambda_{max}+\sigma^2)^2} \geq 1 \\ \Leftrightarrow\ &\hat{\sigma}^2_{(i=0)} \geq (\sqrt{\frac{27}{8}}-1)(\lambda_{max}+\sigma^2). \end{aligned} \tag{4.53}$$

The necessary condition $\max_x(f'_2(x)) > 1$ is reached for $\hat{\sigma}^2_{(i=0)} \geq (\sqrt{\frac{27}{8}}-1)(\lambda_{max}+\sigma^2)$. Since λ_{max} and σ^2 are unknown, the condition is necessary but not sufficient so as to assess that f_2 has a fixed point that is different from zero. However, λ_{max} is, by definition, the maximum eigenvalue of the channel covariance matrix, so $\lambda_{max} \geq \frac{1}{M}\sum_{m=0}^{M-1}\lambda_m$. Furthermore, as $M_2 = \frac{1}{M}\sum_{m=0}^{M-1}\lambda_m + \sigma^2$, so, thanks to (4.53) we can minimize $\hat{\sigma}^2_{(i=0)}$, and get

$$\hat{\sigma}^2_{(i=0)} \geq (\sqrt{\frac{27}{8}}-1)M_2. \tag{4.54}$$

4.4.2.3 Sufficient Condition for the Convergence of the Sequence $(\hat{\sigma}^2_{(i)})$

The lower bound (4.54) satisfies the necessary condition $f'_{r2} \geq 1$. Thus, this entails that f_{r2} has a fixed point that is different from zero. In order to give a sufficient condition, the initialization value $\hat{\sigma}^2_{(i=0)}$ has to be set equal to ΛM_2, with $\Lambda >> 1$. Indeed, for all $x \in [0, M_2]$, f_{r2} satisfies

$$\lim_{\hat{\sigma}^2_{(i=0)}\to+\infty} f_{r2}(x) = M_2, \tag{4.55}$$

so it is possible to find $\hat{\sigma}^2_{(i=0)}$ such as $f_{r2}(x) > x$. Given that $\lim_{x\to+\infty} f_{r2}(x) = M_2$, we deduce that a fixed point different from zero exists for a well chosen initialization $\hat{\sigma}^2_{(i=0)} = \Lambda M_2$. However, the previous development only proves the existence of a sufficient condition on $\hat{\sigma}^2_{(i=0)}$ for the convergence of $(\hat{\sigma}^2_{(i)})$ to a non-null limit but it does not give a precise characterization

of $\hat{\sigma}^2_{(i=0)}$. In order to get a suitable value of $\hat{\sigma}^2_{(i=0)}$, the receiver should test some initialization values (e.g. thanks to an abacus) until it finds the expected one, as depicted on Fig. 4.12. It illustrates the shape of f_{r2} considering $\sigma^2 = 2$ for two examples: one with a relevant initialization $\hat{\sigma}^2_{(i=0)} = 10M_2$ (we see a fixed point that is different from zero) and one with an initialization which does not match the necessary condition (zero is the sole fixed point). It is then verified that if $\hat{\sigma}^2_{(i=0)}$ is not chosen large enough, then $\hat{\sigma}^2_{(i)}$ converges to zero. A second drawback occurs: the ratio between the noise variance σ^2 to be estimated and the initialization $\hat{\sigma}^2_{(i=0)}$ is not constant for all the values of σ^2, as shown on Fig. 4.13 for $\Lambda = 10$ and $P_s = 1$. Indeed, Fig. 4.13 displays the noise variance σ^2 and its estimation $\hat{\sigma}^2$ versus σ^2. Thus, a given value Λ can be well chosen for a given value σ^2 but not for another one. The solution is then not appropriate if the noise variance have a varying level during the transmission.

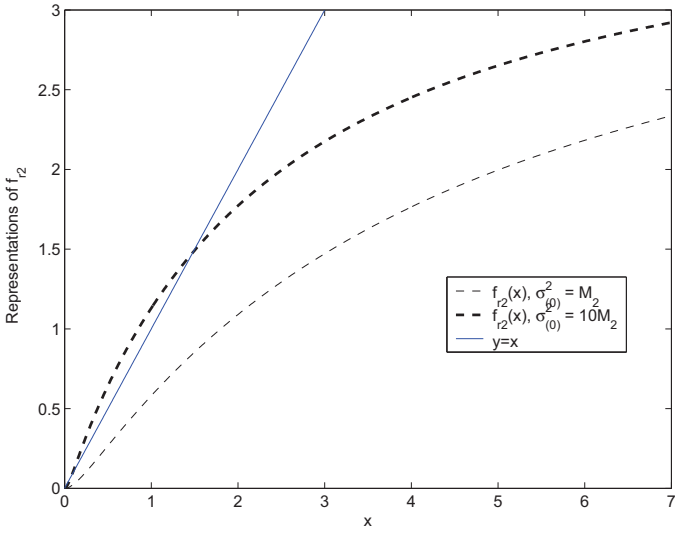

FIGURE 4.12 – Shape of f_{r2} in two different cases, compared with $y = x$.

In order to get the optimal value $\sigma^2_{(i=0)}$, an abacus with different curves of f_{r2} can be created. However, the solution is not applicable in practice, since the channel frequency response and the noise variance can take an infinite number of values. Furthermore, we assume that the receiver has no a priori knowledge of the set of the parameters $\{\lambda_m, \sigma^2\}$, which makes the a priori choice of the optimal initialization impossible. A solution close to the optimal one is nevertheless proposed in the next section.

4.4.2.4 Optimal Choice of the Initialization $\hat{\sigma}^2_{(i=0)}$

The conditions on $\hat{\sigma}^2_{(i=0)}$ given in the previous sections are either not relevant enough ($\hat{\sigma}^2_{(i=0)} = \Lambda M_2$ with $\Lambda >> 1$), or too complex (use of abacus of f_2). Here, a simple characterization of $\hat{\sigma}^2_{(i=0)}$ is proposed, thanks to the noise variance estimation $\hat{\sigma}^2$, which is performed on the last frame. It supposes that the noise variance does not vary significantly from a frame to another. If we note $n_{\mathcal{F}}$ the index of the current frame, the proposed method is:

– For the first frame $n_{\mathcal{F}} = 1$, perform the algorithm thanks to the arbitrary initialization $\hat{\sigma}^2_{(i=0)} = \Lambda M_2$ chosen with the sufficient condition $\Lambda >> 1$.

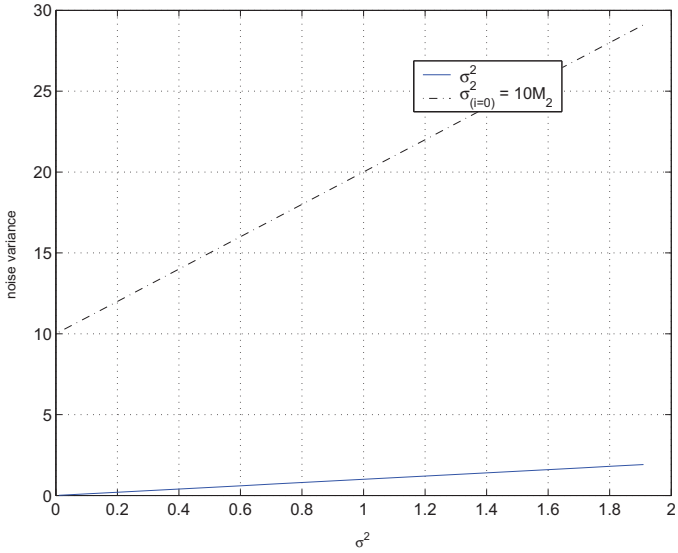

FIGURE 4.13 – σ^2 and $\hat{\sigma}^2_{(i=0)}$ versus σ^2.

– For $n_{\mathcal{F}} > 1$, get the noise variance $\hat{\sigma}^2$ and the eigenvalues of the channel covariance matrix $\underline{\tilde{\mathbf{R}}}_H^{LMMSE}$ (4.37), estimated at the previous frame $n_{\mathcal{F}} - 1$.
– Considering the expression of f_{r2} given in (4.47), look for $\hat{\sigma}^2_{(i=0),opt}$ so that

$$\frac{\hat{\sigma}^4}{M} \sum_{m=0}^{M-1} \frac{\lambda_m + \hat{\sigma}^2}{(\frac{(\lambda_m+\hat{\sigma}^2)^3}{(\lambda_m+\hat{\sigma}^2+\hat{\sigma}^2_{(i=0),opt})^2} + \hat{\sigma}^2)^2} - \hat{\sigma}^2 = 0. \tag{4.56}$$

The direct solving of (4.56) is very complex, but in practice, the receiver can use a simple binary search algorithm to approach the optimal solution. This solution $\hat{\sigma}^2_{(i=0),opt}$, close to the optimal one, can then be found at the frame $n_{\mathcal{F}}$ by means of the previous estimation. The next section depicts the performance of the proposed algorithm and finally shows that the performance in the realistic scenario is close to the one of the theoretical case.

4.4.3 Simulations Results - Realistic Approach

The parameters used for the simulations are exactly the same as the ones used in for the theoretical scenario.

4.4.3.1 Convergence of the Noise Variance Estimation

Similarly to Fig. 4.5, Fig. 4.14 displays the noise variance estimation versus the iteration number, from $i = 0$ to $i = 20$. In order to validate the results whatever the SNR, two values are considered $\rho = 0$ dB and $\rho = 10$ dB. The initialization is chosen according to the sufficient condition $\sigma^2_{(i=0)} = 20M_2$. The curves of the theoretical case are compared to the ones of the theoretical scenario (with $\underline{\mathbf{R}}_H$) and the exact value σ^2. The curves are obtained after 4000 simulations runs.

For iterations $i \geq 1$, Fig. 4.14 shows that the sequence $(\hat{\sigma}^2_{(i)})$ is monotonous and converges to a sole non-null value, which verifies the theoretical developments given in Section 4.4.2.

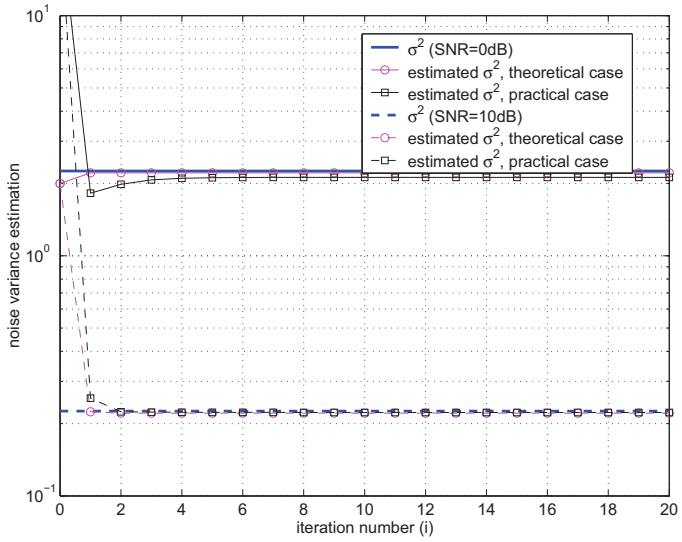

FIGURE 4.14 – Noise variance estimation versus the iteration number, comparison to the theoretical case.

Even in the practical case, the algorithm quickly converges, since from $i = 7$, the noise variance estimation seems to reach its limit. This observation will be confirmed in the next section. Fig. 4.14 also characterizes the noise variance estimation thanks to the normalized bias β calculated by $\beta = |(\hat{\sigma}^2_{(i)}) - \sigma^2|/\sigma^2$. Expressed in percentage, the bias of the proposed estimation is equal to 5.9 % for $\rho = 0$ dB and 1.2 % for $\rho = 10$ dB. These results are very close to the estimation performed in the perfect case. It also shows that the method is less accurate for low SNR values, which can be explained by the fact that the ratio between σ^2 and $\hat{\sigma}^2_{(i=0)}$ is not constant according to the level of the noise variance.

4.4.3.2 Characterization of the Threshold e_σ

Fig. 4.15 depicts the values of the difference $|\hat{\sigma}^2_{(i)} - \hat{\sigma}^2_{(i-1)}|$ versus the number of iterations for $i \geq 2$. The practical case is compared with the theoretical one performed with $\underline{\mathbf{R}}_H$. Simulations are performed with $\rho = 10$ dB and the initialization value $\hat{\sigma}^2_{(i=0)} = 2$ in the theoretical case and $\hat{\sigma}^2_{(i=0)} = 20M_2$ in the practical case. These curves evaluate the required number of iterations to get an expected value of the threshold e_σ.

Although the gradient of $|\hat{\sigma}^2_{(i)} - \hat{\sigma}^2_{(i-1)}|$ is smaller in the practical case than in theoretical one, Fig. 4.15 confirms that $|\hat{\sigma}^2_{(i)} - \hat{\sigma}^2_{(i-1)}|$ converges to zero. It also allows to evaluate the required number of iterations, considering a given threshold value. For instance, in order to reach $e_\sigma = 0.01$, three iterations are required in the practical case and two in the perfect case. For $e_\sigma = 0.0001$, seven iterations are required in the practical case and three in the perfect case.

4.4.3.3 Comparison of SNR Estimation with other methods

Fig. 4.16 displays the NMSE of the SNR estimation of the proposed method for the practical scenario, and compares it to Ren's method [40], Xu's method [41] and the usual M_2M_4 [42]. We remind that Ren's method requires a two pilot-symbols preamble in order to avoid the

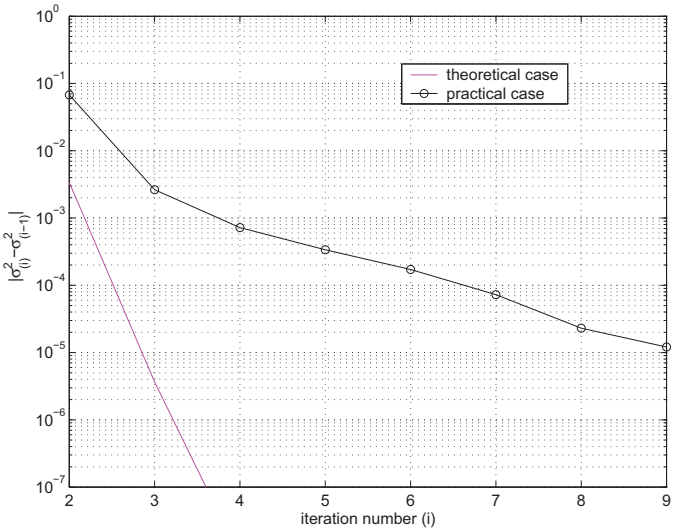

FIGURE 4.15 – $|\hat{\sigma}^2_{(i)} - \hat{\sigma}^2_{(i-1)}|$ versus the iteration number i.

effect of the frequency selective channel, whereas Xu's method and M_2M_4 require only one pilot-symbol by preamble. Figs. 4.16 (a) and (b) compare the SNR estimation performed with two different initializations. For Fig. 4.16 (a), the sufficient condition $\hat{\sigma}^2_{(i=0)} = 20M_2$ is considered at each frame. In Fig. 4.16 (b), the initialization step $\hat{\sigma}^2_{(i=0)} = 20M_2$ is used for the first frame $n_{\mathcal{F}} = 1$, and then $\hat{\sigma}^2_{(i=0)}$ is updated thanks to the proposed method presented in Section 4.4.2.4. Whether Fig. 4.16 (a) or (b) is considered, the number of iterations is set $i_0 = 7$. In the theoretical case, the initialization value is $\hat{\sigma}^2_{(i=0)} = 0.1$, and the number of iterations is $i_0 = 3$. The NMSE given by $NMSE = E\{|\hat{\rho} - \rho|^2/\rho^2\}$, is approximated and simulated thanks to an average made over 200000 samples.

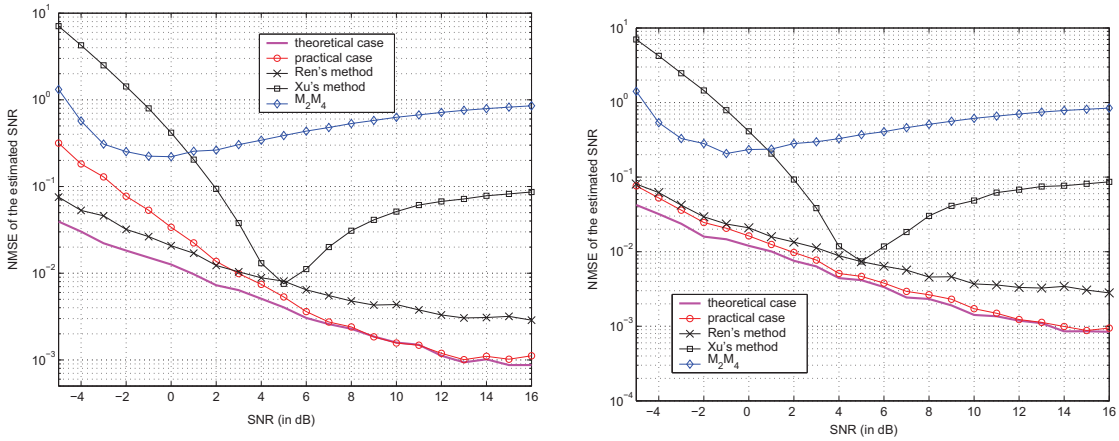

(a) Sufficient initialization $\sigma^2_{(i=0)} = 20M_2$ (b) Optimal initialization

FIGURE 4.16 – NMSE of the SNR estimation of the proposed method compared to three existing methods, for two different initializations.

As previously mentioned for the theoretical scenario and noticed in [42], the performance

of the M_2M_4 method is degraded in Rayleigh channels. Unlike the theoretical case performed with $\underline{\breve{\mathbf{R}}}_H$, the proposed iterative method outperforms Xu's one, whatever the considered SNR. In Fig. 4.16 (a), the performance of the algorithm is degraded compared to the one obtained with Ren's method for low SNR values (<3 dB). It confirms the observations made concerning the evaluation of the bias, that is for low values of SNR, $\hat{\sigma}^2_{(i=0)}$ is not large enough compared to the value of the noise variance σ^2. However, when the algorithm is used with an updated initialization (Fig. 4.16 (b)), the method outperforms Ren's one whatever the SNR is, and the SNR gap with the perfect case is less than 1 dB from $SNR = 0$ dB. This proves the efficiency of the proposed algorithm and the validity of the improvement with regard to the choice of $\hat{\sigma}^2_{(i=0)}$, when performed with an update each frame. Compared to the other methods, the proposed algorithm then improves the trade-off between the number of required pilots and the performance of the SNR estimation.

4.4.3.4 Channel Estimation

Fig. 4.17 shows the BER curves of the proposed estimator versus the SNR (in dB), and for different iteration numbers. It also compares the results with the theoretical scenario, the perfect estimation and the usual LS. The simulations parameters are exactly the same as the ones used to simulate Fig. 4.9. The BER curves are performed by the means of simulating a 2.5×10^6 bits transmission.

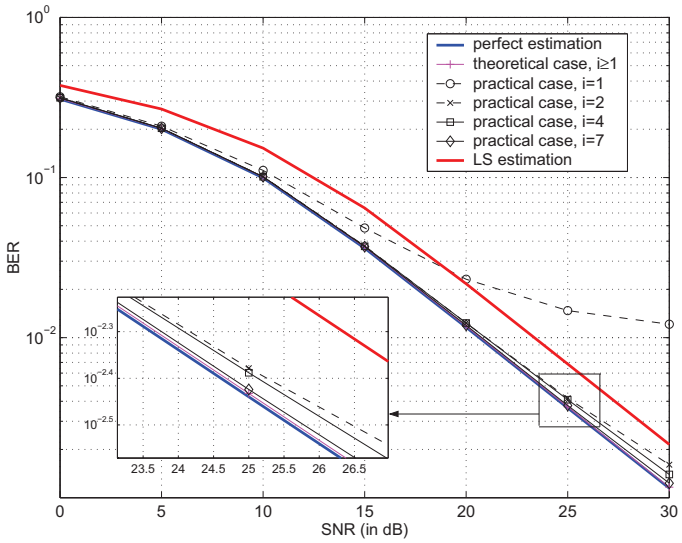

FIGURE 4.17 – Bit error rate (BER) of the proposed method versus SNR, and comparison with perfect estimation, theoretical case and LS.

The proposed method outperforms again the LS estimator. Furthermore, after seven iterations of the algorithm, the gap between the BER curve of the proposed method and the perfect estimation is less than 0.2 dB. The iterative estimation, performed in the practical scenario almost reaches the performance of the theoretical one. One can conclude that the algorithm converges, after only several iterations, and has a high performance for the estimation of both channel and SNR.

4.5 Application of the Algorithm to Spectrum Sensing

In the previous part, it was supposed that the receiver is synchronized with a pilot preamble. Let us now study the behavior of the algorithm if only white Gaussian noise is added to the useful signal. Thus, this part aims to show the ability of the proposed algorithm (in the practical scenario) to be used as a free band detector.

4.5.1 Spectrum Sensing

Wireless communications in general are facing a constant increase of data rate-consuming transmissions, due to the multiplications of the applications and services, while the usable spectrum is naturally limited. Furthermore, most of the bands are already allocated to specific licenses. However, some of these licensed bands are not used at full capacity, which results in spectrum holes along the time and frequency axes [130], whereas they could be exploited in order to achieve the requirements of data rate. Away from the usual paradigm in which the channels are allocated only for licensed users, Joseph Mitola defines the cognitive radio [131], allowing an opportunistic access by unlicensed users to the unused frequency bands. In such a network, the opportunistic users, called secondary users (SUs) can use licensed bands when primary users (PUs) are absent from those ones. The main condition for the SUs to use the licensed bands is to minimize the interferences with PUs. Thus, they must be able to sense the presence of the PUs, even if the PU's signal is attenuated compared to the noise level. Fig. 4.18 depicts the concept of spectrum sensing: A PU transmitter (PU-Tx) is transmitting to a PU receiver (PU-Rx) while a SU transmitter intends to transmit in the same band. In order to avoid the interferences with the PU, the SU has to perform spectrum sensing. In order to lighten the drawing, only one PU-Rx and two SU-Rx are depicted, but the network can obviously be more complex.

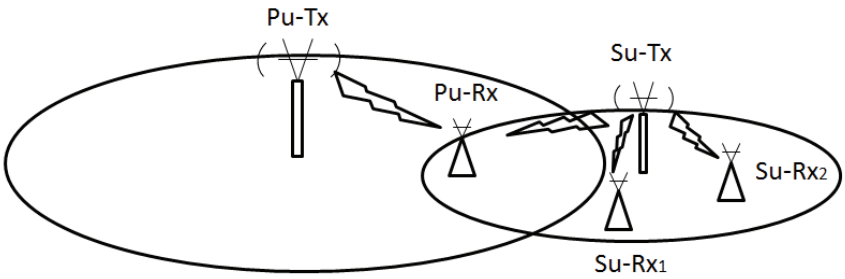

FIGURE 4.18 – Illustration of the use of the spectrum sensing.

The process set up by the SUs to sense the presence of the PUs is called spectrum sensing. The authors of [132–134] propose detailed reviews of the different techniques of spectrum sensing proposed in the literature. The different methods are usually classified into two main categories: the non-cooperative detection and the cooperative detection.

4.5.1.1 Non-cooperative Methods

The non-cooperative detection concerns a sole SU who tries to detect the presence of the PU alone. Among the wide range of methods [132–135], the following list shortly describes the main ones:

- The energy detector measures the energy of the received signal and compares it with a threshold. It has a low complexity of implementation and does not require any knowledge on the PU's signal features. However, the choice of the threshold value depends on the noise variance, and uncertainties on the noise level may cause important degradations of the detector performance [136], [137].
- The matched-filter correlates the received signal to the one transmitted by the PU, which is supposed to be known at the receiver [87], [138]. This is the optimal detector when the signal is transmitted with AWGN only and supposed to be known at the receiver. Due to these hypotheses, this method is generally not applicable in practice, and its performance is degraded when the knowledge of the signal is erroneous [139].
- Less binding than the matched-filter, the feature detectors only use several characteristics of the signal to detect the PU. Thus, the waveform-base sensing uses the preamble of the PU's signal (used for the synchronization, the estimation etc.) to perform a correlation with the received signal [140]. However, the performance of the waveform-based sensing is degraded in the presence of selective channels. In the same way, when a CP is used in an OFDM signal, its autocorrelation function becomes time-varying, so a method consists of detecting the peaks in the autocorrelation function at time-lag T_s.
- More generally, the cyclostationarity detector exploits the periodic redundancy of all telecommunications signals to differentiate it from a pure Gaussian noise [141, 142]. As indicated in [134], the redundancy can be due to periodic patterns such as the CP, the symbol rate or the channel code. However, these second-order detectors requires great sensing time, i.e. a large number of symbols to be performed. In [143], an hybrid architecture composed of both energy and cyclostationarity is proposed. It allows to compensate the limitation of the energy detector due to the noise uncertainty thanks to a cyclostationarity detection stage whose computation time is reduced.

4.5.1.2 Cooperative Methods

In the case of the cooperative detection, it is assumed that several SUs (called nodes of the network) share out some information about the state of the spectrum. This sharing allows the SUs to increase the probability of detection of the PU, in particular for the SUs who might receive the PU's signal disrupted by fading or noise uncertainty. Furthermore, it allows to reduce the sensing time. The different techniques can be summed up as follows:

- The detection with soft combing (or centralized) decision, in which each SU transmits its sensing data to a central unit called fusion center. The fusion center then combines the different soft decisions to make a decision on the presence or the absence of the PU, and this decision is transmitted back to the SUs. In [144], the performance of different data combination schemes are compared. Although it considered as the optimal detection scheme, the required bandwidth to transmit the sensing information from the SUs and the computation complexity of the data processing might be great, according to the sensing method.
- The detection with hard combining (or distributed) decision, in which each SU makes its own decision and transmits to the fusion center a binary information 0 or 1. The fusion center then combines the hard decisions of the SUs to make a common decision. The decision can be made by following the AND-logic, the OR-logic or the voting rule [134, 135]. Although the hard decision is less efficient than the soft decision, it is also less complex and less bandwidth consuming. Furthermore, if a high number of

nodes are considered, the hard decision and the soft decision become equivalent in term of performance [135].
- The fully distributed detection differs from the previous one in the sense that no fusion center is considered in the network. However, both approaches are often mistaken in the literature and simply called "distributed detection". In [145], an example of fully distributed detection algorithm is given: at each iteration, a sensing step followed by a gossiping step is performed. In the gossiping step, the SUs transmit the results of the sensing step to their neighbors, without the help of a fusion center. This approach appears as efficient in the case of a SU who is hidden from the PU by an obstacle.
- The external detection, in which the sensing is not performed by the SUs, but by external sensors. According to the arrangement of the sensors in the networks, the external detection also avoids the hidden SUs effect. As mentioned in [135], this solution is developed in the standard IEEE 802.22, designed for the opportunistic access to the free TV bands.

Complementary to these two main differences, the detection techniques can also be differentiated according to the bandwidth on which they are performed. Indeed, some methods can detect several holes over a wide bandwidth, while others are adapted to the detection of a sole hole in a given channel. Since we consider a sole receiver, the context of the next sections will be the non-cooperative detection of a PU by a single SU in a given narrow band.

4.5.2 Proposed Detector

4.5.2.1 Detection Hypothesis

In order to link this part to the rest of the chapter, let us consider the problem of the detection of a preamble over a Rayleigh channel in a given band to be sensed. To this end, it is a priori supposed that the SU is perfectly synchronized with the PU. According to previously in the dissertation, the signal that is received by the SU is noted $\mathbf{U}$ after the M-points DFT. The SU has no a priori knowledge of the presence or the absence of the PU, so the detection hypothesis test is written as follows:

$$\begin{cases} \mathbb{H}_0 & : \mathbf{U} = \mathbf{W} \\ \mathbb{H}_1 & : \mathbf{U} = \underline{\mathbf{C}}\mathbf{H} + \mathbf{W}, \end{cases} \tag{4.57}$$

$\mathbb{H}_0$ and $\mathbb{H}_1$ denoting the absence and the presence of the PU, respectively. In the following, the matrix $\underline{\mathbf{C}}$ corresponds to a preamble, such as $\forall m = 0, 1, .., M-1$ we have $C_m C_m^* = 1$.

The performance of a detector is characterized by its probability of detection, noted P_d, and its false alarm probability P_{fa}. P_d corresponds to the probability of choosing the correct $\mathbb{H}_1$ while the signal is present, whereas P_{fa} corresponds to the probability of choosing $\mathbb{H}_1$ while the signal is absent. In a general way, the more P_d is close to 1 and P_{fa} close to 0, the more the detector is efficient. It is also usual to use the missing probability $P_m = 1 - P_d$, as the probability of choosing $\mathbb{H}_0$ while the signal is present.

As mentioned in [135, 145], the sensibility of the detector (the expected value of P_{fa} and P_d) depends on the application. In a cognitive radio context, the SU has to minimize the interference with the PU, so the probability of detection has to be maximized, whereas if the false alarm probability is not optimized, it only implies that the SU misses white spaces. On the contrary, in a radar application, a false alarm could have serious consequences, especially in a military context.

In the previous parts of this chapter, the convergence of the algorithm under $\mathbb{H}_1$ has been shown. In the next sections, the convergence of the algorithm under $\mathbb{H}_0$ is studied, and an analytical expression of P_d and P_{fa} is also proposed.

4.5.2.2 Convergence of the MMSE-based Algorithm under the Hypothesis $\mathbb{H}_0$

The signal $\underline{\mathbf{C}}$ is supposed to be absent, so the received signal is $\mathbf{U} = \mathbf{W}$. The convergence of the proposed algorithm in the case of absence of signal is going to be proved. Furthermore, it will be proved afterward that the non-null solution allows to make the MMSE-based algorithm a free band detector. To this end, the three first steps of Algorithm 3 presented in Section 4.4 are now expressed under the hypothesis $\mathbb{H}_0$.

a. Expression of the Algorithm under $\mathbb{H}_0$

Let us consider that the receiver does not know if the signal is present or absent, so the same formalism as in Section 4.4 is used, and the steps of the algorithm are recalled:

1. Firstly, the LS channel estimation is performed:

$$\hat{\mathbf{H}}^{LS} = \underline{\mathbf{C}}^{-1}\mathbf{U} = \underline{\mathbf{C}}^{-1}\mathbf{W}. \tag{4.58}$$

The channel covariance matrix

$$\tilde{\underline{\mathbf{R}}}_H^{LS} = \hat{\mathbf{H}}^{LS}(\hat{\mathbf{H}}^{LS})^H = \mathbf{W}\mathbf{W}^H \tag{4.59}$$

is deduced from (4.58). Furthermore, a stopping criterion e_σ and an initialization $\hat{\sigma}^2_{(i=0)}$ are set.

2. At iteration $i = 1$ of the algorithm, the LMMSE channel estimation $\hat{\mathbf{H}}^{LMMSE}_{(i=1)}$ is performed by using $\tilde{\underline{\mathbf{R}}}_H^{LS}$:

$$\hat{\mathbf{H}}^{LMMSE}_{(i=1)} = \tilde{\underline{\mathbf{R}}}_H^{LS}(\tilde{\underline{\mathbf{R}}}_H^{LS} + \hat{\sigma}^2_{(i=0)}\underline{\mathbf{I}})^{-1}\hat{\mathbf{H}}^{LS}. \tag{4.60}$$

3. The MMSE noise variance estimation $\hat{\sigma}^2_{(i=1)}$ is performed with $\hat{\mathbf{H}} = \hat{\mathbf{H}}^{LMMSE}_{(i=1)}$:

$$\hat{\sigma}^2_{(i=1)} = \frac{1}{M}E\{||\hat{\mathbf{H}}^{LS} - \hat{\mathbf{H}}^{LMMSE}_{(i=1)}||^2_F\}, \tag{4.61}$$

and a new covariance matrix is computed by

$$\tilde{\underline{\mathbf{R}}}_H^{LMMSE} = \hat{\mathbf{H}}^{LMMSE}_{(i=1)}(\hat{\mathbf{H}}^{LMMSE}_{(i=1)})^H. \tag{4.62}$$

Indeed, it is proved in Appendix B.2 that if the algorithm keeps on computing with $\tilde{\underline{\mathbf{R}}}_H^{LS} = \mathbf{W}\mathbf{W}^H$, then the sequence $\hat{\sigma}^2_{(i)}$ necessarily converges to zero. When $\tilde{\underline{\mathbf{R}}}_H^{LS}$ is used, and in spite of its inputs are different, the algorithm has exactly the same response whatever the hypothesis $\mathbb{H}_0$ or $\mathbb{H}_1$.

Then, for $i \geq 2$, perform the channel and the noise variance estimation

$$\hat{\mathbf{H}}^{LMMSE}_{(i)} = \tilde{\underline{\mathbf{R}}}_H^{LMMSE}(\tilde{\underline{\mathbf{R}}}_H^{LMMSE} + \hat{\sigma}^2_{(i-1)}\underline{\mathbf{I}})^{-1}\hat{\mathbf{H}}^{LS}, \tag{4.63}$$

$$\hat{\sigma}^2_{(i)} = \frac{1}{M}E\{||\hat{\mathbf{H}}^{LS} - \hat{\mathbf{H}}^{LMMSE}_{(i)}||^2\}. \tag{4.64}$$

For the application of the algorithm to spectrum sensing, it only require these three steps.

b. Scalar Expression of the Sequence $(\hat{\sigma}^2_{(i)})$

The convergence of the algorithm is now going to be proved, and its limit characterized. First, remembering that $\underline{\tilde{\mathbf{R}}}_H^{LS}$ is an Hermitian matrix, we develop (4.62) as

$$\begin{aligned}\underline{\tilde{\mathbf{R}}}_H^{LMMSE} &= \hat{\mathbf{H}}_{(1)}^{LMMSE}(\hat{\mathbf{H}}_{(1)}^{LMMSE})^H \\ &= \underline{\tilde{\mathbf{R}}}_H^{LS}(\underline{\tilde{\mathbf{R}}}_H^{LS} + \hat{\sigma}^2_{(i=0)}\underline{\mathbf{I}})^{-1}\hat{\mathbf{H}}^{LS}(\underline{\tilde{\mathbf{R}}}_H^{LS}(\underline{\tilde{\mathbf{R}}}_H^{LS} + \hat{\sigma}^2_{(i=0)}\underline{\mathbf{I}})^{-1}\hat{\mathbf{H}}^{LS})^H \\ &= \underline{\tilde{\mathbf{R}}}_H^{LS}(\underline{\tilde{\mathbf{R}}}_H^{LS} + \hat{\sigma}^2_{(i=0)}\underline{\mathbf{I}})^{-1}\hat{\mathbf{H}}^{LS}(\hat{\mathbf{H}}^{LS})^H(\underline{\tilde{\mathbf{R}}}_H^{LS}(\underline{\tilde{\mathbf{R}}}_H^{LS} + \hat{\sigma}^2_{(i=0)}\underline{\mathbf{I}})^{-1}). \end{aligned} \tag{4.65}$$

Let us assume that M is large enough to justify the approximation $tr(\mathbf{W}\mathbf{W}^H) = tr(\sigma^2\underline{\mathbf{I}})$. Since the estimation of the noise variance is calculated by means of the trace in (4.64), we make the assumption that, as a first approximation $\underline{\tilde{\mathbf{R}}}_H^{LS} \approx \sigma^2\underline{\mathbf{I}}$, and then it possible to replace $\underline{\mathbf{R}}_H^{LMMSE}$ by

$$\begin{aligned}\underline{\tilde{\mathbf{R}}}_H^{LMMSE} &= \sigma^2\underline{\mathbf{I}}(\sigma^2\underline{\mathbf{I}} + \hat{\sigma}^2_{(i=0)}\underline{\mathbf{I}})^{-1}\underline{\tilde{\mathbf{R}}}_H^{LS}(\sigma^2\underline{\mathbf{I}}(\sigma^2\underline{\mathbf{I}} + \hat{\sigma}^2_{(i=0)}\underline{\mathbf{I}})^{-1}) \\ &= \frac{\sigma^6}{(\sigma^2 + \hat{\sigma}^2_{(i=0)})^2}\underline{\mathbf{I}} \end{aligned} \tag{4.66}$$

in (4.64). Thus, by reinjecting (4.66) in (4.63) and (4.64), it yields

$$\begin{aligned}\hat{\sigma}^2_{(i+1)} &= \frac{1}{M}E\{||\hat{\mathbf{H}}^{LS} - \hat{\mathbf{H}}_{(i+1)}^{LMMSE}||^2\} \\ &= \frac{1}{M}E\{||\hat{\mathbf{H}}^{LS} - \underline{\tilde{\mathbf{R}}}_H^{LMMSE}(\underline{\tilde{\mathbf{R}}}_H^{LMMSE} + \hat{\sigma}^2_{(i)}\underline{\mathbf{I}})^{-1}\hat{\mathbf{H}}^{LS}||^2\} \\ &= \frac{1}{M}E\{||\mathbf{W} - \frac{\sigma^6}{(\sigma^2 + \hat{\sigma}^2_{(i=0)})^2}\underline{\mathbf{I}}(\frac{\sigma^6}{(\sigma^2 + \hat{\sigma}^2_{(i=0)})^2}\underline{\mathbf{I}} + \hat{\sigma}^2_{(i)}\underline{\mathbf{I}})^{-1}\mathbf{W}||^2\} \\ &= \frac{1}{M}E\{||(\hat{\sigma}^2_{(i)}\underline{\mathbf{I}}((\frac{\sigma^6}{(\sigma^2 + \hat{\sigma}^2_{(i=0)})^2} + \hat{\sigma}^2_{(i)})\underline{\mathbf{I}})^{-1})\mathbf{W}||^2\} \\ &= \frac{\sigma^2\hat{\sigma}^4_{(i)}(\sigma^2 + \hat{\sigma}^2_{(i=0)})^4}{(\sigma^6 + \hat{\sigma}^2_{(i)}(\sigma^2 + \hat{\sigma}^2_{(i=0)})^2)^2}. \end{aligned} \tag{4.67}$$

c. Convergence of the Sequence $(\hat{\sigma}^2_{(i)})$ **to a non-null Solution**

For a better readability, we note in the following mathematical developments

$$A = \sigma^2 + \hat{\sigma}^2_{(i=0)}. \tag{4.68}$$

It is once more noticeable that the sequence $(\hat{\sigma}^2_{(i+1)})$ is built from a function f_{s1} such as, if we note $x = \hat{\sigma}^2_{(i)}$:

$$f_{s1}(x) = \frac{\sigma^2A^4x^2}{(\sigma^6 + A^2x)^2}. \tag{4.69}$$

The sequence converges if f_{s1} has at least a fixed point. Zero is an obvious fixed point, but it has been proved in Appendix B.2 that the algorithm enters into an endless loop if $(\hat{\sigma}^2_{(i)})$ converge to zero. We then solve the equation $f_{s1}(x) = x$ to find the others fixed points:

$$\begin{aligned} & f_{s1}(x) = x \\ \Leftrightarrow & \frac{\sigma^2 A^4 x^2}{(\sigma^6 + A^2 x)^2} = x \\ \Leftrightarrow & \sigma^2 A^4 x^2 = x(\sigma^6 + A^2 x)^2. \end{aligned} \tag{4.70}$$

Since we consider that zero is not a solution to the equation, the previous expressions can be simplified by x, and the problem amounts to look for real roots of the polynomial $A^4 x^2 + x(2A^2\sigma^6 - \sigma^2 A^4) + \sigma^{12}$. Since it is a second order polynomial, in order to find real solutions, the first condition on the initialization $\hat{\sigma}^2_{(i=0)}$ is to obtain the discriminant $\Delta = (2A^2\sigma^6 - \sigma^2 A^4)^2 - 4A^4\sigma^{12}$ positive, i.e.:

$$\begin{aligned} & \Delta \geq 0 \\ \Leftrightarrow & (2A^2\sigma^6 - \sigma^2 A^4)^2 \geq 4A^4\sigma^{12} \\ \Leftrightarrow & 4A^4\sigma^{12} + A^8\sigma^6 - 4A^6\sigma^8 \geq 4A^4\sigma^{12} \\ \Leftrightarrow & A^2 \geq 4\sigma^4 \\ \Leftrightarrow & (\sigma^2 + \hat{\sigma}^2_{(i=0)})^2 \geq 4\sigma^4 \\ \Leftrightarrow & \hat{\sigma}^2_{(i=0)} \geq 3\sigma^2. \end{aligned} \tag{4.71}$$

As σ^2 is absolutely unknown, one can find a stronger condition on $\hat{\sigma}^2_{(i=0)}$, conditionally to $\Delta > 0$. We then find the roots r_s^+ and r_{s-} of the polynomial under the condition $\Delta > 0$:

$$\begin{aligned} r^+_{s-} &= \frac{(\sigma^2 A^4 - 2A^2\sigma^6) \pm^+ \sqrt{(2A^2\sigma^6 - \sigma^2 A^4)^2 - 4A^4\sigma^{12}}}{2A^4} \\ \Leftrightarrow r^+_{s-} &= \frac{(\sigma^2 A^2 - 2\sigma^6) \pm^+ \sqrt{\sigma^4 A^4 - 4\sigma^8 A^2}}{2A^2}. \end{aligned} \tag{4.72}$$

If we notice that when $\hat{\sigma}^2_{(i=0)}$ tends to $+\infty$, then $A = \sigma^2 + \hat{\sigma}^2_{(i=0)}$ also tends to $+\infty$, and we get:

$$\lim_{A\to\infty} r_s^+ = \frac{\sigma^2 A^2 + \sigma^2 A^2}{2A^2} = \sigma^2, \tag{4.73}$$

and

$$\lim_{A\to\infty} r_{s-} = \frac{\sigma^2 A^2 - \sigma^2 A^2}{2A^2} = 0. \tag{4.74}$$

It can be seen that, by choosing the initialization value $\hat{\sigma}^2_{(i=0)}$ as large as wanted, the sequence $(\hat{\sigma}^2_{(i)})$ converges to a value as close as possible to the exact value of the noise variance σ^2. This characterization of the initialization value $\hat{\sigma}^2_{(i=0)}$ perfectly tallies with the one made for the sufficient condition under hypothesis $\mathbb{H}_1$ in Section 4.4.2.3. Furthermore, It will be

further shown that this solution allows to detect $\mathbb{H}_0$ from $\mathbb{H}_1$. Thus, choosing $\hat{\sigma}^2_{(i=0)}$ with a large value is the condition for the algorithm to converge to a non-null solution for both hypotheses $\mathbb{H}_0$ and $\mathbb{H}_1$. Furthermore, since it converges, the stopping criterion $|\hat{\sigma}^2_{(i)} - \hat{\sigma}^2_{(i-1)}| < e_\sigma$ can also be same under $\mathbb{H}_0$. Finally, the MMSE-based algorithm can be used as a free band detector.

Fig. 4.19 displays the function f_{s1} for different values of $(\hat{\sigma}^2_{(i=0)})$, compared with $y = x$ and for a fixed $\sigma^2 = 1$. By comparing the curves of f_{s1} for different initializations values, we verify that, the larger the value of $\hat{\sigma}^2_{(i=0)}$, the closer to the real value of $\sigma^2 = 1$ the fixed point.

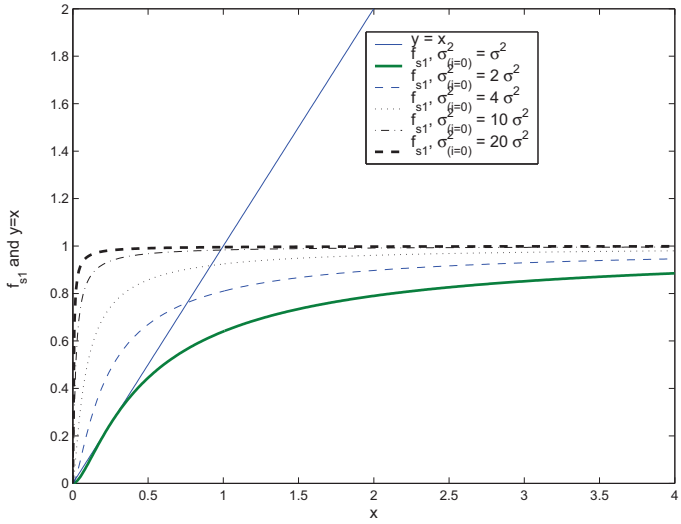

FIGURE 4.19 – Aspect of f_{s1} for different values of $\sigma^2_{(0)}$, $\sigma^2 = 1$ compared with $y = x$.

4.5.2.3 Decision Rule for the Proposed Detector

In this section, a decision rule for the detector is proposed. To this end, whatever $\mathbb{H}_0$ or $\mathbb{H}_1$, it is supposed that the algorithm has converged, i.e. the condition $|\hat{\sigma}^2_{(i)} - \hat{\sigma}^2_{(i-1)}| < e_\sigma$ is reached and then $i = i_0$.

The second-order moment $M_2 = \frac{1}{M}\sum_{m=0}^{M-1} |U_m|^2$ of the received signal is expressed under the hypotheses $\mathbb{H}_0$ and $\mathbb{H}_1$, respectively:

$$M_2 = \begin{cases} \frac{1}{M}\sum_{m=0}^{M-1} |W_m|^2, & \text{if } \mathbb{H}_0 \\ \frac{1}{M}\sum_{m=0}^{M-1} |C_m H_m + W_m|^2, & \text{if } \mathbb{H}_1 \end{cases}. \tag{4.75}$$

The second order-moment is the decision metric used for the energy-base detector. Here, a different metric noted $\mathcal{M}$ is proposed, and defined by

$$\mathcal{M} = |M_2 - \hat{\sigma}^2|, \tag{4.76}$$

where $\hat{\sigma}^2 = \hat{\sigma}^2_{(i_0)}$ is the noise variance estimation performed by means of the iterative algorithm. From (4.75), the metric (4.76) is rewritten according to the hypotheses $\mathbb{H}_0$ and $\mathbb{H}_1$:

$$\mathcal{M} = \begin{cases} |\frac{1}{M}\sum_{m=0}^{M-1} |W_m|^2 - \hat{\sigma}^2|, & \text{under } \mathbb{H}_0 \\ |\frac{1}{M}\sum_{m=0}^{M-1} |C_m H_m + W_m|^2 - \hat{\sigma}^2|, & \text{under } \mathbb{H}_1 \end{cases}. \tag{4.77}$$

By fixing a threshold ς, the detection and false alarm probabilities are defined by:

$$P_d = P(\mathcal{M} > \varsigma | \mathbb{H}_1) \tag{4.78}$$
$$P_{fa} = P(\mathcal{M} > \varsigma | \mathbb{H}_0), \tag{4.79}$$

and the decision criterion is

$$\begin{aligned} &\mathbb{H}_0, \text{ if } \mathcal{M} < \varsigma \\ &\mathbb{H}_1, \text{ else.} \end{aligned}$$

It is then possible to rewrite the practical algorithm proposed in the scenario of the joint estimation of the SNR and the channel for free band detections, as it is summed up in Algorithm 4.

begin
  Initialization: $\underline{\tilde{\mathbf{R}}}_H^{LS}$, $e_\sigma > 0$, $\hat{\sigma}^2_{(i=0)}$ and ς ;
  $i \leftarrow 1$;
  while $|\hat{\sigma}^2_{(i)} - \hat{\sigma}^2_{(i-1)}| > e_\sigma$ **do**
    if *i = 1* **then**
      Perform LMMSE channel estimation ;
      Perform the noise variance estimation ;
      Calculate the matrix $\underline{\tilde{\mathbf{R}}}_H^{LMMSE}$;
    else
      Perform an LMMSE channel estimation with $\underline{\tilde{\mathbf{R}}}_H^{LMMSE}$;
      Perform the noise variance estimation ;
    end
    $i \leftarrow i + 1$;
  end
  Calculate the metric $\mathcal{M}$;
  if $\mathcal{M} < \varsigma$ **then**
    return $\mathbb{H}_0$;
  else
    return $\mathbb{H}_1$;
    Estimate the SNR $\hat{\rho}$ (4.40) with $\hat{\sigma}^2_{(i_0)}$;
  end
end

Algorithm 4: Application of the MMSE-based algorithm to free band detection.

It can be seen that the structure of Algorithm 4 is the same as Algorithm 3, but with a detection part. Thus, compared with the method of the literature, the proposed method not only return the decision $\mathbb{H}_0$ and $\mathbb{H}_1$, but also:

– the noise variance estimation, if $\mathbb{H}_0$,
– the channel and SNR estimations, if $\mathbb{H}_1$.

An a priori qualitative analysis of the detector can be done. Indeed, from (4.77), one can deduce that, by supposing a good estimation of $\hat{\sigma}^2$, $\mathcal{M}$ tends to a value close to zero under $\mathbb{H}_0$, and to a value close to P_s under $\mathbb{H}_1$. By supposing a normalized signal power, one can suppose that choosing a value ς between zero and one allows to get a viable detector. Concerning the value of the threshold e_σ, since it ensures the convergence of the algorithm, it has no effect on the detector performance. This property will be shown by simulations afterward.

In the context of cognitive radio, the SUs have to target a given detection probability, noted P_d^t. Thus, according to the Neyman-Pearson criterion [146], the best value of the threshold ς can be analytically derived (when it is possible) by solving $P(\mathcal{M} > \varsigma|\mathbb{H}_1) \geq P_d^t$, and by maximazing the likelihood ratio test (LRT)

$$\Lambda(x) = \frac{p(x|\mathbb{H}_1)}{p(x|\mathbb{H}_0)} \gtrless_{\mathbb{H}_0}^{\mathbb{H}_1} \varsigma. \tag{4.80}$$

To this end, the probability density functions (pdfs) of $\mathcal{M}$ have to be expressed, which is proposed in the next section.

4.5.3 Analytical Expressions of the Detection and False Alarm Probabilities

4.5.3.1 Probability Density Function of $\mathcal{M}$ under $\mathbb{H}_1$

Under the hypothesis $\mathbb{H}_1$, from the results of the section 4.4 it is reasonable to suppose that the noise variance estimation is good enough to consider that $\hat{\sigma}^2 \approx \frac{1}{M}\sum_{m=0}^{M-1}|W_m|^2$, so the contribution of $C_m H_m$ is prevailling in $\mathcal{M}$ so that:

$$\begin{aligned}\mathcal{M} &= |\frac{1}{M}\sum_{m=0}^{M-1}(|C_m H_m + W_m|^2) - \hat{\sigma}^2| \\ &= |\frac{1}{M}\sum_{m=0}^{M-1}(|C_m H_m|^2 + |W_m|^2 + CF_m) - \hat{\sigma}^2|,\end{aligned} \tag{4.81}$$

where $\forall m = 0, .., M-1$, CF_m are the cross factors $(C_m H_m W_m^*) + (C_m H_m W_m^*)^*$, whose mean (for a sufficiently large value of M) is equal to zero, since H_m and W_m are zero-mean uncorrelated Gaussian processes. The development of (4.81) then simply yields:

$$\begin{aligned}\mathcal{M} &= |\frac{1}{M}\sum_{m=0}^{M-1}|C_m H_m|^2 + |W_m|^2 - \hat{\sigma}^2| \\ &= \frac{1}{M}\sum_{m=0}^{M-1}|H_m C_m|^2,\end{aligned} \tag{4.82}$$

such as $\mathcal{M}$ is linked to P_s by $P_s = E\{\mathcal{M}\}$, according to the hypothesis $\mathbb{H}_1$. The result (4.82) obtained with the approximation $\hat{\sigma}^2 \approx \frac{1}{M}\sum_{m=0}^{M-1}|W_m|^2$ can be matter of debate, since it has been seen in Section 4.4 that the noise estimation under hypothesis $\mathbb{H}_1$ is biased. However, it will be shown in Section 4.5.4 that this approximation proves good for low values of σ^2. Thus,

the developments keeps going on from (4.82). Whatever $m = 0, .., M-1$, the m^{th} sample of the channel frequency response given by (1.39) is reminded:

$$H_m = \sum_{l=0}^{L-1} h_{l,n} \exp(-2j\pi \frac{m}{M} \beta_l), \tag{4.83}$$

as $C_m C_m^* = 1$, the metric (4.82) can be rewritten by

$$\begin{aligned}
\mathcal{M} &= \frac{1}{M} \sum_{m=0}^{M-1} \left| \sum_{l=0}^{L-1} h_l \exp(-2j\pi \frac{m\beta_l}{M}) C_m \right|^2 \\
&= \frac{1}{M} \sum_{m=0}^{M-1} \left(\sum_{l=0}^{L-1} h_l \exp(-2j\pi \frac{m\beta_l}{M}) C_m \right) \left(\sum_{l=0}^{L-1} h_l \exp(-2j\pi \frac{m\beta_l}{M}) C_m \right)^* \\
&= \sum_{l=0}^{L-1} |h_l|^2 + \frac{1}{M} \sum_{m=0}^{M-1} \sum_{l_1=0}^{L-1} \sum_{\substack{l_2=0 \\ l_2 \neq l_1}}^{L-1} h_{l_1} h_{l_2}^* \exp\left(-2j\pi \frac{m(\beta_{l_1} - \beta_{l_2})}{M} \right).
\end{aligned} \tag{4.84}$$

According to the Rayleigh distributed WSSUS channel model, whatever $l = 0, .., L-1$, the gains h_l are uncorrelated zero mean Gaussian processes. For a large enough value M, let us assume that the mean of the cross factors on the right side of (4.84) is equal to zero. Finally, the metric $\mathcal{M}$ is simply written as follows

$$\mathcal{M} = \sum_{l=0}^{L-1} |h_l|^2, \text{ under } \mathbb{H}_1. \tag{4.85}$$

$\mathcal{M}$ then follows a chi-square distribution with $2L$ degrees of liberty. The probability density function (pdf) noted $p_{\mathcal{M}}(x)$ of the decision statistic under $\mathbb{H}_1$ is then expressed by

$$p_{\mathcal{M}}(x) = \frac{1}{2^L P_s^L \Gamma(L)} x^{L-1} \exp\left(-\frac{x}{2P_s} \right), \text{ under } \mathbb{H}_1, \tag{4.86}$$

where $\Gamma(.)$ is the gamma function [147]. Fig. 4.20 (a) displays $p_{\mathcal{M}}(x)$ under $\mathbb{H}_1$.

4.5.3.2 Probability Density Function of $\mathcal{M}$ under $\mathbb{H}_0$

The theoretical expression under the hypothesis $\mathbb{H}_0$ of the pdf of the metric

$$\mathcal{M} = |\frac{1}{M} \sum_{m=0}^{M-1} |W_m|^2 - \hat{\sigma}_{(i)}^2| \tag{4.87}$$

is now developed. To this end, let assume that the initialization of the algorithm is chosen large enough to allow the approximation $\hat{\sigma}^2 \approx \sigma^2$, that suits with both hypotheses. Whatever $m = 0, ..., M-1$, each sample W_m is a zero-mean Gaussian process with variance σ^2, $|W_m|^2$ has a chi-square distribution χ_2^2 with a degree of liberty equal to 2:

$$\chi_2^2(x) = \frac{1}{\sigma^2} e^{-\frac{x}{\sigma^2}}. \tag{4.88}$$

The mean and the variance of this distribution are equal to σ^2 and σ^4, respectively. In an OFDM context, we reasonably suppose that M is large enough (e.g. $M > 100$) to consider

that, from the central limit theorem, $\frac{1}{M}\sum_{m=0}^{M-1}|W_m|^2$ has a normal distribution $\mathcal{N}\sim(\sigma^2,\frac{\sigma^4}{M})$, and then $\frac{1}{M}\sum_{m=0}^{M-1}|W_m|^2-\hat{\sigma}^2$ has a centered normal distribution $\mathcal{N}\sim(0,\frac{\sigma^4}{M})$. Consequently, the metric $\mathcal{M}=|\frac{1}{M}\sum_{m=0}^{M-1}|W_m|^2-\hat{\sigma}^2_{(i)}|$ has a chi distribution χ_1 with one degree of liberty:

$$p_{\mathcal{M}}(x)=\frac{\sqrt{2}}{\Gamma(\frac{1}{2})\sqrt{\sigma^4/M}}\exp\left(-\frac{1}{2}(\frac{x}{\sqrt{\sigma^4/M}})^2\right),\text{under }\mathbb{H}_0 \tag{4.89}$$

The probability density functions of the metric $\mathcal{M}$, according to $\mathbb{H}_0$ and $\mathbb{H}_1$

$$p_{\mathcal{M}}(x)=\begin{cases}\frac{\sqrt{2}}{\Gamma(\frac{1}{2})\sqrt{\sigma^4/M}}\exp\left(-\frac{1}{2}(\frac{x}{\sqrt{\sigma^4/M}})^2\right), & \text{under }\mathbb{H}_0\\ \frac{1}{2^L P_s^L\Gamma(L)}x^{L-1}\exp\left(-\frac{x}{2P_s}\right), & \text{under }\mathbb{H}_1\end{cases} \tag{4.90}$$

are depicted on Fig. 4.20 (b) using the following parameters: $L=4$, $P_s=\sigma^2=1$ and $M=148$.

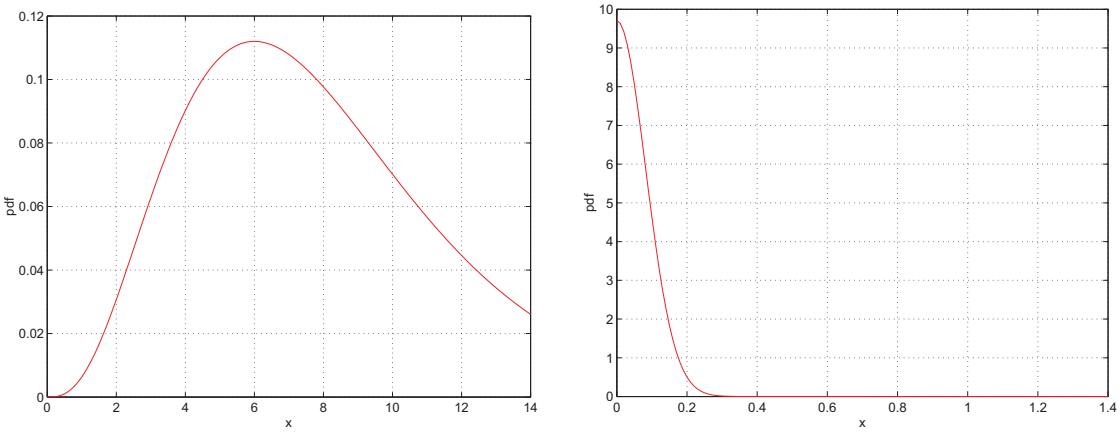

(a) Pdf $p_{\mathcal{M}}(x)$ under $\mathbb{H}_1$ (b) Pdf $p_{\mathcal{M}}(x)$ under $\mathbb{H}_1$

FIGURE 4.20 – $p_{\mathcal{M}}(x)$ under hypotheses $\mathbb{H}_0$ and $\mathbb{H}_1$.

4.5.3.3 Analytical Expressions of P_d and P_{fa}

The detection and false alarm probabilities P_d and P_{fa} are obtained by integrating (4.90) between the fixed level ς and $+\infty$. For the calculation of P_d, the solution is given in [148] and [149]:

$$\begin{aligned}P_d&=P(\mathcal{M}>\varsigma|\mathbb{H}_1)\\&=\int_{\varsigma}^{+\infty}\frac{x^{L-1}}{2^L P_s^L\Gamma(L)}\exp\left(-\frac{x}{2P_s}\right)dx\\&=\frac{\Gamma(L,\frac{\varsigma}{2P_s})}{\Gamma(L)},\end{aligned} \tag{4.91}$$

where $\Gamma(.,.)$ is the incomplete gamma function [147]. In the case $\mathbb{H}_0$, we have:

$$\begin{aligned} P_{fa} &= P(\mathcal{M} > \varsigma | \mathcal{H}_0) \\ &= \int_{\varsigma}^{+\infty} p_{\mathcal{M}}(x) dx \\ &= \int_{\varsigma}^{+\infty} \frac{\sqrt{2}}{\Gamma(\frac{1}{2})\sqrt{\sigma^4/M}} e^{-\frac{1}{2}(\frac{x}{\sqrt{\sigma^4/M}})^2} dx. \end{aligned} \tag{4.92}$$

By using the change of variable $X = \frac{x}{\sqrt{2\sigma^4/M}}$, and knowing that $\Gamma(\frac{1}{2}) = \sqrt{\pi}$, one can recognize the complementary error function $erfc(x) = 1 - erf(x)$:

$$\begin{aligned} P_{fa} &= \int_{\frac{\varsigma}{\sqrt{2\sigma^4/M}}}^{+\infty} \frac{2}{\sqrt{\pi}} e^{-X^2} dX \\ &= erfc(\frac{\varsigma\sqrt{M}}{\sqrt{2}\sigma^2}). \end{aligned} \tag{4.93}$$

Since the incomplete gamma function is not directly invertible in (4.91), it is not possible to derive an analytical expression of the threshold ς function of the target detection probability P_d^t. However, an approximation by means of a computer calculation or a series expansion of the invert of (4.91), or a simple characterization of ς by simulations can be done. We shall consider this third solution thereafter. Furthermore, the next section aims to characterize the performance of the proposed detection algorithm, and the validity of the proposed analytical developments.

4.5.4 Simulations Results

The parameters are the same as the ones used for the theoretical and the practical approach of the algorithm.

4.5.4.1 Choice of the threshold ς

Fig. 4.21 depicts the metric $\mathcal{M} = |M_2 - \hat{\sigma}^2|$ versus the number of iterations, under the hypotheses $\mathbb{H}_0$ and $\mathbb{H}_1$. The SNR is fixed equal to 0 dB. In presence of signal, the average signal power P_s is equal to 1. The simulation is obtained thanks to 4000 simulation runs.

It can be seen that the a priori qualitative analysis is verified. Indeed, for a sufficient number of iterations (according to the value e_σ, as shown thereafter), $\mathcal{M}$ converges to P_s under $\mathbb{H}_1$, and converges to zero under $\mathbb{H}_0$. It has been noticed that it is not possible to find an exact value of ς according to $P(\mathcal{M} > \varsigma | \mathbb{H}_1) = P_d^t$. However, it is observable on Fig. 4.21 that the choice of the threshold is not restricting. Indeed, choosing ς so small as desired ensures a probability P_d close to one, and, for a sufficient number of iterations, it also ensure a low value for P_{fa}. However, reducing the value of e_σ increases the number of required iterations, as shown in the following. For an expected detection probability, a trade-off between the complexity and the acceptable level of false alarm probability has to be taken into account.

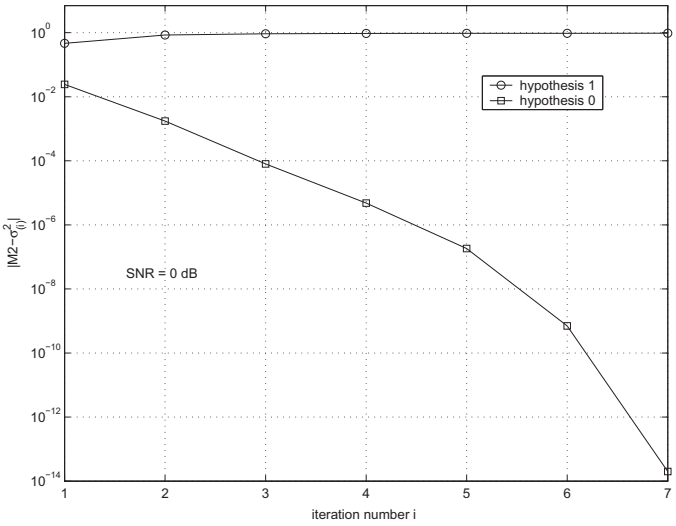

FIGURE 4.21 – $|M_2 - \hat{\sigma^2}|$ versus the iterations number under $\mathbb{H}_0$ and $\mathbb{H}_1$, for SNR = 0 dB.

4.5.4.2 Effect on the Choice of e_σ on the Detector Performance

It is shown in this section that the choice of the threshold e_σ value does not have any effect on the detection performance of the proposed method, but only plays a role on the speed of convergence of the algorithm. Fig. 4.22 depicts the curves of probabilities of detection P_d and false alarm P_{fa} versus the SNR from -15 dB to 10 dB. In order to ensure the convergence of the algorithm, e_σ must have a low value. Subfigures (a) and (b) then depict the curves P_d and P_{fa} for $e_\sigma = 0.01$ and $e_\sigma = 0.0001$ respectively. According to these recommendations, the initialization $\sigma^2_{(i=0)}$ is equal to $40 \times M_2$. We also arbitrary fix the threshold $\varsigma = 0.01$, its effect on the detection performance being further studied. The figure is obtained thanks to 2000 simulation runs.

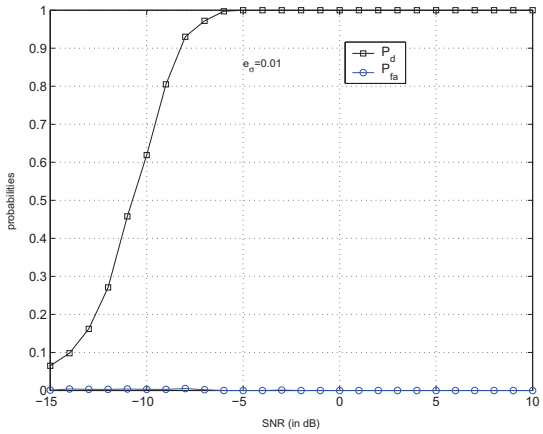

(a) Detection and false alarm probabilities P_d and P_{fa} versus SNR, for $e_\sigma = 0.01$

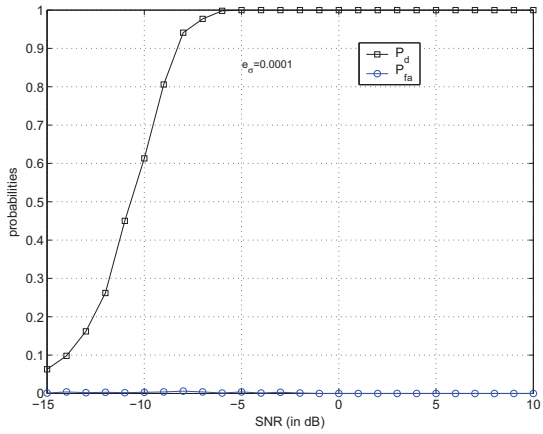

(b) Detection and false alarm probabilities P_d and P_{fa} versus SNR, for $e_\sigma = 0.0001$

FIGURE 4.22 – Detection and false alarm probabilities in function of SNR, for two values e_σ and for a fixed value $\varsigma = 0.01$.

We observe that the curves of P_d and P_{fa} match from subfigure (a) to (b). P_{fa} is equal to zero or nearly for all SNR values and P_d reaches one from SNR=-5 dB. The detector can then reach the perfect one from $SNR \geq -5$ dB, i.e. in low SNR environment. We conclude that, assuming a value of e_σ low enough to ensure the convergence of the algorithm, this threshold does not have any effect on the detection performance of the proposed method.

Fig. 4.23 displays the iterations number the algorithm needs before it stops versus the SNR from -10 to 10 dB. We consider three different values for the threshold: e_σ= 0.01, 0.001 and 0.0001. The conditions of simulations remain the same.

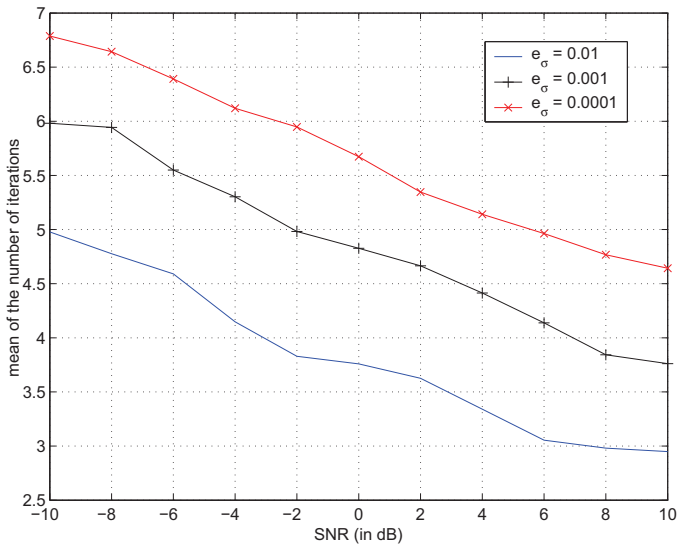

FIGURE 4.23 – Means of the number of iterations needed by the algorithm to stop versus SNR (in dB), for three values of threshold e_σ.

Although the figures 4.22 (a) and (b) present almost the same probabilities whatever the threshold e_σ, they differ from each other according to the number of iterations the algorithm requires before stopping. Indeed, remembering that we compare $|\hat{\sigma}^2_{(i)} - \hat{\sigma}^2_{(i-1)}|$ with e_σ, the lower e_σ, the larger the number i of iterations needed to reach e_σ. However, Fig. 4.23 shows that the maximum mean of iterations is less than 7 for SNR=-10 dB and shows the maximum mean of iterations is less than 5 for SNR=-10 dB and $e_\sigma = 0.0001$, which is a reasonable number of iterations. We conclude that the choice of e_σ has no effect on the detector efficiency, while it allows the convergence of the algorithm. Furthermore, the number of required iterations reasonably increases when e_σ and the SNR have low values. The detector then remains usable in practice under these conditions.

4.5.4.3 Receiver Operating Characteristic of the Detector

The performance of a detector is usually evaluated by means of the receiver operating characteristic (ROC) curves, depicting the detection probability P_d function of the false alarm probability P_{fa}. The optimal detector is logically reached at the point $(P_{fa} = 0, P_d = 1)$. The curve $P_{fa} = P_d$ is called line of chance, and corresponds to a detector which make as much good decisions as false alarms. If the ROC curve is above the first bisector, the detector is qualified as efficient, since $P_d > P_{fa}$.

Fig. 4.24 shows the ROC curves of the proposed detector for low SNR values: SNR = -10 dB and SNR = 0 dB. The conditions of simulation remain the same, and we fix the threshold $e_\sigma = 0.01$. The proposed detector is also compared to the usual energy detector, whose metric $\mathcal{M}$ is equal to the second order-moment of the received signal M_2. This metric is compared to the threshold ς to obtain the following decision rule

$$\mathbb{H}_0, \text{ if } \mathcal{M} < \varsigma$$
$$\mathbb{H}_1, \text{ else.}$$

Each point of the curves is obtained thanks to 2000 simulation runs.

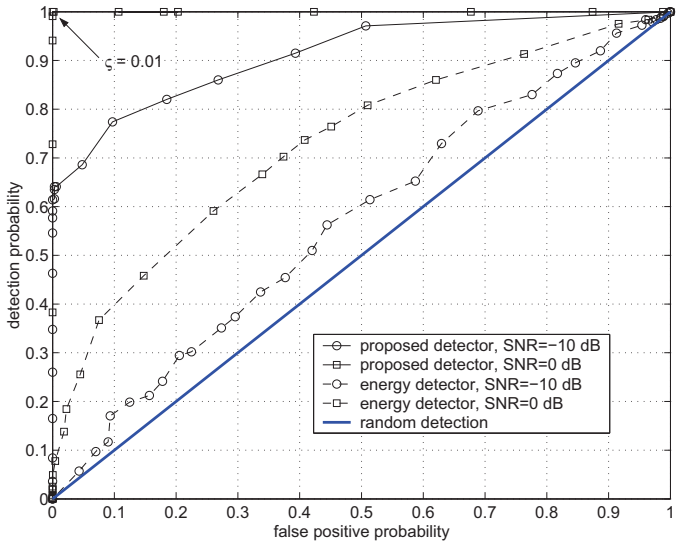

FIGURE 4.24 – Receiver operating characteristic (ROC) curves of the proposed method compared to the energy detector for SNR=-10 dB and SNR=0 dB.

We observe that the proposed detector outperforms the energy detector, whatever the SNR. The reason is that we consider the detection of a preamble transmitted over a Rayleigh channel. As a consequence, the power of the received signal P_S in (4.81) is not constant and follows a chi-square distribution. The result of this is that, for simulations made at a fixed SNR, the noise variance is also a varying process, which deteriorates the detector performance. For more precisions, the theoretical development of the energy detection of signal with random amplitude are given in [148,149]. Fig. 4.24 also confirms that the proposed detector is able to reach the perfect detector for $\varsigma = 0.01$. Indeed, for SNR=0 dB, we observe that ROC curve reaches the point $(P_{fa} = 0, P_d = 1)$, as we remarked in Fig. 4.22 for $SNR \geq -5$ dB. We conclude that the proposed detector is very efficient for the detection of preamble over fading channels, even for low SNR values.

Fig. 4.25 compares the ROC curves of the proposed detector given by simulation with the theoretical ones P_d and P_{fa} given by (4.91) and (4.93) respectively. It is observable that the theoretical curve for SNR=0 dB is very close to the one obtained by simulation, whereas for SNR=-10 dB, the difference is more noticeable. This observation tallies with the discussion on the approximation $\hat{\sigma}^2 \approx \frac{1}{M}\sum_{m=0}^{M-1}|W_m|^2$ in the calculation of the metric $\mathcal{M}$ under the hypothesis $\mathbb{H}_1$. Indeed, this approximation is justified for high values of SNR, but becomes

wrong for the very low SNR values. However, the theoretical curves allows to give an idea on the detector performance for a given SNR, even for the low SNR values.

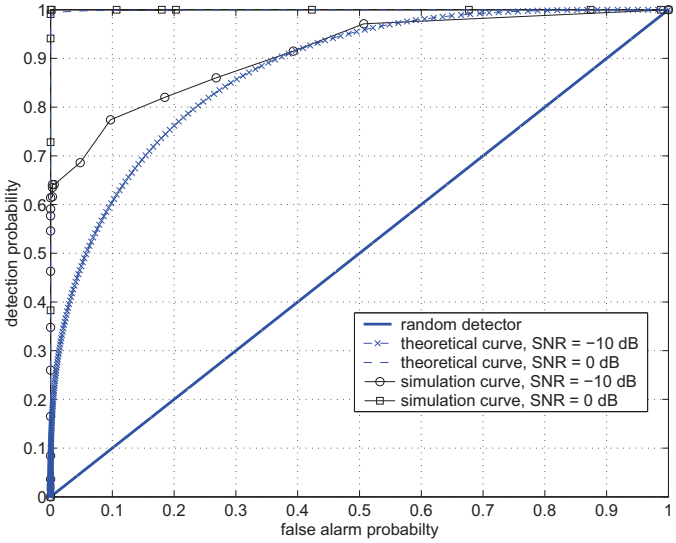

FIGURE 4.25 – Comparison of the receiver operating characteristic (ROC) curves obtained by simulation and in theory.

4.6 Conclusion

In this chapter, an MMSE-based algorithm for the joint SNR and channel estimations has been presented. Unlike the technique presented in Chapter 3, the proposed method does not require neither any a priori knowledge of the channel statistics nor the noise level. To this end, the MMSE noise variance estimation feeds the LMMSE channel estimation, and vice versa. A theoretical and a more realistic scenario of the algorithm have been proposed. In the two cases, the convergence to a non-null solution has been proved. Moreover, compared to several techniques of the literature, the performance of the estimator is close to the optimal one, for both SNR and channel frequency response. Finally, based on the realistic scenario, an application of the method to spectrum sensing has been presented. Thus, if a PU is detected, the algorithm also estimates the channel and the SNR. If not, the SU can access the free band and get a measure of the noise level, as depicted on Fig. 4.26.

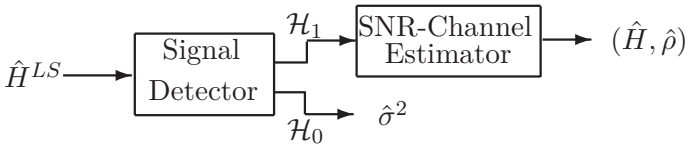

FIGURE 4.26 – Diagram of the proposed algorithm, usable as detector and estimator.

This figure is a summary of the chapter. The detector block has been presented in Section 4.5, and the channel-SNR estimator corresponds to the practical case of Section 4.4. To conclude, the proposed algorithm has different applications with the same structure, so it perfectly comes in the scope of cognitive radio.

Chapter 5

Study of the Interpolation on the Rayleigh Channel Estimation Performance

5.1 Introduction

In a wide range of applications, when a function is known only in some points, an interpolation is necessary to estimate the function between the nodes. In some communications standards, such as DRM/DRM+ [1], the pilots tones are sparse in the OFDM frame, so an interpolation is performed to estimate the channel frequency response over the time-frequency lattice. In the same way, the comb-type pilot arrangement requires an interpolation over the frequency axis. Such interpolations lead to estimation errors, which can induce some errors of decision and finally a corrupted signal at the receiver. It results an error floor on the BER curves for high SNR level.

We here study interpolation methods based only on mathematics, such as the linear interpolation [25,27], but without physical consideration such as LMMSE [7,18] or using FFT [13]. In [150], the effect of several channel models (e.g. Rayleigh, Rice, Nakagami) have been studied to express the theoretical symbol error rates (SER) of linear modulations in a single carrier context. This study has been extended in [151, 152] to the effects of the channel estimation errors on the BER for a single carrier signal transmitted over a Rayleigh channel. In an OFDM context, [153] shows the BER floor due to different interpolation methods and for different constellation sizes. In [46, 154], an analytical expression of the SER and BER for a transmission in presence of channel frequency offset and channel estimation errors is derived for different modulation schemes. However, the developments are made by using the probability density functions (pdfs) given in [155], in which the channel coefficients and the error of estimation are supposed to be uncorrelated.

In this chapter, the effect of the estimation errors due to the interpolations is analytically characterized by means of the MSE of the estimation and the error floor of the BER, in an OFDM context. To this end, since we consider Rayleigh channels, it is possible to derive the statistical parameters of the interpolation error, such as its variance, its mean or its bias. Furthermore, it is shown that the channel coefficients and the errors are correlated, and the correlation coefficient is expressed. In order to perform the analytical developments, two

interpolation methods are considered: the nearest neighbor and the linear ones, although it will be shown that the study can be done for all interpolation techniques from which it is possible to theoretically derive statistics.

First, the statistics of the interpolation errors are derived, according to the interpolation method and the frequency gap between two consecutive pilot tones δ_p (see Section 2.4.2). Second, the MSE of the channel estimation is expressed thanks to these parameters. Finally, the BER floor is given for two constellations sizes: a BPSK and a 4-QAM. To this end, a geometrical analysis function of the constellation is proposed. A short study of the effect of the interpolation errors on the BER floor has been presented in [43].

5.2 System Model

This section aims to recall some principles presented in Chapter 2 and to give the notations and the simulations parameters used throughout this chapter. Let us consider OFDM symbols with a comb-type pilot arrangement such as the pilot tones are evenly distributed in each symbol, with a frequency gap noted δ_p. As illustrated on Fig. 5.1, three values $\delta_p \in \{2, 3, 4\}$ are considered, so as to generalize the further developments whatever δ_p. On Fig. 5.1, the pilot tones are black and the data carriers are white. For simulations reasons, each symbol has $M = 241$ subcarriers. Indeed, it is noticeable that $241 = k \times \delta_p + 1$. Furthermore, the developments and the simulations are achieved without channel coding.

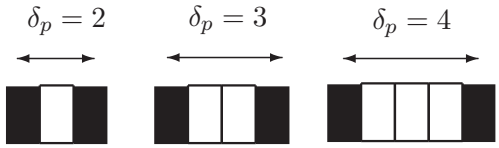

Figure 5.1 – Illustration of the pilot arrangements for different values of δ_p.

Thus, the carriers index $m = p$ points out the pilot tones, such as $p = 0, \delta_p, ..., M - 1$.

Since the interpolations methods are usually expressed for continuous functions, some developments will be achieved in a continuous formalism. However, it will be shown that the developments remain valid in the discrete formalism. Thus, the channel frequency response will be equivalently expressed by

$$H(f) = \sum_{l=0}^{L-1} h_l e^{-2j\pi f \tau_l} \Longleftrightarrow H_m = \sum_{l=0}^{L-1} h_l e^{-2j\pi \frac{\beta_l m}{M}}, \tag{5.1}$$

where $\beta_l = \tau_l / \tau_s$, with τ_s the sampling time. In order to validate the further developments by simulations, two channel noted $\mathcal{H}_{(1)}$ and $\mathcal{H}_{(2)}$ are considered. Their parameters (the delay and variance of each non-null path) are summed up in Tables 5.1 and 5.2. We remind that σ_l^2 is the variance of the l^{th} path. It can be seen that the number of paths, the maximum delay and the variance of the channels differ from $\mathcal{H}_{(1)}$ to $\mathcal{H}_{(2)}$. Furthermore, it is verified that the pilot gap δ_p is chosen according to

$$\delta_f \leq \frac{B_C}{2} \Longleftrightarrow \frac{\delta_p}{M\tau_s} \leq \frac{1}{2\beta_L \tau_s}. \tag{5.2}$$

TABLE 5.1 – Channel $\mathcal{H}_{(1)}$ parameters.

Channel $\mathcal{H}_{(1)}$				
paths l	0	1	2	3
delays β_l	0	6	13	16
variance σ_l^2	1	0.5	0.4	0.2

TABLE 5.2 – Channel $\mathcal{H}_{(2)}$ parameters.

Channel $\mathcal{H}_{(2)}$							
paths l	0	1	2	3	4	5	6
delays β_l	0	4	9	14	16	18	21
variance σ_l^2	1	0.5	0.4	0.3	0.3	0.2	0.1

We remind that the frequency positions of the pilot tones are denoted f_p and p in the continuous and discrete formalism, respectively, and N_p is the number of pilot tones by OFDM symbol. Once more, let us assume that the power of the pilots is normalized, i.e. $\mathcal{P} = C_p C_p^* = 1$. According to the pilot positions or not, the channel estimation is equivalently expressed by

$$\hat{H}(f) = \begin{cases} \hat{H}(f)^{LS} = H(f) + \frac{W(f)}{C(f)} & \text{if } f = f_p \\ \hat{H}(f)^{int} + (\frac{W(f)}{C(f)})^{int} & \text{if } f \neq f_p \end{cases} \iff \hat{H}_m = \begin{cases} \hat{H}_m^{LS} = H_m + \frac{W_m}{C_m} & \text{if } m = p \\ \hat{H}_m^{int} + (\frac{W_m}{C_m})^{int} & \text{if } m \neq p \end{cases}, \tag{5.3}$$

where the exponent ^{int} denotes the interpolated values of the channel and the noise. Since the channel and the noise are uncorrelated, the interpolation of the sum of the channel and noise is the sum of the respective interpolations. A characterization of the interpolated noise is given afterward.

5.3 Statistics of the Interpolation Errors

In this section, we first interest in the statistics of the error $H_m - \hat{H}_m^{int}$ without taking into account the noise. Second, the interpolated noise $(\frac{W_m}{C_m})^{int}$ is separately characterized. The statistics of the noise and the channel estimation error will be then used in order to derive the analytical expressions of the MSE and the BER floor.

5.3.1 Nearest Neighbor Interpolation

5.3.1.1 Notations and Reminder

As presented in Section 2.4.2, let us consider three consecutive frequency pilot positions $f_{p-\delta_p}$, f_p and $f_{p+\delta_p}$, such as f_p is not at the edge of the channel, i.e. $p \notin \{0, M-1\}$. We remind that we denote f_{p^-} and f_{p^+} the centers of the intervals $[f_{p-\delta_p}, f_p]$ and $[f_p, f_{p+\delta_p}]$ respectively, and, $\forall f \in [f_{p^-}, f_{p^+}]$, the channel estimation made by a nearest neighbor (NN) interpolation on this interval is

$$\hat{H}(f) = \hat{H}(f_p)^{LS} = H(f_p) + \frac{W(f_p)}{C(f_p)}, \tag{5.4}$$

where $\hat{H}(f_p)^{LS}$ is the LS estimation performed on the position f_p. Obviously, if $p = 0$ or $p = M-1$, the NN interpolation is limited to the intervals $[f_0, f_{0^+}]$ and $[f_{M-1^-}, f_{M-1}]$, respectively, but the expression (5.4) remains the same. Since the center of the intervals $[f_{p-\delta_p}, f_p]$ does not necessarily match with an integer number in the discrete formalism, Fig. 5.2 displays the discrete interval to be considered for the different δ_p values. Thus, the subscripts of the interpolated value $m \neq p$ can be expressed by $m = p+k$, where $k \in \{1\}$ for $\delta_p = 2$, $k \in \{-1, 1\}$ for $\delta_p = 3$, $k \in \{-1, 1, 2\}$ for $\delta_p = 4$, and so on.

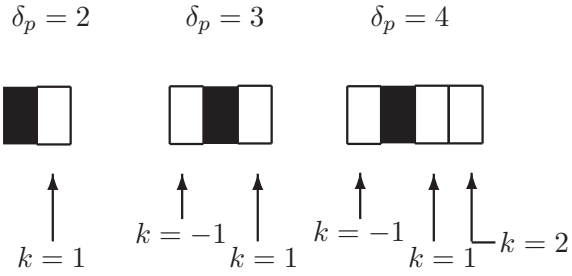

Figure 5.2 – Discrete intervals for the nearest neighbor interpolation, for different values of δ_p.

5.3.1.2 Pdf of the Errors of the NN Interpolation

From (5.4), for a given frequency $f \neq f_p$, the errors of the NN interpolation noted $e_{h,NN}$ and ξ_{NN} are defined without taking into account the noise, such as

$$\begin{aligned} e_{h,NN} &= \hat{H}(f)^{int} - H(f) \\ \xi_{NN} &= |\hat{H}(f)^{int} - H(f)| \\ &= |H(f_p) - H(f)|, \end{aligned} \tag{5.5}$$

and, by replacing H by its value given by (5.1), it yields

$$\xi_{NN} = |\sum_{l=0}^{L-1} h_l e^{-2j\pi f_p \tau_l}(1 - e^{-2j\pi \Delta_f \tau_l})|, \tag{5.6}$$

where $\Delta_f = f - f_p$, which does not be mistaken with $\delta_f = f_{p+\delta_p} - f_p$. As $e^{-2j\pi f_p \tau_l}(1-e^{-2j\pi \Delta_f \tau_l})$ is deterministic, we conclude that, since $|H(f)|$ follows a Rayleigh distribution, then ξ_{NN} is also a Rayleigh variable. From (5.6), whatever $p = 0, \delta_p, .., M-1$ and whatever δ_p, we now express ξ_{NN} in the discrete formalism:

$$\xi_{NN} = |\sum_{l=0}^{L-1} h_l e^{-2j\pi \frac{p\beta_l}{M}}(1 - e^{-2j\pi \frac{k\beta_l}{M}})|. \tag{5.7}$$

It can be seen in (5.7) that the variance of ξ_{NN} depends on the value $|k|$, so it is better to note the error $\xi_{k,NN}$. The variance of $\xi_{k,NN}$, noted $\sigma^2_{\xi_{k,NN}}$, logically also depends on $|k|$, and is defined by

$$\begin{aligned}
\sigma^2_{\xi_{k,NN}} &= E\{|\xi|^2\} \\
&= E\{\left(\sum_{l_1=0}^{L-1} h_{l_1} e^{-2j\pi\frac{p\beta_{l_1}}{M}}(1-e^{-2j\pi\frac{k\beta_{l_1}}{M}})\right)\left(\sum_{l_2=0}^{L-1} h_{l_2} e^{-2j\pi\frac{p\beta_{l_2}}{M}}(1-e^{-2j\pi\frac{k\beta_{l_2}}{M}})\right)^*\} \\
&= E\{\sum_{l=0}^{L-1}|h_l|^2(2-e^{-2j\pi\frac{k\beta_l}{M}}-e^{2j\pi\frac{k\beta_l}{M}})\} \\
&= \sum_{l=0}^{L-1}\sigma_l^2(2-2\cos(2\pi\frac{k\beta_l}{M})). \qquad (5.8)
\end{aligned}$$

We observe in (5.8) that, since $\sigma^2_{\xi_{k,NN}}$ depends on $|k|$, it also depends on the considered gap δ_p. Thus, for $\delta_p \in \{2,3\}$, $|k|=1$, so $\sigma^2_{\xi_{k,NN}}$ takes a sole value. For $\delta_p = 4$, $|k|=1$ for two thirds of the estimated carriers in a discrete interval described by Fig. 5.2, and $|k|=2$ for one third. Thus, we deduce the variance $\sigma^2_{\xi_{NN}}$ of the error ξ_{NN} (considered for all k)

$$\begin{aligned}
\sigma^2_{\xi_{NN}} &= \sigma^2_{\xi_{1,NN}} = \sum_{l=0}^{L-1}\sigma_l^2(2-2\cos(2\pi\frac{\beta_l}{M})), \text{ if } \delta_p \in \{2,3\} \\
\sigma^2_{\xi_{NN}} &= \frac{2}{3}\sigma^2_{\xi_{1,NN}} + \frac{2}{3}\sigma^2_{\xi_{2,NN}} \\
&= \frac{2}{3}\sum_{l=0}^{L-1}\sigma_l^2(2-2\cos(2\pi\frac{\beta_l}{M})) + \frac{1}{3}\sum_{l=0}^{L-1}\sigma_l^2(2-2\cos(2\pi\frac{2\beta_l}{M})), \text{ if } \delta_p = 4, \qquad (5.9)
\end{aligned}$$

as well as the pdf $p_{\xi_{NN}}$:

$$\begin{aligned}
p_{\xi_{NN}}(\xi) &= \frac{\xi}{\sigma^2_{\xi_{1,NN}}} e^{-\frac{\xi^2}{2\sigma^2_{\xi_{1,NN}}}}, \text{ for } \delta_p = 2 \text{ and } \delta_p = 3 \\
p_{\xi_{NN}}(\xi) &= \frac{2}{3}(\frac{\xi}{\sigma^2_{\xi_{1,NN}}} e^{-\frac{\xi^2}{2\sigma^2_{\xi_{1,NN}}}}) + \frac{1}{3}(\frac{\xi}{\sigma^2_{\xi_{2,NN}}} e^{-\frac{\xi^2}{2\sigma^2_{\xi_{2,NN}}}}), \text{ for } \delta_p = 4. \qquad (5.10)
\end{aligned}$$

The weights 2/3 and 1/3 in (5.9) and (5.10) correspond to the rate of the carriers such as $|k|=1$ and $|k|=2$ divided by the number of data-carriers in each discrete interval described on Fig. 5.2, for $\delta = 4$. Figs. 5.3 (a) and (b) depicts the pdf $p_{\xi_{NN}}(\xi)$ for $\delta_p \in \{2,3,4\}$. The simulations curves are compared to the ones analytically obtained for both channels $\mathcal{H}_{(1)}$ and $\mathcal{H}_{(2)}$. For the channel $\mathcal{H}_{(1)}$, we have $\sigma^2_{\xi_{1,NN}} = 0.092$ and $\sigma^2_{\xi_{2,NN}} = 0.3567$. For the channel $\mathcal{H}_{(2)}$, we have $\sigma^2_{\xi_{1,NN}} = 0.1908$ and $\sigma^2_{\xi_{2,NN}} = 0.73$. We can see that the curves drawn by simulations exactly match the ones drawn according to the theoretical expression (5.10), which validates the development.

Since the curves perfectly match, the expression of $p_{\xi_{NN}}(\xi)$ can be reasonably extrapolated whatever $\delta_p > 2$:

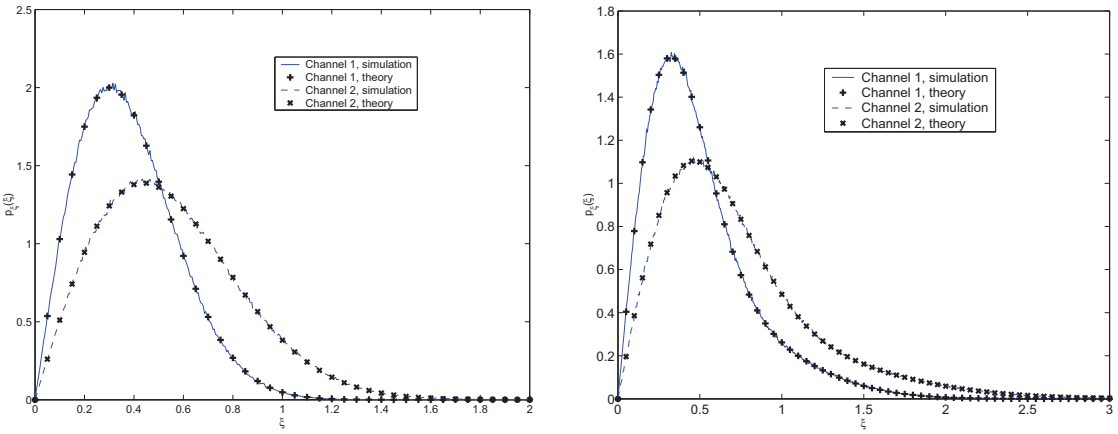

(a) NN interpolation, $\delta_p \in \{2, 3\}$ (b) NN interpolation, $\delta_p = 4$

Figure 5.3 – Probability density function $p_{\xi_{NN}}(\xi)$ for the NN interpolation, comparison between simulation and theory for $\delta_p \in \{2, 3, 4\}$ and for the channels $\mathcal{H}_{(1)}$ and $\mathcal{H}_{(2)}$.

$$p_{\xi_{NN}}(\xi) = \frac{1}{\delta_p - 1} \frac{\xi}{\sigma^2_{\xi_{\delta_p/2}}} e^{-\frac{\xi^2}{2\sigma^2_{\xi_{\delta_p/2}}}} + \frac{2}{\delta_p - 1} \sum_{k=1}^{\delta_p/2-1} \frac{\xi}{\sigma^2_{\xi_k}} e^{-\frac{\xi^2}{2\sigma^2_{\xi_k}}}, \text{ if } \delta_p \text{ is even}$$

$$p_{\xi_{NN}}(\xi) = \frac{2}{\delta_p - 1} \sum_{k=1}^{(\delta_p-1)/2} \frac{\xi}{\sigma^2_{\xi_k}} e^{-\frac{\xi^2}{2\sigma^2_{\xi_k}}}, \text{ if } \delta_p \text{ is odd .} \tag{5.11}$$

The limit $\delta_p/2$ (or $\delta_p - 1)/2$) in the sum and the coefficient 2 which multiplies the sum are due to the fact that $\sigma^2_{\xi_k} = \sigma^2_{\xi_{\delta_p - k}}$.

5.3.1.3 Joint pdf of the Errors of the NN Interpolation

It is obvious from (5.1) and (5.6) that the channel frequency response and the interpolation error are correlated. The model proposed in [155] is then not valid in this context. Since the channel and the error follow a Rayleigh distribution ($r = |H(f)|$ and ξ, respectively), we know from [44, 45] that the joint pdf of two correlated Rayleigh variables is It is obvious from (5.1) and (5.6) that the channel frequency response and the interpolation error are correlated. The model proposed in [155] is then not valid in this context. Since the channel and the error follow a Rayleigh distribution ($r = |H(f)|$ and ξ, respectively), we know from [44, 45] that the joint pdf of two correlated Rayleigh variables is

$$p_{r,\xi}(r, \xi) = \frac{r\xi}{\sigma^2_r \sigma^2_\xi (1 - \rho^2_{r\xi})} \exp\left(-\frac{\sigma^2_\xi r^2 + \sigma^2_r \xi^2}{2\sigma^2_r \sigma^2_\xi (1 - \rho^2_{r\xi})} \right) I_0\left(\frac{r\xi\rho_{r\xi}}{\sigma_r \sigma_\xi (1 - \rho^2_{r\xi})} \right), \tag{5.12}$$

where $\rho_{r\xi}$ is the correlation coefficient between the channel and the error of estimation due to the interpolation, which is noted $\rho_{r\xi,NN}$ in the case of a NN interpolation, and is expressed by

$$\begin{aligned}\rho_{r\xi,NN} &= \frac{|E\{H(f)e_h^*\}|}{\sigma_h\sigma_{\xi_{NN}}} \\ &= \frac{|E\{H(f)(\hat{H}^{int}(f)-H(f))^*\}|}{\sigma_h\sigma_{\xi_{NN}}} \\ &= \frac{|\sum_{l=0}^{L-1} E\{|h_l|^2(e^{2j\pi\tau_l(f_p-f)}-1)\}|}{\sigma_h\sigma_{\xi_{NN}}} \\ &= \frac{|\sum_{l=0}^{L-1} \sigma_l^2(e^{-2j\pi\tau_l\Delta_f}-1)|}{\sigma_h\sigma_{\xi_{NN}}}. \end{aligned} \tag{5.13}$$

In the discrete domain, the error depends on the value of k, so we obtain:

$$\rho_{r\xi_k,NN} = \frac{|\sum_{l=0}^{L-1} \sigma_l^2(e^{-2j\pi\frac{\beta_l k}{M}}-1)|}{\sigma_h\sigma_{\xi_{k,NN}}}. \tag{5.14}$$

Since it is not convenient to compare the simulated and analytical joint pdf, we derive from (5.12) the conditional pdf $p_{\xi|r,\xi_k}(\xi|r,\xi_k)$ defined for a given value k by

$$\begin{aligned}p_{\xi|r,\xi_k}(\xi|r,\xi_k) &= \frac{p_{r,\xi_k}(r,\xi_k)}{p_r(r)} \\ &= \frac{\xi}{\sigma_{\xi_k}^2(1-\rho_{r\xi_k}^2)}\exp\left(-\frac{\rho_{r\xi_k}^2 r^2}{2\sigma_r^2(1-\rho_{r\xi_k}^2)}\right)\exp\left(-\frac{\xi^2}{2\sigma_{\xi_k}^2(1-\rho_{r\xi_k}^2)}\right) \\ &\quad \times I_0\left(\frac{r\xi\rho_{r\xi_k}}{\sigma_r\sigma_{\xi_k}(1-\rho_{r\xi_k}^2)}\right). \end{aligned} \tag{5.15}$$

As it has been made for the pdf of ξ, the conditional pdf is also a weighted sum of the conditional pdfs (5.15) for different k values, and for which the correlation coefficient given is by (5.14) in the case of the NN interpolation. The generalized expression of the joint pdf is directly given by:

$$\begin{aligned}p_{\xi|r}(\xi|r) &= \frac{1}{\delta_p-1}p_{\xi|r,\xi_{\delta_p/2}}(\xi|r,\xi_{\delta_p/2}) + \frac{2}{\delta_p-1}\sum_{k=1}^{\delta_p/2-1} p_{\xi|r,\xi_k}(\xi|r,\xi_k), \text{ if } \delta_p \text{ is even} \\ p_{\xi|r}(\xi|r) &= \frac{2}{\delta_p-1}\sum_{k=1}^{(\delta_p-1)/2} p_{\xi|r,\xi_k}(\xi|r,\xi_k), \text{ if } \delta_p \text{ is odd .} \end{aligned} \tag{5.16}$$

The conditional pdf (5.16) is a general formulation, which can also be used for other interpolation methods. Figs. 5.4 (a) and (b) display the conditional pdf $p_{\xi|r}(\xi|r)$ for $\delta_p = 3$ and $\mathcal{H}_{(1)}$, and $\delta_p = 2$ and $\mathcal{H}_{(2)}$, respectively. The correlation coefficients calculated by means of (5.14) are equal to $\rho_{r\xi_1,NN} = 0.6723$ for the channel $\mathcal{H}_1$ and $\rho_{r\xi_1,NN} = 0.7128$ for the channel $\mathcal{H}_2$. In order to validate the development whatever r, on each figure 5.4 (a) and (b), $p_{\xi|r}(\xi|r)$ is obtained conditionally to two different values $r = 0.1$ and $r = 4$. Since the functions are not continuous in digital simulations, it is not possible to perform a perfect equality $r = 0.1$ or $r = 4$. Here are the steps to get the simulations curves of Fig. 5.4:

1. The channel samples H_m are created,
2. Due to $H(f)$ is sampled into H_m, it is decided that $|H_m| = r$ if $r - 0.001 \leq |H_m| \leq r + 0.001$,
3. The error ξ is measured conditionally to r.

Since r is approximated by the interval $[r - 0.001; r + 0.001]$, it could explain the slight difference between the simulations and the analytical curves.

First, it is noticeable that the correlation coefficients have high values (i.e. >0.5), so it is verified that the uncorrelated model of [155] is not valid in the proposed context. Second, the curves obtained by simulations match the analytical ones, so it validates the previous theoretical developments.

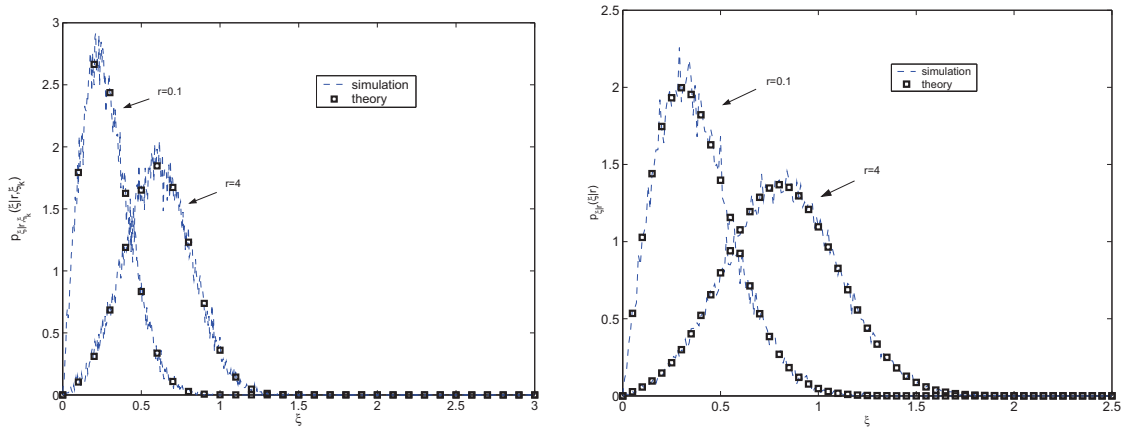

(a) $\delta_p = 3$, channel $\mathcal{H}_{(1)}$ (b) $\delta_p = 2$, channel $\mathcal{H}_{(2)}$

Figure 5.4 – Conditional probability density functions $p_{\xi|r}(\xi|r)$, comparison between analytical and simulations curves.

5.3.2 Linear Interpolation

In this section, as previously, a similar development is performed for the linear interpolation. We first recall the expression of the linear interpolation, for $f \in [f_p, f_{p+1}]$, $\hat{H}(f)$ is obtained by

$$\hat{H}(f) = \hat{H}^{LS}(f_p) + (f - f_p)\frac{\hat{H}^{LS}(f_{p+\delta_p}) - \hat{H}^{LS}(f_p)}{f_{p+\delta_p} - f_p}, \tag{5.17}$$

where $\hat{H}^{LS}(f_p)$ is the LS estimation performed on the p^{th} pilot tone. We remind that, in this section, we only interest to the interpolation errors, so (5.17) is rewritten without the noise component by

$$\hat{H}(f)^{int} = H(f_p) + (f - f_p)\frac{H(f_{p+\delta_p}) - H(f_p)}{f_{p+\delta_p} - f_p}. \tag{5.18}$$

5.3.2.1 Pdf of the Errors of the Linear Interpolation

For the linear interpolation, it is known that the error between a given function g of class $\mathcal{C}^2$ and its approximation $\hat{g}$ by a linear function at a point x is given by

$$|g(x) - \hat{g}(x)| = \frac{1}{2}|(x_{p+\delta_p} - x)(x_p - x)| \times |g''(y)|, \tag{5.19}$$

where x_p and $x_{p+\delta_p}$ are two consecutive nodes such as $\hat{g}(x_p) = g(x_p)$ and $\hat{g}(x_{p+\delta_p}) = g(x_{p+\delta_p})$, and $y \in [x_p, x_{p+\delta_p}]$. The proof of this assertion is given in Appendix C. It is obvious that the channel frequency response (5.1) is $\mathcal{C}^2$ on $[f_0, f_{M-1}]$, so (5.19) can be used to determine the error of interpolation noted ξ_{li}, on each interval $[f_p, f_{p+\delta_p}]$:

$$\xi_{li} = |H(f) - \hat{H}(f)| = \frac{1}{2}|(f_{p+\delta_p} - f)(f_p - f)| \times |H''(\alpha)|, \tag{5.20}$$

where $\alpha \in [f_p, f_{p+\delta_p}]$ and

$$H''(f) = -4\pi^2 \sum_{l=1}^{L-1} h_l \tau_l^2 e^{-2j\pi f \tau_l}. \tag{5.21}$$

It is obvious from (5.21) that if $H(f)$ is a Rayleigh channel, then $H''(f)$ also follows a Rayleigh distribution. We then deduce the variance of $H''(f)$

$$\begin{aligned} \sigma_{H''}^2 &= E\{H''(f)H''(f)^*\} \\ &= \sum_{l=1}^{L-1} E\{|4\pi^2 h_l \tau_l^2|^2\} \\ &= 16\pi^4 \sum_{l=1}^{L-1} \tau_l^4 \sigma_l^2, \end{aligned} \tag{5.22}$$

and by inserting (5.22) into (5.20), we deduce the variance of ξ_{li}:

$$\begin{aligned} \sigma_{\xi_{li}}^2 &= \frac{1}{4}|(f_{p+\delta_p} - f)(f_p - f)|^2 \sigma_{H''}^2 \\ &= |(f_{p+\delta_p} - f)(f_p - f)|^2 4\pi^4 \sum_{l=1}^{L-1} \tau_l^4 \sigma_l^2. \end{aligned} \tag{5.23}$$

In the discrete formalism, $\sigma_{\xi_{li}}^2$ depends on the value k, and we note $\sigma_{\xi_{k,li}}^2$ the variance given by

$$\begin{aligned} \sigma_{\xi_{k,li}}^2 &= |\frac{(p + \delta_p - m)(p - m)}{M^2}|^2 4\pi^4 \sum_{l=1}^{L-1} \beta_l^4 \sigma_l^2 \\ &= |\frac{(\delta_p - k)k}{M^2}|^2 4\pi^4 \sum_{l=1}^{L-1} \beta_l^4 \sigma_l^2, \end{aligned} \tag{5.24}$$

for $k = 1, .., \delta_p - 1$. It is noticeable that if the channel tends to have flat fading (i.e. β_l tends to zero), then $\sigma_{\xi_{k,li}}^2$ logically tends to zero. Indeed, the linear interpolation of a constant function leads to an error equal to zero.

The pdf of the error of the linear interpolation is noted $p_{\xi_{li}}(\xi)$, and has exactly the same formulation than the NN interpolation given by (5.10). Figs. 5.3 (a) and (b) depicts the pdf $p_{\xi_{li}}(\xi)$ for $\delta_p = 2, 3$. The simulations curves are compared to the analytical ones obtained for both channels $\mathcal{H}_{(1)}$ and $\mathcal{H}_{(2)}$. We derive the values of $\sigma^2_{\xi_{k,li}}$ from (5.24):

- Channel $\mathcal{H}_{(1)}$: $\sigma^2_{\xi_{1,li}} = 0.0029$ for $\delta = 2$, and $\sigma^2_{\xi_{2,li}} = \sigma^1_{\xi_{1,li}} = 0.0116$ for $\delta = 3$.
- Channel $\mathcal{H}_{(2)}$: $\sigma^2_{\xi_{1,li}} = 0.0086$ for $\delta = 2$, and $\sigma^2_{\xi_{2,li}} = \sigma^1_{\xi_{1,li}} = 0.0344$ for $\delta = 3$.

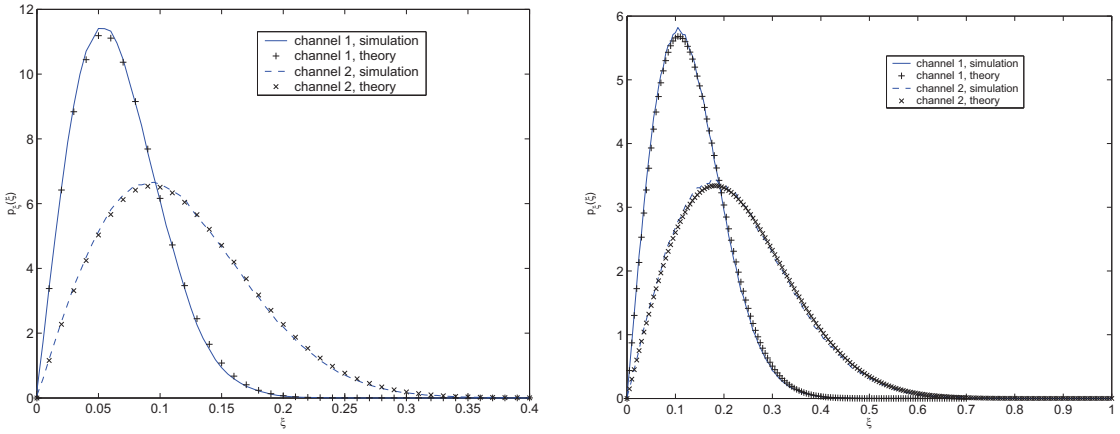

(a) Linear interpolation, $\delta_p = 2$ (b) Linear interpolation, $\delta_p = 3$

Figure 5.5 – Pdf $p_{\xi_{li}}(\xi)$ for the linear interpolation, comparison between simulation and theory for $\delta_p = 2, 3$ and for the channels $\mathcal{H}_{(1)}$ and $\mathcal{H}_{(2)}$.

It can be seen that the simulations curves and the analytical ones match. It then validate the previous development leading to the expression of the error variance (5.24). Furthermore, we logically observe that the errors are closer to zero than for the NN interpolation, which is in accordance with the fact that the linear interpolation is more precise than the NN one.

5.3.2.2 Joint pdf of the Errors of the Linear Interpolation

Since $|H''(f)|$ in (5.21) also follows a Rayleigh distribution, the joint pdf $p_{\xi,r}(\xi, r)$ of the channel and the linear interpolation follows the distribution given by (5.12). We now express the correlation coefficient $\rho_{r\xi,li}$ between the channel and linear interpolation error:

$$\begin{aligned}
\rho_{r\xi,li} &= \frac{|E\{H(f)e_h^*\}|}{\sigma_h \sigma_{\xi_{li}}} \\
&= \frac{\frac{1}{2}|(f_{p+\delta_p} - f)(f_p - f)| \times |E\{H(f)H''(f)^*\}|}{\sigma_h \sigma_{\xi_{li}}} \\
&= \frac{|(f_{p+\delta_p} - f)(f_p - f)| 2\pi^2 \sum_{l=1}^{L-1} \tau_l^2 \sigma_l^2}{\sigma_h \sigma_{\xi_{li}}}.
\end{aligned} \tag{5.25}$$

As previously, from (5.25), we notice that $\rho_{r\xi,li}$ depends on f. We directly derive the discrete expression of the correlation coefficient depending on k and noted $\rho_{r\xi_k,li}$:

$$\rho_{r\xi_k,li} = \frac{|\frac{(\delta_p - k)k}{M^2}| 2\pi^2 \sum_{l=1}^{L-1} \beta_l^2 \sigma_l^2}{\sigma_r \sigma_{\xi_{k,li}}}. \tag{5.26}$$

Figs 5.6 (a) and (b) display the conditional pdf $p_{\xi|r}(\xi|r) = p_{\xi,r}(\xi, r)/p_r(r)$, and compare the analytical expressions with the curves obtained by simulations, for $\delta_p \in 2, 3$ and $r \in \{0.1, 4\}$. From (5.26), we derive the correlation coefficient values: $\rho_{r\xi_1,li} = 0.5958$ for $\mathcal{H}_{(1)}$ and $\rho_{r\xi_1,li} = 0.624$ for $\mathcal{H}_{(2)}$.

Once more, it can be seen that the simulations curves and the theoretical ones match, whatever the channel and the value r, which validates the previous developments.

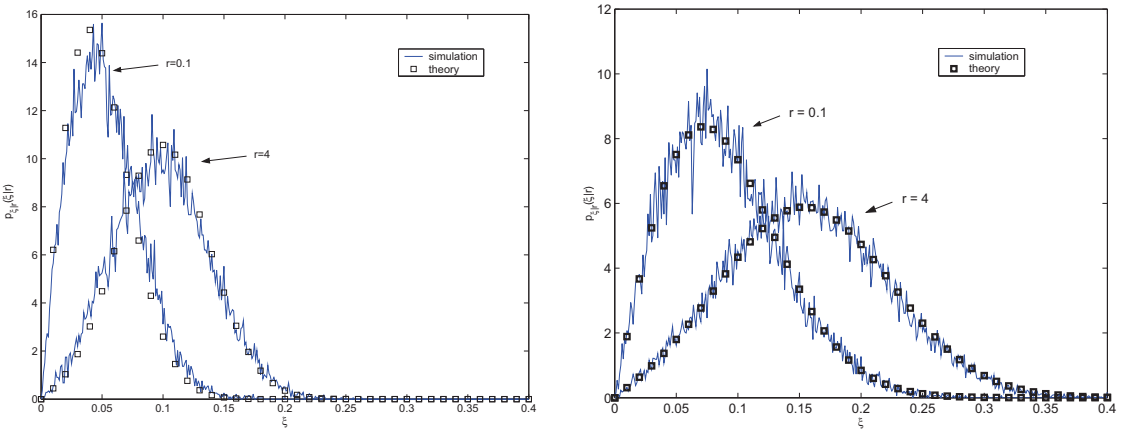

(a) $\delta_p = 3$, channel $\mathcal{H}_{(1)}$ (b) $\delta_p = 2$, channel $\mathcal{H}_{(2)}$

FIGURE 5.6 – Conditional pdf $p_{\xi|r}(\xi|r)$, comparison between analytical and simulations curves.

Finally, it has been shown that the statistics of the interpolation errors can be analytically derived. Although only two interpolation methods have been presented, it is possible to express the statistical properties of the interpolation errors as soon as the interpolation has an analytical expression of its error.

5.3.3 Statistics of the Interpolated Noise

Since the interpolation of the channel is independent from the one of the noise, we now study the statistics of $(\frac{W_m}{C_m})^{int}$ (5.3) separately. Since it is assumed that $|C_m| = 1$, $(\frac{W_m}{C_m})^{int}$ has the same statistics as W_m, and we simply note $\hat{W}_m^{int} = (\frac{W_m}{C_m})^{int}$ in the following.

5.3.3.1 NN-Interpolated Noise

Whatever the values of δ_p and k, and for a fixed p, the interpolated noise sample $\hat{W}_m^{int}$ such as with $m = p + k$, is expressed by

$$\hat{W}_m^{int} = W_p/C_p. \tag{5.27}$$

From (5.27), we simply deduce that the NN-interpolated noise has exactly the same statistics as the initial noise $\hat{W}_m$, i.e. $\hat{W}_m^{int} \sim \mathcal{N}(0, \sigma^2)$.

5.3.3.2 Linear-Interpolated Noise

Using the linear interpolation (5.17) in the discrete formalism and without taking into account the channel, the expression of $\hat{W}_m^{int}$ with $m = p + k$ is derived as:

$$\hat{W}_m^{int} = W_p/C_p + k\frac{W_{p+1}/C_{p+\delta_p} - W_p/C_p}{\delta_p}. \tag{5.28}$$

As whatever $p = 0, \delta_p, .., M-1$, we have $E\{W_p\} = 0$, we directly deduce that $E\{\hat{W}_m^{int}\} = 0$. Since k appears in (5.28), the variance of the linear interpolated noise, noted $\sigma_{li,k}^2$, is a function of k such as

$$\begin{aligned}\sigma_{li,k}^2 &= E\{|\hat{W}_m^{int}|^2\} \\ &= E\{|W_p/C_p + k\frac{W_{p+1}/C_{p+\delta_p} - W_p/C_p}{\delta_p}|^2\} \\ &= E\{|\frac{W_p/C_p(\delta_p - k) + kW_{p+1}/C_{p+\delta_p}}{\delta_p}|^2\}.\end{aligned} \tag{5.29}$$

Reminding that the noise samples have the same variance and are uncorrelated, we get

$$\sigma_{li,k}^2 = \frac{(\delta_p - k)^2 + k^2}{\delta_p^2}\sigma^2. \tag{5.30}$$

The total variance of $\hat{W}_m^{int}$, noted σ_{li}^2 is the weighted sum of $\sigma_{li,k}^2$:

$$\begin{aligned}\sigma_{li}^2 &= \frac{1}{\delta_p - 1}\sigma_{li,\delta_p/2}^2 + \frac{2}{\delta_p - 1}\sum_{k=1}^{\delta_p/2-1}\sigma_{li,k}^2 \text{ if } \delta_p \text{ is even} \\ \sigma_{li}^2 &= \frac{2}{\delta_p - 1}\sum_{k=1}^{(\delta_p-1)/2}\sigma_{li,k}^2 \text{ if } \delta_p \text{ is odd.}\end{aligned} \tag{5.31}$$

In the same way, since the noise is considered to be Gaussian, then $|W_p|$ follows a Rayleigh distribution, and the distribution of $|\hat{W}_m^{int}|$ noted $p_{\omega,li}(\omega)$ with $\omega = |\hat{W}_m^{int}|$, is expressed by

$$\begin{aligned}p_{\omega,li}(\omega) &= \frac{1}{\delta_p - 1}\frac{\omega}{\sigma_{li,\delta_p/2}^2}e^{-\frac{\omega^2}{2\sigma_{li,\delta_p/2}^2}} + \frac{2}{\delta_p - 1}\sum_{k=1}^{\delta_p/2-1}\frac{\omega}{\sigma_{li,k}^2}e^{-\frac{\omega^2}{2\sigma_{li,k}^2}} \text{ if } \delta_p \text{ is even} \\ p_{\omega,li}(\omega) &= \frac{2}{\delta_p - 1}\sum_{k=1}^{(\delta_p-1)/2}\frac{\omega}{\sigma_{li,k}^2}e^{-\frac{\omega^2}{2\sigma_{li,k}^2}} \text{ if } \delta_p \text{ is odd.}\end{aligned} \tag{5.32}$$

Figs. 5.7 (a) and (b) depict the pdfs $p_{\omega,li}(\omega)$ of the interpolated noise, for the NN and the linear interpolations, respectively, and for $\delta \in 2, 4$. The noise variance σ^2 is normalized to one in both figures. First, we observe that the simulations and the theoretical curves match, which validates the previous developments. It is also observable on the subfigure (a) that the pdf of the NN-interpolated noise remains the same whatever the value δ_p. On subfigure (b), it can be seen that $\sigma_{li}^2 < \sigma^2 = 1$, i.e. the interpolated noise is a lower power than the initial noise.

In this first part, the interpolation errors and the interpolated noise have been statistically characterized. It can now be used to express the MSE of the LS with interpolations estimation, and the BER floor, in the two next sections.

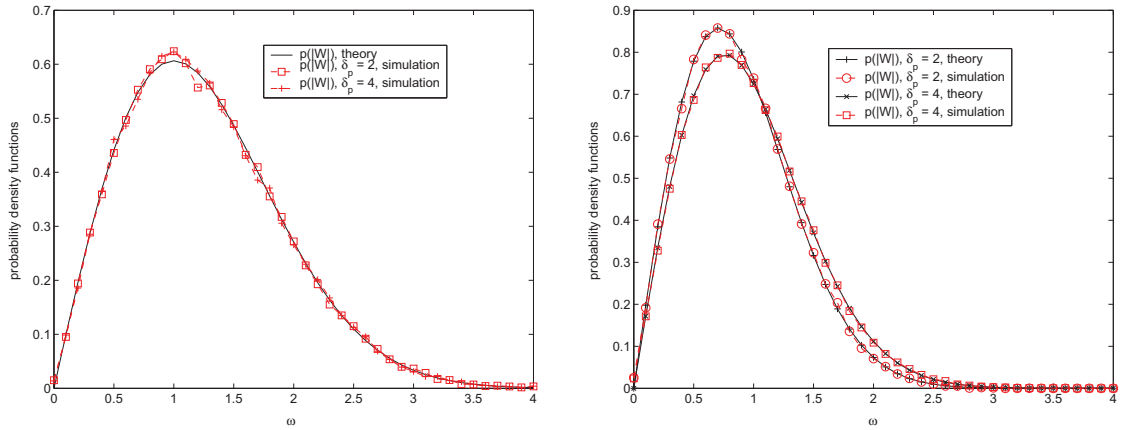

(a) Nearest Neighbor interpolation (b) Linear Interpolation

FIGURE 5.7 – Pdfs of the module of the interpolated noise, for two interpolations methods, and for $\delta_p = 2$ and $\delta_p = 4$.

5.4 Mean Square Error of the Estimations Performed with Interpolation

In [34, 35], it is assumed that the mean square error of the estimations performed by LS with interpolations cannot be analytically expressed. Thus, the different methods are compared by means of simulations. In this section, thanks to the previous results concerning the statistics of the interpolations errors, a theoretical expression of the MSE is proposed.

The mean square error of a given interpolation is noted MSE_{int} and is written

$$MSE_{int} = \frac{1}{M} E\{||\hat{\mathbf{H}} - \mathbf{H}||_F^2\}. \tag{5.33}$$

Each OFDM symbol being composed of pilot tones and data carriers, we split the development into two parts. On each pilot tone, the MSE has already been expressed in Section 2.3. In that case, the MSE is noted MSE_p and it is recalled that

$$MSE_p = \frac{\sigma^2}{\mathcal{P}}. \tag{5.34}$$

Although in this chapter, it is assumed that $\mathcal{P} = 1$, we keep it in the development for providing a general expression of the MSE. On the data carriers $m \neq p$, the MSE is noted MSE_d, and from (5.3), we obtain

$$MSE_d = E\{|\hat{H}_m^{int} + (\frac{W_m}{C_m})^{int} - H_m|^2\}, \tag{5.35}$$

and as the noise and the channel are uncorrelated, it yields

$$\begin{aligned} MSE_d &= E\{|\hat{H}_m^{int} + (\frac{W_m}{C_m})^{int} - H_m|^2\} \\ &= E\{|\hat{H}_m^{int} - H_m|^2\} + E\{|(\frac{W_m}{C_m})^{int}|^2\} \\ &= \sigma_\xi^2 + \frac{\sigma_{int}^2}{\mathcal{P}}, \end{aligned} \tag{5.36}$$

where σ_{int}^2 is equal to σ^2 for the NN interpolation, and is equal to σ_{li}^2 (5.31) for the linear interpolation. Finally, the MSE is obtained by inserting (5.36) and (5.34) in (5.33):

$$MSE_{int} = \frac{N_p}{M}\frac{\sigma^2}{\mathcal{P}} + \frac{M-N_p}{M}(\sigma_\xi^2 + \frac{\sigma_{int}^2}{\mathcal{P}}), \tag{5.37}$$

where N_p is the number of pilot tones in an OFDM symbol. Unlike the MSE of LS performed on a preamble, MSE_{int} tends to $\frac{M-N_p}{M}\sigma_\xi^2$ for high SNR values. This is the result of the residual error due to the interpolation. Applied to the NN and the linear interpolations, (5.37) becomes

$$\begin{aligned} MSE_{NN} &= \frac{\sigma^2}{\mathcal{P}} + \frac{M-N_p}{M}\sigma_\xi^2 \\ MSE_{li} &= \frac{N_p}{M}\frac{\sigma^2}{\mathcal{P}} + \frac{M-N_p}{M}(\sigma_\xi^2 + \frac{\sigma_{li}^2}{\mathcal{P}}). \end{aligned} \tag{5.38}$$

Figs. 5.8 (a) and (b) display the MSE of the channel estimations ($\mathcal{H}_{(1)}$ and $\mathcal{H}_{(2)}$, respectively) performed with the NN and linear interpolations versus the linear SNR. Two values $\delta \in \{2, 4\}$ are considered. For $\delta_p = 4$, the channel variances for the linear interpolation are $\sigma_{1,li}^2 = 0.0262$ and $\sigma_{2,li}^2 = 0.0465$ for the channel $\mathcal{H}_{(1)}$ and $\sigma_{1,li}^2 = 0.0773$ and $\sigma_{2,li}^2 = 0.1375$ for the channel $\mathcal{H}_{(2)}$. The variance values for the NN interpolation have been previously given. The curves are obtained by means of 2400 simulations runs.

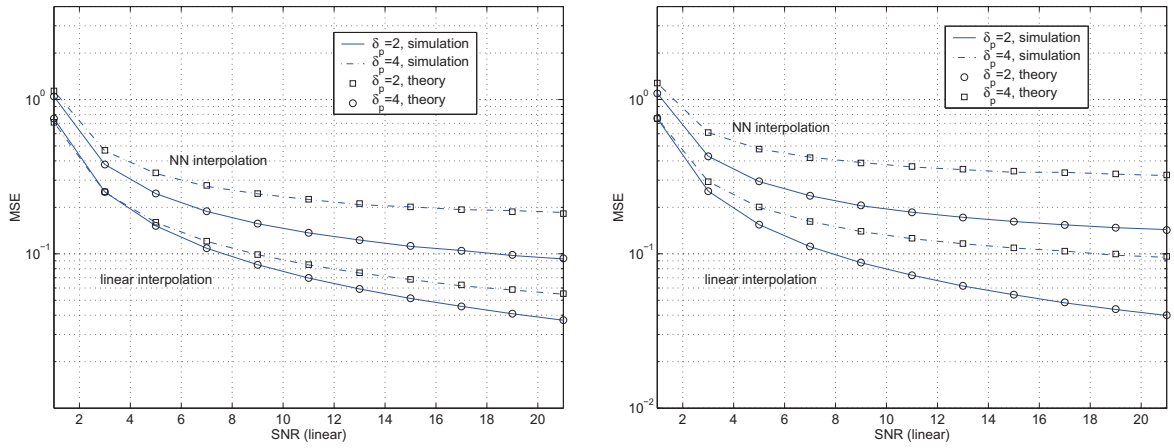

(a) Channel $\mathcal{H}_{(1)}$ (b) Channel $\mathcal{H}_{(2)}$

Figure 5.8 – MSE of the channel estimation performed with NN and linear interpolation, for $\delta_p \in \{2, 4\}$, and for the channels $\mathcal{H}_{(1)}$ and $\mathcal{H}_{(2)}$.

We observe that the theoretical curves and the ones drawn by simulations perfectly match. It then validates all the developments concerning the statistics of the interpolations errors, and the interpolated noise. As expected, the MSE reaches an error floor. Furthermore, these errors floors are higher for the channel $\mathcal{H}_{(2)}$ (subfigure (b)) than for the channel $\mathcal{H}_{(1)}$ (subfigure (a)). This is in accordance with the theory, since $\mathcal{H}_{(2)}$ is more frequency selective than $\mathcal{H}_{(1)}$. In addition to the MSE, the following section shows that it is possible to analytically measure the BER floor reached for high SNRs.

5.5 Geometrical Considerations

5.5.1 System Model

In this section, the error floor reached by the BER curves for high SNR values is analytically evaluated when interpolation errors occur. As it is assumed high SNR values, the noise is then neglected, in order to only consider the residual errors due to the interpolations. Since we focus on the effects of the interpolations errors on the BER, the geometry of the constellation has to be taken into account. In the following, a BPSK ($C \in \{-1, +1\}$) and a 4-QAM ($C \in \{^{+}_{-}d^{+}_{-}jd\}$) mapped with a Gray encoding are considered, as depicted on Fig. 5.9, with C a transmitted symbol and d a normalization coefficient.

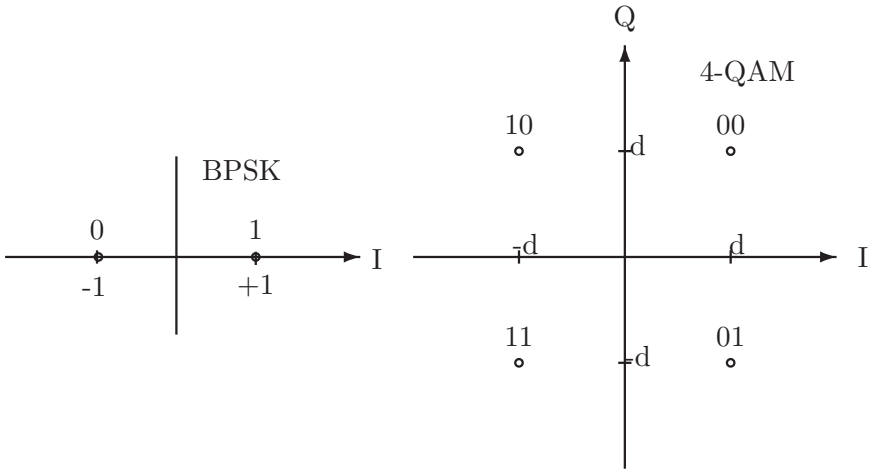

FIGURE 5.9 – BPSK and 4-QAM constellations with Gray encoding.

At the receiver side, the channel is estimated by means of LS with interpolations. Then, the received symbol is estimated by a simple zero forcing equalizer. As the noise is supposed to be null, the estimated symbol $\hat{C}$ is written as follows

$$\hat{C} = \frac{H(f)}{H(f) + e_h} C. \tag{5.39}$$

For a BPSK, the decision domains are exactly symmetric for $C =^{+}_{-} 1$. Let us then set $C = +1$ in the following developments. The probability of detection error, noted P_e^{BPSK} is then given by

$$P_e^{BPSK} = P\left(\mathfrak{Re}\{\hat{C}\} < 0 | C = 1\right). \tag{5.40}$$

In the same way for a 4-QAM, and as mentioned in [46], the decision domains are exactly symmetric according to the Q and I axes for the most significant bit (MSB) and for the least significant bit (LSB), respectively. Thus, let us then set $C = +d + jd$ in the following developments. In that case, the probability of error of detection, noted P_e^{4QAM} is then given by

$$P_e^{4QAM} = P\left(\mathfrak{Re}\{\hat{C}\} < 0 | C = d + jd\right). \tag{5.41}$$

For a given value $|H(f)| = r$, we denote the complex expressions of the channel $H(f) = re^{j\Theta_H}$ and the error $e_h = \xi e^{j\Theta_\xi}$, and we define $\Theta = \Theta_H - \Theta_\xi$. Let us now derive the analytical expression of (5.40) and (5.41).

5.5.2 BPSK Constellation

The inequality in (5.40) is developed:

$$\begin{aligned}
&\mathfrak{Re}\{\hat{C}\} < 0 \text{ with } C = 1 \\
\Leftrightarrow\ &\mathfrak{Re}\{\frac{H(f)}{H(f)+e_h} \times 1\} < 0 \\
\Leftrightarrow\ &\mathfrak{Re}\{\frac{H(f)(H(f)+e_h)^*}{|H(f)+e_h|^2}\} < 0 \\
\Leftrightarrow\ &\mathfrak{Re}\{\frac{re^{j\Theta_H}(re^{-j\Theta_H} + \xi e^{-j\Theta_\xi})}{|H(f)+e_h|^2}\} < 0 \\
\Leftrightarrow\ &\frac{r^2 + r\xi\cos(\Theta_H - \Theta_\xi)}{|H(f)+e_h|^2} = \frac{r^2 + r\xi\cos(\Theta)}{|H(f)+e_h|^2} < 0.
\end{aligned} \tag{5.42}$$

Since $|H(f) + e_h|^2 > 0$, we limit the study to the numerator of (5.42). It can be seen that if $\xi \leq r$, then $\forall\ \Theta \in [0, 2\pi]$ the inequality cannot be valid because $-1 \leq \cos(\Theta) \leq 1$. Thus, $P_e^{BPSK} = 0$ as long as $\xi \leq r$. For $\xi \geq r$, the inequation (5.42) is valid for

$$\Theta \in [-\arccos(-\frac{r}{\xi}), \arccos(-\frac{r}{\xi})]. \tag{5.43}$$

As Θ is defined in $[0, 2\pi]$, we then express P_e^{BPSK} for $\xi \geq r$ as a function of r and ξ

$$\begin{aligned}
P_e^{BPSK} &= \frac{\arccos(-\frac{r}{\xi}) - (-\arccos(-\frac{r}{\xi}))}{2\pi} \\
&= 1 - \frac{\arccos(-\frac{r}{\xi})}{\pi},
\end{aligned} \tag{5.44}$$

and then, finally, P_e^{BPSK} is expressed by

$$P_e^{BPSK} = \begin{cases} 0 & \text{if } \xi \leq r \\ 1 - \frac{\arccos(-\frac{r}{\xi})}{\pi} & \text{if } \xi \geq r \end{cases}. \tag{5.45}$$

As $\frac{\arccos(1)}{\pi} = 1$, then P_e^{BPSK} is a continuous function on $\mathbb{R}^+$. From the conditional pdf $p_{\xi|r}(\xi|r)$, we extract the conditional pdf of errors of estimation causing a wrong decision on the bits for a BPSK, that we denote $\Phi_{\xi|r,BPSK}(\xi|r, \mathfrak{Re}\{\hat{C}\} \neq \mathfrak{Re}\{C\})$:

$$\Phi_{\xi|r,BPSK}(\xi|r, \mathfrak{Re}\{\hat{C}\} \neq \mathfrak{Re}\{C\}) = P_e^{BPSK} p_{\xi|r}(\xi|r). \tag{5.46}$$

For a reason of clarity, but in order to validate the previous developments, the simulations are performed by supposing that the channel and the errors are uncorrelated, i.e. $\rho_{r\xi} = 0$. Indeed, (5.46) is obtained independently of the pdf, so it is reasonable to suppose that if it is validated for a given pdf, it can be generalized whatever the pdfs. Thus, Fig. 5.10 displays the Rayleigh density $p_{\xi|r}(\xi|r)$ for $r = 1$, $\sigma_\xi^2 = 1$, $\rho_{r\xi} = 0$ (i.e. $p_\xi(\xi)$) and the extracted function $\Phi_{\xi|r,BPSK}(\xi|r, \mathfrak{Re}\{\hat{C}\} \neq \mathfrak{Re}\{C\})$, drawn by simulations and by means of (5.46). The curves are obtained thanks to 10^6 bits.

It is verified that $\Phi_{\xi|r,BPSK}(\xi|r, \mathfrak{Re}\{\hat{C}\} \neq \mathfrak{Re}\{C\}) = 0$ for $\xi \leq r$, with $r = 1$ in the simulation. Furthermore, the theoretical curve and the one drawn by simulations exactly match, so it validates the previous developments for the BPSK.

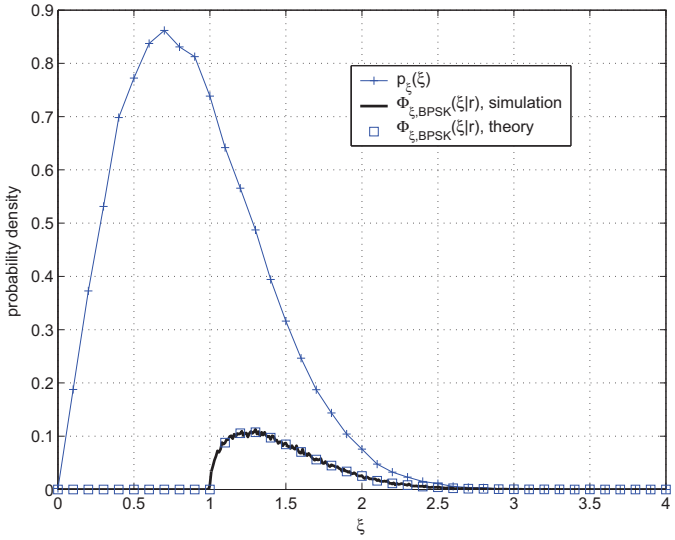

FIGURE 5.10 – Extracted conditional pdf $\Phi_{\xi,BPSK}(\xi|r)$, for a BPSK.

5.5.3 4-QAM Constellation

5.5.3.1 Getting the Polynomial to be Studied

The inequality $\mathfrak{Re}\{\hat{C}\} < 0$ in (5.41) is developed knowing that $C = d + jd$:

$$\begin{aligned}
&\mathfrak{Re}\{\hat{C}\} < 0 \\
\Leftrightarrow\ &\mathfrak{Re}\{\frac{H(f)}{H(f)+e_h} C\} < 0 \\
\Leftrightarrow\ &\mathfrak{Re}\{\frac{H(f)}{H(f)+e_h} (d+jd)\} < 0 \\
\Leftrightarrow\ &\mathfrak{Re}\{\frac{H(f)(H(f)+e_h)^*}{|H(f)+e_h|^2} (1+j)\} < 0 \\
\Leftrightarrow\ &\mathfrak{Re}\{H(f)(H(f)+e_h)^*(1+j)\} < 0
\end{aligned} \tag{5.47}$$

It can be seen that the d value does not have any effect on the detection error. We recall that we denote $H(f) = re^{j\Theta_H}$, $e_h = \xi e^{j\Theta_\xi}$ and $\Theta = \Theta_H - \Theta_\xi$ to continue the development as

$$\begin{aligned} & \mathfrak{Re}\{H(f)(H(f)+e_h)^*(1+j)\} < 0 \\ \Leftrightarrow\ & \mathfrak{Re}\{(re^{j\Theta_H}(re^{-j\Theta_H} + \xi e^{-j\Theta_\xi}))(1+j)\} < 0 \\ \Leftrightarrow\ & \mathfrak{Re}\{(r^2 + r\xi e^{j(\Theta_H - \Theta_\xi)})(1+j)\} < 0 \\ \Leftrightarrow\ & r + \xi(\cos(\Theta) - \sin(\Theta)) < 0 \end{aligned} \tag{5.48}$$

If we set $t = \tan(\frac{\Theta}{2})$, then we get $\cos(\Theta) = \frac{1-t^2}{1+t^2}$ and $\sin(\Theta) = \frac{2t}{1+t^2}$, and (5.48) becomes

$$\begin{aligned} & r + \xi(\cos(\Theta) - \sin(\Theta)) < 0 \\ \Leftrightarrow\ & \frac{r(1+t^2) + \xi(1 - t^2 - 2t)}{1+t^2} < 0. \end{aligned} \tag{5.49}$$

Since $1 + t^2 > 0$ whatever the value of t, we study the sign of the numerator in (5.49), and we denote Q the polynomial:

$$Q(t) = t^2(r - \xi) - 2\xi t + r + \xi. \tag{5.50}$$

5.5.3.2 Study of the Polynomial Q

We look for the roots of Q, by deriving its discriminant:

$$\Delta_Q = 4\xi^2 - 4(r^2 - \xi^2). \tag{5.51}$$

The polynomial Q has roots if $\Delta_Q \geq 0$, that is if

$$\xi \geq \frac{r}{\sqrt{2}}. \tag{5.52}$$

Furthermore, we notice in (5.50) that Q is convex if $\xi < r$ and concave if $\xi > r$. Thus, we deduce that the solution of (5.48) depends on the value of ξ:

1. $\xi \in [0, \frac{r}{\sqrt{2}}[$: Q is convex and has no root, so (5.48) is not valid for any value Θ. In this interval, the probability P_e^{4QAM} is then equal to zero.
2. $\xi \in [\frac{r}{\sqrt{2}}, r[$: Q is convex and has two roots t_2^- and t_2^+ such as

$$t_2^{\pm} = \frac{2\xi_-^+\sqrt{\Delta_p}}{2(r-\xi)}, \tag{5.53}$$

so the inequation $Q(t) < 0$ is valid for $t \in [t_2^-, t_2^+]$. We deduce that (5.48) is valid for

$$\Theta \in [2\arctan(t_2^-), 2\arctan(t_2^+)]. \tag{5.54}$$

In this interval, the probability P_e^{4QAM} is then equal to

$$\begin{aligned} P_e^{4QAM} &= \frac{2\arctan(t_2^+) - 2\arctan(t_2^-)}{2\pi} \\ &= \frac{\arctan(t_2^+) - \arctan(t_2^-)}{\pi}. \end{aligned} \tag{5.55}$$

3. $\xi \in [r, +\infty[$: Q is concave and has two roots t_3^- and t_3^+ such as

$$t_3^{\pm} = \frac{2\xi_+^- \sqrt{\Delta_p}}{2(r-\xi)}, \tag{5.56}$$

so the inequation $Q(t) < 0$ is valid for $t \in]-\infty, t_3^-] \cup [t_3^+, +\infty[$. We deduce that (5.48) is valid for

$$\Theta \in \left[-\pi, 2\arctan(t_3^-)\right] \cup \left[2\arctan(t_3^+), \pi\right]. \tag{5.57}$$

In this interval, the probability P_e^{4QAM} is then equal to

$$\begin{aligned} P_e^{4QAM} &= \frac{\pi - 2\arctan(t_3^+) + 2\arctan(t_3^-) + \pi}{2\pi} \\ &= 1 + \frac{\arctan(t_3^-) - \arctan(t_3^+)}{\pi}. \end{aligned} \tag{5.58}$$

From the conditional pdf $p_{\xi|r}(\xi|r)$, we extract the pdf of errors of estimation causing wrong decision on the bits for a 4-QAM, that we denote $\Phi_{\xi,4QAM}(\xi|r)$. Since the I and Q components of the 4-QAM constellation are symmetric, we get

$$\Phi_{\xi,4QAM}(\xi|r) = P_e^{4QAM} p_{\xi|r}(\xi|r) = \begin{cases} 0, \text{ if } 0 \leq \xi \leq \frac{r}{\sqrt{2}} \\ \frac{\arctan(t_2^+) - \arctan(t_2^-)}{\pi} p_{\xi|r}(\xi|r), \text{ if } \frac{r}{\sqrt{2}} \leq \xi \leq r \\ (1 + \frac{\arctan(t_3^-) - \arctan(t_3^+)}{\pi}) p_{\xi|r}(\xi|r), \text{ if } r \leq \xi \end{cases} \tag{5.59}$$

The continuity of $\Phi_{\xi,4QAM}(\xi|r)$ is verified on the points $\xi = \frac{r}{\sqrt{2}}$ and $\xi = r$:

1. On $\xi = \frac{r}{\sqrt{2}}$: $\Delta_Q = 0$, which yields $t_2^- = t_2^+$ and so $P_e^{4QAM} = 0$.
2. On $\xi = r$: We use a Taylor expansion to get a definite form of t_3^+. By setting $x = \xi - r$ and $X = \frac{4}{r}x + \frac{2}{r^2}x^2$, we obtain $\Delta_Q = 4r^2(1+X)$. Thus, it is possible to develop t_3^+ when ξ tends to r. Indeed, as $\sqrt{\Delta_Q} \sim 2r(1 + \frac{1}{2}X)$, we get

$$\begin{aligned} \lim_{\xi \to r} t_3^+ &= \lim_{x \to 0} \frac{-2x - \frac{2}{r}x^2}{-2x} \\ &= 1. \end{aligned} \tag{5.60}$$

For the limit of t_3^-, we directly get $\lim_{\xi \to r^+} t_3^+ = -\infty$. Thus, P_e^{4QAM} in (5.58) is equal to $\frac{1}{4}$. Based on the same reasonment, we trivially get the same result for P_e^{4QAM} in (5.55).

Fig. 5.11 depicts the Rayleigh density $p_{\xi|r}(\xi|r)$ and the function $\Phi_{\xi|r,4QAM}(\xi|r, \mathfrak{Re}\{\hat{C}\} \neq \mathfrak{Re}\{C\})$ drawn with the same parameters as previously. Once more, it is verified that the theoretical curve and the one drawn by simulation perfectly match. It validates the development made for the 4-QAM.

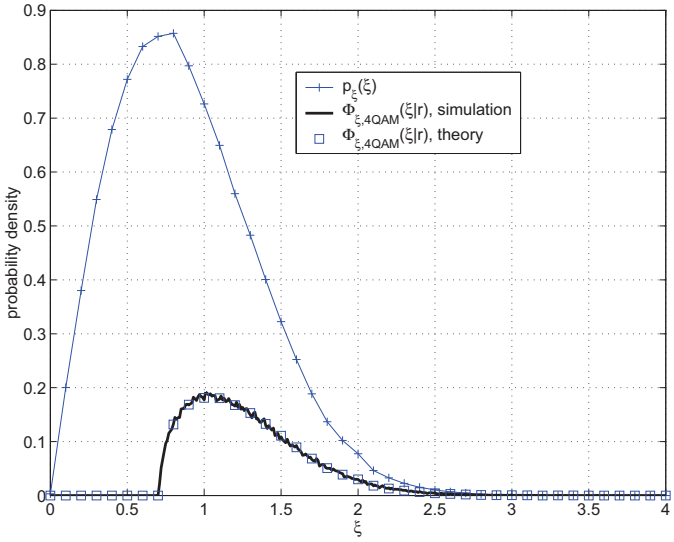

Figure 5.11 – Extracted conditional pdf $\Phi_{\xi,4QAM}(\xi|r)$, for a 4-QAM.

5.5.4 Analytical Expression of the BER Floor

Finally, the bit error rate floor, noted BER^{floor}, is the double integral of the conditional pdf $\Phi_{\xi|r,const}(\xi|r, \mathfrak{Re}\{\hat{C}\} \neq \mathfrak{Re}\{C\})$ multiplied by $p_r(r)$. Some simplifications lead to:

$$\begin{aligned} BER^{floor} &= \int_0^{+\infty} p_r(r) \int_0^{+\infty} \Phi_{\xi|r,const}(\xi|r, \mathfrak{Re}\{\hat{C}\} \neq \mathfrak{Re}\{C\}) d\xi dr \\ &= \int_0^{+\infty} p_r(r) \int_0^{+\infty} P_e^{const} p_{\xi|r}(\xi|r) d\xi dr \\ &= \int_0^{+\infty} \int_0^{+\infty} P_e^{const} p_{r,\xi}(r,\xi) d\xi dr, \end{aligned} \tag{5.61}$$

where P_e^{const} depends on the constellation.

5.6 Simulation Results

5.6.1 Simulations Parameters

In order to make the simulations reproducible, all the parameters (i.e. the error variances and the correlation coefficients) are summed up in Tables 5.3 and 5.4.

5.6.2 Analytical BER Floor

In a first time, the BER floor values analytically calculated with (5.61) are computed for all the parameters, and summarized in Tables 5.5 and 5.6. It is verified that the NN interpolation is less efficient than the linear one, and the BER floor logically increases with δ_p.

In a second time, it is shown on Figs. 5.12 and 5.13 that the simulated BER curves match the BER floor values. Fig. 5.12 display the BER curves versus the SNR for the NN

TABLE 5.3 – NN interpolation parameters.

Nearest Neighbor Interpolation		
	$\delta_p = 2\,;\, \delta_p = 3$	$\delta_p = 4$
Channel $\mathcal{H}_{(1)}$	$\sigma^2_{\xi_{1,NN}} = 0.0092$	$\sigma^2_{\xi_{1,NN}} = 0.0092\,;\, \sigma^2_{\xi_{2,NN}} = 0.3567$
	$\rho^2_{r\xi_{1,NN}} = 0.6723$	$\rho^2_{r\xi_{1,NN}} = 0.6723\,;\, \rho^2_{r\xi_{2,NN}} = 0.6712$
Channel $\mathcal{H}_{(2)}$	$\sigma^2_{\xi_{1,NN}} = 0.1908$	$\sigma^2_{\xi_{1,NN}} = 0.1908\,;\, \sigma^2_{\xi_{2,NN}} = 0.73$
	$\rho^2_{r\xi_{1,NN}} = 0.7128$	$\rho^2_{r\xi_{1,NN}} = 0.7128\,;\, \rho^2_{r\xi_{2,NN}} = 0.7061$

TABLE 5.4 – Linear interpolation parameters.

Linear Interpolation			
	$\delta_p = 2$	$\delta_p = 3$	$\delta_p = 4$
Channel $\mathcal{H}_{(1)}$	$\sigma^2_{\xi_{1,li}} = 0.0029$	$\sigma^2_{\xi_{1,li}} = 0.0116$	$\sigma^2_{\xi_{1,li}} = 0.0262\,;\, \sigma^2_{\xi_{2,li}} = 0.0465$
	$\rho^2_{r\xi_{1,li}} = 0.5958$	$\rho^2_{r\xi_{1,li}} = 0.5958$	$\rho^2_{r\xi_{1,li}} = 0.5946\,;\, \rho^2_{r\xi_{2,li}} = 0.5951$
Channel $\mathcal{H}_{(2)}$	$\sigma^2_{\xi_{1,li}} = 0.0086$	$\sigma^2_{\xi_{1,li}} = 0.0344$	$\sigma^2_{\xi_{1,li}} = 0.0773\,;\, \sigma^2_{\xi_{2,li}} = 0.1375$
	$\rho^2_{r\xi_{1,li}} = 0.624$	$\rho^2_{r\xi_{1,li}} = 0.624$	$\rho^2_{r\xi_{1,li}} = 0.6244\,;\, \rho^2_{r\xi_{2,li}} = 0.6242$

interpolation, and Fig. 5.13 for the linear interpolation. In order to validate the proposed developments, the simulations are made for both channels $\mathcal{H}_{(1)}$ and $\mathcal{H}_{(2)}$, and for $\delta_p \in \{2, 4\}$. The curves are obtained thanks to 2×10^6 bits.

It can be seen on Figs. 5.12 and 5.13 that, whatever the chosen set of parameters, the simulated curves reach a BER floor which match or almost match with the analytical values. The very slight differences can be explained by the fact that the integral (5.61) is calculated in a discrete formalism. However, the results allow to validate the theoretical developments proposed in this chapter.

TABLE 5.5 – Analytical BER floor for the NN interpolation.

Nearest Neighbor Interpolation			
	$\delta_p = 2,\, \delta_p = 3$	$\delta_p = 4$	
BPSK	6.0×10^{-3}	1.2×10^{-2}	Channel $\mathcal{H}_{(1)}$
4-QAM	1.23×10^{-2}	2.64×10^{-2}	
BPSK	8.6×10^{-3}	1.72×10^{-2}	Channel $\mathcal{H}_{(2)}$
4-QAM	1.82×10^{-2}	4.05×10^{-2}	

Table 5.6 – Analytical BER floor for the linear interpolation.

Linear Interpolation				
	$\delta_p = 2$	$\delta_p = 3$	$\delta_p = 4$	
BPSK	2.52×10^{-4}	8.76×10^{-4}	2.5×10^{-3}	Channel
4-QAM	4.46×10^{-4}	1.9×10^{-3}	5.1×10^{-3}	$\mathcal{H}_{(1)}$
BPSK	4.59×10^{-4}	1.9×10^{-3}	5.3×10^{-3}	Channel
4-QAM	9.38×10^{-4}	3.8×10^{-3}	1.07×10^{-2}	$\mathcal{H}_{(2)}$

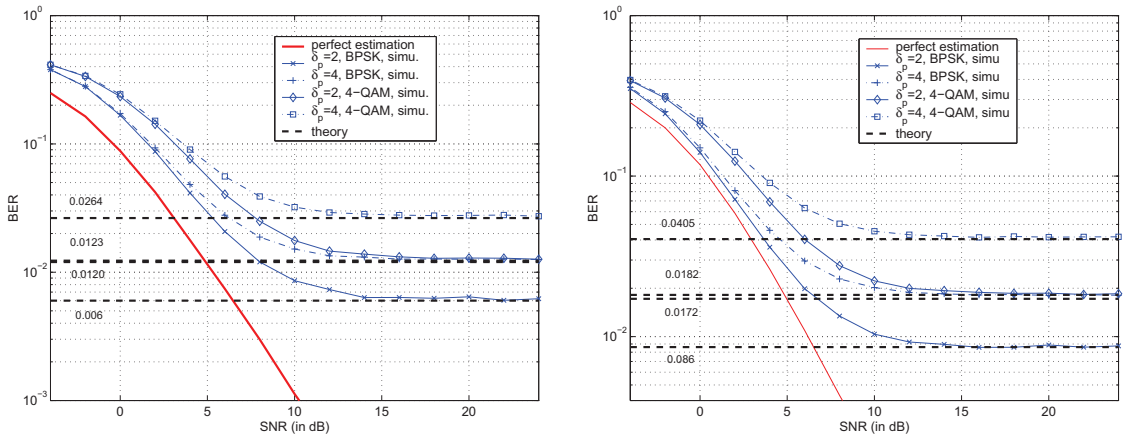

(a) Channel $\mathcal{H}_{(1)}$ (b) Channel $\mathcal{H}_{(2)}$

Figure 5.12 – BER of the channel estimation performed with NN interpolation, for $\delta_p \in \{2, 4\}$, and for the channels $\mathcal{H}_{(1)}$ and $\mathcal{H}_{(2)}$.

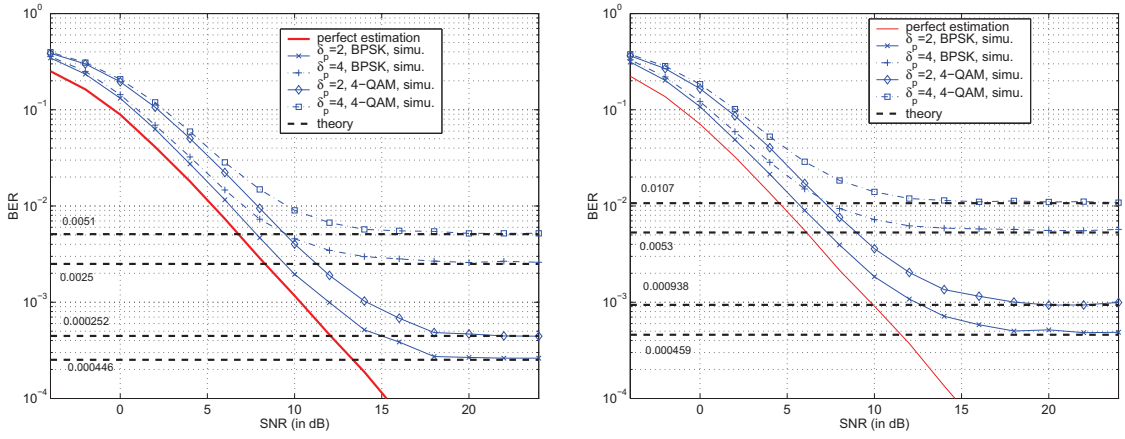

(a) Channel $\mathcal{H}_{(1)}$ (b) Channel $\mathcal{H}_{(2)}$

Figure 5.13 – BER of the channel estimation performed with linear interpolation, for $\delta_p \in \{2, 4\}$, and for the channels $\mathcal{H}_{(1)}$ and $\mathcal{H}_{(2)}$.

5.7 Conclusion

In this chapter, a theoretical study of the interpolation errors applied to the channel estimation has been presented. First, a characterization of the errors statistics is performed, and a geometrical analysis of the effect of the error on the constellation has been made. Then, an analytical expression of the MSE of the LS estimation performed with interpolation has been derived, just as the expression of the BER floor. For a given channel, these values are function of the frequency gap between the pilot tones δ_p, the interpolation technique and the constellation size. It differs from the existing work of the literature, as the errors and the channel are correlated, and the MSE and BER can be exactly characterized.

The developments have been made for the nearest neighbor and the linear interpolations, and for the BPSK and the 4-QAM constellations. Thus, further works are going to be achieved to extend the proposed study to other interpolation methods, and constellations of highest orders. Moreover, the proposed analysis can be used in other contexts, in which interpolations of random functions are required. For instance, one can reasonably imagine that it can be used in image processing, in order to characterize the quality of resolution increasing.

Chapter 6

Application of Cyclic Delay Diversity to a Single Frequency Network

6.1 Introduction

This chapter presents some transmission diversity techniques, and especially studies the cyclic delay diversity (CDD). In single frequency networks (SFNs), it may appear that flat fading corrupts the signal over all the bandwidth. Contrary to the model of Section 3.5, this is due to a particular kind of multipath channel, where the delays are very short. In that case, the frequency multiplexing of the OFDM becomes useless, as all the carriers may be disrupted. The principle of the CDD is to artificially increase the frequency selectivity in order to retrieve the frequency diversity of the OFDM.

This study has been made in the framework of the project OCEAN, in which an analytical work and a measure campaign have been achieved. Thus, it is an application of the cyclic delay diversity to the DRM/DRM+ standard [1]. Consequently, as the pilot tones are in staggered rows in the frame, an interpolation is required for the channel estimation. Thus, it will be shown that the increase of the frequency selectivity has to be taken into account in the choice of the interpolation method. The results have been presented in [47]

First, some diversity techniques are presented, with their field of application, their advantages and drawbacks. Second, we focus on the delay diversity in a simple model with two cells, which is extended to a multi-cell network. Furthermore, the impact of the CDD on the channel estimation is shown.

6.2 Different Kinds of Diversity

The goal of the diversity is to statistically increase the quality of the received signal. To this end, the signal is transmitted via different channels. Indeed, a signal that produces errors through a given channel may become error-free if it is transmitted over another channel. As presented in this part, the increase of the received signal quality can be obtained by several ways, like the time, frequency, polarization or spatial diversity.

6.2.1 Time Diversity

The principle of the time diversity is to transmit, from one antenna, the same signal over two time uncorrelated channels. If we denote Δ_T the delay between the transmission of the two signals, it is known that the two channels are uncorrelated if

$$\Delta_T > T_C. \tag{6.1}$$

A more precise approximation of the coherence time than the one given in Chapter 1 is $T_C = \sqrt{\frac{9}{16\pi\nu_{D_{max}}^2}} \approx \frac{0.423}{\nu_{D_{max}}}$ (see [68]), where $\nu_{D_{max}}$ is the maximum Doppler spread. In order to illustrate the time uncorrelation effect on the efficiency of the delay diversity, Fig. 6.1 depicts the BER curves versus E_b/N_0 for three different Δ_T values: Δ_T = 20, 200, and 400 ms. We consider the *US Consortium* channel, whose parameters are given in Table 1.1 of the section 1.4. We recall that $\nu_{D_{max}} = 2$ Hz, so the coherence time T_C is equal to 211.5 ms. The robustness mode C is considered for the simulations. A 64-QAM constellation maps symbols that are transmitted without any channel encoding. A LS estimation is performed on the pilot tones, and a spline interpolation is made to get the channel frequency response over the complete time and frequency lattice. Assuming the robustness mode C, the three different values of Δ_T correspond to one OFDM symbol duration T_s, ten OFDM symbols duration and one OFDM frame duration, respectively.

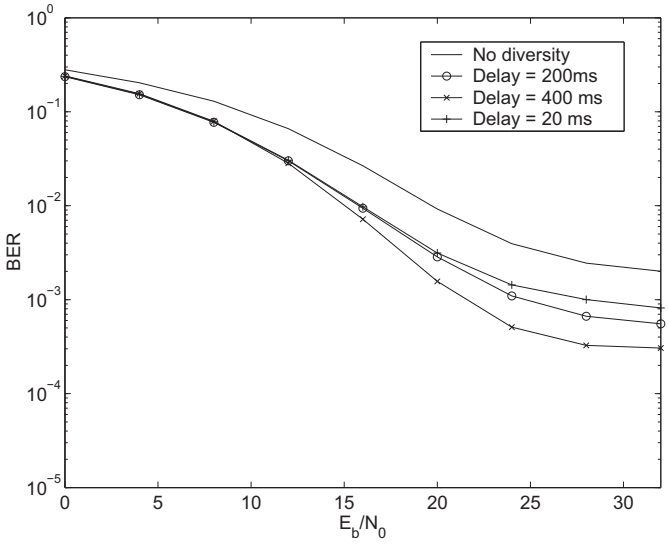

FIGURE 6.1 – BER curves of transmissions with time diversity versus E_b/N_0, comparison between three delays Δ_T = 20, 200, and 400 ms.

We notice on Fig. 6.1 that the four BER curves all reach an error floor. This is due to the interpolation which creates some errors of estimation, as it has been studied in Chapter 5. Furthermore, as we consider a transmission without channel encoding, these errors are not mitigated. However, we notice that the greater Δ_T, the lower the BER. This result is in accordance with the uncorrelation condition given in (6.1). Indeed, for Δ_T = 400 ms, the bit error rate is eight times lower than a transmission without time diversity.

Finally, one can verify the BER gain brought by the time diversity. Nevertheless, the main

drawback of this kind of diversity is the data rate loss. Indeed, transmitting two times the same signal divides the data rate by two. The time diversity is then rarely used in transmission schemes.

6.2.2 Spatial Diversity

6.2.2.1 Principle of the MIMO

The principle of the spatial diversity is based on the use of multiple antennas at the transmitter and/or at the receiver. This principle, illustrated on Fig. 6.2 with N_T transmitting antennas and N_R receiving antennas, is called multi-input multi-output (MIMO). The associated variants are the MISO and SIMO, in the presence of a unique antenna at the receiver and a unique antenna at the transmitter, respectively. In such transmissions, the uncorrelation between the different versions of the signal depends on the distance between the antennas at both the transmitter and the receiver side. The spatial correlation will be studied in Section 6.2.2.2. As shown in Fig. 6.2 in the case of the transmission of an OFDM signal, the MIMO channel is composed of $N_T \times N_R$ SISO channels. However, the MIMO technique can be used as well for the single as the multicarrier signals.

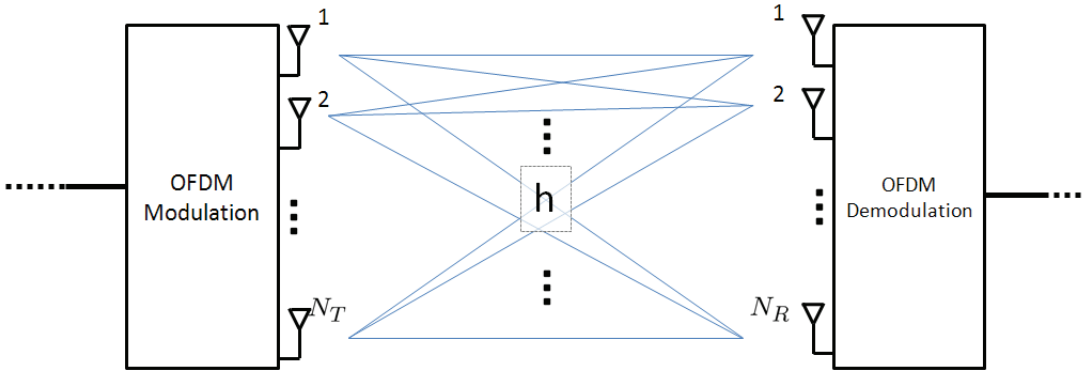

FIGURE 6.2 – Diagram of a $N_T \times N_R$ MIMO system.

The mathematical expression of the received signal on the k^{th} antenna is given by

$$\mathbf{u}_{n,k} = \sum_{i=1}^{N_T} \mathbf{h}_{n,i,k}\mathbf{s}_{n,i} + \mathbf{w}_{n,k}, \tag{6.2}$$

or, equivalently in the frequency domain:

$$\mathbf{U}_{n,k} = \sum_{i=1}^{N_T} \mathbf{H}_{n,i,k}\mathbf{C}_{n,i} + \mathbf{W}_{n,k}. \tag{6.3}$$

where $i \in \{1, 2, .., N_T\}$ and $k \in \{1, 2, .., N_R\}$ are the subscripts of the transmitting and the receiving antennas, respectively. As mentioned in [156], a "diversity gain" is obtained if the same signal is transmitted over the $N_T \times N_R$ channels. In order to minimize the errors in the received signal, different kinds of combination of the N_R outputs can be performed [157]. The most simple is the equal-gain combining. In that case, the N_R versions of the signal are averaged to get final signal. Another solution is to choose the output whose signal maximizes

the SNR. Whatever the chosen combination of the outputs, this MIMO scheme has the same data rate as in a SISO one, but the fading disrupting the signal statistically decrease if the $N_T \times N_R$ branches are uncorrelated enough.

It is also possible to get a "multiplexing gain" if each of the N_T antennas transmits a different signal. In that case, it is possible to separate the different signals only if $N_R \geq N_T$. In an OFDM context, the usual expression [158–160] of such a MIMO transmission is derived from (6.3), and expressed for each subcarrier m, $m = 0, 1, ..., M-1$ as

$$\mathbf{U}_{m,n}^{MIMO} = \mathbf{H}_{m,n}^{MIMO}\mathbf{C}_{m,n}^{MIMO} + \mathbf{W}_{m,n}^{MIMO}, \tag{6.4}$$

$$\begin{pmatrix} U_{m,n,0} \\ U_{m,n,1} \\ \vdots \\ U_{m,n,N_R-1} \end{pmatrix} = \begin{pmatrix} H_{m,n,0,0} & H_{m,n,1,0} & \cdots & H_{m,n,N_T-1,0} \\ H_{m,n,0,1} & \ddots & & H_{m,n,N_T-1,1} \\ \vdots & & \ddots & \\ H_{m,n,0,N_R-1} & \cdots & & H_{m,n,N_T-1,N_R-1} \end{pmatrix} \begin{pmatrix} C_{m,n,0} \\ C_{m,n,1} \\ \vdots \\ C_{m,n,N_T-1} \end{pmatrix} + \begin{pmatrix} W_{m,n,0} \\ W_{m,n,1} \\ \vdots \\ W_{m,n,N_R-1} \end{pmatrix}. \tag{6.5}$$

Let us assume that $N_T = N_R$. Thus, the recovery of the transmitted symbols is possible only if $\mathbf{H}_{m,n}^{MIMO}$ is invertible. The channel matrix is invertible only if the rank of $\mathbf{H}_{m,n}^{MIMO}$ is equal to N_T. This condition is verified only if the $N_T \times N_R$ paths are uncorrelated. Finally, the gain (in term of data rate) is effective only if $N_R \geq N_T$. The second condition is the uncorrelation between the channels, which is ensured only if the antennas are sufficiently spaced out from one to the other. In a general way, the authors of [161] show that data rate increases when the correlation decreases.

6.2.2.2 Spatial Correlation

a. Correlation at the Receiver

Practically, in multi-antennas systems, there is a coupling between the antennas. This coupling is characterized by a correlation coefficient, depending on the distance between the antennas, the wavelength of the signal, the distance between the transmit/receiving antennas and the scatterers, and their arrangement. Fig. 6.3 illustrates the transmission of a signal coming from one single scatterer to a pair of receiving antennas.

We denote Θ the angle between the path and the bissection of the segment formed by the two antennas. Furthermore, we suppose that the distance to the scatterer is much greater than the spacing d between the antennas. From [157], we express the correlation coefficient $\rho_r(d)$ between the two antennas:

$$\rho_r(d) = \int_{\Theta=0}^{2\pi} p_\Theta(\Theta) exp(j\alpha d \sin(\Theta)) d\Theta, \tag{6.6}$$

where α is a real number, and $p_\Theta(\Theta)$ is the probability density function of Θ. The subscript r of $\rho_r(d)$ means "receiver". Let us assume a usual model, in which the scatterers are uniformly

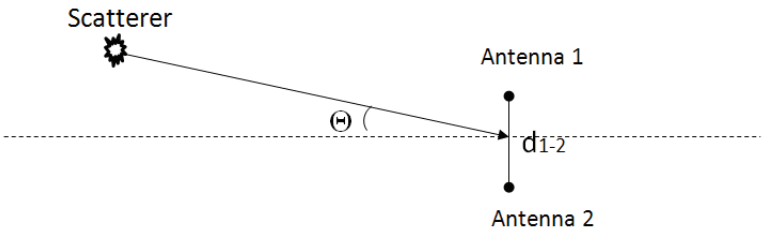

FIGURE 6.3 – Two correlated receiving antennas, reproduced from [157] with the permission of the author.

distributed around the receiving antennas. In that case, $p_\Theta(\Theta)$ is a uniform probability density function on the interval $[0; 2\pi]$. Then, the integral (6.6) yields

$$\rho_r(d) = J_0\left(\frac{2\pi d}{\lambda}\right), \tag{6.7}$$

where λ is the wavelength of the signal and J_0 is the Bessel function of the first kind with order zero. We observe that the expression (6.7) is quite similar to the expression of the time correlation function of the mobile channel (1.13) given in Chapter 1. Fig. 6.4 shows the magnitude of the correlation coefficient $|\rho_r|$ versus d/λ. We observe that a low correlation can be obtained for a spacing d/λ between the antennas about 0.5. For instance, if we consider a transmission at a frequency equal to 100 MHz (in the current FM bands or using the DRM/DRM+ standard), ρ_r reaches a low value for $d = 1.5$ m. In such a condition, we conclude that designing a spatial diversity at the receiver is hardly feasible in practice. Indeed, separating two receiving antennas by $d = 1.5$ m is hard to conceive for domestic radio sets. However, we may imagine such a possibility in another context (DRM receiver for cars for instance).

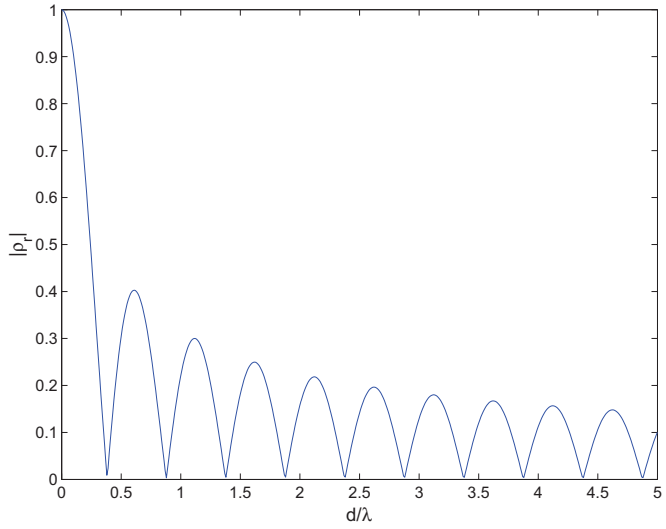

FIGURE 6.4 – Spatial correlation between two receiving antennas versus d/λ.

b. Correlation at the Transmitter

In order to express the correlation between two transmit antennas, let us assume a usual model in which the scatterers are uniformly distributed around the mobile station, as illustrated in Fig. 6.5. We also suppose that the scatterers are at the same altitude as the mobile station. We define r the distance between the base station and the mobile station, and r_s the scattering radius, i.e. the distance between the mobile station and the scatterers.

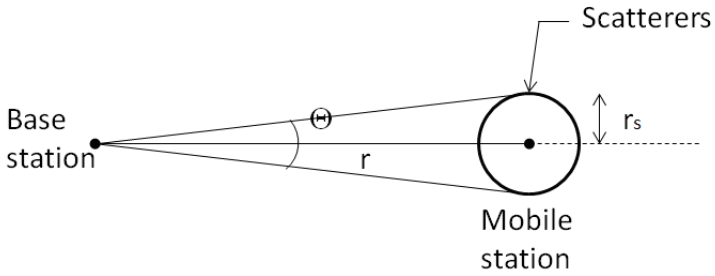

FIGURE 6.5 – Base station transmitting on reflectors arranged around the mobile station, reproduced from [157] with the permission of the author.

From [60, 157], we directly express the correlation coefficient $\rho_t(d)$ between two antennas of the base station:

$$\rho_t(d) = J_0\left(\frac{2\pi d}{\lambda}\frac{r_s}{r}cos(\Theta)\right) J_0\left(\frac{\pi d}{\lambda}(\frac{r_s}{r})^2\sqrt{1-\frac{3}{4}sin^2(\Theta)}\right). \tag{6.8}$$

where the subscript t of $\rho_t(d)$ means "transmitter". For a ratio $\frac{r_s}{r} = 0,01$ and an angle $\Theta = 45^o$, $|\rho_t(d)|$ is plotted on Fig. 6.6, showing the magnitude of the correlation coefficient versus d/λ. We observe that in order to get $\rho_t < 0.1$, d/λ has to be around 50. If we keep the same parameters as previously (simulating a transmission with DRM/DRM+ standard), the distance d between the transmit antennas must be about 150 m. Once again, we conclude that, in DRM/DRM+ standard, the device is not feasible in practice.

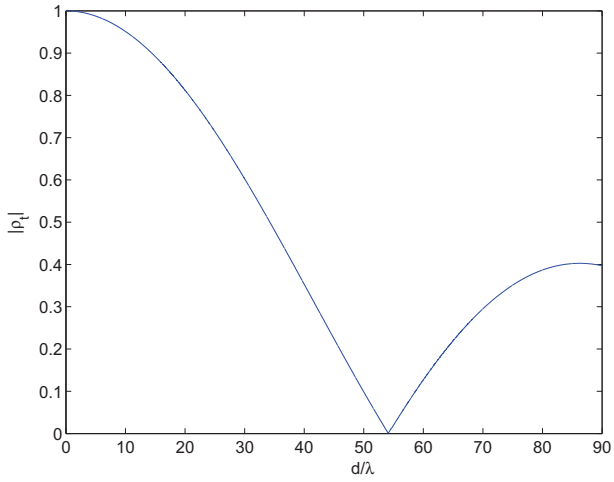

FIGURE 6.6 – Spatial correlation between two transmitters versus d/λ.

The two aforementioned models are simple, but they highlight the problem of the spatial correlation in MIMO system. In practice, as we consider an isotropic transmitter, the incident directions of the different paths are not necessarily in the plane of the antennas. For instance in the DRM standard, ionospheric reflections are considered. Furthermore, the arrangement of the scatterers is not necessarily a ring around the mobile station. In order to complete this short description, some other models are presented in [161–163]. Finally, we conclude that the MIMO technique provides a high diversity gain, but it loses its advantage when the antennas are correlated. Since this correlation depends on the space between the antennas and the wavelength of the signal, MIMO is very hardly implementable in the context of the DRM standard, for instance.

6.2.3 Polarization Diversity

In the environments or standards in which the spatial diversity is unsuitable, it is possible to implement the polarization diversity, based on the polarization of the electrical field. To this end, the mobile station is composed of two antennas in the same plane but whose directions differ with regard to the ground. The principle of this diversity is presented in [164] in a simple case, in which the signal is considered in an azimuth plane that is orthogonal to the plane of the antennas. A generalized model is provided in [157], and described in Fig. 6.7. In this model, we suppose that the arrival directions of the different signal components are not restricted to the azimuth plane. Let us define E_x and E_y the components of the electrical field. The induced voltages V_1 and V_2 in the antennas (1 and 2) are functions of the angles α, Ω, Φ and θ:

$$\begin{aligned} V_1 &= a(\alpha, \Omega, \Phi)E_x + b(\alpha, \Omega, \theta)E_y \\ V_2 &= c(\alpha, \Omega, \Phi)E_x + d(\alpha, \Omega, \theta)E_y, \end{aligned} \tag{6.9}$$

where the expressions of a, b, c and d are given in [157]. The complex correlation coefficient is then calculated by

$$\rho_{12} = \frac{\overline{V_1 V_2^*} - \bar{V}_1 \bar{V}_2^*}{\sqrt{\overline{V_1 V_1^* V_2 V_2^*}}}, \tag{6.10}$$

where $\overline{(.)}$ defines the average value. The envelope correlation coefficient is approximated by $\rho_e \approx |\rho_{12}|$, then the mean value $\overline{\rho_e}$ of this real envelope is calculated by means of the integrals

$$\overline{\rho_e} = \int_{-\pi}^{0} \int_{0}^{2\pi} \rho_e(\Phi, \theta) p_\Phi(\Phi) p_\theta(\theta) \cos\theta d\Phi d\theta, \tag{6.11}$$

where p_ϕ and p_θ are the probability density functions of the horizontal and the vertical arrival angles of the signal, respectively. The authors of [165, 166] provide some measurements of the electrical fields at the receiver in order to compare them to the theoretical results. In [166], a uniform distribution p_ϕ and a Gaussian distribution p_θ are assumed. For given angle values ϕ and θ, the two components of the signal can be perfectly uncorrelated. However, polarization diversity has drawbacks. Indeed, it is hard to obtain a perfect uncorrelation in practice, due to the mobility of the receiver. Furthermore, the SNR at each output is very low, as the field is split into its two components.

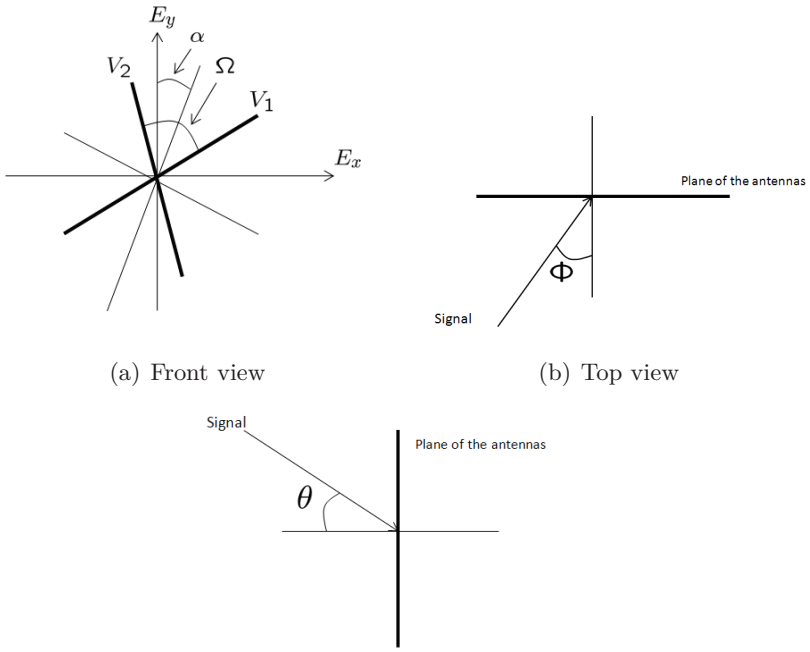

(a) Front view

(b) Top view

(c) Side view

FIGURE 6.7 – Definition of the angles of arrival of the signal, reproduced from [157] with the permission of the author.

6.2.4 Frequency Diversity

The principle of the frequency diversity is to split the useful bandwidth into several narrower channels. The data symbols are then transmitted on these subcarriers. The usual multiplexing technique is the OFDM, as previously described. Combined with a channel encoding, the C-OFDM is very robust against the frequency selective channels. Indeed, only a part of the subcarriers can be disrupted because of the frequency fading of the channel, and the errors occurring are offset by the channel encoding on the other hand. The advantage of the frequency diversity is detailed in Chapter 1.

6.3 Application of the Cyclic Delay Diversity in a SFN

This part describes the work achieved within the framework of the project OCEAN. It presents an application of the cyclic delay diversity in a single frequency network simulated with the DRM/DRM+ parameters [1]. This study fits into the global project, in which some practical measurement of the DRM/DRM+ channel have also been performed. Thus, it is interesting to parallel the following theoretical model with the realistic one.

6.3.1 Model Description

In this section, we study a channel model in which the fading may affect all the considered bandwidth. In that case, the frequency diversity of the OFDM modulation becomes not sufficient to fight against the frequency fading, even with a channel encoding. Although it is

not the only context, this phenomenon usually occurs in single frequency networks (SFNs). In this model, all the base stations of the network broadcast the signals at the same frequencies. For instance, the networks using digital audio broadcasting (DAB) [53], DRM/DRM+ [1] or DVB-T [52] are SFNs. To begin, let us consider a very simple network, composed of only two transmit antennas (denoted by Tx_1 and Tx_2) and illustrated in Fig. 6.8. It is assumed that, in the overlapping area between the two cells, the power of the signal from Tx_1 is equal to the power of the one from Tx_2. Furthermore, the delay of arrival between the signal from Tx_1 and Tx_2 can be very short, which may cause flat fading in the considered bandwidth.

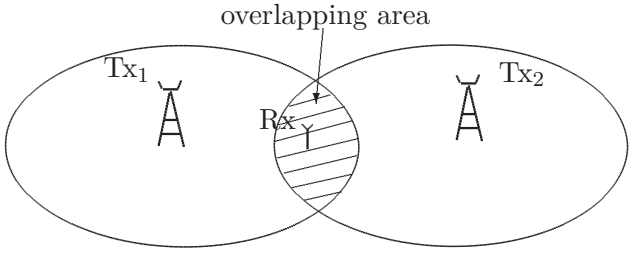

FIGURE 6.8 – Simplified SFN network, with two transmitters Tx.

As depicted in Fig. 6.8, we now consider a receiver Rx in the overlapping area. Moreover, we suppose that Rx is in motion, and is in the line of sight of the transmit antennas. After removal of the CP, we recall that the signal at the receiver side is expressed by $\mathbf{U} = \underline{\mathbf{C}}\mathbf{H} + \mathbf{W}$. From the receiver Rx point of view, the contribution of the signal from the two transmitters is a signal transmitted over a single channel. The samples H_m, $m = 0, 1, ..., M-1$ of the frequency response vector is then the sum of two independent components from the two different channels, as

$$\begin{aligned} H_m &= \sum_{l_1=0}^{L_1-1} h_{l_1} e^{-2j\pi \frac{m\beta_{l_1}}{M}} + \sum_{l_2=0}^{L_2-1} h_{l_2} e^{-2j\pi \frac{m\beta_{l_2}}{M}} \\ &= \sum_{l=0}^{L-1} h_l e^{-2j\pi \frac{m\beta_l}{M}}, \end{aligned} \tag{6.12}$$

where h_l, h_{l_1}, h_{l_2} are the time-varying complex path weights, which are zero mean Gaussian random processes. $\beta_l, \beta_{l_1}, \beta_{l_2}$ are the corresponding sampled path delays $\beta_l = \tau_l/\tau_s$. L is the number of paths of the equivalent channel, and we assume that each channel has the same number of paths $L_1 = L_2$ and we have $L \leq L_1 + L_2$. The gap between the delays βl is very short. In such conditions, the gains $|H_m|$ (on the Z axis) may be deeply attenuated over a large number of consecutive carriers. As made in [49], we illustrate this flat fading on Fig. 6.9, over 103 carriers (on the Y axis) and for 30 consecutive OFDM symbols (on the X axis). Furthermore, a dynamic representation of the phenomenon is available by clicking on this link

`http://www.youtube.com/watch?v=cyy1bVE8W24&feature=relmfu` .

In order to complete this theoretical model, [167, 168] propose some practical measurements of a DRM/DRM+ channel in an urban environment.

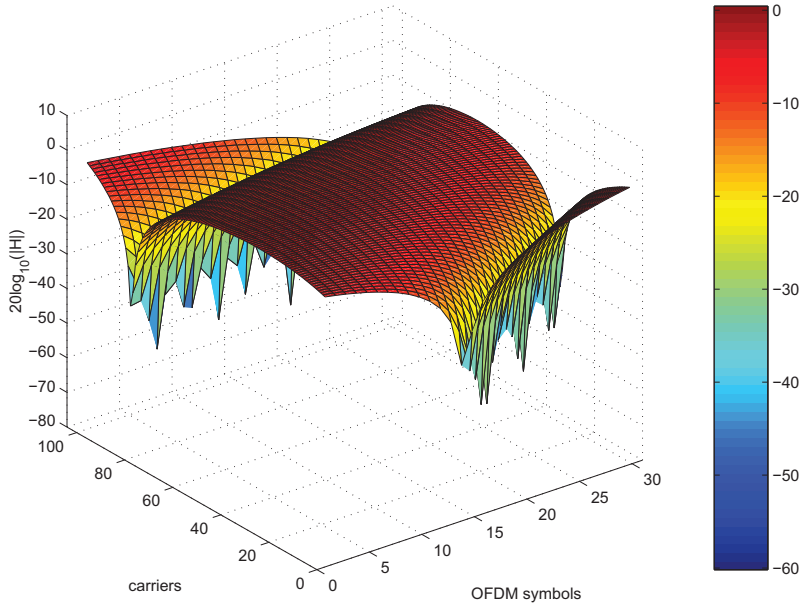

FIGURE 6.9 – Frequency response of the equivalent channel, without diversity.

When the flat fading affect many consecutive subcarriers in the frequency and time axis, the frequency diversity gain of the OFDM becomes null. Thus, a lot of errors occur at the receiver. If we consider the DRM/DRM+ standard, the practical consequence is that the radio program becomes inaudible.

6.3.2 Simulation Parameters

Fig. 6.9 is obtained by using parameters based on the ones of the DRM/DRM+ standard [1]. The considered signal follows the robustness mode B recommendations. We simulated a transmission with channel bandwidth $B = 5$ kHz. Each OFDM symbol is composed of 103 carriers (where one carrier is set to zero), and each frame includes 15 symbols. The bit stream is mapped with a 4-QAM constellation. The symbol and the cyclic prefix durations are $T_s = 21.33$ ms and $T_{CP} = 5.33$ ms respectively. We also applied a RS code [48] with a rate equal to 0.5. These parameters are summed up in Table 6.1.

TABLE 6.1 – Simulations Parameters.

Robustness B	
Symbol duration T_s	21.33 ms
CP duration T_{CP}	5.33 ms
Frame duration	400 ms
number of carriers M	103
Signal bandwidth B	5 kHz
Signal constellation	4-QAM
RS code rate	0.5

Each channel (from Tx_1 and Tx_2) follows a simple model inspired from the *CCIR poor* channel model [1]. It is a two paths channel with a uniform gain profile and which follows the WSSUS model. Thus, the equivalent channel is composed of four paths. This channel model is sufficiently relevant to highlight the flat fading illustrated in Fig. 6.9. The maximum delay of the equivalent channel noted τ_{max} is equal to $1/2B = 0.1$ ms, which allows to simulate a flat fading. Each path has a Gaussian Doppler spectrum, and the maximum Doppler frequency is equal to 2 Hz. It corresponds to a mobile receiver with a velocity roughly equal to 72 km/h.

6.4 Cyclic Delay Diversity

6.4.1 Principle of CDD

The solution to overcome the flat fading consists in artificially increasing the frequency selectivity of the channel. In [50,169,170], different diversity schemes are presented. The basic way to increase the frequency selectivity is to transmit the signal from one antenna with an additional delay denoted by Δ_D. This method is called delay diversity (DD). As mentioned in [50], the condition on the additional delay to get the expected effect is $\Delta_D > \frac{2}{B}$. In a discrete formalism, as $\Delta_D = k_{\Delta_D} T_s/M$ and $B = M/T_s$, then k_{Δ_D} must respect $k_{\Delta_D} > 2$. The main drawback of DD is that from the receiver point of view, the maximum delay of the channel is now equal to $\tau_{max} + \Delta_D$. However, in order to avoid the ISI, the maximum delay must respect $\tau_{max} + \Delta_D \leq T_{CP}$. This condition may not be respected if Δ_D is too large or if the value of τ_{max} increases during the transmission. An obvious solution consists of lengthening the guard interval, but it leads to a reduction of the useful data rate.

Another way to increase the frequency selectivity is to directly apply an additional phase to the signal in the frequency domain. This method is called phase diversity (PD). We denote $\Phi_m = -2\pi k_\Phi m/M$ the phase added to the m^{th} carrier. This carrier noted $C_{m,div}$, then becomes

$$C_{m,div} = C_m e^{-2j\pi k_\Phi m/M}. \tag{6.13}$$

The advantage of the PD compared to the DD is that for the same performance as DD, no condition on the length of the cyclic prefix is required in PD. The third way to increase the frequency selectivity is to apply to the signal a cyclic delay $k_{\Delta_D}(modM)$, where *mod* means modulo. This method is called cyclic delay diversity (CDD). If we note $u_{k,div}$ the k^{th} sample of the signal with CDD, the link with u_k is then given by

$$u_{k,div} = u_{k-k_{\Delta_D}(modM)}. \tag{6.14}$$

In the same way as PD, CDD does not require any condition on the length of the CP. As mentioned in [49], thanks to the cyclic property of the DFT and if we set $k_\Phi = k_{\Delta_D}$, CDD and PD are strictly equivalent :

$$u_{k,div} = u_{k-k_\Phi(modM)} = \sum_{m=0}^{M-1} (C_m e^{-2j\pi k_\Phi m/M}) e^{2j\pi km/M}. \tag{6.15}$$

Thus, the method is called PD or CDD when it is applied before or after the IDFT, respectively. The advantage of CDD with regard to PD is that it avoids making M multiplications as (6.13), because it only requires a rotation of the OFDM symbol samples. Different versions

of these methods have been proposed in the literature. Thus, the authors of [50] propose the time-variant phase diversity, in which Φ_m is considered to be time-variant. However, it may introduce ICI if the variations of the phase are to rapid. In [49], the CDD is applied at the receiver side. The main advantage is that a maximum ratio combining can be performed to maximize the SNR on each subcarrier. However, it increases the complexity of each receiver of the network.

Since Tx_1 and Tx_2 play a symmetric role, let us assume in the following that CDD is only applied at Tx_2, without loss of generality. From (6.12), we derive the channel frequency response, from the receiver point of view when CDD is used :

$$\begin{aligned} H_m &= \sum_{l_1=0}^{L_1-1} h_{l_1} e^{-2j\pi \frac{m\beta_{l_1}}{M}} + \sum_{l_2=0}^{L_2-1} h_{l_2} e^{-2j\pi \frac{m\beta_{l_2}}{M}} e^{\Phi_m} \\ &= \sum_{l_1=0}^{L_1-1} h_{l_1} e^{-2j\pi \frac{m\beta_{l_1}}{M}} + \sum_{l_2=0}^{L_2-1} h_{l_2} e^{-2j\pi \frac{m(\beta_{l_2}+k_\Phi)}{M}}. \end{aligned} \tag{6.16}$$

As presented in [47], Fig. 6.10 illustrates the frequency selectivity caused by CDD with $k_\Phi = 6$. The snapshot is obtained over 103 carriers and for 30 OFDM symbols. By comparison with Fig. 6.9, we observe that there is more frequency fading, but they affect less consecutive carriers. We then retrieve a channel similar to those which are described in the previous chapters. To complete the observation, a dynamic view of channel variations with CDD can be consulted by clicking this link

`http://www.youtube.com/watch?v=p5vyyNpYIgo` .

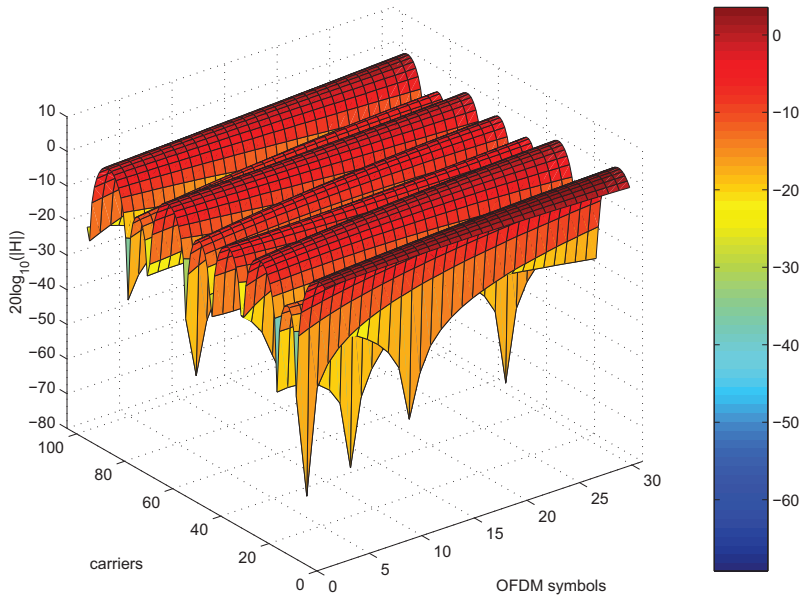

FIGURE 6.10 – Frequency response of the equivalent channel with cyclic delay diversity.

In such conditions, an efficient channel estimation [7, 18], combined with coded-OFDM and bit interleaving, allows to very efficiently reduce the errors of decision at the receiver [49, 50, 169, 170]. The effect of the increasing of the frequency selectivity on the choice of the channel estimation will be discussed in Section 6.5.

6.4.2 Generalization to a Multitransmitter Network

The previous model using only two transmit antennas is very simple. In practice, several antennas must be taken into account to model a more realistic SFN. Thus, in this section, we consider a multiple transmit-antennas network, as depicted in Fig. 6.11. In the proposed model, we consider transmitters without CDD (marked with an empty circle, such as BS_1) with transmitters with CDD (marked with a full circle or a cross, such as BS_2 and BS_3). Obviously, the phase of BS_2 noted Φ_{m2} has to be different of the one of BS_3 noted Φ_{m3}, in order to get the expected CDD effect in each overlapping area. Thus, the arrangement is made so that two adjacent areas do not share the same phase shifting. Should the opposite situation occur, the received frequency response would be given by

$$H_m = \left(\sum_{l=0}^{L-1} h_l e^{-2j\pi \frac{m\beta_l}{M}} \right) e^{j\Phi_m}. \tag{6.17}$$

In that case, whatever the value of the phase shifting Φ_m, (6.17) is equivalent to a transmission without CDD (6.12). As a consequence, three different values of phase shifting are required to develop the network. In the following, we will set $k_{\Phi 1} = 0$, $k_{\Phi 2} = 3$, $k_{\Phi 3} = 6$, as it ensures the condition $k_\Phi \geq 2$, as shown thereafter.

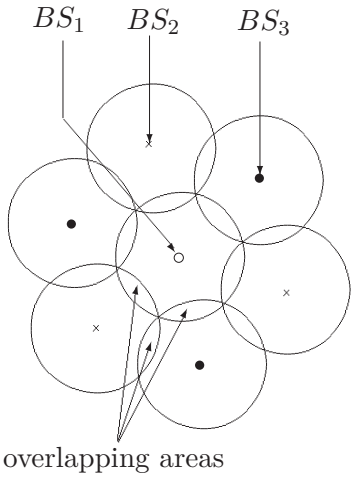

FIGURE 6.11 – SFN Network, with multiple transmitters Tx.

Although Fig. 6.11 remains a theoretical representation, it highlights the three different overlapping areas between the cells: two areas between cell with and without CDD (presented in the previous section) and one area between cells with CDD. In that case, whatever $i, j \in \{1, 2, 3\}$ we express the resulting frequency response as

$$H_m = \left(\sum_{l_1=0}^{L_1-1} h_{l_1} e^{-2j\pi \frac{m\beta_{l_1}}{M}} \right) e^{j\Phi_{mi}} + \left(\sum_{l_2=0}^{L_2-1} h_{l_2} e^{-2j\pi \frac{m\beta_{l_2}}{M}} \right) e^{j\Phi_{mj}}$$
$$= \sum_{l_1=0}^{L_1-1} h_{l_1} e^{-2j\pi \frac{m(\beta_{l_1}+k_{\Phi i})}{M}} + \sum_{l_2=0}^{L_2-1} h_{l_2} e^{-2j\pi \frac{m(\beta_{l_2}+k_{\Phi j})}{M}}. \quad (6.18)$$

By factorizing $e^{j\Phi_{mi}}$ or $e^{j\Phi_{mj}}$ with $e^{j\Phi_{mi}} \neq e^{j\Phi_{mj}}$, the expression (6.18) is equivalent to (6.16):

$$H_m = \left(\sum_{l_1=0}^{L_1-1} h_{l_1} e^{-2j\pi \frac{m\beta_{l_1}}{M}} + (\sum_{l_2=0}^{L_2-1} h_{l_2} e^{-2j\pi \frac{m\beta_{l_2}}{M}}) e^{j\Phi_{mj} - j\Phi_{mi}} \right) e^{j\Phi_{mi}}. \quad (6.19)$$

Finally, whatever the considered overlapping area, the study amounts to the same thing. Only the phase shifting will be different: Φ_{m1}, Φ_{m2} or $\Phi_{m2} - \Phi_{m1}$, but each one respects $k_\Phi \geq 2$. In order to complete this theoretical model with examples of real FM networks, it is possible to consult these two links :

`http://www.emetteurs.ch/list_freq.php?Frequence=100&search=Rechercher` ,

`http://www.annuaireradio.fr/cartevisu.php?rowid=55` ,

in which the FM transmit antennas are mapped, in France and in Switzerland respectively. It is also possible to choose the power and the transmit frequency to locate some antennas more precisely.

6.5 Simulations Results

6.5.1 Realistic DRM+ Cell

Fig. 6.12 displays the coverage area of an antenna broadcasting a DRM+ signal in the band II. It has been performed by means of the software Atoll, within the framework of the project OCEAN, and presented in [171]. The antenna is near Brest, at the west Brittany. It can be seen that the cell is not a circle as in the theoretical model. Indeed, in practice, the landscape has to be taken into account in the network planning. However, the results presented in the previous part remain valid in the realistic overlapping areas.

6.5.2 Measurement of the Fading

First, the effect of CDD on the frequency width of the fading, independently of the rest of the system (channel estimation, channel encoding etc.) is investigated. To this end, we measure the maximum number of consecutive carriers which are disrupted by the deep fading, i.e. the ratio of consecutive carriers disrupted by an arbitrary set channel level $20\log_{10}(|H_m|)$ equal or less than -10 dB. Fig. 6.13 displays the value of this measure versus time (represented as a number of OFDM symbols), for the same transmission with and without CDD.

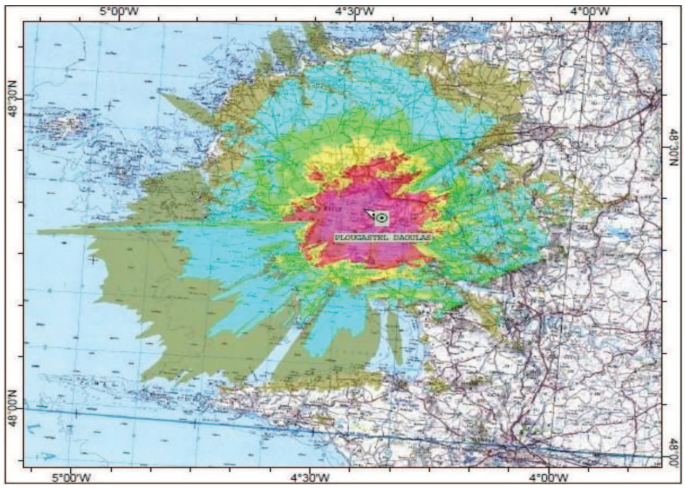

FIGURE 6.12 – Coverage area of an antenna transmitting in the band II.

The comparison is given for one simulation run and during 420 consecutive OFDM symbols, corresponding to a signal time duration equal to 11.20 s. In this example, we set $k_\Phi = 6$.

For one process, we observe on Fig. 6.13 that the maximum ratio of consecutive carriers disrupted by fading less than -10 dB can reach 100%, and even during several consecutive OFDM symbols. In that case, the channel decoding becomes inefficient and a large number of errors occurs in the bit stream. Considering the same transmission with CDD on one Tx, we observe a decrease of this maximum to 40%. As a consequence, we deduce that the number of errors is lower than in a transmission without CDD. On the other hand, for a transmission without CDD, we observe that it is possible to obtain a flat channel (no carriers under -10 dB), which tallies with an AWGN transmission. In these conditions, for the transmission with CDD, we observe that the percentage reaches around 8%. The effect of CDD is then to statistically keep the maximum ratio of consecutive carriers disrupted by fading to a value close to zero.

Table 6.2 shows the average percentage values of the number of consecutive corrupted carriers for two different phase shifting values $k_{\Phi 1} = 3$ and $k_{\Phi 2} = 6$, pointed out by "0" and "I", respectively. The use of two shifting values allows to describe the model of the previous section: one transmitter without CDD, and two transmitters with CDD such as $k_{\Phi 1} \neq k_{\Phi 2}$. By choosing $k_{\Phi 2} = 2k_{\Phi 1}$, we simplify the number of cases to consider as $k_{\Phi 1} = k_{\Phi 2} - k_{\Phi 1}$. Two thresholds -10 and -20 dB are considered. Furthermore, in order to complete the study, we simulated CDD with a time-varying value of k_Φ during the transmission. To do so, we consider that the delay k_Φ alternately takes the value $k_\Phi - 1$, k_Φ and $k_\Phi + 1$. This is pointed out by "var. k_Φ" in Table 6.2, and the mark "0" and "I" shows if k_Φ is fixed or variable. Each of the three delay values has a probability equal to 1/3. The average is calculated thanks to 100 simulation runs. For a transmission without CDD, the average of the maximum ratio of the consecutive carriers disrupted by fading is 22.6% at -10 dB and 7.34% at -20 dB.

In average, we observe that the maximum percentage of the consecutive carriers disrupted by fading decreases compared to a transmission without CDD, whatever the threshold, and for the two values $k_\Phi = 3$ and $k_\Phi = 6$. It confirms the observations made for one simulation run. Furthermore, according to the theory, we notice that the ratio of consecutive disrupted

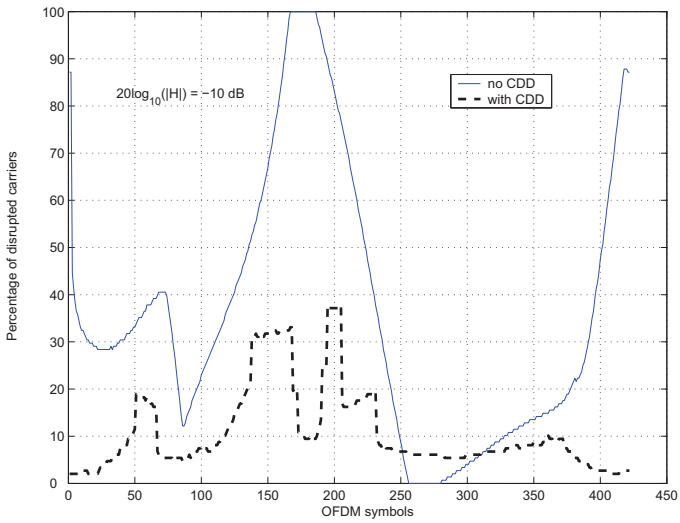

FIGURE 6.13 – Ratio of corrupted carriers by a channel gain equal to $20\log_{10}(|H|) = -10$ dB, over 420 OFDM symbols, with and without CDD.

TABLE 6.2 – Average ratio of consecutive carriers disrupted by fading at -10 or -20 dB. Comparison in function of different delay values.

	$k_\Phi = 3 \rightarrow 0$	fixed $k_\Phi \rightarrow 0$	ratio at	
	$k_\Phi = 6 \rightarrow$ I	var. $k_\Phi \rightarrow$ I	-10 dB	-20 dB
test 1	0	0	15.17 %	4.52 %
test 2	I	0	10.50 %	3.19 %
test 3	0	I	15.59 %	4.55 %
test 4	I	I	10.78 %	3.53 %
no CDD			22.6 %	7.34 %

carriers is lower for $k_\Phi = 6$ than for $k_\Phi = 3$. When varying delays k_Φ are used, we almost find the same results as for a fixed k_Φ. The reason is that in average, $E\{k_\Phi\}$ (when k_Φ varies) is equal to the fixed k_Φ value. Moreover, at the receiver, a varying k_Φ value increases the difficulty of making an efficient estimation, or requires methods which do not depend on the variations of the channel parameters as in [34,35]. We then finally recommend the use of fixed k_Φ delays.

6.5.3 Bit Error Rate Performance

We now characterize the performance of the global system, including channel encoding and channel estimation. We use a Reed-Solomon code with rate 1/2. A least square (LS) estimation is performed on the pilot tones, and a cubic spline interpolation allows to get the channel estimation on all the bandwidth.

Fig. 6.14 depicts the bit error rate (BER) as a function of OFDM symbols, for a transmission duration of 11.20 s (420 symbols). Two independent processes are displayed, in which the transmission of the signal without CDD is compared to the one with CDD, for the same channel. We used a delay value $k_\Phi = 6$, and the signal to noise ratio is set equal to 10 dB.

The observation duration is almost equal to $10T_C$ for both processes, which allows to get a sufficient statistic to draw conclusions.

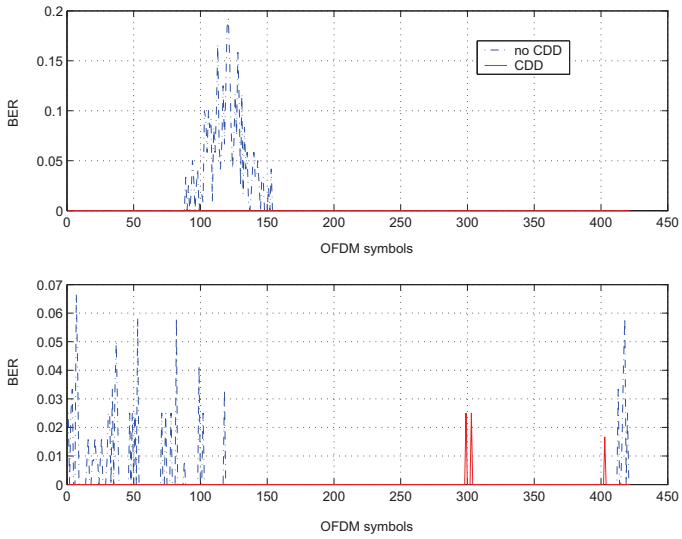

FIGURE 6.14 – BER versus OFDM symbols, for two independent process.

For the two processes, we clearly observe a decrease of the BER for the transmission with CDD compared to the one without CDD. Indeed, two effect are noticeable. Firstly, the symbols with non-null BER are sparsely distributed in transmissions with CDD, while they occur much more and consecutively in transmissions without CDD. Thus, on the top plot of Fig. 6.14, the duration of consecutive corrupted OFDM symbols without CDD is roughly equal to 1.5 s, while the BER is null during all the transmission duration with CDD. Secondly, the BER value is lower if diversity is used: on the bottom plot of Fig. 6.14, the BER reaches 0.025 (with CDD) versus 0.065 without CDD. In the context of radio transmission with DRM/DRM+, we conclude that the use of CDD allows to obtain a listening time almost without audible disruptions.

Fig. 6.15 displays the BER curves of transmission without CDD compared to the one with CDD, for $k_\Phi = 3$ and $k_\Phi = 6$. As a lower bound reference, we also added the BER performance of a transmission over an AWGN channel. The simulations have been performed on 500 runs, corresponding to 2.10^6 bits. We observe, for SNR values from -4 to 16 dB, the gain provided by CDD. Compared to a transmission without CDD at BER=10^{-3}, the gain in SNR is equal to 2 dB for CDD with $k_\Phi = 3$ and 3 dB for $k_\Phi = 6$.

In order to study the effect of CDD on the performance of the global system, it is important to show the impact of the increase of the frequency selectivity on the channel estimation performance. The author of [172] discusses this consequence of CDD. In the simulations, the distribution of the pilot tones in the frame is one for seven carriers along the frequency axis and one for four symbols along the time axis (see [1], Appendix L). A least square (LS) estimation is performed on pilot tones and an interpolation is made to obtain the channel estimation all over the frame. Thus, Fig. 6.16 compares the BER curves of channel estimation made with a spline interpolation and with a linear interpolation, in the case of transmissions without CDD, and with CDD such as $k_\Phi = 6$. The spline interpolation is more accurate than the linear one, but also more complex. Indeed, the spline interpolation requires $\mathcal{O}(M^2)$

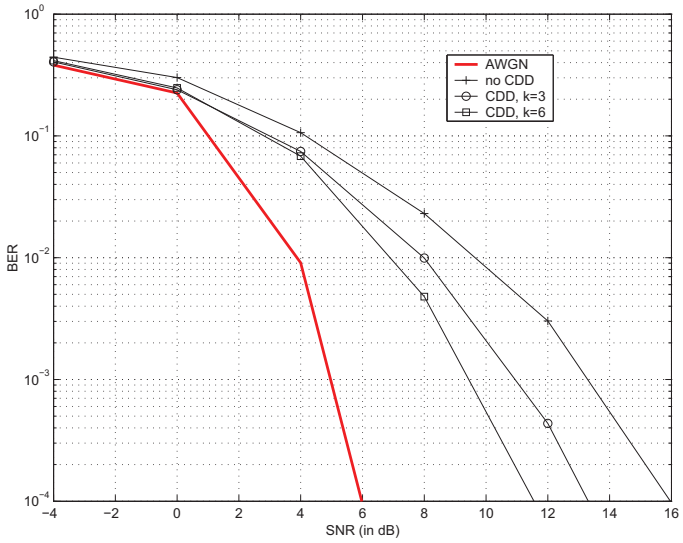

FIGURE 6.15 – BER versus SNR for transmissions with and without CDD.

operations and the linear interpolation only $\mathcal{O}(M)$ operation.

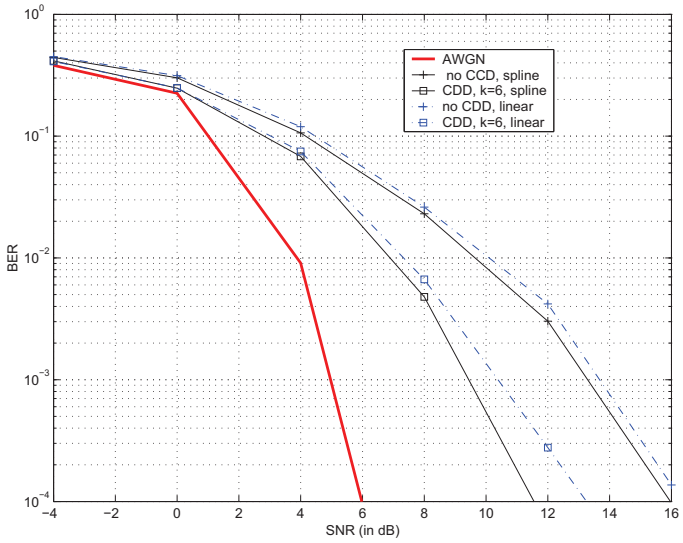

FIGURE 6.16 – BER versus SNR, effect of the interpolation, with and without CDD.

In both cases, the linear interpolation is less efficient than the spline one. For CDD, we observe that the SNR gap between spline and linear interpolation is equal to 1 dB at BER=10^{-3} and 2 dB for BER=10^{-4}. For the linear interpolation, the SNR gap remains equal to 0.5 dB. Without CDD, the channel has a low frequency selectivity, so spline and linear interpolations have almost the same performance. However, in presence of CDD with $k_\Phi = 6$, spline is more efficient than linear. We also observe that there is no BER floor, as it has been described in Chapter 5. The is the result of the use of the channel coding. We conclude that the channel estimation method must be taken into account when CDD is used in a network in order to reach a given BER. Although CDD clearly reduces the flat fading

in the overlapping areas of the SFN, the consequence is the increase of the complexity of the estimation method.

6.6 Conclusion

In this chapter, different diversity methods was presented, with their advantages and drawbacks, which are summarized in Table 6.3. The goal of the diversity is to statistically reduce the errors at the receiver, by transmitting the signal over different uncorrelated channels. Moreover, we mainly focused on the cyclic delay diversity and its application to a SFN using the DRM/DRM+ standard, in which flat fading channels may disrupt the signal on all the bandwidth. This study is also a contribution of this thesis for the project OCEAN. The principle of CDD is to retrieve the frequency diversity of the OFDM by artificially increasing the frequency selectivity of the channel. The simulations actually validated the gain brought by CDD in the case of flat fading channels. However, in the model, the pilot tones are sparsely distributed in the OFDM frame, and an interpolation has to be performed along the frequency axis for the channel estimation. Since the CDD increases the frequency selectivity of the channel, we showed that the channel estimation has to be taken into account in the global performance of the system.

Table 6.3 – Comparison of the different diversity schemes.

Diversities	Advantages	Drawbacks	Remark
Time	easy implementation	data rate loss	transmitter
Spatial	no data rate loss	correlation between antennas	transmitter/ receiver
Polarization	no data rate loss	weakening of the SNR	receiver
Frequency	robust against the frequency selective channels	sensible to the time selective channels	robust when combined with channel codes
Cyclic delay	robust against flat fading	adaptation of the channel estimation method	transmitter/ receiver

General Conclusion

In this dissertation, contributions to the multipath channel estimation in the OFDM context were proposed. According to the channel severity that may be induced by the time or the frequency selectivity, an adapted solution was proposed to struggle against the distortions caused by the channel.

In wireless communications, the environment between two antennas is often considered as a multipath channel. Thus, the received version of the signal transmitted through such a channel is a sum of delayed versions of the original signal. These echoes are due to reflections of the electromagnetic waves on obstacles of different natures. Although it allows the signal to be transmitted to an hidden receiver, the multipath propagation channel is one of the main source of disturbance for the signal. Indeed, this is the source of frequency holes in the spectrum of the signal. This kind of channel is then called frequency selective channel. An effective usual solution consist of transmitting the signal with the orthogonal frequency division multiplexing (OFDM) waveform. The principle is to split the bandwidth into some narrowband subcarriers, each one carrying only a part of the entire information. If the system is well designed, each sub-channel can be seen as a Gaussian channel. It is then straightforward to recover the entire information thanks to a one-tap equalization, i.e. a simple division. However, the performance of the equalization depends on the accuracy of the channel estimation.

In the first chapter, a background concerning the transmission channel was presented. As it is the basics of the channel models, different statistical functions and properties of the channel were detailed, and the links between them was covered. Furthermore, the basic principles of the OFDM modulation were introduced. We then reminded that this waveform is robust against multipath channels, with the help of the cyclic prefix (CP), as it cancels the intersymbol interferences (ISI) and gives the channel matrix its cyclic property at the same time.

The second chapter proposed a state of the art of the different channel estimation methods. In this dissertation, we focused on the semi-blind estimation techniques that require some pilot tones to be performed. These pilot tones are non-data subcarriers whose values are known from both the transmitter and the receiver. Among the different estimators widely detailed in [22–27], we particularly took an interest on the methods based on the least square (LS) and the minimum mean square error (MMSE) criteria. LS is a straightforward technique but is very sensitive to the noise. On the contrary, the linear-MMSE (or LMMSE) estimator is very accurate, but requires a prohibitive calculation cost, due to matrix inversions and multiplications. Furthermore, LMMSE needs the knowledge of the noise variance and the channel covariance matrix. Yet, in most of the cases, these parameters are unknown at the receiver so LMMSE is hardly useable in practice.

A method called artificial channel aided-LMMSE (ACA-LMMSE) was proposed in the third chapter. This is an MMSE-based channel estimator that does not require the a priori knowledge of the channel covariance matrix, nor its estimation. To do so, at the receiver side, a signal composed by pilots only is transmitted through a filter acting like an artificial channel, and is added to the useful signal. From the estimator point of view, an hybrid channel composed of the physical and the artificial channel has to be estimated. The particularity of this method lies in the fact that the added filter is designed so that an LMMSE estimation of the hybrid channel can be performed using the artificial channel covariance matrix, which is perfectly known. The estimation of the physical channel is then achieved by subtracting the artificial channel coefficients. Simulations results showed that the performance of the ACA-LMMSE estimator is close to the optimal one. In addition to the avoidance of the a priori need of the channel covariance matrix, this method is simpler than the usual LMMSE in the case of time-varying channel. In the LMMSE case, if the channel or its statistics varies, the channel covariance matrix and the inversion have to be updated. In ACA-LMMSE, the artificial channel covariance matrix is designed independently of the physical channel, so it must be computed only once during the entire transmission duration. From this, we may combine ACA-LMMSE with an interference cancellation algorithm called residual ISI cancellation (RISIC) [36]. The ISIs appear in a particular channel model, when the maximum path delays is higher than the cyclic prefix duration. The RISIC algorithm is efficient for a static or a slowly varying channel. The combination of RISIC with ACA-LMMSE allows an extension of the RISIC algorithm to time-varying channels.

In the proposed ACA-LMMSE method, the noise variance was supposed to be known at the receiver side. This is the reason why an MMSE-based estimation for both the SNR and the channel was proposed in the chapter 4. As the MMSE estimation of the noise variance requires the channel response and the LMMSE channel estimation requires the noise level, each estimation feeds the other one so an iterative algorithm is proposed. In the first part of the chapter, a theoretical approach, in which the channel covariance matrix is supposed to be known, was introduced. Then, a more realistic approach considering an estimated covariance matrix was proposed. The convergence of the algorithm is proved in both scenarios, and simulations showed that the optimal estimation is almost reached for both SNR and channel parameters. Finally, a third part developed an application of the method to the spectrum sensing in a cognitive radio context. Indeed, it is possible to differentiate the behavior of the algorithm if a signal or only noise is received, and an analytical expression of the detection and false alarm probabilities was derived. Finally, this practical algorithm allows to detect the presence or absence of a user in a given channel, to estimate the noise level if the user is absent, and to estimate both the channel and the SNR if the user is present.

Chapters 3 and 4 dealt with MMSE-based methods that simplify LMMSE or make possible its implementation in practice. Unlike the two previous chapters, Chapter 5 focused on the problem of interpolations for the Rayleigh channel estimation. Indeed, when the pilot tones are sparsely distributed in the OFDM frame, an interpolation is required to get the channel frequency response over the entire time and frequency lattice. When simple methods such as the linear interpolation are used, a residual error of estimation appears, even if the noise power tends to zero. Chapter 5 proposed to statistically characterize this error in function of the interpolation method and the gap between two consecutive pilot tones. From that, a theoretical expression of the mean square error (MSE) is developed, and the lower bound of the

bit error rate (BER) is derived, the latter being also function of the size of the constellation. Two kinds of interpolations are considered: the nearest neighbor (NN) and the linear ones. The analytical expression was validated, as the curves obtained by simulations perfectly matched the theoretical ones. This study then allows predicting the performance of an interpolation, in function of the channel statistics, the distribution of the pilot tones and the constellation size.

In the sixth and final chapter, an application of the cyclic delay diversity (CDD) to a single frequency network (SFN) using the DRM/DRM+ standard [1] was presented. In such a network, the signal is transmitted at the same frequency from all the base stations. In the overlapping area between two adjacent cells, one may observe that the maximum delays can be very short. In such conditions, the fading may disrupt the entire bandwidth. Consequently, the frequency diversity of the OFDM becomes inefficient, and the signal might be fully corrupted, even if a channel coding is used. The solution consists of artificially increasing the channel frequency selectivity in order to recover the advantage of the coded-OFDM (COFDM), thanks to the cyclic delay diversity. The contribution of CDD is effectively proved by simulations. However, since the pilots are in staggered rows in the DRM/DRM+ standard, the channel estimation requires an interpolation. Thus, admittedly the CDD improves the transmission quality, but the increase of the frequency selectivity has to be taken into account in the system performance, as the channel estimation requires an interpolation. This study has been done within the framework of the project OCEAN, whose goal was to improve the digital radio broadcasting with the DRM/DRM+ standard.

This thesis is a contribution to the channel estimation. Several solutions for the simplification of the LMMSE have been proposed, and an analysis of the errors of interpolation has been achieved. However, we can investigate new leads from the present work. Some prospects can be, for instance:

- The study of the effect of a synchronization mismatch on the ACA-LMMSE efficiency. Indeed, it was assumed that the artificial signal and the useful one are perfectly synchronized, which is not the case in practice. Furthermore, it would be interesting to practically implement the method thanks to a simple line, as proposed in the chapter 3.
- The improvement of the theoretical expression of the detection probability for the spectrum sensing algorithm. It was noticed that the analytical curves was obtained after some approximation. It would be interesting to consider a more accurate model.
- The extension of the interpolation errors analysis to other interpolation methods (such as a piecewise cubic interpolation) and constellations of higher orders (16-QAM for instance). Furthermore, if the method is extended to a two-dimension plan, it could be possible to use the analysis in image processing.

Appendix A

Appendix of the Chapter 1

A.1 Expression of the Channel Covariance

The channel intensity profile $\Gamma(\tau)$ is calculated from the impulse response channel (1.2). The general development of the link between $\Gamma(\tau)$ and $R_H(\Delta_f)$ is proposed in [59]. Here, we apply it to our model. The autocorrelation function is usually defined by $r_h(\Delta_t, \tau_1, \tau_2)$, but remembering $\Delta_t = 0$,we get :

$$\begin{aligned} r_h(\tau_1, \tau_2) &= E\{h(t, \tau_1)h^*(t, \tau_2)\} \\ &= E\{(\sum_{l_1=0}^{L-1} h_{l_1}(t)\delta(\tau_1 - \tau_{l_1}))(\sum_{l_2=0}^{L-1} h_{l_2}(t)\delta(\tau_2 - \tau_{l_2}))^*\} \end{aligned} \tag{A.1}$$

Remembering the channel follows a WSSUS model, we have $E\{h_{l_1}(t)h^*_{l_2}(t)\} = 0$ if $l_1 \neq l_2$, so we simply (A.1) as

$$\begin{aligned} r_h(\tau_1, \tau_2) &= E\{\sum_{l=0}^{L-1} h_l(t)\delta(\tau_1 - \tau_l)h^*_l(t)\delta(\tau_2 - \tau_l))\} \\ &= E\{\sum_{l=0}^{L-1} |h_l(t)|^2\delta(\tau_1 - \tau_2)\} \\ &= \sum_{l=0}^{L-1} E\{|h_l(t)|^2\delta(\tau_1 - \tau_2)\} \\ &= \sum_{l=0}^{L-1} \Gamma_l(\tau_1)\delta(\tau_1 - \tau_2). \end{aligned} \tag{A.2}$$

$\Gamma_l(\tau)$ is time-limited on $\tau \in [0, \tau_{max}]$, with τ_{max} the maximum path delay. The frequency correlation function, being defined as the FT of $r_h(\tau_1, \tau_2)$, we get from (A.2)

$$
\begin{aligned}
R_H(f_1,f_2) &= \int_{-\infty}^{+\infty}\int_{-\infty}^{+\infty} r_h(\tau_1,\tau_2)e^{(-2j\pi(f_1\tau_1-f_2\tau_2))}d\tau_1 d\tau_2 \\
&= \int_{0}^{\tau_{max}}\int_{0}^{\tau_{max}} r_h(\tau_1,\tau_2)e^{(-2j\pi(f_1\tau_1-f_2\tau_2))}d\tau_1 d\tau_2 \\
&= \int_{0}^{\tau_{max}}\int_{0}^{\tau_{max}} \sum_{l=0}^{L-1}\Gamma_l(\tau_1)\delta(\tau_1-\tau_2)e^{(-2j\pi(f_1\tau_1-f_2\tau_2))}d\tau_1 d\tau_2 \\
&= \sum_{l=0}^{L-1}\int_{0}^{\tau_{max}} \Gamma_l(\tau_1)e^{(-2j\pi(f_1-f_2)\tau_1)}d\tau_1 \\
&= \sum_{l=0}^{L-1}\int_{0}^{\tau_{max}} \Gamma_l(\tau_1)e^{(-2j\pi\delta_f\tau_1)}d\tau_1. \qquad \text{(A.3)}
\end{aligned}
$$

We retrieve the expression given in (1.17). This development also prove the assumption of stationarity $R_H(f_1,f_2) = R_H(\delta_f)$ for the frequency correlation function.

A.2 Proof of the Diagonalization of a Circulant Matrix in the Fourier Basis

This proof is inspired of the work proposed in [12]. Let us consider $\underline{\mathbf{A}}$ as a $M \times M$ circulant matrix with complex coefficients $(a_0, a_1, ..., a_{M-1})$, with $M \geq 2$

$$
\underline{\mathbf{A}} = \begin{pmatrix}
a_0 & a_1 & \cdots & a_{M-2} & a_{M-1} \\
a_{M-1} & a_0 & \ddots & a_{M-3} & a_{M-2} \\
\vdots & & \ddots & & \vdots \\
a_2 & & \ddots & a_0 & a_1 \\
a_1 & \cdots & \cdots & a_{M-1} & a_0
\end{pmatrix}. \qquad \text{(A.4)}
$$

We here prove that this matrix is diagonalizable. Let us consider $\underline{\mathbf{J}}$ the $M \times M$ elementary matrix as

$$
\underline{\mathbf{J}} = \begin{pmatrix}
0 & 1 & 0 & \cdots & 0 \\
0 & 0 & 1 & \vdots & 0 \\
\vdots & & \ddots & \ddots & \vdots \\
0 & 0 & \ddots & 0 & 1 \\
1 & 0 & \cdots & 0 & 0
\end{pmatrix}. \qquad \text{(A.5)}
$$

We define $B = (\mathbf{e}_1, \mathbf{e}_2, ..., \mathbf{e}_M)$ a basis as

$$
\mathbf{e}_1 = \begin{pmatrix} 1 \\ 0 \\ \vdots \\ 0 \end{pmatrix}, \mathbf{e}_2 = \begin{pmatrix} 0 \\ 1 \\ \vdots \\ 0 \end{pmatrix}, ..., \mathbf{e}_M = \begin{pmatrix} 0 \\ 0 \\ \vdots \\ 1 \end{pmatrix}. \qquad \text{(A.6)}
$$

f is the endomorphism such as, in the basis B, $\underline{\mathbf{J}}$ is the matrix of f. Thus, we get the relations :

$$\begin{cases} f(\mathbf{e}_M) = \mathbf{e}_1, & \text{and} \\ f(\mathbf{e}_k) = \mathbf{e}_{k-1}, & \text{for } 2 \leq k \leq M \quad . \end{cases} \tag{A.7}$$

We deduce :

$$\begin{aligned} f^M(\mathbf{e}_k) &= f \circ f \circ ... \circ f(\mathbf{e}_k) \\ &= f^{M-k+1}(\mathbf{e}_1) \\ &= f^{M-k}(\mathbf{e}_M) \\ &= \mathbf{e}_k. \end{aligned} \tag{A.8}$$

Finally, we have :

$$f^M = I_d, \tag{A.9}$$

where I_d is the identity application. In its matrix form, we have :

$$\underline{\mathbf{J}}^M = \underline{\mathbf{I}}. \tag{A.10}$$

We define the polynomial $Q = X^M - 1$ and we prove that Q is the minimal polynomial of $\underline{\mathbf{J}}$, or in an equivalent manner, the minimal polynomial of f. Let us consider $S = \sum_{i=0}^{M'-1} s_i X^i$ a polynomial of degree $M' < M$. If S cancels out f, we would have, especially for $\mathbf{e}_M$ (the demonstration is the same for each vector of the basis, but simpler by considering $\mathbf{e}_M$) :

$$S(f(\mathbf{e}_M)) = \sum_{i=0}^{M'-1} s_i f^i(\mathbf{e}_M) = \sum_{i=0}^{M'-1} s_i \mathbf{e}_{M-i} \neq 0, \tag{A.11}$$

because of $\mathbf{e}_1, \mathbf{e}_2, ..., \mathbf{e}_M$ are linearly dependent (B is a basis indeed). We proved that a polynomial s whose degree is $\leq M$ does not exist. Q is the monic polynomial of least degree such as $Q(\underline{\mathbf{J}}) = 0$, so Q is the minimal polynomial of $\underline{\mathbf{J}}$. The roots of Q are then the M roots of unity $(1, e^{\frac{2i\pi}{M}}, e^{\frac{4i\pi}{M}}, ..., e^{\frac{2(M-1)i\pi}{M}})$. We rewrite Q as

$$Q = \prod_{k=0}^{M-1} (X - e^{\frac{2ik\pi}{M}}). \tag{A.12}$$

Property : an endomorphism f is diagonalizable if its minimal polynomial has only simple roots.

As Q has only simple roots, we can define $\underline{\mathbf{D}}$ the diagonalized form of $\underline{\mathbf{J}}$, with $(1, e^{\frac{2i\pi}{M}}, e^{\frac{4i\pi}{M}}, ..., e^{\frac{2(M-1)i\pi}{M}})$ the eigenvalues of $\underline{\mathbf{J}}$. The transformation matrix $\underline{\mathbf{P}}$ is defined so that

$$\underline{\mathbf{D}} = \underline{\mathbf{P}}^{-1} \underline{\mathbf{J}} \underline{\mathbf{P}}, \tag{A.13}$$

with $\underline{\mathbf{D}}$ the diagonal matrix having the eigenvalues of $\underline{\mathbf{J}}$ on its diagonal:

$$\underline{\mathbf{D}} = \begin{pmatrix} 1 & 0 & \cdots & 0 \\ 0 & e^{\frac{2i\pi}{M}} & \ddots & \vdots \\ \vdots & & \ddots & 0 \\ 0 & \cdots & 0 & e^{\frac{2(M-1)i\pi}{M}} \end{pmatrix}. \tag{A.14}$$

Now, we show that $\underline{\mathbf{P}}$ is similar to the Fourier matrix $\underline{\mathcal{F}}$ defined in the chapter 1 :

$$\underline{\mathcal{F}} = \frac{1}{\sqrt{M}} \begin{pmatrix} 1 & 1 & 1 & \cdots & 1 \\ 1 & \omega & \omega^2 & \cdots & \omega^{(M-1)} \\ 1 & \omega^2 & \omega^4 & \cdots & \omega^{2(M-1)} \\ \vdots & \vdots & \vdots & \ddots & \vdots \\ 1 & \omega^{(M-1)} & \omega^{2(M-1)} & \cdots & \omega^{(M-1)^2} \end{pmatrix}, \tag{A.15}$$

with $\omega = e^{-\frac{2j\pi}{M}}$. We define the eigenvectors $\mathbf{P}_0, \mathbf{P}_1, ..., \mathbf{P}_{M-1}$ forming the matrix $\underline{\mathbf{P}}$ and we note

$$\mathbf{P}_k = \begin{pmatrix} P_{0,k} \\ P_{1,k} \\ \vdots \\ P_{M-1,k} \end{pmatrix} \tag{A.16}$$

Whatever k, $0 \leq k \leq M-1$, $\mathbf{P}_k$ being an eigenvector, we have

$$(\underline{\mathbf{J}} - e^{\frac{2ik\pi}{M}}\underline{\mathbf{I}})\mathbf{P}_k = (\underline{\mathbf{J}} - \omega^k\underline{\mathbf{I}})\mathbf{P}_k = (0), \tag{A.17}$$

and if we develop

$$\begin{pmatrix} -\omega^k & 1 & 0 & \cdots \\ \vdots & -\omega^k & 1 & \vdots \\ 0 & \ddots & \ddots & 1 \\ 1 & 0 & \cdots & -\omega^k \end{pmatrix} \begin{pmatrix} P_{0,k} \\ P_{1,k} \\ \vdots \\ P_{M-1,k} \end{pmatrix} = (0). \tag{A.18}$$

We obtain the following system of equations:

$$\begin{cases} \omega^k P_{0,k} = P_{1,k}, \\ \omega^k P_{1,k} = P_{2,k}, \\ \vdots \\ \omega^k P_{M-2,k} = P_{M-1,k} \\ P_{0,k} = \omega^k P_{M-1,k} \end{cases} \tag{A.19}$$

By recurrence, we have

$$P_{M-1,k} = \omega^k P_{M-2,k} = ... = \omega^{(M-1)k} P_{0,k}. \tag{A.20}$$

We get the developed expression of the matrix $\underline{\mathbf{P}}$:

$$\underline{\mathbf{P}} = \begin{pmatrix} P_{0,0} & P_{0,1} & P_{0,2} & \cdots & P_{0,M-1} \\ P_{0,0} & \omega P_{0,1} & \omega^2 P_{0,2} & \cdots & \omega^{(M-1)} P_{0,M-1} \\ P_{0,0} & \omega^2 P_{0,1} & \omega^4 P_{0,2} & \cdots & \omega^{2(M-1)} P_{0,M-1} \\ \vdots & \vdots & \vdots & \ddots & \vdots \\ P_{0,0} & \omega^{(M-1)} P_{0,1} & \omega^{2(M-1)} P_{0,2} & \cdots & \omega^{(M-1)^2} P_{0,M-1} \end{pmatrix}. \tag{A.21}$$

In order to get the orthonormal Fourier matrix, it is sufficient to chose :

$$P_{0,0} = P_{0,1} = \cdots = P_{0,M-1} = \frac{1}{\sqrt{M}} \tag{A.22}$$

We define the polynomial R as

$$R = \sum_{k=0}^{M-1} a_k X^k, \tag{A.23}$$

we then simply get from (A.4)

$$\underline{\mathbf{A}} = R(\underline{\mathbf{J}}). \tag{A.24}$$

As $\underline{\mathbf{J}}$ is diagonalizable, we easily prove that:

$$\underline{\mathbf{A}} = R(\underline{\mathbf{P}}\underline{\mathbf{D}}\underline{\mathbf{P}}^{-1}) = \underline{\mathbf{P}}R(\underline{\mathbf{D}})\underline{\mathbf{P}}^{-1}, \tag{A.25}$$

or, in other terms:

$$\underline{\mathbf{A}} = \underline{\mathbf{P}}\overbrace{(a_0\underline{\mathbf{I}} + a_1\underline{\mathbf{D}} + a_2\underline{\mathbf{D}}^2 + ... + a_{M-1}\underline{\mathbf{D}}^{M-1})}^{\text{diagonal matrix}}\underline{\mathbf{P}}^{-1}, \tag{A.26}$$

By taking $\underline{\mathbf{P}} = \underline{\mathcal{F}}$, we then verify that every circulant matrix is diagonalizable in the Fourier basis.

Appendix B

Appendix of the Chapter 4

B.1 Proof of the Convergence to Zero of the Algorithm when Using the Matrix $\underline{\tilde{\mathbf{R}}}_H^{LS}$

This appendix proves that the algorithm converges towards zero when it is performed with only $\underline{\tilde{\mathbf{R}}}_H^{LS}$. It justifies the substitution of this matrix by $\underline{\tilde{\mathbf{R}}}_H^{LMMSE}$ for $i \geq 2$. If the steps (4.35) and (4.36) are performed with, then it yields:

$$\begin{aligned}\hat{\sigma}^2_{(i+1)} &= \frac{1}{M} E\{||\hat{\mathbf{H}}^{LS} - \hat{\mathbf{H}}^{LMMSE}_{(i+1)}||^2\} \\ &= \frac{1}{M} tr\left(\hat{\sigma}^4_{(i)} (\underline{\tilde{\mathbf{R}}}_H^{LS} + \hat{\sigma}^2_{(i)} \underline{\mathbf{I}})^{-1} (\underline{\mathbf{R}}_H + \sigma^2 \underline{\mathbf{I}}) ((\underline{\tilde{\mathbf{R}}}_H^{LS} + \hat{\sigma}^2_{(i)} I)^{-1})^H\right). \end{aligned} \tag{B.1}$$

We remind that for a large value M, $\frac{1}{M} tr(\underline{\tilde{\mathbf{R}}}_H^{LS}) = \frac{1}{M} tr(\underline{\mathbf{R}}_H + \sigma^2 \underline{\mathbf{I}})$ so let us aaume that, in a first approximation, $\underline{\tilde{\mathbf{R}}}_H^{LS} = \underline{\mathbf{R}}_H + \sigma^2 \underline{\mathbf{I}}$ in order to develop (B.1):

$$\hat{\sigma}^2_{(i+1)} = \frac{1}{M} tr\left(\hat{\sigma}^4_{(i)} (\underline{\mathbf{R}}_H + (\hat{\sigma}^2_{(i)} + \sigma^2) \underline{\mathbf{I}})^{-1} (\underline{\mathbf{R}}_H + \sigma^2 \underline{\mathbf{I}}) ((\underline{\mathbf{R}}_H + (\hat{\sigma}^2_{(i)} + \sigma^2) \underline{\mathbf{I}})^{-1})^H\right). \tag{B.2}$$

$\underline{\mathbf{R}}_H$ being an Hermitian matrix, it is possible to the the same diagonalization property given in [37] and in Section 4.3 for the expression (B.2), and we finally find the scalar form of (B.2):

$$\hat{\sigma}^2_{(i+1)} = \frac{\hat{\sigma}^4_{(i)}}{M} \sum_{m=0}^{M-1} \frac{\lambda_m + \sigma^2}{(\lambda_m + \sigma^2 + \hat{\sigma}^2_{(i)})^2}, \tag{B.3}$$

where λ_m are the eigenvalues of the covariance matrix $\underline{\mathbf{R}}_H$. If we note $x = \hat{\sigma}^2_{(i)}$, the sequence $(\hat{\sigma}^2_{(i+1)})$ is built from a function f_{r1} so that

$$f_{r1}(x) = \frac{x^2}{M} \sum_{m=0}^{M-1} \frac{\lambda_m + \sigma^2}{(\lambda_m + \sigma^2 + x)^2}, \tag{B.4}$$

with $x \in [0, +\infty[$. The proof of the convergence towards zero of the sequence $(\hat{\sigma}^2_{(i+1)})$ in (B.3) is based on the fixed point theorem, i.e. we show that the only solution to the equation $f_{r1}(x) = x$ is zero. The limits of f_{r1} are $f_{r1}(0) = 0$ and $\lim_{x \to \infty} f_1(x) = \frac{1}{M} \sum_{m=0}^{M-1} (\lambda_m + \sigma^2) = M_2$. Furthermore, the derivative of f_{r1}

$$f'_{r1}(x) = \frac{2x}{M} \sum_{m=0}^{M-1} \frac{(\lambda_m + \sigma^2)^2}{(\lambda_m + \sigma^2 + x)^3}, \tag{B.5}$$

is positive for $x \in [0, +\infty[$, so f_{r1} is growing on this interval. We then deduce the inclusion $f_{r1}([0, +\infty[) \subset [0, M_2]$ and so $f_{r1}([0, M_2]) \subset [0, M_2]$. Thus f_{r1} has at least one fixed point on $[0, M_2]$. As f_{r1} is growing on $[0, M_2]$, we conclude that the sequence $(\hat{\sigma}^2_{(i+1)})$ converges to one of the fixed point of f_{r1}. An obvious fixed point of f_{r1} is zero, since $f_{r1}(0) = 0$. We now prove that 0 is the sole fixed point of f_{r1} on $[0, M_2]$. To this end, we show that $f'_{r1}(x) < 1$, which is equivalent to $(f_{r1}(x) - x)' < 0$. Let us define the functions $f_{r1_m}(x)$ extracted from $f_{r1}(x)$ so that $f_{r1}(x) = \frac{1}{M} \sum_m^{M-1} f_{r1_m}(x)$:

$$f_{r1_m}(x) = \frac{x^2(\lambda_m + \sigma^2)}{(\lambda_m + \sigma^2 + x)^2}. \tag{B.6}$$

Since f_{r1} is defined by a sum, we also have for the derivative $f'_{r1}(x) = \frac{1}{M} \sum_m^{M-1} f'_{r1_m}(x)$, with:

$$f'_{r1_m}(x) = \frac{2x(\lambda_m + \sigma^2)^2}{(\lambda_m + \sigma^2 + x)^3}. \tag{B.7}$$

For any value of $m = 0, 1, ..., M-1$ and $x \geq 0$, $f'_{r1_m}(x) \geq 0$, so the following triangle inequality on the derivate of f_{r1} is applied as

$$\max_x(f'_{r1}(x)) \leq \frac{1}{M} \sum_{m=0}^{M-1} \max_{x,m}(f'_{r1_m}(x)). \tag{B.8}$$

For $m = 0, 1, ..., M-1$, we find the maximum of $f'_{r1_m}(x)$ thanks to a second derivation so that

$$f''_{r1_m}(x) = \frac{2(\lambda_m + \sigma^2)^2(\lambda_m + \sigma^2 - 2x)}{(\lambda_m + \sigma^2 + x)^4}. \tag{B.9}$$

The second derivative of $f_{r1_m}(x)$ in (B.9) is null for $x = \frac{1}{2}(\lambda_m + \sigma^2)$, so we find, thanks to expression (B.7):

$$\max_x(f'_{r1_m}(x)) = f'_{r1_m}(x = \frac{1}{2}(\lambda_m + \sigma^2)) = \frac{8}{27}. \tag{B.10}$$

Eq. (B.10) shows that for any value of $m = 0, 1, ..., M-1$, the maximum of f'_{r1_m} is equal to $\frac{8}{27}$, so the triangle inequality is simplified:

$$\max_x(f'_{r1}(x)) \leq \frac{8}{27}, \tag{B.11}$$

which then proves that $f'_{r1}(x) < 1$, i.e. f has only one fixed point equal to zero. Fig. 9 displays an example of $f_{r1}(x)$ and $f'_{r1}(x)$. One can conclude that if the algorithm is performed with the covariance matrix $\underline{\tilde{\mathbf{R}}}^{LS}_H$, then the sequence $(\hat{\sigma}^2_{(i)})$ converges to zero and the algorithm enters into an endless loop, whatever the value of the initialization $\hat{\sigma}^2_{(0)}$ is.

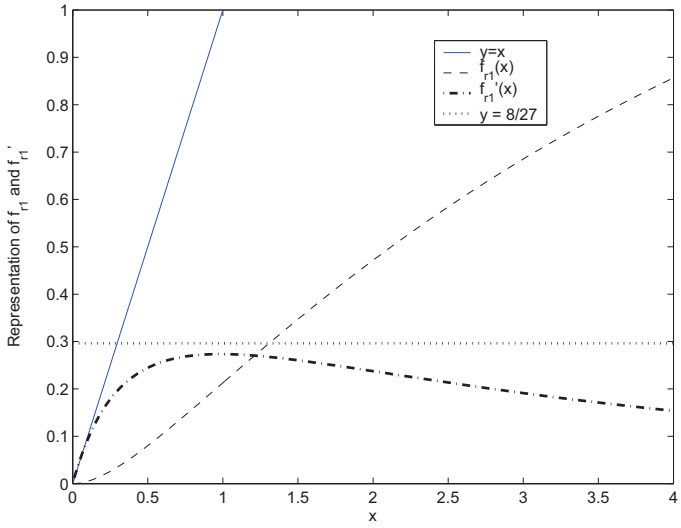

FIGURE B.1 – Shape of $f_{r1}(x)$, $f'_{r1}(x)$ compared with $y = x$ and $y = 8/27$.

B.2 Proof of the Convergence to Zero of the Algorithm under the Hypothesis $\mathbb{H}_0$

If the algorithm keeps on computing at each iteration i with the covariance matrix $\underline{\tilde{\mathbf{R}}}_H^{LS}$ under hypothesis $\mathbb{H}_0$, then we deduce for step 4:

Perform the LMMSE channel estimation:

$$\hat{\mathbf{H}}_{(i+1)}^{LMMSE} = \underline{\tilde{\mathbf{R}}}_H^{LS}(\underline{\tilde{\mathbf{R}}}_H^{LS} + \hat{\sigma}^2_{(i)}\underline{\mathbf{I}})^{-1}\hat{\mathbf{H}}^{LS}. \tag{B.12}$$

Perform the MMSE noise variance estimation:

$$\hat{\sigma}^2_{(i+1)} = \frac{1}{M}E\{||\hat{\mathbf{H}}^{LS} - \hat{\mathbf{H}}_{(i+1)}^{LMMSE}||_F^2\}. \tag{B.13}$$

It is assumed that M is large enough to get $tr(\mathbf{W}\mathbf{W}^H) = tr(\sigma^2\underline{\mathbf{I}})$, we make, in first approximation $\underline{\tilde{\mathbf{R}}}_H^{LS} \approx \sigma^2\underline{\mathbf{I}}$, so the development of (B.13) yields:

$$\begin{aligned}\hat{\sigma}^2_{(i+1)} &= \frac{1}{M}E\{||\hat{\mathbf{H}}^{LS} - \hat{\mathbf{H}}_{(i+1)}^{LMMSE}||_F^2\} \\ &= \frac{1}{M}E\{||\hat{\mathbf{H}}^{LS} - \underline{\tilde{\mathbf{R}}}_H^{LS}(\underline{\tilde{\mathbf{R}}}_H^{LS} + \hat{\sigma}^2_{(i)}\underline{\mathbf{I}})^{-1}\hat{\mathbf{H}}^{LS}||_F^2\},\end{aligned} \tag{B.14}$$

and, by factorizing by $\underline{\mathbf{C}}^{-1}$:

$$\begin{aligned}
&= \frac{1}{M} E\{||\mathbf{W} - \sigma^2 \underline{\mathbf{I}}(\sigma^2 \underline{\mathbf{I}} + \hat{\sigma}^2_{(i)} \underline{\mathbf{I}})^{-1} \mathbf{W}||_F^2\} \\
&= \frac{1}{M} E\{||(\underline{\mathbf{I}} - (\sigma^2 + \hat{\sigma}^2_{(i)} - \hat{\sigma}^2_{(i)}) \underline{\mathbf{I}}((\sigma^2 + \hat{\sigma}^2_{(i)}) \underline{\mathbf{I}})^{-1}) \mathbf{W}||_F^2\} \\
&= \frac{1}{M} E\{||(\hat{\sigma}^2_{(i)} \underline{\mathbf{I}}((\sigma^2 + \hat{\sigma}^2_{(i)}) \underline{\mathbf{I}})^{-1}) \mathbf{W}||_F^2\} \\
&= \frac{\hat{\sigma}^4_{(i)}}{(\sigma^2 + \hat{\sigma}^2_{(i)})^2} \frac{1}{M} E\{||\mathbf{W}||_F^2\} \\
&= \frac{\hat{\sigma}^4_{(i)} \sigma^2}{(\sigma^2 + \hat{\sigma}^2_{(i)})^2}.
\end{aligned} \tag{B.15}$$

The sequence $(\hat{\sigma}^2_{(i)})$ is built from a function f_s such as, if we note $x = \hat{\sigma}^2_{(i)}$, we obtain

$$f_s(x) = \frac{x^2 \sigma^2}{(\sigma^2 + x)^2}, \tag{B.16}$$

with $x \in \mathbb{R}^+$. Fig. B.2 displays the curve of f_s for different values of σ^2 and compares them with $y = x$.

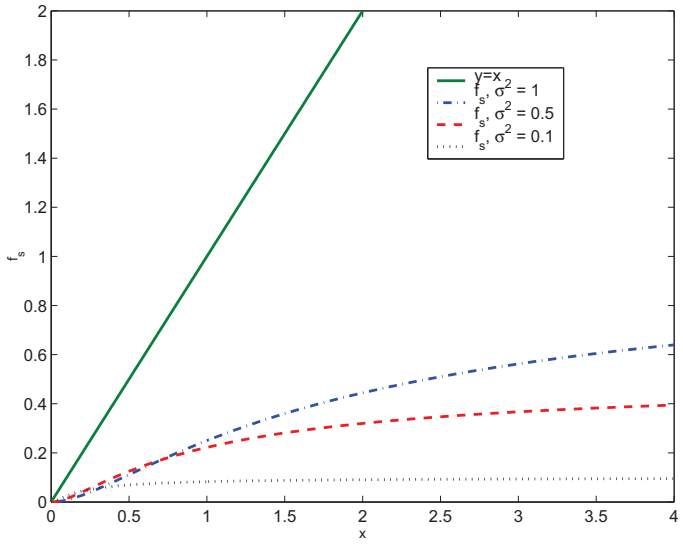

FIGURE B.2 – Aspect of f for different values of σ^2 compared with $y = x$.

The sequence converges if f_s has at least one fixed point, i.e. a solution of the equation $f_s(x) = x$. Obviously, zero is one fixed point. We now show that zero is the only fixed point of f_s. To this end, the derivative f'_s and the second derivative f''_s of f_s are expressed:

$$f'_s(x) = \frac{2\sigma^4 x}{(\sigma^2 + x)^3}, \tag{B.17}$$

and

$$f''_s(x) = \frac{2\sigma^4(\sigma^2 - 2x)}{(\sigma^2 + x)^4}. \tag{B.18}$$

From (B.17), we deduce that $\forall x \in \mathbb{R}^+$, $f'_s(x) \geq 0$, so f_s is growing on $\mathbb{R}^+$. From (B.18), we find that $f''_s(x) = 0$ for $x = \frac{\sigma^2}{2}$, then the maximum value of f'_s is $f'(\frac{\sigma^2}{2}) = \frac{8}{81} < 1$. Due to $f_s(0) = 0$ and $\max(f'_s) = \frac{8}{81} < 1$, we conclude that the only fixed point of f_s is 0. We find the same results as in the case of a received pilot preamble under hypothesis $\mathbb{H}_1$, that is if the algorithm is exclusively performed with $\underline{\tilde{\mathbf{R}}}_H^{LS}$, then the sole limit to $\hat{\sigma}^2_{(i+1)}$ is zero and the algorithm enters into an endless loop. It justifies the change of channel covariance matrix from $\underline{\tilde{\mathbf{R}}}_H^{LS}$ to $\underline{\tilde{\mathbf{R}}}_H^{LMMSE}$ under hypothesis $\mathbb{H}_1$ as well under hypothesis $\mathbb{H}_0$.

Appendix C

Appendix of the Chapter 5

C.1 Error of the Linear Interpolation

This apprendix aims to prove that, considering a $\mathcal{C}^2$ function g on an interval $[x_p, x_{p+\delta_p}]$, the interpolation error $|g(x) - \hat{g}(x)|$ is written

$$|g(x) - \hat{g}(x)| = \frac{1}{2}|(x_{p+\delta_p} - x)(x_p - x)| \times |g''(y)|, \tag{C.1}$$

where $y \in [x_p, x_{p+\delta_p}]$, and $\hat{g}(x)$ is the linear interpolation of g:

$$\hat{g}(x) = g(x_p) + (x - x_p)\frac{g(x_{p+\delta_p}) - g(x_p)}{x_{p+\delta_p} - x_p}. \tag{C.2}$$

The proof is trivial by using the Taylor's theorem [1]. The Taylor's expansion is used to express $g(x_p)$ and $g(x_{p+\delta_p})$:

$$g(x_p) = g(x) + (x_p - x)g'(x) + \frac{1}{2}(x_p - x)^2 g''(x) + ... \tag{C.3}$$

$$g(x_{p+\delta_p}) = g(x) + (x_{p+\delta_p} - x)g'(x) + \frac{1}{2}(x_{p+\delta_p} - x)^2 g''(x) + ..., \tag{C.4}$$

in order to rewrite (C.2):

$$\begin{aligned}\hat{g}(x) &= g(x) + (x_p - x)g'(x) + \frac{1}{2}(x_p - x)^2 g''(x) \\ &\quad + (x - x_p)\frac{(x_{p+\delta_p} - x_p)g'(x) + \frac{1}{2}\left((x_{p+\delta_p} - x)^2 - (x_p - x)^2\right)g''(x)}{x_{p+\delta_p} - x_p} + ... \\ &= g(x) + \frac{1}{2}(x - x_{p+\delta_p})(x - x_p)g''(x) + ...\end{aligned} \tag{C.5}$$

Using one of the remainder formulation, it exists $y \in [x_p, x_{p+1}]$ such as

$$\hat{g}(x) = g(x) + \frac{1}{2}(x - x_{p+\delta_p})(x - x_p)g''(y). \tag{C.6}$$

1. see for example: `http://www-solar.mcs.st-andrews.ac.uk/~clare/Lectures/num-analysis/Numan_chap3.pdf`

List of figures

List of tables

List of Algorithms

Publications and contributions during the PhD

International Journals

- V. Savaux, Y. Louët, M. Djoko-Kouam, A. Skrzypczak "Artificial channel aided LMMSE estimation for time-frequency selective channels in OFDM context", *Signal Processing*, Elsevier, Sept. 2013, vol. 93, pp. 2369 - 2380
- Vincent Savaux, Yves Louët, Moise Djoko Kouam, Alexandre Skrzypczak "Application of a joint and iterative MMSE-based estimation of SNR and frequency selective for OFDM systems", *EURASIP, Journal on Advances in Signal Processing (JASP)*, 2013, 2013 :128
- Vincent Savaux, Yves Louët, Moise Djoko Kouam, Alexandre Skrzypczak "Minimum Mean Square Error Expression of LMMSE Channel Estimation in SISO OFDM Systems", *IET Electronics Letters*, vol. 49, issue 18, pp. 1152-1154

International Conferences

- V. Savaux, Y. Louët, M. Djoko-Kouam, A. Skrzypczak "An Iterative and Joint Estimation of SNR and Frequency Selective Channel for OFDM Systems", *European Wireless*, April 2012, Poznan, Poland
- V. Savaux, A. Skrzypczak, Y. Louët, M. Djoko-Kouam "Near LMMSE Channel Estimation Performance with Artificial Channel at Receiver for OFDM Systems", *SPAWC*, June 2012, Cesme, Turkey
- V. Savaux, M. Djoko-Kouam, A. Skrzypczak, Y. Louët "Study of Cyclic Delay Diversity for Single Frequency Network using DRM Standard", *European Wireless*, April 2013, Guildford, UK
- V. Savaux, Y. Louët, M. Djoko-Kouam, A. Skrzypczak "Application of an Algorithm for Channel and Noise Estimation to Spectrum Sensing in a Cognitive Radio Context ", 4^{th} *Workshop of the COST Action IC0902*, October 2013, Roma, Italy

National Conference

- V. Savaux, Y. Louët, M. Djoko-Kouam, A. Skrzypczak "Estimation MMSE itérative et conjointe du rapport signal à bruit et du canal sélectif en fréquence pour les systèmes OFDM", *GRETSI*, Septembre 2013, Brest, France
- V. Savaux, Y. Louët, M. Djoko-Kouam, A. Skrzypczak "Etude statistique des erreurs d'interpolation et de leur impact sur l'estimation du canal de Rayleigh dans un contexte OFDM", *GRETSI*, Septembre 2013, Brest, France

Other National Communications

- V. Savaux "Estimation conjointe de canal et de rapport signal à bruit dans un contexte OFDM", séminaire SCEE, 26 Avril 2012, Rennes, France
- V. Savaux "Optimisation d'une chaîne d'émission-réception pour la Radio Numérique Terrestre", journée des doctorants de l'IETR, juin 2011, juin 2012, Rennes, France
- V. Savaux "Estimation MMSE itérative et conjointe du rapport signal à bruit et du canal sélectif en fréquence pour les systèmes OFDM ", journée des doctorants de l'IETR, juin 2013, Rennes, France

Bibliography

[1] ETSI, "Digital Radio Mondiale (DRM);System Specification," ETSI, Tech. Rep. ETSI ES 201 980 V 3.1.1, August 2009.

[2] P. Bello, "Characterization of randomly time-variant linear channels," *IEEE Trans. on Communications Systems*, vol. 11, no. 4, pp. 360–393, December 1963.

[3] M. Patzold, *"Mobile fading channels"*. John Wiley & Sons, 1999.

[4] W. Weibull, "A Statistical Distribution Function of Wide Applicability," *Journal of Applied Mechanics*, vol. 18, pp. 293–297, 1951.

[5] M. Nakagami, *The m-distribution - A general formula of intensity distribution of rapid fading*. Symposium Publications Division, Pergamon Press, 1960, ch. Statistical Methods in Radio Wave Propagation, pp. 3–36.

[6] M. D. Yacoub, "The κ-μ Distribution: A General Fading Distribution," in *VTC'00 Fall*, vol. 2, Boston, MA, September 2000, pp. 872 – 877.

[7] O. Edfors, M. Sandell, J.-J. van de Beek, S. K. Wilson, and P. O. Börjesson, "OFDM Channel Estimation by Singular Value Decomposition," *IEEE Trans. on Communications*, vol. 46, no. 7, pp. 931 – 939, July 1998.

[8] H. Steendam and M. Moeneclaey, "Analysis and Optimization of the Performance of OFDM on Frequency-Selective Time-Selective Fading Channels," *IEEE Trans. on Communications*, vol. 47, no. 12, pp. 1811 – 1819, December 1999.

[9] J. R. Foerster, "The Effects of Multipath Interference on the Performance of UWB Systems in an Indoor Wireless Channel," in *Vehicular Technology Conference Spring*, vol. 2, Rhodes, May 2001, pp. 1176 – 1180.

[10] A. Peled and A. Ruiz, "Frequency Domain Data Transmission using Reduced Computational Complexity algorithms," in *ICASSP'80*, vol. 3, April 1980, pp. 964–967.

[11] R. M. Gray, "Toeplitz and Circulant Matrices : A review," Department of Electrical Engineering, Standford University, Tech. Rep., 2006.

[12] G. Constantini, "Déterminant d'une matrice circulante." [Online]. Available: http://gilles.costantini.pagesperso-orange.fr/agreg_fichiers/themes_fichiers/detcirc.pdf

[13] B. Le Saux, "Estimation de canal pour système multi-antennes multi-porteuses," Ph.D. dissertation, INSA Rennes, 2007.

[14] P. Fertl and G. Matz, "Channel Estimation in Wireless OFDM Systems With Irregular Pilot Distribution," *IEEE Transactions on Signal Processing*, vol. 58, no. 6, pp. 3180 – 3194, June 2010.

[15] M. Biguesh and A. B. Gershman, "Downlink Channel Estimation in Cellular Systems with Antenna Arrays at Base Stations Using Channel Probing with Feedback," *EURASIP Journal on Applied Signal Processing*, vol. 9, pp. 1330–1339, September 2004.

[16] H. Nooralizadeh and S. S. Moghaddam, "A New Shifted Scaled LS Channel Estimator for Rician Flat Fading MIMO Channel," in *ISIEA*, vol. 1, Kuala Lumpur, Malaysia, October 2009, pp. 243 – 247.

[17] I. Barhumi, G. Leus, and M. Moonen, "Optimal training design for MIMO OFDM systems in mobile wireless channels," *IEEE Transaction on signal processing*, vol. 51, no. 6, pp. 1615 – 1624, June 2003.

[18] M. Biguesh and A. B. Gershman, "Training-Based MIMO Channel Estimation: A Study of Estimator Tradeoffs and Optimal Training Signals," *IEEE Transactions on Signal Processing*, vol. 54, no. 3, pp. 884–893, March 2006.

[19] S. Kay, *Fundamentals of statistical signal processing : estimation theory*, 2003, ch. 12, pp. 388–391.

[20] V. Savaux, Y. Louët, M. Djoko-Kouam, and A. Skrzypczak, "Minimum mean-square-error expression of LMMSE channel estimation in SISO OFDM systems," *IET Electronics Letters*, vol. 49, no. 18, pp. 1152 – 1154, August 2013.

[21] E. Isaacson and H. Keller, *Analysis of numerical methods*. John Wiley & Sons, 1966.

[22] M.-H. Hsieh and C.-H. Wei, "Channel Estimation for OFDM Systems Based on Comb-Type Pilot Arrangement in Frequency Selective Fading Channels," *IEEE Transations on Consumer Electronics*, vol. 44, no. 1, pp. 217 – 225, February 1998.

[23] E. Jaffrot, "Estimation de canal très sélectif en temps et en fréquence pour les systèmes OFDM," Ph.D. dissertation, ENSTA, 2000.

[24] M. Morelli and U. Mengali, "A Comparisaon of Pilot-Aided Channel Estimation Methods for OFDM Systems," *IEEE Transactions on Signal Processing*, vol. 49, no. 12, pp. 3065–3073, December 2001.

[25] S. Coleri, M. Ergen, A. Puri, and A. Bahai, "A study of channel estimation in OFDM systems," in *Vehicular Technology Conference Fall*, vol. 2, september 2002, pp. 894–898.

[26] Y. Shen and E. Martinez, "Channel Estimation in OFDM Systems," Freescale Semiconductor, Tech. Rep., 2006.

[27] X. Dong, W.-S. Lu, and A. Soong, "Linear Interpolation in Pilot Symbol Assisted Channel Estimation for OFDM," *IEEE Trans. on wireless Communications*, vol. 6, no. 5, pp. 1910 – 1920, May 2007.

[28] P. Hoeher, S. Kaiser, and P. Robertson, "Two-Dimensional Pilot-Symbol-Aided Channel Estimation by Wiener Filtering," in *ICASSP*, vol. 3, Munich, April 1997, pp. 1845 – 1848.

[29] J. Schoukens, R. Pintelon, and H. V. Hamme, "The Interpolated Fast Fourier Transform: A Comparative Study," *IEEE Transactions on Instrumentation and Measurement*, vol. 41, no. 2, pp. 226 – 232, April 1992.

[30] S. M. Kay, *Fundamentals of Statistical Signal Processing : Estimation Theory*. Prentice Hall, 2003, ch. Maximum Likelihood Estimation, pp. 157–214.

[31] M. Abuthinien, S. Chen, and L. Hanzo, "Semi-blind Joint Maximum Likelihood Channel Estimation and Data Detection for MIMO Systems," *IEEE Signal Processing Letters*, vol. 15, pp. 202–205, 2008.

[32] J. J. van de Beek, O. Edfors, M. Sandell, S. K. Wilson, and P. O. Börjesson, "On Channel Estimation In OFDM Systems," in *IEEE conference on vehicular technology*, vol. 2, Chicago, IL, September 1995, pp. 815 – 819.

[33] W. Zhou and W. H. Lam, "A Fast LMMSE Channel EstimationMethod for OFDM Systems," *EURASIP Journal on Wireless Communications and Networking*, March 2009.

[34] V. Savaux, A. Skrzypczak, Y. Louët, and M. Djoko-Kouam, "Near LMMSE Channel Estimation Performance with Artificial Channel at Receiver for OFDM Systems," in *SPAWC 2012*, Cesme, Turkey, June 2012, pp. 545 – 549.

[35] V. Savaux, Y. Louët, M. Djoko-Kouam, and A. Skrzypczak, "Artificial channel aided LMMSE estimation for time-frequency selective channels in OFDM context," *Signal Processing, Elsevier*, vol. 93, no. 9, pp. 2369 – 2380, September 2013.

[36] D. Kim and G. L. Stüber, "Residual ISI Cancellation for OFDM with Applications to HDTV Broadcasting," *IEEE journal on selected areas in communications*, vol. 16, no. 8, pp. 1590 – 1599, octobre 1998.

[37] V. Savaux, Y. Louët, M. Djoko-Kouam, and A. Skrzypczak, "An Iterative and Joint Estimation of SNR and Frequency Selective Channel for OFDM Systems," in *European Wireless*, Poznan, Poland, April 2012, pp. 1 – 7.

[38] ——, "Application of a Joint and Iterative MMSE-based Estimation of SNR and Frequency Selective Channel for OFDM Systems," *EURASIP Journal on Advances in Signal Processing*, July 2013.

[39] ——, "Estimation MMSE itérative et conjointe du rapport signal à bruit et du canal sélectif en fréquence pour les systèmes OFDM," in *GRETSI*, Brest, France, September 2013.

[40] G. Ren, H. Zhang, and Y. Chang, "SNR Estimation Algorithm Based on the Preamble for OFDM Systems in Frequency Selective Channels," *IEEE Transactions on Communications*, vol. 57, no. 8, pp. 2230 – 2234, August 2009.

[41] X. Xu, Y. Jing, and X. Yu, "Subspace-Based Noise Variance and SNR Estimation for OFDM Systems," in *IEEE Mobile Radio Applications Wireless Communication Networking Conference*, vol. 1, March 2005, pp. 23 –26.

[42] H. Xu, G. Wei, and J. Zhu, "A Novel SNR Estimation Algorithm for OFDM," in *IEEE Vehicular Technology Conference Spring*, vol. 5, May 2005, pp. 3068 – 3071.

[43] V. Savaux, Y. Louët, M. Djoko-Kouam, and A. Skrzypczak, "Etude statistique des erreurs d'interpolation et de leur impact sur l'estimation du canal de Rayleigh dans un contexte OFDM," in *GRETSI*, Brest, France, September 2013.

[44] Y. A. Chau and K. Y.-T. Huang, "On the Second-Order Statistics of Correlated Cascaded Rayleigh Fading Channels," *International Journal of Antennas and Propagation*, vol. 2012, p. 6, June 2012.

[45] M. K. Simon, *Probability Distributions Involving Gaussian Random Variables: A Handbook For Engineers and Scientists*. Springer, 2006.

[46] C.-H. Yih, "Effects of Channel Estimation Error in the Presence of CFO on OFDM BER in Frequency-Selective Rayleigh Fading Channels," *Journal of Communications*, vol. 3, no. 3, pp. 10 – 18, July 2008.

[47] V. Savaux, M. Djoko-Kouam, A. Skrzypczak, and Y. Louët, "Study of Cyclic Delay Diversity for Single Frequency Network using DRM Standard," in *European Wireless*, Guildford, UK, April 2013.

[48] I. S. Reed and G. Solomon, "Polynomial Codes Over Certain Finite Fields," *SIAM Journal of Applied Math.*, vol. 8, no. 2, pp. 300–304, June 1960.

[49] A. Dammann and S. Kaiser, "Standard Conformable Antenna Diversity Techniques for OFDM and its Application to the DVB-T System," in *GLOBECOM'01*, vol. 5, San Antonio, TX, November 2001, pp. 3100 – 3105.

[50] S. Kaiser, "Spatial Transmit Diversity Techniques for Broadband OFDM Systems," in *GLOBECOM'00*, vol. 3, San Fransisco, CA, December 2000, pp. 1824 – 1828.

[51] IEEE Std 802.11, "Wireless LAN Medium Access Control (MAC) and Physical Layer (PHY) Specifications," IEEE, Tech. Rep., 2007.

[52] ETSI, "Digital video broadcasting (DVB) framing structure, channel coding and modulation for digital terrestrial television," ETSI, Tech. Rep. ETSI EN 300 744 V1.5.1, 2004.

[53] ——, "Digital Audio Broadcasting (DAB); DMB video service; User application specification," ETSI, Tech. Rep. ETSI TS 102 428, April 2009.

[54] A. P. Barsis, "Radio Wave Propagation Over Irregular Terrain in the 76- to 9200-MHz Frequency Range," *IEEE Transactions on Vehicular Technology*, vol. VT-20, no. 2, pp. 41 – 62, August 1971.

[55] M. Hata, "Empirical Formula for Propagation Loss in Land Mobile Radio Services," *IEEE Transactions on Vehicular Technology*, vol. VT-29, no. 3, pp. 317 – 325, August 1980.

[56] N. Amitay, "Modeling and Computer Simulation of Wave Propagation in Lineal Line-of-Sight Microcells," *IEEE Transactions on Vehicular Technology*, vol. 41, no. 4, pp. 337 – 342, November 1992.

[57] H. R. Anderson, "A Ray-Tracing Propagation Model for Digital Broadcast Systems in Urban Areas," *IEEE Transactions on Broadcasting*, vol. 39, no. 3, pp. 309 – 317, September 1993.

[58] S. O. Rice, "Statistical Properties of a Sine Wave Plus Random Noise," *Bell Sytem Technical Journal*, vol. 27, pp. 109–157, 1948.

[59] J. G. Proakis and M. Salehi, *Digital Communications*. Mc Graw-Hill, 2008, ch. Fading Channels I : Characterization and Signaling, pp. 830– 898.

[60] W. C. Jakes, *Microwave Mobile Communications*. Wiley-IEEE Press, 1994.

[61] R. H. Clarke, "A Statistical Theory of Mobile-Radio Reception," *Bell Sytem Technical Journal*, vol. 47, pp. 957–1000, 1968.

[62] C. C. Watterson, J. R. Juroshek, and W. D. Bensema, "Experimental Confirmation of an HF Channel Model," *IEEE Tansactions on Communication Technology*, vol. com-18, no. 6, pp. 792 – 803, December 1970.

[63] L. Ehrman, L. B. Bates, J. F. Eschle, and J. M. Kates, "Real-Time Software Simulation of the HF Radio Channel," *IEEE Trans. on Communications*, vol. com-30, no. 8, pp. 1809 – 1817, August 1982.

[64] P. A. Bello, "Aeronautical Channel Characterization," *IEEE Trans. on Communications*, vol. com-21, no. 5, pp. 548 – 463, May 1973.

[65] I. Holleman, "Doppler Radar Wind Profiles," Koninklijk Nederlands Meteorologisch Instituut (KNMI), Tech. Rep., 2003.

[66] R. H. Clarke and W. L. Khoo, "3-D mobile radio channel statistics," *IEEE Transaction on vehicular technology*, vol. 46, no. 3, pp. 798–799, August 1997.

[67] R. Iqbal, T. Abhayapala, and T. Lamahewa, "Generalised clarke model for mobile-radio reception," *IET Communications*, vol. 3, no. 4, pp. 644–654, April 2009.

[68] B. Sklar, "Rayleigh fading channels in mobile digital communication systems .i. characterization," *IEEE Communications Magazine*, vol. 35, no. 7, pp. 90 – 100, July 1997.

[69] J. Scott, "The how and why of COFDM," *EBU Technical Review*, January 1999.

[70] M. Debbah, "OFDM." [Online]. Available: http://www.supelec.fr/d2ri/flexibleradio/cours/cours-ofdm-french.pdf

[71] A. Skrzypczak, "Contribution à l'étude des momodulation multiporteuses OFDM/OQAM et OFDM suréchantillonnées," Ph.D. dissertation, Rennes 1, November 2007.

[72] H.Steendam and M. Moeneclaey, "Different Guard Interval Techniques for OFDM: Performance Comparison," in *Proceedings from the 6th International Workshop on Multi-Carrier Spread Spectrum*, vol. 1, May 2007, pp. 11–24.

[73] B. L. Floch, M. Alard, and C. Berrou, "Coded Orthogonal Frequency Division Multiplex," *Proceedings of the IEEE*, vol. 83, no. 6, pp. 982–996, June 1995.

[74] P. Elias, "Predictive Conding - Part I," *IEEE Transaction on Information Theory*, vol. 1, no. 1, pp. 16–24, March 1955.

[75] ——, "Predictive Coding - Part II," *IEEE Transaction on Information Theory*, vol. 1, no. 1, pp. 24–33, March 1955.

[76] P.-J. Bouvet, "Récepteurs itératifs pour systèmes multi-antennes," Ph.D. dissertation, INSA Rennes, 2006.

[77] C.-D. Iskander, "A MATLAB-based Object-Oriented Approach to Multipath Fading Channel Simulation," *Hi-Tek Multisystems*, 21 février 2008.

[78] Y.-S. Choi, P. J. Voltz, and F. A. Cassara, "On Channel Estimation and Detection for Multicarrier Signals in Fast and Selective Rayleigh Fading Channels," *IEEE Transactions on Communications*, vol. 49, no. 8, pp. 1375 – 1387, August 2001.

[79] C. Suh, C.-S. Hwang, and H. Choi, "Comparative Study of Time-Domain and Frequency-Domain Channel Estimation in MIMO-OFDM Systems," in *PIMRC*, vol. 2, 2003, pp. 1095 – 1099.

[80] S. Kinjo, "Time domain channel estimation schemes for OFDM systems with multiple antenna transmissions," in *ISPACS*, Kanazawa, January 2009, pp. 232 – 235.

[81] S. Werner, M. Enescu, and V. Koivunen, "Combined Frequency and Time Domain Channel Estimation in Mobile MIMO-OFDM Systems," in *ICASSP*, vol. 4, Toulouse, France, May 2006.

[82] Y.-Q. Jiang, "Novel Channel Estimation for MIMO-OFDM Systems with High Efficiency and Accuracy," in *WCSP*, Suzhou, China, October 2010, pp. 1 – 6.

[83] A. Scaglione, G. B. Giannakis, and S. Barbarossa, "Redundant Filterbank Precoders and Equalizers Part II: Blind Channel Estimation, Synchronization, and Direct Equalization," *IEEE Transactions on Signal Processing*, vol. 47, no. 7, pp. 2007 – 2022, July 1999.

[84] S. Wang, J. Cao, and J. Hu, "A frequency domain subspace blind channel estimation method for trailing zero OFDMsystems," *Journal of Network and Computer Applications, Elsevier*, vol. 34, no. 1, pp. 116 – 120, January 2011.

[85] C. Li and S. Roy, "Subspace-Based Blind Channel Estimation for OFDM by Exploiting Virtual Carriers," *IEEE Transactions on Wireless Communications*, vol. 2, no. 1, pp. 141 – 150, January 2003.

[86] P. Guguen, "Techniques multi-antennes émission-réception - Applications aux réseaux domestiques sans fil," Ph.D. dissertation, INSA Rennes, January 2003.

[87] J. Proakis and M. Salehi, *Digital Communications*. McGraw-Hill, 2008.

[88] T. Dubois, M. Crussière, and M. Hélard, "On the use of Time Reversal for Digital Communications with Non-Impulsive Waveforms," in *ICSPCS*, Gold Coast, QLD, December 2010, pp. 1 – 6.

[89] K. B. Petersen and M. S. Pedersen, "The Matrix Cookbook," November 2012, http://matrixcookbook.com.

[90] H. Lütkepohl, *Handbook of matrices*. John Wiley & Sons, 1996.

[91] S. M. Kay, *Fundamentals of Statistical Signal Processing : Estimation Theory*. Prentice Hall, 2003.

[92] G. Auer, S. Sand, A. Dammann, and S. Kaiser, "Analysis of cellular interference for MC-CDMA and its impact on channel estimation," *European Transactions on Telecommunications*, vol. 15, no. 3, pp. 173 – 184, 2004.

[93] Article from Wikipedia, "Computational complexity of mathematical operations," http://en.wikipedia.org/wiki/Computational_complexity_of_mathematical_operations.

[94] D. C. Rife and G. A. Vincent, "Use of the Discrete Fourier Transform in the Measurement of Frequencies and Levels of Tones," *Bell System Technical Journal*, vol. 49, pp. 197 – 228, 1970.

[95] A. Wiesel, Y. C. Eldar, and A. Beck, "Maximum Likelihood Estimation in Linear Models With a Gaussian Model Matrix," *IEEE Signal Processing Letters*, vol. 13, no. 5, pp. 292 – 295, May 2006.

[96] A. P. Dempster, N. M. Laird, and D. B. Rubin, "Maximum Likelihood from Incomplete Data via the EM Algorithm," *Journal of the Royal Statistical Society. Series B*, vol. 39, no. 1, pp. 1–38, 1977.

[97] H. Zamiri-Jafarian and S. Pasupathy, "EM-Based Recursive Estimation of Channel Parameters," *IEEE Transaction on Communications*, vol. 47, no. 9, pp. 1297 – 1302, September 1999.

[98] Y. Xie and C. Georghiades, "An EM-based Channel Estimation Algorithm For OFDM With Transmitter Diversity," in *GLOBECOM'01*, vol. 2, San Antonio, TX, November 2001, pp. 871 – 875.

[99] X. Wautelet, C. Herzet, A. Dejonghe, J. Louveaux, and L. Vandendorpe, "Comparison of EM-Based Algorithms for MIMO Channel Estimation," *IEEE Trans. on Communications*, vol. 55, no. 1, pp. 216 – 226, January 2007.

[100] X. Ma, H. Kobayashi, and S. C. Schwartz, "EM-Based Channel EstimationAlgorithms for OFDM," *EURASIP Journal on Applied Signal Processing*, vol. 10, pp. 1460 – 1477, 2004.

[101] N. Omri and S. Jarboui, "Optimisation d'une transmission de données haut débit sur un canal CPL," in *MajecSTIC*, November 2005.

[102] F. N. Fritsch and R. E. Carlson, "Monotone piecewise cubic interpolation," *SIAM Journal of Numerical Analysis.*, vol. 17, no. 2, pp. 238 – 246, April 1980.

[103] C.-S. Yang, S.-P. Kao, F.-B. Lee, and P.-S. Hung, "Twelve Different Interpolation Methods: a Case Study of Surfer 8.0," in *Proceedings of the XXth ISPRS Congress*, 2004.

[104] S. Buzzi, M. Lops, and S. Sardellitti, "Performance of Iterative Data Detection and Channel Estimation for Single-Antenna and Multiple-Antennas Wireless Communications," *IEEE Transactions on Vehicular Technology*, vol. 53, no. 4, pp. 1085 – 1104, July 2004.

[105] T. Zemen, C. F. Mecklenbräuker, J. Wehinger, and R. R. Müller, "Iterative Joint Time-Variant Channel Estimation and Multi-User Detection for MC-CDMA," *IEEE Trans. on Wireless Communications*, vol. 5, no. 6, pp. 1469 – 1478, June 2006.

[106] R. Otnes and M. Tüchler, "Iterative Channel Estimation for Turbo Equalization of Time-Varying Frequency-Selective Channels," *IEEE Transactions on Wireless Communications*, vol. 3, no. 6, pp. 1918 – 1923, November 2004.

[107] R. C. Lamare, R. Sampaio-Neto, and A. Hjorungnes, "Joint Iterative Interference Cancellation and Parameter Estimation for CDMA Systems," *IEEE Communications Letters*, vol. 11, no. 12, pp. 916 – 918, December 2007.

[108] S.-H. Wu, U. Mitra, and C.-C. J. Kuo, "Iterative Joint Channel Estimation and Multiuser Detection for DS-CDMA in Frequency-Selective Fading Channels," *IEEE Transactions on Signal Processing*, vol. 56, no. 7, pp. 3261 – 3277, July 2008.

[109] Y. Kojima, H. Tomeba, K. Takeda, and F. Adachi, "RLS Channel Estimation with Adaptive Forgetting Factor for DS-CDMA Frequency-Domain Equalization," *IEICE Transaction on Communications*, vol. E92-B, no. 5, pp. 1457–1465, May 2009.

[110] G. Matz, "Recursive MMSE Estimation of Wireless Channels Based onTraining Data and Structured Correlation Learning," in *SSP'05*, Bordeaux, France, July 2005, pp. 1342 – 1347.

[111] S. Ohno, S. Munesada, and E. Manasseh, "Low-complexity approximate LMMSE channel estimation for OFDM systems," in *APSIPA ASC*, Hollywood, CA, December 2012, pp. 1 – 4.

[112] N. Geng, L. Ping, X. Yuan, and L. F. Yeung, "Iterative Dual Diagonal LMMSE Channel Estimation in OFDM Systems," in *VTC fall*, Ottawa, ON, September 2010, pp. 1 – 4.

[113] R. Kumar, "A Fast Algorithm for Solving a Toeplitz System of Equations," *IEEE Transactions on Acoustics, Speech and Signal Processing*, vol. 33, no. 1, pp. 254–267, February 1985.

[114] M.-S. Alouini, A. Scaglione, and G. B. Giannakis, "PCC : Principal Components Combining for Dense Correlated Multipath Fading Environments," in *VTC*, vol. 5, Boston, MA, September 2000, pp. 2510 – 2517.

[115] R. M. Gray, "On the Asymptotic Eigenvalue Distribution of Toeplitz Matrices," *IEEE Transaction on Information Theory*, vol. 18, no. 6, pp. 725 – 730, 1972.

[116] C. Laot, A. Glavieux, and J. Labat, "Turbo Equalization: Adaptive Equalization and Channel Decoding Jointly Optimized," *IEEE Journal on Selected Areas in Communications*, vol. 19, no. 9, pp. 1744 – 1752, September 2001.

[117] X. Wautelet, A. Dejonghe, and L. Vandendorpe, "MMSE-Based Fractional Turbo Receiver for Space-Time BICM Over Frequency-Selective MIMO Fading Channels," *IEEE Transactions on Signal Processing*, vol. 52, no. 6, pp. 1804 – 1809, June 2004.

[118] J. M. Cioffi and J. A. C. Bingham, "A Data-Driven Multitone Echo Canceller," *IEEE Transaction on Communications*, vol. 42, no. 10, pp. 2853 – 2869, October 1994.

[119] A. F. Molisch, M. Toeltsch, and S. Vermani, "Iterative Methods for Cancellation of Intercarrier Interference in OFDM Systems," *IEEE Transactions on Vehicular Technology*, vol. 56, no. 4, pp. 2158 – 2167, July 2007.

[120] V.-D. Nguyen, M. Pätzold, F. Maehara, H. Haas, and M.-V. Pham, "Channel Estimation and Interference Cancellation for MIMO-OFDM Systems," *IEICE Transaction on Communications*, vol. E90-B, no. 2, pp. 277 – 290, February 2007.

[121] T. Keller and L. Hanzo, "Adaptive Multicarrier Modulation: A Convenient Framework for Time-Frequency Processing in Wireless Communications," *Proceedings of the IEEE*, vol. 88, no. 5, pp. 611 – 640, May 2000.

[122] T. A. Summers and S. G. Wilson, "SNR Mismatch and Online Estimation in Turbo Decoding," *IEEE Trans. on Communications*, vol. 46, no. 4, pp. 421 – 423, April 1998.

[123] D. R. Pauluzzi and N. C. Beauieu, "A Comparison of SNR Estimation Techniques for the AWGN Channel," *IEEE Trans. on Communications*, vol. 48, no. 10, pp. 1681 – 1691, October 2000.

[124] B. Li, R. D. Fazio, and A. Zeira, "A Low Bias Algorithm to Estimate Negative SNRs in an AWGN Channel," *IEEE Communications Letters*, vol. 6, no. 11, pp. 469 – 471, November 2002.

[125] G. Ren, Y. Chang, and H. Zhang, "A New SNR's Estimator for QPSK Modulations in an AWGN Channel," *IEEE Transactions on Circuits and Systems*, vol. 52, no. 6, pp. 336 – 338, June 2005.

[126] T. R. Benedict and T. T. Soong, "The Joint Estimation of Signal and Noise from the Sum Envelope," *IEEE Transaction on Information Theory*, vol. 13, pp. 447 – 454, July 1967.

[127] T. Krisjansson, B. Frey, L. Deng, and A. Acero, "Joint estimation of noise and channel distortion in a generalized EM framework," in *IEEE Workshop on ASRU'01*, 2001, pp. 155–158.

[128] Z. Baranski, A. Haimovich, and J. Garcia-Frias, "EM-based Iterative Receiver for Space-Time Coded Modulation with Noise Variance Estimation," in *GLOBECOM'02*, vol. 1, 2002, pp. 355–359.

[129] S. Boumard, "Novel noise variance and SNR estimation algorithm for wireless MIMO OFDM systems," in *Global Telecommunications Conference*, vol. 3, December 2003, pp. 1330 – 1334.

[130] Spectrum Efficiency Working Group, "Report of the Spectrum Efficiency Working Group," Federal Communications Commission, Tech. Rep., November 2002.

[131] J. Mitola and G. Q. Maguire, "Cognitive Radio: Making Software Radios More Personal," *IEEE Personal Communications Magazine*, vol. 6, no. 4, pp. 13 – 18, August 1999.

[132] T. Yücek and H. Arslan, "A Survey of Spectrum Sensing Algorithms for Cognitive Radio Applications," *IEEE Communications Surveys and Tutorials*, vol. 11, no. 1, pp. 116 –130, 2009.

[133] L. Lu, X. Zhou, U. Onunkwo, and G. Y. Li, "Ten years of research in spectrum sensing and sharing in cognitive radio," *EURASIP Journal on Wireless Communications and Networking*, January 2012.

[134] E. Axell, G. Leus, E. G. Larsson, and H. V. Poor, "Spectrum Sensing for Cognitive Radio: State-of-the-Art and Recent Advances," *IEEE Signal Processing Magazine*, vol. 29, no. 3, pp. 101 – 116, May 2012.

[135] Z. Khalaf, "Contributions à l'étude de détection des bandes libres dans le contexte de la radio intelligente," Ph.D. dissertation, Supélec, Rennes, February 2013.

[136] R. Tandra and A. Sahai, "SNR Walls for Signal Detection," *IEEE Journal of Selected Topics in Signal Processing*, vol. 2, pp. 4 – 17, February 2008.

[137] W. Jouini, "Energy Detection Limits under Log-Normal Approximated Noise Uncertainty," *IEEE Signal Processing Letters*, vol. 18, no. 7, pp. 423 – 426, July 2011.

[138] R. Price and N. Abramson, "Detection Theory," *IEEE Transactions on Information Theory*, vol. 7, no. 3, pp. 135 – 139, July 1961.

[139] A. Sahai, N. Hoven, and R. Tandra, "Some Fundamental Limits on Cognitive Radio," in *Forty-Second Allerton Conference on Communication, Control and Computing*, September 2004.

[140] H. Tang, "Some physical layer issues of wide-band cognitive radio systems," in *IEEE International Symposium on New Frontiers in Dynamic Spectrum Access Networks*, Baltimore, Maryland, UA, November 2005, pp. 151 – 159.

[141] W. A. Gardner, "Exploitation of Spectral Redundancy in Cyclostationary Signals," *IEEE Signal Processing Magazine*, vol. 8, no. 2, pp. 14 – 36, April 1991.

[142] J. Lundén, V. Koivunen, A. Huttunen, and H. V. Poor, "Spectrum Sensing in Cognitive Radios Based on Multiple Cyclic Frequencies," in *Crowncom*, Orlando, USA, August 2007, pp. 37 – 43.

[143] Z. Khalaf, A. Nafkha, J. Palicot, and M. Ghozzi, "Hybrid Spectrum Sensing Architecture for Cognitive Radio Equipment," in *Advanced International Conference on Telecommunications*, May 2010, pp. 46 – 51.

[144] J. Ma and Y. Li, "Soft Combination and Detection for Cooperative Spectrum Sensing in Cognitive Radio Networks," in *GLOBECOM*, Washington, DC, November 2007, pp. 3139 – 3143.

[145] F. Iutzler and P. Ciblat, "Fully distributed signal detection: Application to cognitive radio," in *EUSIPCO*, September 2013.

[146] S. M. Kay, *Fundamentals of Statistical Signal Processing: Detection Theory.* Prentice-Hall, 1998, vol. 2.

[147] M. Abramowitz and I. Stegun, *Handbook of Mathematical Functions with Formulas, Graphs, and Mathematical Tables.* Ney York: Dover, 1970, ch. 6.

[148] V. I. Kostylev, "Energy Detection of a Signal with Random Amplitude," in *ICC 2002*, vol. 3, 2002, pp. 1606 – 1610.

[149] F. F. Digham, M.-S. Alouini, and M. K. Simon, "On the Energy Detection of Unknown Signals Over Fading Channels," *IEEE Trans. on Communications*, vol. 55, no. 1, pp. 21 – 24, 2007.

[150] M.-S. Alouini and A. J. Goldsmith, "A Unified Approach for Calculating Error Rates of Linearly Modulated Signals over Generalized Fading Channels," *IEEE Trans. on Communications*, vol. 47, no. 9, pp. 1324 – 1334, September 1999.

[151] X. Tang, M.-S. Alouini, and A. J. Goldsmith, "Effect of Channel Estimation Error on M-QAM BER Performance in Rayleigh Fading," *IEEE Trans. on Communications*, vol. 47, no. 12, pp. 1856 – 1864, December 1999.

[152] L. Cao and N. C. Beauieu, "Exact Error-Rate Analysis of Diversity 16-QAM With Channel Estimation Error," *IEEE Trans. on Communications*, vol. 52, no. 6, pp. 1019 – 1029, June 2004.

[153] A. Z. M. T. Islam and I. Misra, "Performance of Wireless OFDM System with LS-Interpolation-based Channel Estimation in Multi-path Fading Channel," *International Journal on Computational Sciences & Applications*, vol. 2, no. 5, October 2012.

[154] M. Krondorf, T.-J. Liang, and G. Fettweis, "Symbol Error Rate of OFDM Systems with Carrier Frequency Offset and Channel Estimation Error in Frequency Selective Fading Channels," in *ICC'07*, Glasgow, 2007, pp. 5132 – 5136.

[155] S. K. Wilson and J. M. Cioffi, "Probability Density Functions for Analyzing Multi-Amplitude Constellations in Rayleigh and Ricean Channels," *IEEE Trans. on Communications*, vol. 47, no. 3, pp. 380 – 386, March 1999.

[156] P. Djiknavorian, *"MIMO pour les nuls"*. Université de Laval, 2007.

[157] S. R. Saunders and A. Aragón-Zavala, *Antenna and propagation for wireless communication systems*, J. Wiley and Sons, Eds., 2007.

[158] J.-F. Pardonche, "Systèmes de transmission sans fil multi-émetteurs, multi-récepteurs pour des applications transports. etude des modèles de canal de propagation." Ph.D. dissertation, Université des sciences et technologies de Lille, 2004.

[159] A. Botonjié, "MIMO channel models," Master's thesis, Linköpings Universitet, 2004.

[160] A. Diallo, "Systèmes Multi-Antennes pour Diversité et MIMO," Ph.D. dissertation, Université de Nice-Sophia Antipolis, 2010.

[161] K. I. Pedersen, J. B. Andersen, J. P. Kermoal, and P. Mogensen, "A stochastic multiple-input-multiple-output radio channel model for evaluation of space-time coding algorithms," in *Vehicular Technology Conference Fall*, vol. 2, Boston, MA, September 2000, pp. 893 – 897.

[162] T. Fulghum, K. J. Molnar, and A. Duel-Hallen, "The Jakes Fading Model for Antenna Arrays Incorporating Azimuth Spread," *IEEE transactions on vehicular technologiy*, vol. 51, no. 5, pp. 968 – 977, September 2002.

[163] W. Weichselberg, M. Herdin, H. Özcelik, and E. Bonek, "A stochastic MIMO channel model with joint correlation of both link ends," *IEEE Tansactions on Wireless Communications*, vol. 5, no. 1, pp. 90 – 100, January 2006.

[164] S. Kozono, T. Tsuruhara, and M. Sakamoto, "Base station polarization diversity reception for mobile radio," *IEEE Transactions on vehicular technology*, vol. 33, no. 4, November 1984.

[165] R. G. Vaughan, "Polarization Diversity in Mobile Communications," *IEEE Transaction on Vehicular Technology*, vol. 39, no. 3, pp. 177 – 186, August 1990.

[166] T. Taga, "Analysis for Mean Effective Gain of Mobile Antennas in Land Mobile Radio Environments," *IEEE Transactions on Vehicular Technology*, vol. 39, no. 2, pp. 117 – 131, May 1990.

[167] F. Maier, A. Tissen, and A. Waal, "Evaluations and Measurements of a Transmitter Delay Diversity System for DRM+," in *WCNC*, Paris, France, 2012, pp. 1180 – 1184.

[168] ——, "Evaluations and Measurements of a Single Frequency Network with DRM+," in *European Wireless*, Poznan, Poland, April 2012.

[169] L. J. Cimini, B. Daneshrad, and N. R. Sollenberger, "Clusteired OFDM with Transmitter Diversity and Coding," in *GLOBECOM*, vol. 1, London, November 1996, pp. 703 – 707.

[170] Y. Li, J. C. Chuang, and N. R. Sollenberger, "Transmitter Diversity for OFDM Systems and Its Impact on High-Rate Data Wireless Networks," *IEEE Transactions on Selected Areas in Communications*, vol. 17, no. 7, pp. 1233 – 1243, July 1999.

[171] R. Obreja, H. Kneller, H. Zensen, E. Engberg, and A. Zink, "The Flexible Way from FM to Digital," June 2013.

[172] G. Auer, "Channel Estimation for OFDM with Cyclic Delay Diversity," in *PIMRC*, vol. 3, September 2004, pp. 1792 – 1796.

Abstract

In wireless communications systems, the transmission channel between the transmitter and the receiver antennas may disrupt the signal. Indeed, the channel can be frequency selective due to the multipath, and time selective if any element of the propagation environment is in motion. The multicarrier modulations, such as the orthogonal frequency division multiplexing (OFDM), are very robust against the multipath effect, and allow to recover the transmitted signal with a low error rate, when it is combined with a channel encoding. Furthermore, it is usual to consider that the channel frequency response is constant on each subcarrier, so the equalization is simply performed by a per subcarrier division. The channel estimation then plays a key role in the performance of the communications systems. For this reason, a great number of papers that propose various methods have been published for many years. Among them, we interest to the pilot aided techniques that use pilot tones to estimate the channel on some time and frequency positions. To do so, a lot of techniques are based on the least square (LS) and the minimum mean square error (MMSE) criteria. The LS is simple, but is sensitive to the noise level, and an interpolation is required if the pilot tone are scattered in the OFDM frame. The MMSE is optimal, but is much more complex than LS, and requires the a priori knowledge of the second order moment of the channel and the noise.

In this manuscript, two methods that allow to reach a performance close to the one of LMMSE while getting around its drawback are investigated. Thus, the proposed method called artificial channel aided-LMMSE (ACA-LMMSE) does not require the a priori knowledge of the channel covariance matrix nor its estimation. Moreover, this method is independent of the physical or statistical variations of the channel, so it reduces the complexity, since the covariance matrix just has to be computed once during the transmission. However, ACA-LMMSE supposes that the noise level is known at the receiver side. A second method then proposes to perform the joint estimation of the noise and the channel by means of the MMSE criterion. Consequently, as the estimation of each parameter requires the estimation of the other one, the proposed algorithm is iterative. In another way, a third part of this dissertation investigates the errors of estimation due to the interpolations. By combining a statistical and a geometrical study of the errors of interpolation, it is possible to derive an analytical expression of the mean square error (MSE) of the estimation and a theoretical expression of the lower bound of the bit error rate (BER) curves. Finally, a application of the cyclic delay diversity to a single frequency network (SFN) using the DRM/DRM+ standard is presented. The consequence of the increase of the frequency selectivity on the channel estimation is shown.